THE INTERACTIONS OF MOLECULAR FLUORINE AND XENON DIFLUORIDE WITH SILICON

by

MATTHEW RICHARD TATE

S.B. CHEMISTRY
UNIVERSITY OF CHICAGO
(1994)

SUBMITTED TO THE DEPARTMENT OF CHEMISTRY
IN PARTIAL FULFILLMENT OF THE REQUIREMENTS
FOR THE DEGREE OF

DOCTOR OF PHILOSOPHY

at the

MASSACHUSETTS INSTITUTE OF TECHNOLOGY

JUNE 1999

Signature of Author _____
Department of Chemistry
25 May 1999

Certified by _____
Sylvia T. Ceyer
Professor of Chemistry
Thesis Supervisor

Accepted by _____
Dietmar Seyferth
Chairman, Departmental Committee on Graduate Students

This doctoral thesis has been examined by a Committee of the Department of Chemistry as follows:

Professor Robert G. Griffin _____
Chairman

Professor Sylvia T. Ceyer _____
Thesis Supervisor

Professor Robert W. Field _____

The Interactions of Molecular Fluorine and Xenon Difluoride with Silicon

by

Matthew Richard Tate

Submitted to the Department of Chemistry
on 25 May 1999
in Partial Fulfillment of the Requirements
for the Degree of
Doctor of Philosophy in Chemistry

ABSTRACT

An experimental study of the chemical dynamics of the interactions of F_2 and XeF_2 with Si(100), two model gas-surface systems for semiconductor etching, is presented.

Three scattering channels are present in the interaction of low energy (E_i=0.7 kcal/mol) F_2 with Si(100) at 250 K: unreactive scattering and dissociative chemisorption via single atom abstraction or two atom adsorption, which are distinguished by the number of F atoms that adsorb to the surface. The absolute probabilities of these three scattering channels are determined as a function of fluorine coverage θ. On the clean Si(100) surface, two atom adsorption is the dominant reaction channel (P_2=0.83±0.03) relative to that of single atom abstraction (P_1=0.13±0.03). The total reactivity of the surface decreases with coverage as the number of unoccupied reactive sites, identified to be the Si dangling bonds using He diffraction, decreases. However, the probability of single atom abstraction increases at the expense of two atom adsorption attaining a maximum (P_1=0.35±0.08) at θ=0.5 ML. At θ=1 ML, there are no unoccupied dangling bonds and the reaction with F_2 ceases. No etching is observed to occur.

A statistical model is developed that gives a good description of the coverage dependence of the reaction probabilities of F_2 with Si(100). The model is based on the premise that the two dissociative chemisorption mechanisms share a common initial step, F atom abstraction. The subsequent interaction, if any, of the complementary F atom with the surface determines if the overall result is single atom abstraction or two atom adsorption. The results are consistent with the orientation of the incident F_2 molecular axis with respect to the surface affecting the probability of single atom abstraction relative to two atom adsorption. A perpendicular approach favors single atom abstraction because the complementary F atom cannot interact with the surface, whereas a parallel approach allows the F atom to interact with the surface and adsorb. The fate of the complementary F atom is dependent on the occupancy of the site with which it interacts. The model is also based on the premise that the four distinguishable types of sites on the Si(100)(2x1) surface, based on the occupancy of the site itself and the complementary Si atom in the Si surface dimer, have different reactivities with F_2 and F atoms. The results show that the unoccupied sites on half-filled dimers are more reactive than those on empty dimers, which is consistent with an enhanced reactivity due to a loss of a stabilizing π interaction between the two unoccupied dangling bonds on a dimer.

Three analogous scattering channels are also present in the interaction of XeF_2 with Si(100) at 250 K. Despite the observation that XeF_2 is able to etch Si unlike F_2, the initial adsorption of fluorine upon exposure to XeF_2 occurs primarily at the dangling bonds. However, at a coverage around 1 ML, there are no unoccupied dangling bonds on the well-ordered surface, but XeF_2 continues to react with Si and etch product SiF_4 is desorbed. To better compare the dynamics of the interactions of XeF_2 with Si to those of F_2 with Si, the investigation focuses on the initial fluorination to coverages around 1 ML. There are several significant differences between the two gas-surface systems. First, the reaction probability of XeF_2 is only weakly dependent on coverage indicating the presence of an extrinsic physisorbed precursor. Second, although single atom abstraction is present, the scattered XeF behaves differently than the F atom that is produced in the interaction of F_2 with Si. The angular distribution of the scattered XeF flux is strongly dependent on coverage and is directed along the surface normal at coverages around 1 ML, suggesting that the incident XeF_2 is aligned during the reaction because of steric hindrance from the other adsorbates. The presence of scattered F atoms in the interaction of XeF_2 with Si suggests that there is channeling of a sufficient fraction of the exothermicity of atom abstraction into the internal energy of the weakly bound XeF, leading to the dissociation of XeF and scattering of an F atom into the gas phase. Finally, two atom adsorption is present based on the observation of reactively scattered Xe. Although conclusive identification and characterization of the velocity and angular distribution of this reactively scattered Xe are elusive, the results show that no Xe gains a large fraction of the total exothermicity available from two atom adsorption, suggesting that the interaction of XeF_2 with Si is a stepwise process just as in the interaction of F_2 with Si.

Thesis Supervisor: Sylvia T. Ceyer
Title: J.C. Sheehan Professor of Chemistry

To My Mom and Dad

Acknowledgements

It is well known that the page of acknowledgements is the one part of a thesis that is read by people other than the author, the advisor, and the committee. Perhaps this is appropriate because although this thesis represents the scientific knowledge that I have gained over the past five years, it is only a fraction of all that I have learned during that time. While I learned a lot about interactions of F_2 and XeF_2 with Si(100), I learned the most through my interactions with all of the people that I had the opportunity to collaborate with, whether at work or at play.

Without a doubt, my advisor, Sylvia Ceyer, has been the most influential person during my time at MIT. She constantly challenged me to motivate myself, to teach myself, and to assert myself. It is from these challenges that I learned so much not only about science, but about myself. Regardless of where my future may take me, I will always be able to use the insight that I have gained through my relationship with Sylvia.

Thanos Tsekouras was my mentor in the laboratory during my first two years at MIT. As anyone who has met Thanos can attest, he can be extremely intimidating because of his raw intelligence and brutal honesty. However, instead of hiding from his criticism, I decided to accept his criticism of my ideas, which was constant in the beginning of our relationship, and he showed me how to use my intuition to think about problems that I had no formal training in solving. He also taught me that the answer to, "What do you think about my idea?" is not simply, "It's good." At a time when society is too afraid to criticize and unable to accept criticism, Thanos affirmed my belief that critical thought does not come without critique. Finally, not only did Thanos teach me a great number of things, but, most importantly, he also became a good friend.

David Gosalvez-Blanco and Ted Trautman are great friends from an earlier generation of the Ceyer group. David's enthusiasm for chemical dynamics as well as good food and wine were a perfect match to my own interests. I admire his "European" attitude of working to live as opposed to the "American" attitude of living to work. Ted's midwestern work ethic and his tendency to be a joker at the same time created an ideal environment in the laboratory that made the my first two years of graduate school a joy. Kerstin Haug, the last member of the original Ceyer group that I joined in 1994, became a valuable colleague and good friend who was always willing to discuss any issue, scientific or otherwise, even while she in the midst of finishing her thesis.

My colleagues Stacey Eckman, Judson Holt, and Massimo Bertino were essential for sharing the joys of signal averaging with me. Without their contributions, the signal-to-noise ratio of the time-of-flight data presented in the xenon difluoride chapter would be precisely half of what it is. Stacey and Judson endured my development as a mentor, and, thankfully, we have still managed to remain good friends. Massimo was an encyclopedia of scientific knowledge... and of Italian words that do not exist in any dictionary. Finally, Bob Hefty and Dave Lahr have become a good friends and colleagues in our short time together, whether it was pointing out the

errors in my logic or executing an elaborate practical joke. I sincerely hope that all of you find satisfaction in your future endeavors. The force will be with you all... always.

Laurie Butler was my first scientific mentor and the one who first showed me the beauty of chemical dynamics. She has been a constant source of advice and encouragement. I am grateful for the great interest she has always had in my professional development since I graduated from college.

Marianne and Stephen Empedocles have been wonderful friends outside of the laboratory. I greatly appreciate their honest advice, without which I am certain that there are many things that I would not have accomplished here in five years. I am especially grateful for the two of them entertaining me every other weekend during this past year when I was living alone.

Of course, my parents have been extremely influential in my development. Both of them have always had complete confidence in me, allowing me to make all of the choices that I have been faced with throughout my life. I am especially grateful that they each expressed their belief in me in completely different ways. My mother has always believed that I could do anything I desired. My father has always questioned my idealistic desires and demanded pragmatism. I am extremely grateful for their complementary points of view. It is to them that this thesis is dedicated.

Finally, my life would not be complete without Anu. Her support and encouragement, as well as her ability to make me smile at times when I thought I had no reason to smile, have been absolutely essential to my happiness and any success that I have had over the years. After having lived apart for five of our ten years together, I look forward to spending the rest of my life with her, living under the same roof and never having to count the hours until the weekend again.

Table of Contents

List of Figures

Chapter 1: The Interaction of F_2 with Si(100)

Chapter 2: The Interaction of XeF_2 with Si(100)

Chapter 1: The Interaction of F_2 with Si(100)

I. INTRODUCTION

Dissociative chemisorption is a fundamental step in the mechanism of chemical processes such as heterogeneous catalysis, chemical vapor deposition, and semiconductor etching. The classic picture of dissociative chemisorption is cleavage of a bond between two atoms in a molecule incident on a surface concomitant with the formation of a bond between each of the atoms and the surface. The energy released in the formation of two bonds to the surface is necessary to compensate for the energy required to cleave the molecular bond. In contrast to dissociative chemisorption, cleavage of a molecular bond upon formation of only a single bond to the surface is possible if the molecular bond energy is less than the energy released upon formation of the single bond to the surface. In this case, the complementary fragment of the incident molecule is scattered into the gas phase. By analogy to the well-known gas phase abstraction mechanism, this gas-surface mechanism is called atom abstraction. Phenomenologically, atom abstraction is the reciprocal process to the Eley-Rideal mechanism [1]. In the former case, the surface abstracts an atom from the incident particle whereas in the latter case, the incident particle abstracts an adsorbate from the surface.

Only recently has an experiment, which probed the interaction of F_2 with Si(100), conclusively demonstrated atom abstraction [2,3,4,5,6]. Despite extensive investigations of this particular important model system for semiconductor etching [7], atom abstraction has not been reported [8,9]. The experimental difficulties are similar to those that precluded the direct observation of the Eley-Rideal mechanism until half a century after it was first proposed [10,11]. In the case of atom abstraction, the observable is the atom or radical that is scattered into the gas phase. Because these scattered particles are highly reactive, they must be detected prior to

reaction with other surfaces (i.e., chamber walls) or gas phase species. This requirement necessitates an ultrahigh vacuum environment with sensitive line-of-sight detection of the scattered products. Even though their detection is experimentally difficult, knowledge of the presence or even the plausibility of this mechanism is important from a practical standpoint because atom abstraction produces open shell atoms and radicals in the gas phase that may subsequently react in the gas phase or on other surfaces. The failure to properly account for these additional reactions in many applications may have significant implications not only for semiconductor etching but for such diverse applications as heterogeneous catalysis and chemical vapor deposition.

Of course, the fate of the complementary atom or fragment is not necessarily as a gas phase particle. The scattered complementary species may subsequently interact with the surface of interest and if there is a reactive site near this interaction, it also may adsorb. Consequently, atom abstraction and the subsequent adsorption of the complementary species results in the formation of two surface-adsorbate bonds just as in classic dissociative chemisorption. However, this process, called two atom adsorption, is distinct from classic dissociative chemisorption in that it is not necessarily a concerted process. The fate of the complementary particle is independent of the abstracted atom. The complementary species may adsorb on an adjacent site as in classic dissociative chemisorption or, after undergoing motion along the surface, it may adsorb on a non-adjacent site in contrast to classic dissociative chemisorption. It may also scatter back into the gas phase after undergoing motion along the surface.

Unlike the dearth of experimental results for atom abstraction, several theoretical investigations of the F_2/Si system have emphasized the atom abstraction mechanism. Stillinger

and Weber (SW) developed one of the first potential energy hypersurfaces for the F_2/Si interaction using empirical two- and three-body potentials [12]. Their subsequent molecular dynamics simulations demonstrated the possibility of F atom abstraction. Weakliem, Wu, and Carter (WWC) modified the SW potential by incorporating *ab initio* results of the interaction of F with Si clusters which enhanced the total reactivity of F and F_2 with Si [13,14,15,]. Further molecular dynamics simulations using the WWC potential probed the effects of incident translational and vibrational energy [16,17], as well as surface steps [18] and defects [19]. In addition, Schoolcraft and Garrison [20] performed molecular dynamics simulations on the F_2/Si(100) system using the WWC potential. The experimental observation of atom abstraction now provides the opportunity to test the accuracy of these potential energy surfaces.

The experimental results and data analysis on the interaction of low energy F_2 with Si(100) at 250 K have been presented in detail elsewhere [2,4,5,6]. In the experiment, fluorine atom abstraction was identified by direct observation of the scattered fluorine atoms. The flux of scattered products was measured and the absolute probability for F_2 to undergo either single atom abstraction or two atom adsorption was determined as a function of F_2 exposure. Finally, with the knowledge of the absolute incident molecular beam flux, the absolute probability for F_2 to access one of the two dissociative chemisorption channels was determined as a function of fluorine coverage.

At low coverage the dominant reactive channel is two atom adsorption. In the limit of zero coverage, the probability of two atom adsorption P_2 is 0.83 ± 0.03. Despite being a seemingly second order adsorption process, the probability of two atom adsorption decreases almost linearly with coverage deviating from linearity only near the saturation coverage of one

monolayer (1 ML, one F atom per surface Si atom). Single atom abstraction is the minor reactive channel at low coverage. In the limit of zero coverage, the probability of single atom abstraction P_1 is 0.13±0.03. The probability of single atom abstraction increases with coverage to a maximum value of 0.35±0.08 around 0.5 ML. At the maximum, the probability of single atom abstraction and two atom adsorption are nearly equal. As the coverage increases beyond 0.5 ML, the probability of single atom abstraction and two atom adsorption monotonically decay to zero around 1 ML.

In this chapter, a simple yet physically intuitive statistical model is developed to describe the experimentally observed kinetics of the interaction of low energy F_2 with Si(100). Specifically, the model describes the probability of single atom abstraction and two atom adsorption as a function of exposure to F_2. The F_2 exposure dependence of the reaction probabilities can be related to the dependence of the reaction probabilities on fluorine coverage, which is the parameter of interest because it represents the number of reactive sites on the surface. The model is based on the premise that two atom adsorption is not necessarily a concerted process, like classic dissociative chemisorption, and is, in fact, intimately related to single atom abstraction. In addition the model allows for a different reactivity for the different sites on the Si(100)(2x1) surface, which consists of rows of Si dimers. Each surface Si atom has a single dangling bond projecting into the vacuum that is the site of reactivity. The different reactivity is based on the occupancy of the complementary dangling bond on the Si dimer. The results of the theoretical model match the experimental measurements well. Most importantly, the model correctly predicts two distinct features of the experimental results: 1. the nonmonotonic dependence on the coverage of the probability of single atom abstraction and 2.

the linear dependence on the coverage of the probability of two atom adsorption. Both features are unexpected from the traditional Langmuirian point of view of gas-surface chemical kinetics.

The chapter is divided into several sections. Section II gives a brief overview of the experimental results showing the identification of F atom abstraction and the determination of the absolute probabilities of the three reaction channels as a function of F_2 exposure and fluorine coverage. In Section III, the statistical model is developed from a minimal set of assumptions and compared to the experimental results. Section IV is a discussion of the model and its implications on the dynamics of the interaction between F_2 and Si(100) as well as its limitations in describing a complex chemical interaction in simple statistical terms. The results from the experimental measurements and the theoretical model are compared with the results of previous experimental and theoretical work.

II. REVIEW OF EXPERIMENTAL RESULTS

II.A. Experimental

The apparatus has been described in detail elsewhere [21,22,23,24]. Briefly, the apparatus consists of two supersonic molecular beam sources coupled to an ultrahigh vacuum chamber (base pressure=$5x10^{-11}$ torr) containing the silicon crystal and a triply differentially pumped line-of-sight rotatable quadrupole mass spectrometer as well as an ion sputtering gun, a cylindrical mirror electrostatic analyzer for Auger electron spectroscopy and a mass spectrometer for residual gas analysis.

II.A.1. Molecular fluorine beam

The supersonic molecular beams are skimmed and collimated through two differentially pumped regions. Typical expansion conditions of 200 torr stagnation pressure with a room temperature nozzle of 75 μm orifice diameter yield a nearly monoenergetic molecular beam ($\Delta E/E=0.17$) as determined from the velocity distribution of the incident beam measured using a time-of-flight (TOF) technique. In the experiments described in this chapter, F_2 (97%, Air Products, subsequently purified through an HF trap, Matheson) is seeded in either Kr (99.997%, Spectra Gases) or Ar (99.9995%, Spectra Gases). The average translational energy of F_2 in these mixtures is E_i=0.031 eV (0.7 kcal/mol) and 0.064 eV (1.5 kcal/mol), respectively, determined from TOF measurements of the incident beam. The absolute F_2 flux of the beam incident on the crystal at normal incidence is ~0.09 ML F/s. The method for measuring the absolute flux of a seeded molecular beam has been described in detail [4,6].

II.A.2. Si(100) crystal

The crystal is mounted between two Ta clamps that are attached to the manipulator. The crystal is mounted such that the crystal face is flush with the Ta brackets to preclude its shadowing by the brackets. The crystal normal can be rotated in the scattering plane defined by the axes of the two molecular beams and the detector. The axis of rotation is perpendicular to and intercepts the intersection of these three axes. The crystal can be cooled to 125 K with liquid N_2 and heated resistively to ~1100 K. Its temperature is measured via a W-5%Re/W-26%Re thermocouple spot welded to a thin Ta tab in thermal contact with the back of the crystal. The surface temperature is held constant at 250 K during F_2 exposure.

The Si crystal is cut along the (100) plane. Both lightly n-type and p-type doped Si with resistivities of 8-12 Ω cm have been used. No differences in reactivity have been observed for the two types of doping. The Si crystal is cleaned by a wet etching procedure [25] prior to installation into the vacuum chamber. The crystal is sputtered with 1.5 keV Ar^+ and subsequently annealed to ~1100 K. This process is repeated until C and O contamination are below the 1% sensitivity limit of Auger electron spectroscopy. No metal contamination, such as W, Ta, Cu, Ni, is observed. The crystal is typically mounted such that the scattering plane, defined by the beams, crystal normal and detector, is along the (10) direction of the crystal surface. Helium diffraction confirms the (2x1) periodicity of the reconstructed Si(100) surface. A brief anneal of the crystal to about 1100 K after each F_2 exposure removes all the fluorine and results in recovery of the 2x1 periodicity of the surface. The crystal is sputtered and annealed daily to ensure surface cleanliness and order. The crystal is replaced when an etch spot becomes

visible, typically after several months of experiments. No difference in reactivity is observed over the lifetime of the crystal.

II.A.3. Detection scheme

Primary measurements are made with a triply differentially pumped, rotatable quadrupole mass spectrometer with electron bombardment ionization. A channeltron electron multiplier is used to detect the ions. The detector rotates about the center point of the intersection of the incident beam and the crystal normal. The angular range is 35°-180° with respect to the incident beam. The solid angle subtended by the detector is 5.8×10^{-4} sr. The angular resolution in the scattering plane is 3.52°. The rotation of the crystal and detector allow for a wide range of incident and detection angles. A pseudorandom chopper wheel with 255 slots and spinning at 280 Hz or at 400 Hz at the entrance of the detector allows for measurements of the velocity distribution of both the incident beam as well as the scattered products using a cross correlation TOF technique. The neutral flight path is 29.3±1.27 cm. The energy resolution is limited to $\Delta E/E=0.17$ because of the uncertainty in the path length that is a result of the finite length of the ionizer [26].

II.B. Results

II.B.1. Identification of F atom abstraction

In principle, F atom abstraction could be identified via observation of the scattered F atom, detected as F^+ (m/e=19). However, unreactively scattered F_2 molecules also contribute to the m/e=19 signal because they dissociatively ionize (or crack) to form F^+ in addition to ionizing to form F_2^+ (m/e=38) in the electron bombardment ionizer. The ratio of the F^+ signal to the F_2^+ signal measured by ionization of the incident F_2 beam by 70 eV electrons lies in the range 0.25-

0.40, depending on the ionizer and quadrupole mass filter settings. This ratio is called the F^+/F_2^+ cracking ratio. While a discrepancy between this ratio and that of the F^+/F_2^+ signals of scattered F_2 might signal the production of F atoms by abstraction, the contributions of F atoms and F_2 molecules to the F^+ signal can be distinguished unambiguously by measuring the velocities with which the two particles scatter from the surface. The unreactive F_2 molecules ought to scatter with low velocities not much greater than the incident velocity of 395 m/s and the F^+ formed by dissociative ionization of this F_2 will have the same velocity. On the other hand, the F atoms scattered as products of atom abstraction ought to be translationally hot because of the exothermicity of the reaction. Figure 1(a) shows a superposition of TOF spectra measured at m/e=19 and m/e=38 of low energy F_2 at E_i=0.7 kcal/mol scattered from Si(100) at 250 K and integrated over a range of F_2 exposure, 0-1.9 ML F atom. The flight times are corrected for ion flight time and electronic delay. The m/e=19 distribution is distinctly bimodal with a narrow fast feature and a broad slow feature while the m/e=38 signal is comprised of a single slow feature. The m/e=38 signal is scaled by the measured F^+/F_2^+ cracking ratio. The resulting absolute value of the m/e=38 signal represents the component of the m/e=19 signal resulting from dissociative ionization of F_2 and it matches well the intensity of the broad slow feature of the m/e=19 signal. Therefore, the broad slow feature in the m/e=19 distribution arises from F^+ produced from the cracking of unreactively scattered F_2 whereas the narrow fast feature must arise from F atoms. Figure 1(b) shows the net scattered F atom signal obtained by subtracting the m/e=38 signal multiplied by the cracking ratio from the m/e=19 signal. The average velocity of scattered F atoms and F_2 is 1195±57 m/s and 440±20 m/s, respectively, where the major contribution to the uncertainties is the length of the flight path due to the finite length of the ionization region, 2.54

cm. The velocity distribution of the unreactively scattered F_2 is best fit by a Maxwell-Boltzmann distribution with a temperature of 248 K, essentially identical to the surface temperature of 250 K.

The TOF distributions shown here have been signal averaged over a wide range of F_2 exposure, 0-1.9 ML F, which corresponds to the entire range of fluorine coverage, 0-1 ML, as described in Section II.C. Therefore, the TOF distributions could be artificially broadened if they were sensitive to fluorine coverage. However, TOF distributions signal averaged over narrower ranges of F_2 exposure show that the F atom and F_2 velocity distributions are independent of exposure. The average velocities of some of these distributions are plotted in Figure 2. The full widths at half of the maximum of the corresponding distributions are plotted as the error bars in Figure 2. These results show that the dynamics of the interaction of F_2 with Si are insensitive to neighboring adsorbates.

Although the fast F atoms at m/e=19 that scatter from Si upon reaction with F_2 do not arise from the dissociation of unreactively scattered F_2 in the ionizer, there are other possible sources of signal at m/e=19 to consider. For example, F atoms in the incident beam could survive the collision with Si and be scattered, but this possibility is highly unlikely because there is essentially no dissociation (10^{-8}%) of F_2 to F at 300 K and 200 Torr. The cracking of desorbing etch products (SiF_2, SiF_4, Si_2F_6) could yield signal at m/e=19, but no species other than F, F_2, and Kr carrier gas are observed to scatter within the limit of the detection sensitivity of approximately 10^{10} particles/s or 10^{-5} ML/s The velocity distribution as well as the relative branching of F and F_2 is independent of the scattering geometry. Finally, it is energetically possible for the F atoms produced as a result of atom abstraction to scatter from the surface as

negative ions. This possibility was examined by placing a Faraday cup around the crystal, but no ions above the sensitivity limit of 10^{-7} ML/s were detected upon biasing either the cup or the crystal both positive or negative during exposure to the F_2 beam.

The results presented above are for a single scattering geometry in which the F_2 beam is at normal incidence to the surface, θ_i=0°, and the detector is positioned at 35° from the surface normal, θ_d=35°. Similar TOF measurements have been made at other detection angles as well as at θ_i=35° and other detection angles. Figure 2 shows the average velocities determined from these TOF measurements carried out for a variety of scattering geometries. These average velocities are independent of the scattering geometry. In addition, the velocity distributions from which these averages are determined are independent of the scattering geometry. Although these velocity distributions are not shown here, their full widths at half of the maximum are shown as the error bars in Figure 2 and are observed to be independent of the scattering geometry.

To investigate the nature of the high translational energy of the F atoms, similar TOF measurements were made at a surface temperature of 1000 K. Figure 3(a) shows a superposition of TOF spectra measured at m/e=19, m/e=38, as well as m/e=47, which corresponds to SiF^+ arising from the dissociative ionization of the SiF_2 that desorbs at this high temperature during the exposure to F_2. The m/e=38 and m/e=47 signals are multiplied by the appropriate cracking ratios to represent contributions of F_2 and SiF_2 to the F^+ signal. Figure 3(b) shows the time distribution of the net scattered F atom signal obtained by subtracting the m/e=38 and m/e=47 signals multiplied by the appropriate cracking ratios from the m/e=19 signal. A scaled net F atom TOF distribution measured from a 250 K surface is superimposed for comparison and it is seen to be nearly identical to the one measured at 1000 K. Figure 3(c) shows these distributions

transformed into energy distributions, from which the average energies are calculated to be 3.7±0.4 and 4.1±0.4 kcal/mol at 250 K and 1000 K, respectively. The insensitivity of these distributions to surface temperature demonstrates that the high translational energy of the F atoms is derived from the reaction exothermicity and not from the thermal motion of the surface atoms.

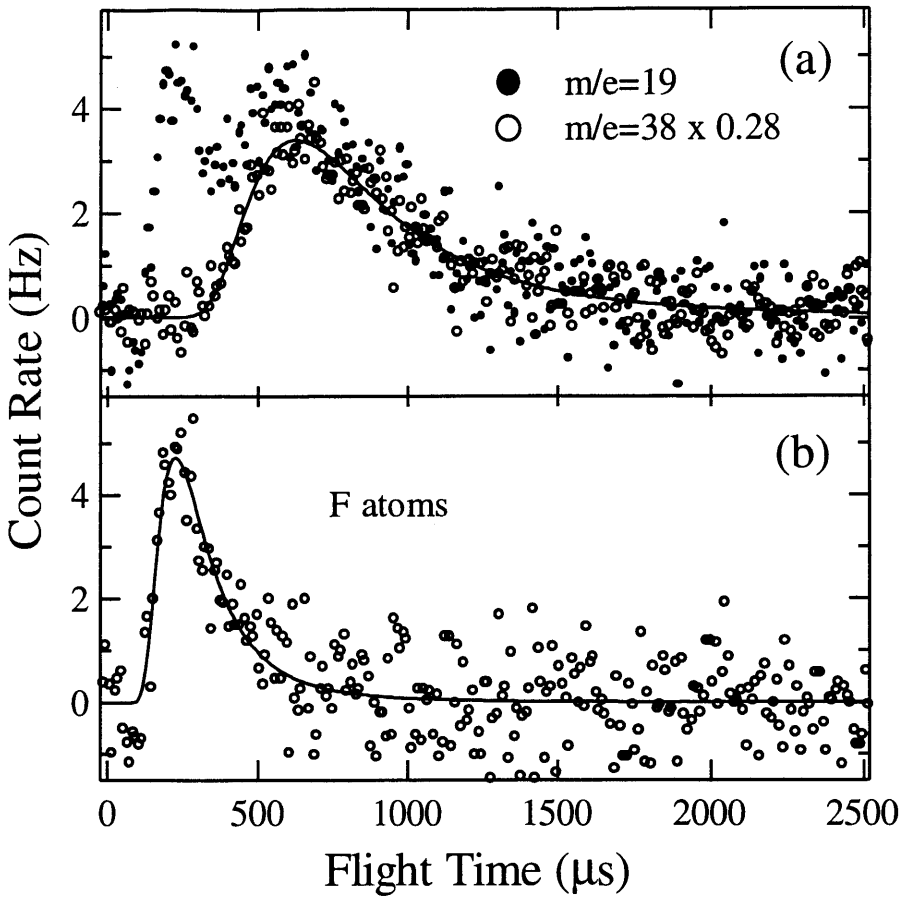

Figure 1 Time-of-flight distributions of F and F_2 scattered from Si(100) at 250 K upon F_2 exposure

(a) TOF spectra at m/e=38 multiplied by F_2 cracking ratio and at m/e=19 measured at θ_i=0°, θ_d=35° and T_s=250 K. (b) Net scattered F atom TOF spectrum obtained by point-by-point subtraction of m/e=38 signal multiplied by cracking ratio from m/e=19 signal in (a). Solid lines show least squares fit of Maxwell-Boltzmann function $F(t)=Bt^{-4}\exp(-m(d/t)^2/2kT)$ for a number density distribution where t is flight time, d is flight length, T is beam temperature and m is mass. Spectra averaged over F_2 exposure of 0-1.9 ML F atom. Average velocities of corresponding flux distributions are $v(F_2)$=440±20 and v(F)=1195±57 m/s.

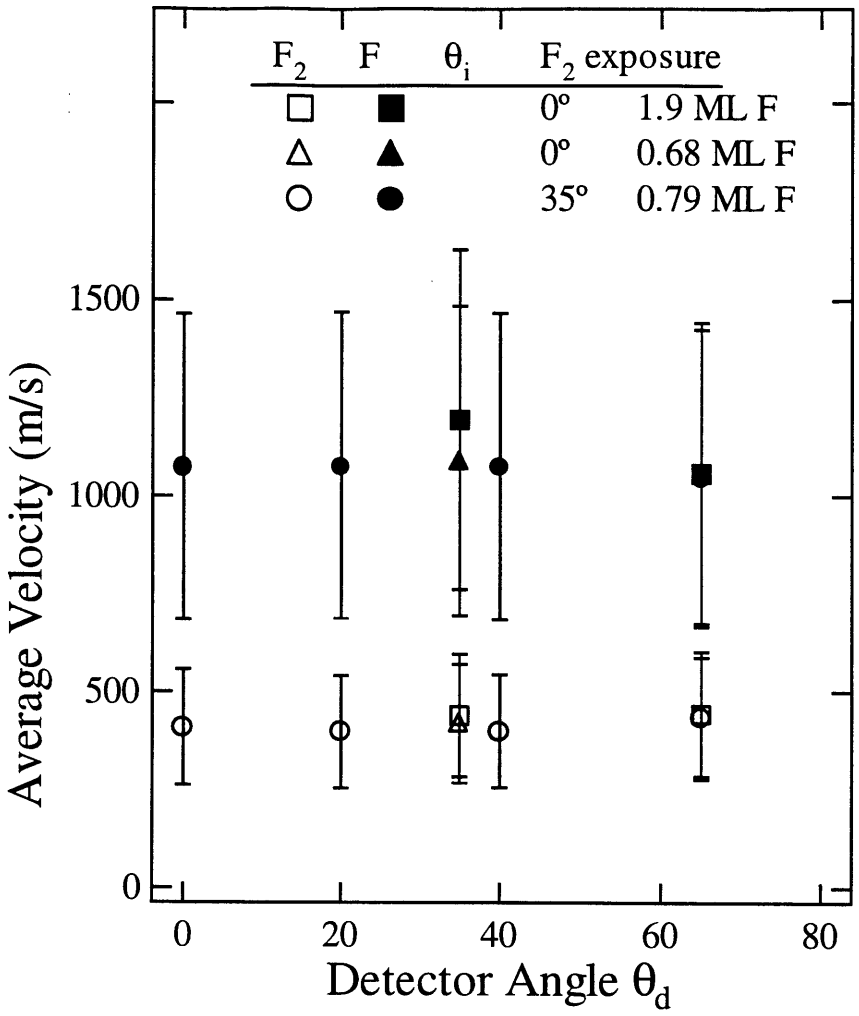

Figure 2 Average velocity of F and F_2 scattered from Si(100) at 250 K as a function of scattering geometry and F_2 exposure

Average velocity of scattered F atom and F_2 for a variety of scattering geometries and F_2 exposures at E_i=0.7 kcal/mol and T_S=250 K, determined from fitting procedure identical to that in Figure 1. Error bars represent full width at half of the maximum of velocity distributions. The uncertainty of the average velocity is typical of that in Figure 1.

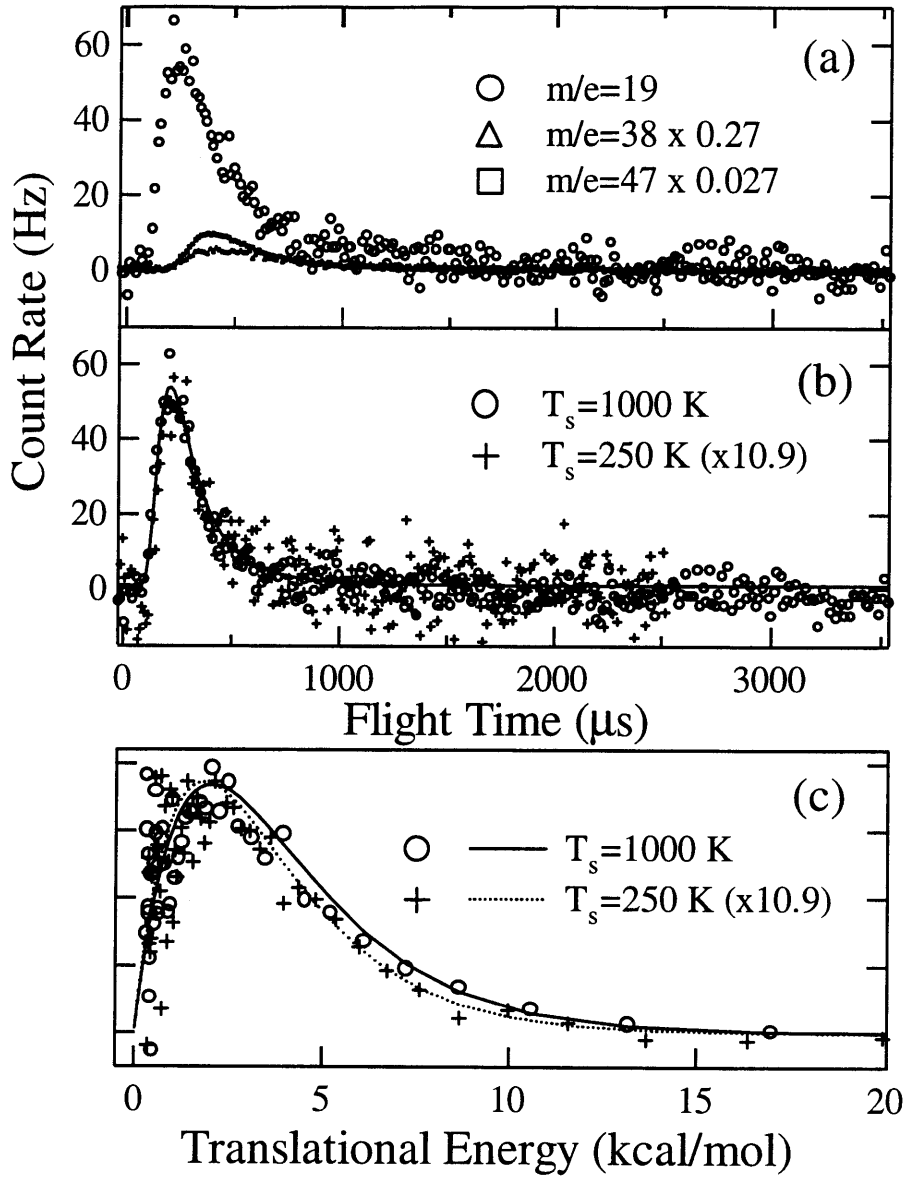

Figure 3 Comparison of kinetic energy distributions of F atoms scattered from Si(100) at 1000 K and 250 K

(a) TOF spectra at m/e=19, m/e=38 and m/e=47 measured at θ_i=0°, θ_d=35° and T_s=1000 K. Data at m/e=38 and m/e=47 multiplied by F_2 and SiF_2 cracking ratios, respectively. (b) Net scattered F atom TOF spectrum obtained by point-by-point subtraction of m/e=38 and m/e=47 signals multiplied by appropriate cracking ratios from m/e=19 signal in (a). Net scattered F atom TOF spectrum at T_S=250 K, scaled by 10.9, is superimposed for comparison. Lines show least squares fit as in Figure 1. (c) Kinetic energy flux distributions of F atoms scattered from surface at T_S=250 and 1000 K. Scaling factor of 10.9 determined by normalizing energy distributions at peak values.

II.B.2. F atom abstraction as a function of exposure

In addition to direct identification of F atom abstraction, this investigation identifies the sites for abstraction and adsorption and determines the absolute probabilities for the three possible outcomes of the interaction of a F_2 molecule with a Si(100) surface: dissociative chemisorption via single atom abstraction, dissociative chemisorption via two atom adsorption and unreactive scattering. These probabilities are quantified in the limit of zero F coverage as well as for all F coverages up to the saturation coverage. These goals require that the exposure dependence of the scattered products be measured.

II.B.2.a. Exposure Dependence of Scattered Products

The coverage dependence of the three reaction channels is contained in measurements of the scattered F and F_2, the products of atom abstraction and unreactive scattering, respectively, as a function of F_2 exposure. Figure 4(a) shows the signals at m/e=19 and m/e=38 as a function of F_2 exposure averaged over 25 exposures of the clean crystal to F_2. These two signals are collected almost simultaneously during a single F_2 exposure by switching the quadrupole mass filter between m/e=19 and m/e=38 at a rate of 10 Hz. Signal is collected beginning 5 ms after each switch to account for the finite switching time of the quadrupole power supply. The incident F_2 flux is low enough that the 5 Hz sampling rate per ion provides sufficient time resolution to observe the kinetics of the reaction. The m/e=38 signal in Figure 4(a) is multiplied by the cracking ratio of F_2 to show the contribution of F_2 to the m/e=19 signal. Two observations are apparent. First, the m/e=19 and scaled m/e=38 signal levels are identical at long exposure. Thus, no F atoms are observed at long exposure, meaning that atom abstraction ceases at high coverage. Second, the m/e=19 and scaled m/e=38 signals evolve differently at low

exposure. The larger signal at low exposure, m/e=19, arises from scattered F atoms as a consequence of atom abstraction. Figure 4(b) shows the net F atom signal as a function of exposure obtained by point-by-point subtraction of the m/e=38 signal multiplied by the F_2 cracking ratio from the m/e=19 signal. The F atom signal, which is proportional to the probability of single atom abstraction, is low, but nonzero, at zero exposure, proceeds through a maximum at intermediate exposure, and decays to zero at long exposure. A quantitative analysis of the exposure dependence of the scattered products is given in Sec. II.C.

The exposure dependence of the scattered products described above is for a single scattering geometry, θ_i=0° and θ_d=35°. Considering the hyperthermal velocity of the F atoms shown in Section II.B.1, it is possible that the F atoms are anisotropically scattered. To investigate this possibility, the exposure dependence of the m/e=19 and m/e=38 signals was measured at θ_d=65° and is compared to that measured at θ_d=35° in Figure 5. Figure 5(a) shows the m/e=38 signal at θ_d=65° multiplied by a factor of 2.14. This factor is determined by requiring the m/e=38 signal at long exposure and at θ_d=65° to equal that at θ_d=35°. As evident in Figure 5(a), scaling the m/e=38 signal at θ_d=65° in such a manner allows the identicalness of the exposure dependence of the signals at the two detection angles to be easily seen in the regime of low exposure, where the probability of dissociative chemisorption of F_2 is not zero. Therefore, the angular distribution of the scattered F_2 does not change as the exposure increases. The net m/e=19 signal at θ_d=35° and that at θ_d=65° scaled by a factor of 2.14, both determined as described for the plot in Figure 4(b), are shown in Figure 5(b). The exposure dependence of the net m/e=19 signal at low exposures is again identical at the two detection angles, indicating that the angular distribution of the F atom signal does not change as the exposure increases. In

addition, not only are the F atom and F_2 angular distributions independent of exposure, but the applicability of the same scale factor, 2.14, to both the F atom and the F_2 data, demonstrates that the F atom and the F_2 angular distributions are the same. The nature of the angular distributions is discussed below.

Figure 6 shows the exposure dependence of the m/e=38 and the net m/e=19 signals, respectively, measured at θ_i=35°and at four detection angles. The m/e=38 signals at θ_d=20°, 40°, 65° are scaled to the m/e=38 signal at θ_d=0° and at long exposure, using the method described for the data in Figure 5(a). The net m/e=19 signals are scaled by the factors determined in Figure 6(a) using the method described for the data in Figure 5(b). Again, the identicalness of the exposure dependence of the scaled signals and the applicability of the same scale factor to both the m/e=38 and the net m/e=19 signals indicates that the F_2 and F atom angular distributions do not vary with exposure and that the F_2 and F atom angular distributions are the same at θ_i=35°. Figure 7 shows the angular distribution of the flux of F_2 and F atom scattered from the surface determined by integrating the scattered signal intensities over various F_2 exposure intervals. The angular distribution of the scattered flux of both F_2 and F are isotropic and independent of fluorine coverage due to F_2 exposure. In addition, the angular distribution arising from scattering F_2 at θ_i=0° and θ_i=35° incident angle are similar indicating the insensitivity of the dynamics of the scattered products of the interaction of F2 with Si(100) on incident angle.

The effect of the crystal's azimuthal orientation with respect to the scattering plane on the exposure dependence of the m/e=38 and m/e=19 signals was also examined. It is well known that orthogonal domains of (2x1) periodicity form on the Si(100) surface as a result of single steps created from even the slightest miscut of the crystal [27]. Therefore, scattering along the

(10) direction actually samples scattering perpendicular to as well as parallel to the dimer rows. The experiments were repeated at θ_i=0° with the crystal azimuth rotated 45° such that the scattering was along the (11) direction and at θ_d=35°. The m/e=38 and m/e=19 signals for this scattering geometry are shown in Figure 8, scaled as described in Figures 5 and 6 to the m/e=38 signal and net m/e=19 signals measured along the (10) azimuth and at θ_i=0° and θ_d=35°. Note that the results for scattering along the (10) and (11) directions are identical. Thus, the interaction of F_2 with Si(100) is essentially isotropic.

The observation that the F_2 signal level attains a steady state implies that there is either continuous constant reaction or no reaction at long exposure. Two observations already noted suggest that the reaction ceases and that F_2 merely passivates the Si surface. First, no etch products are observed to desorb. Therefore, if a continuous constant reaction were taking place, all F_2 that reacts would have to be continually incorporated onto or into the Si. A steady state reaction on a constantly changing surface is unlikely relative to a reaction that ceases when all of the reactive sites are occupied. Secondly, no F atoms are scattered in the steady state regime. As discussed below, single atom abstraction and two atom adsorption are related processes. It is unlikely that one process could cease while the other continues to occur. Thermal desorption and He diffraction measurements discussed in the following sections are utilized to confirm that the interaction of low energy F_2 with Si at 250 K is a passivation reaction.

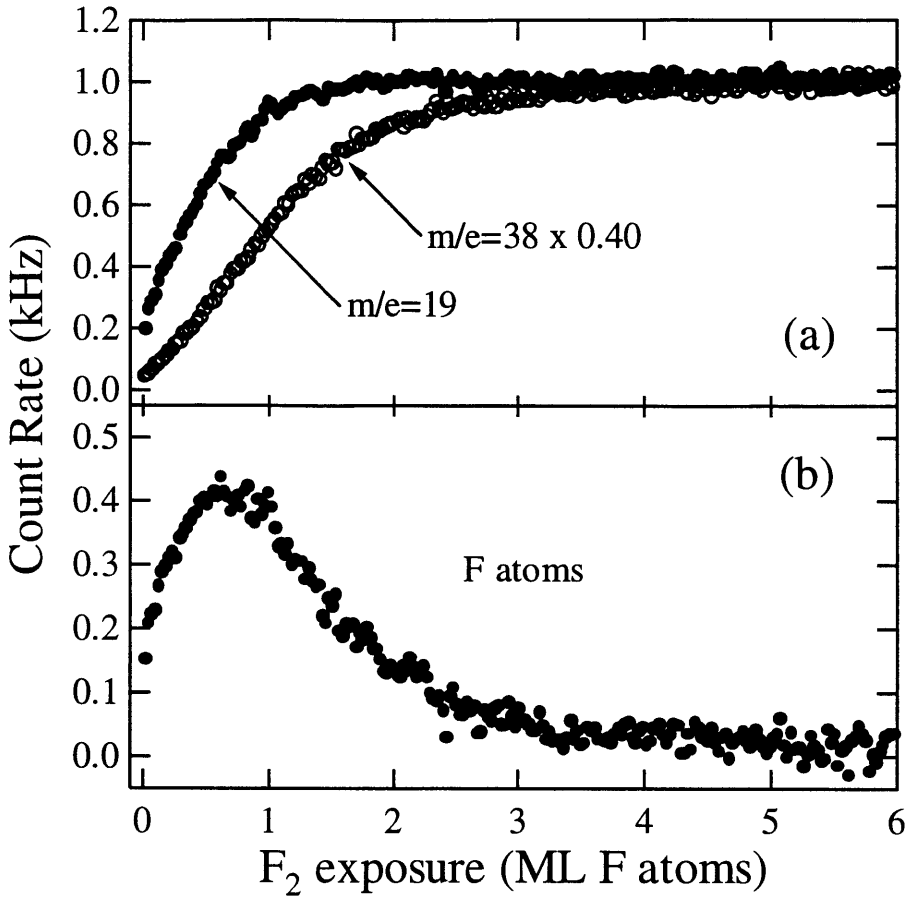

Figure 4 Flux of F_2 and F scattered from Si(100) as a function of F_2 exposure at θ_i=0°
(a) Signal at m/e=19 and m/e=38 multiplied by F_2 cracking ratio as a function of F_2 exposure in ML F atom at θ_i=0°, θ_d=35° and T_s=250 K. Signal is average of 25 measurements. Statistical uncertainty is size of data points. (b) Net scattered F signal calculated by point-by-point subtraction of m/e=38 signal multiplied by cracking ratio from m/e=19 signal in (a).

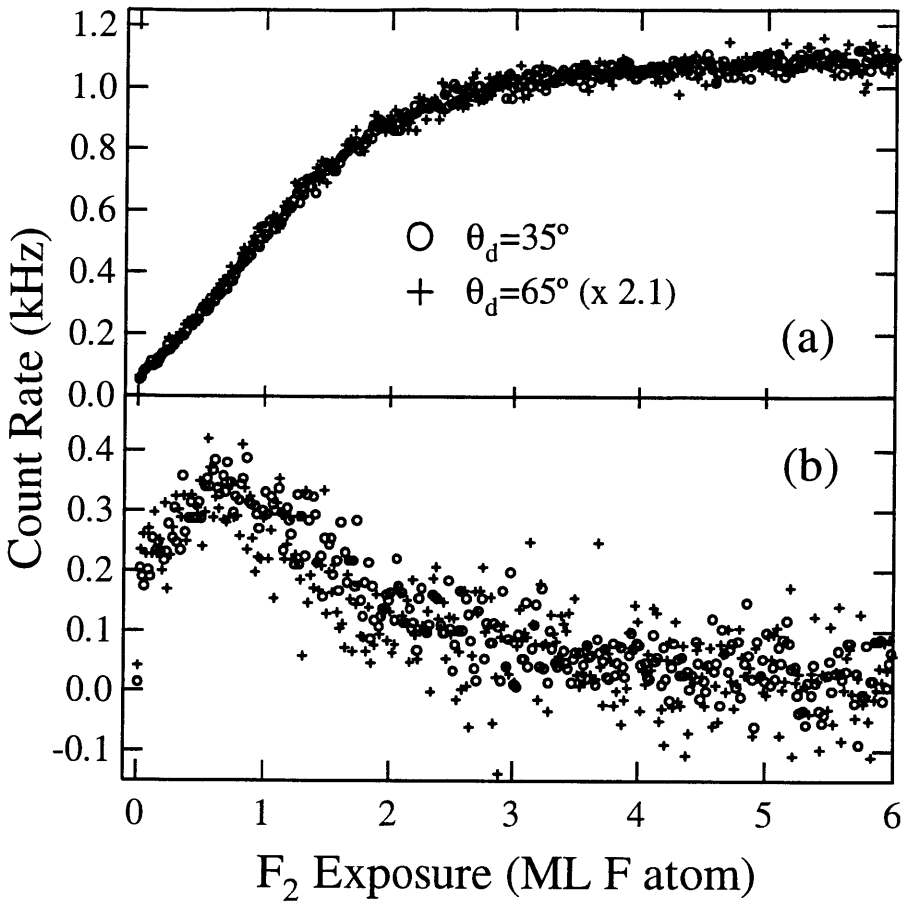

Figure 5 Flux of F_2 and F scattered from Si(100) along two polar angles as a function of F_2 exposure at θ_i=0°

(a) Signal at m/e=38 multiplied by F_2 cracking ratio as a function of F_2 exposure at θ_i=0°, θ_d=35° and θ_d=65°. Scaling factor of 2.1 for θ_d=65° determined by matching its m/e=38 signal to that at θ_d=35° at long exposure. (b) Net scattered F signal at θ_d=35° and θ_d=65° calculated by point-by-point subtraction of scaled m/e=38 signal multiplied by cracking ratio from scaled m/e=19 signal.

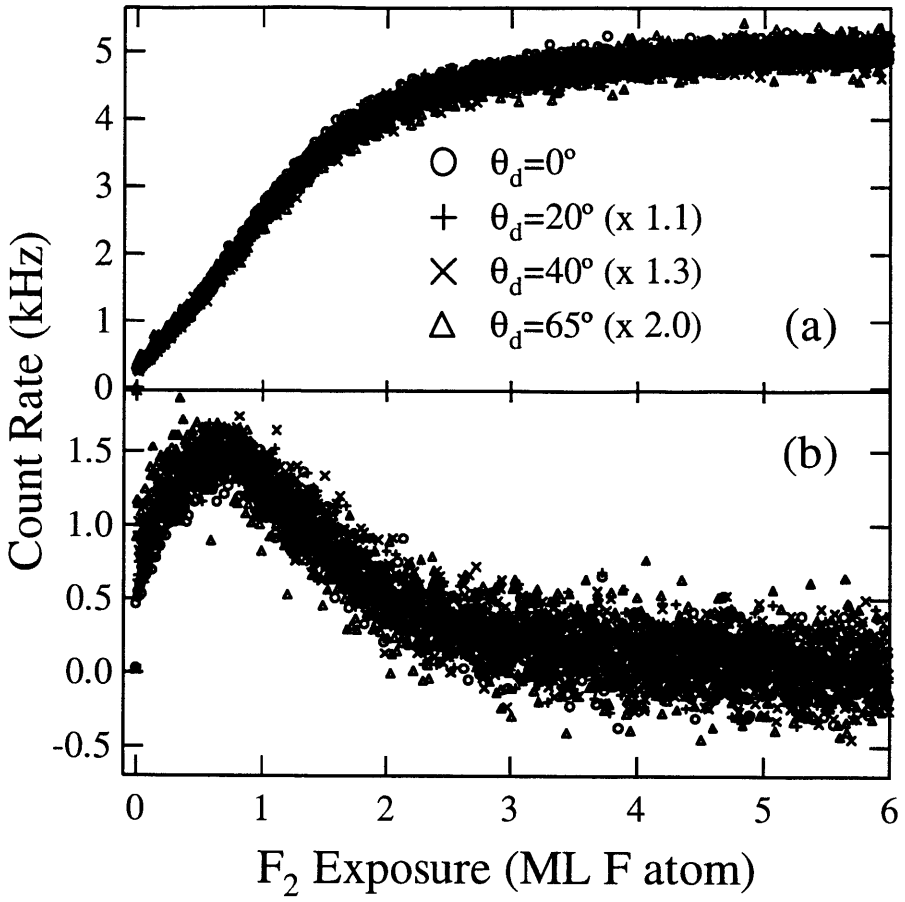

Figure 6 Flux of F_2 and F scattered from Si(100) along four polar angles as a function of F_2 exposure at θ_i=35°

(a) Signal at m/e=38 multiplied by F_2 cracking ratio as a function of F_2 exposure at θ_i=35° and θ_d=0°, 20°, 40° and 65°. Scaling factors determined by matching m/e=38 signals at long exposure as in Figure 5. (b) Net scattered F signal at θ_d=0°, 20°, 40° and 65° calculated as in Figure 5.

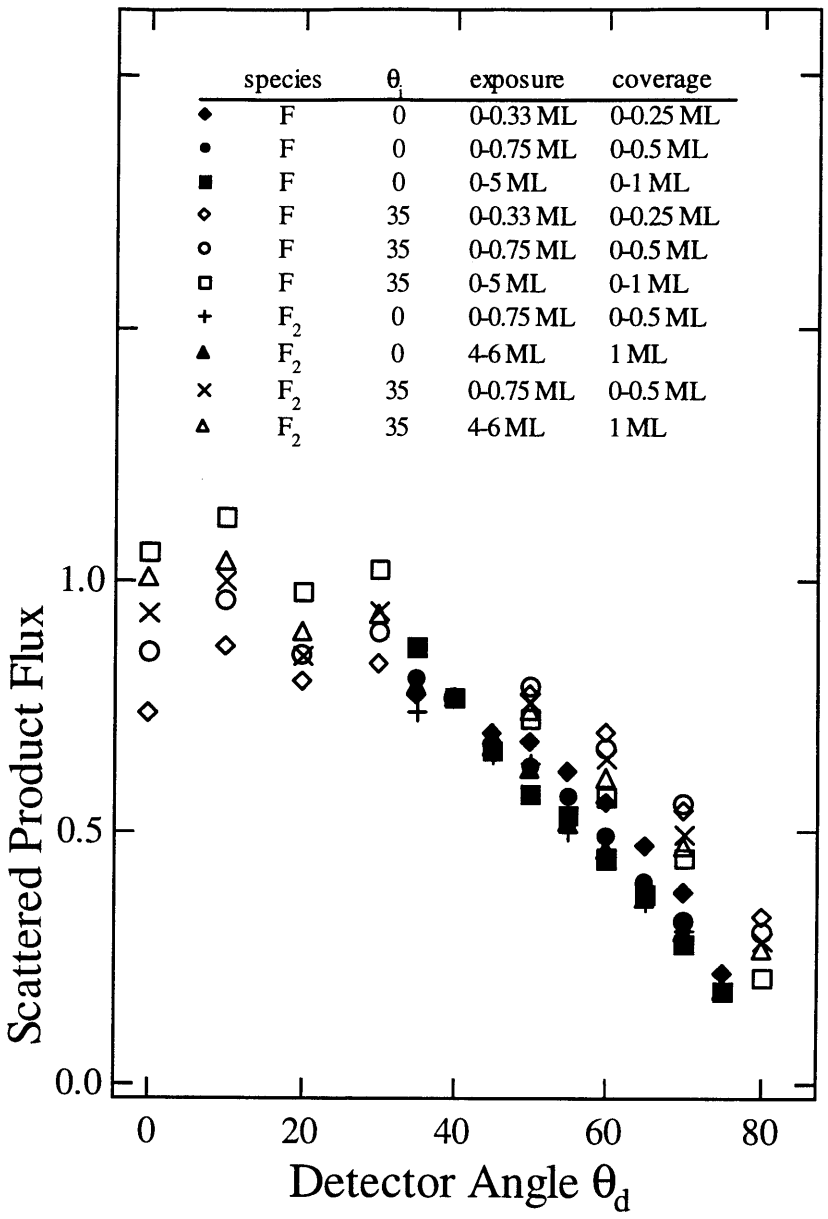

Figure 7 Angular distribution of flux of F and F_2 scattered from Si(100)
Scattered F and F_2 flux as a function of θ_d at θ_i=0° and 35° for various exposures normalized to cos 40° at θ_d=40°. Scattered flux obtained by integrating data similar to those shown in Figures 4-7 over indicated range of exposure in ML F atom. Coverage range determined from Figure 12(d).

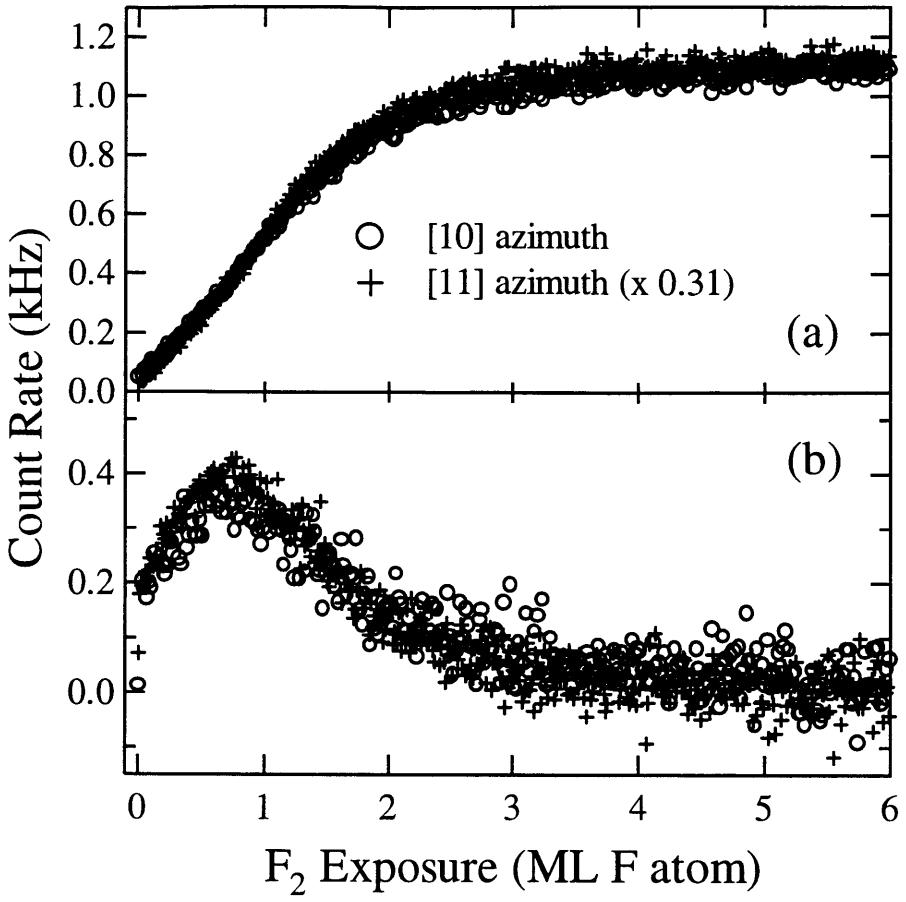

Figure 8 Flux of F_2 and F scattered from Si(100) as a function of F_2 at θ_i=0° exposure along two surface azimuths

(a) Signal at m/e=38 multiplied by F_2 cracking ratio as a function of F_2 exposure at θ_i=0° and θ_d=35° for scattering along (10) and (11) directions. Scaling factors determined by matching m/e=38 signals at long exposure as in Figure 5. (b) Net scattered F signal for scattering along (10) and (11) directions calculated as in Figure 5.

II.B.2.b. Thermal desorption

The crystal, at a temperature of 250 K, is exposed to F_2 at normal incidence, subsequently rotated so that the surface normal is along the axis of the differentially pumped mass spectrometer detector and then heated at a rate of 5 K/s from 250-1000 K. The desorption of multiple species is monitored essentially simultaneously by switching, at a rate of 10 Hz, the mass to which the quadrupole is tuned. Figure 9 shows thermal desorption spectra at m/e=66 and m/e=85 after a sufficiently long F_2 exposure to correspond to the steady state regime of Figure 4. These two signals correspond to SiF_2^+ and SiF_3^+ and arise from SiF_2 and SiF_4, respectively. Comparison of thermal desorption features at m/e=66, m/e=85, as well as m/e=104, which corresponds to SiF_4^+, shows that there is little or no SiF_3 contribution to the SiF_3^+ signal and little or no SiF_4 contribution to the SiF_2^+ signal, in agreement with previous results [28]. The major thermal desorption product, SiF_2, is observed as a single feature centered around 800 K. The minor product, SiF_4, desorbs as two broad features around 550 and 700 K. The SiF_4 yield never exceeds 2.5% of the SiF_2 yield, even at F_2 exposures as large as 100 ML. The different velocity and angular distributions of the desorbing SiF_2 and SiF_4 species as well as their relative ionization cross sections and quadrupole transmissions are taken into account in this determination of their relative yield [5,6].

The present interest in the thermal desorption measurements is to confirm that the reaction of F_2 with Si(100) ceases at long exposure when all of the reactive sites are occupied. Figure 10 shows the integrated thermal desorption yield as a function of F_2 exposure. The integrated yield is the sum of the integrated yields of SiF_2^+ and SiF_3^+ after scaling them for the relative detection sensitivities of the two signals and the factor of two more fluorine atoms that

SiF_4 has relative to SiF_2. The integrated yield increases rapidly to a nearly steady state level. As determined in Section II.C, the steady state level is achieved when the exposure is sufficiently high for the coverage to reach ~ 1 ML. However, careful inspection of Figure 10 reveals that the integrated yield, and hence the coverage, is not exactly constant at very high F_2 exposures. Analysis and calibration of the slope of the plot of the integrated yield versus F_2 exposure beyond 20 ML F yields a value of $9x10^{-4}$ for the dissociative chemisorption probability of F_2 on a Si(100) surface covered with about 1 ML of fluorine. However, for all intents and purposes, the steady state regime corresponds to a cessation of adsorption of F_2 on Si(100) as opposed to a continual adsorption reaction that has achieved a steady state.

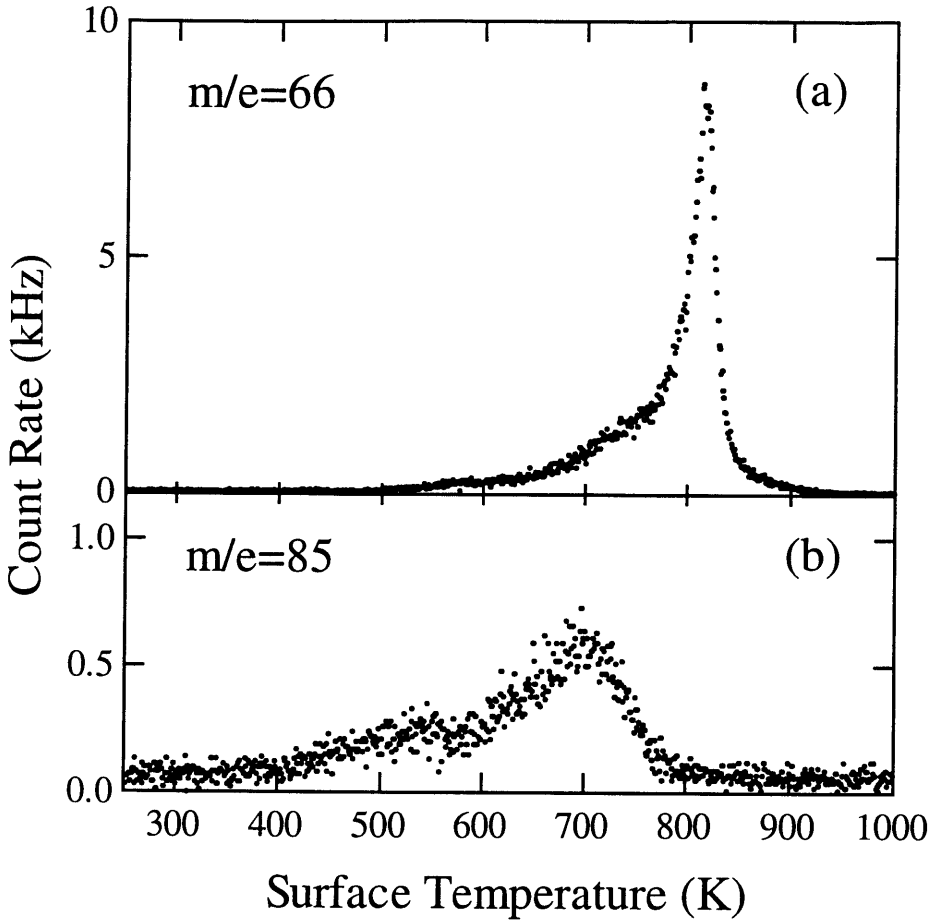

Figure 9 Thermal desorption spectra of Si(100) after F_2 exposure
Thermal desorption spectra at (a) m/e=66 and (b) m/e=85 after F_2 exposure of 19 ML F atom at T_s=250 K. Temperature ramp rate is 5 K/s.

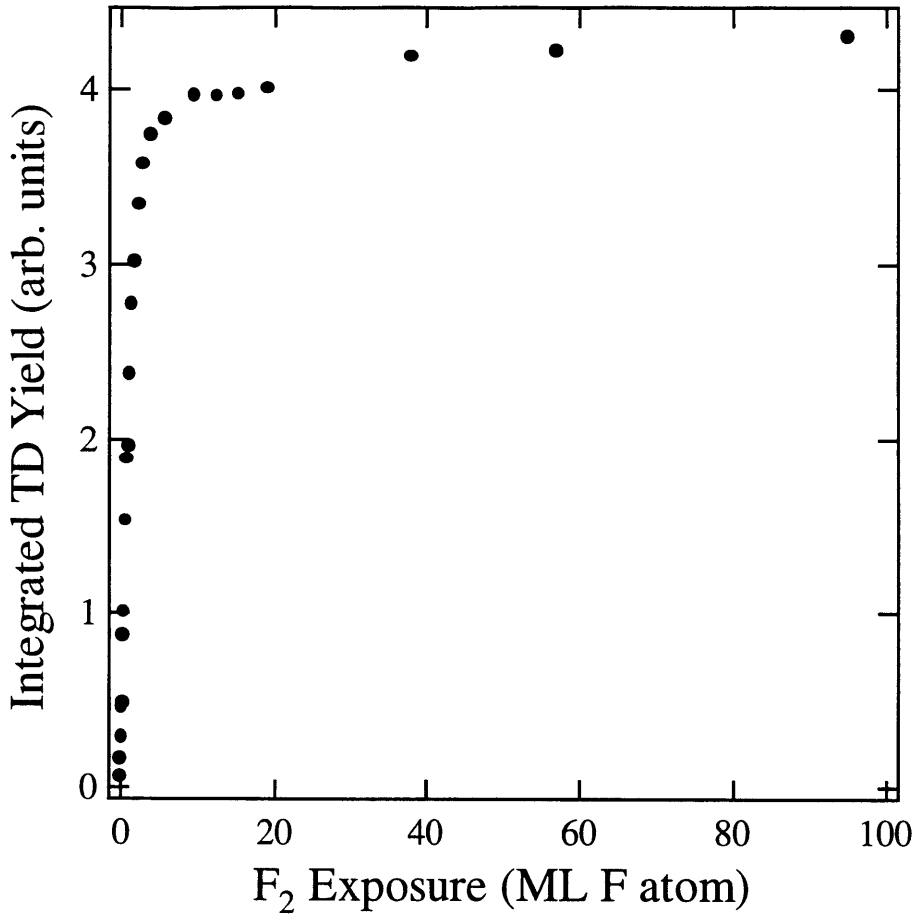

Figure 10 Total fluorine thermal desorption yield as a function of F_2 exposure
Integrated thermal desorption yield as a function of F_2 exposure. Integrated signal at m/e=85 is scaled to correct for experimentally determined detection sensitivity of SiF_3^+ relative to SiF_2^+ as well as number of fluorine atoms per desorbing species.

II.B.2.c. Helium diffraction

Si(100) reconstructs forming rows of surface Si dimers resulting in one partially-filled molecular orbital or dangling bond projecting into the vacuum for each surface Si atom, yielding a (2x1) periodicity that is observable by He diffraction. These dangling bonds, which effectively are radical sites and hence very reactive species, are logical sites for F atom abstraction and adsorption. The goal here is to identify the site of F adsorption as well as to determine the extent of Si-Si bond cleavage, if any. While He diffraction cannot directly identify the F adsorption site, it can reveal the prevailing periodicity to determine which periodic structures have been disrupted upon F adsorption, thereby providing supporting evidence for the dangling bonds as the F atom adsorption sites in the interaction of F_2 with Si(100).

A mixture of He seeded in Ar is expanded to produce a He beam that has an average velocity of 766±65 (FWHM) m/s as determined from TOF measurements. The average wavelength of the incident He is 1.31±0.11 (FWHM) Å, which is comparable to the surface unit cell dimensions of 3.84 Å and 7.68 Å. The beam is incident at θ_i=20 and is modulated at 150 Hz with a tuning fork to allow for background subtraction. The detector is rotated in steps of 0.5° from 15°-55° with respect to the surface normal in the forward scattering direction. Figure 11(a) shows a plot of scattered He intensity as a function of scattering angle, θ_d, measured from the surface normal of a clean Si(100) surface at 250 K. The features are broad because of the low angular resolution of the detector that is necessary to obtain sufficient sensitivity to detect reactive species which typically scatter with very low fluxes. However, three primary features of the diffraction spectrum indicative of the (2x1) periodicity are apparent. These features are a specular peak arising from overall order and smoothness, a half order peak at θ_s=31° arising

from diffraction perpendicular to the dimer rows, and a first order peak at θ_s=43° arising from diffraction parallel to the dimer rows. Figure 11(b) shows He diffraction from a Si(100) surface at 250 K after a sufficiently long F_2 exposure so as to reach the steady state regime of Figures 4 and 9. Although the intensities of the features are changed upon fluorination, the (2x1) periodicity persists. The identical two-dimensional unit cells of the fluorine overlayer and the Si(100) surface strongly suggests that each dangling bond serves as an adsorption site for one F atom. Most importantly, the persistence of the half order feature indicates that no silicon lattice bonds, not even the σ Si dimer bonds, are broken upon reaction with F_2.

The thermal desorption and He diffraction results along with the quantitative determination of the saturation coverage carried out in the next section will be used to confirm that the reaction proceeds via adsorption on the Si dangling bonds. When all of the dangling bonds have been fluorinated, the reaction stops.

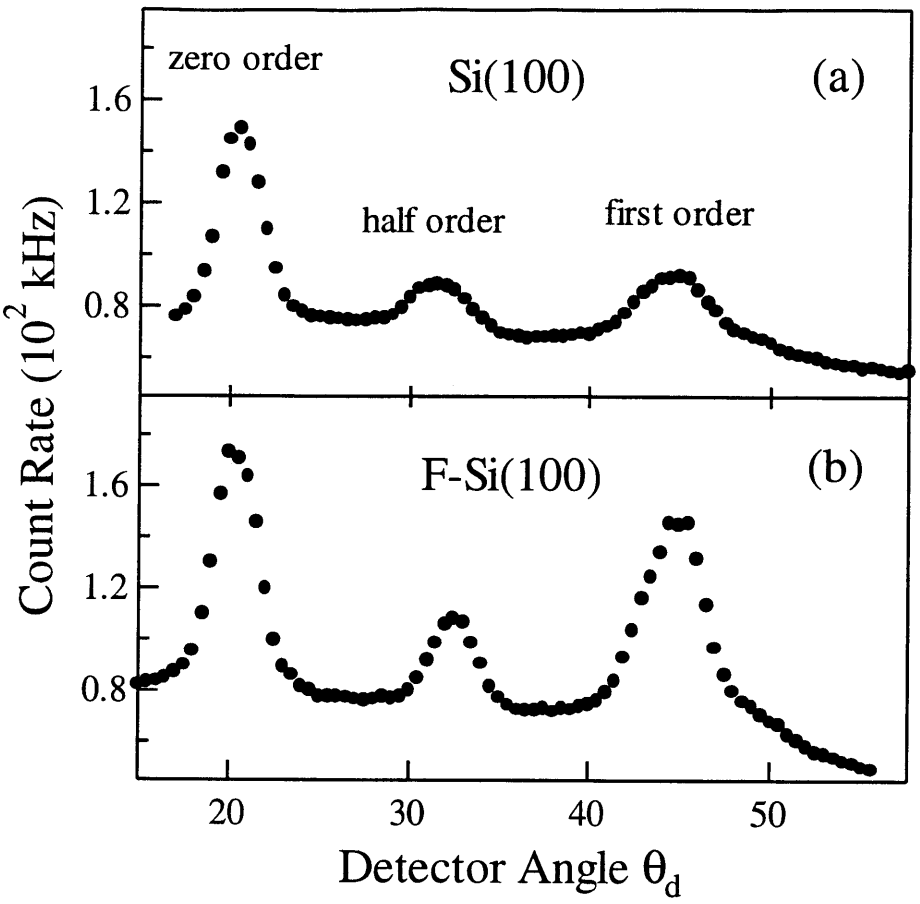

Figure 11 Helium diffraction spectra of clean and fluorinated Si(100)
Helium signal scattered from Si(100) at 250 K and at θ_i=20° as a function of θ_d (a) clean surface (b) after F_2 exposure of 30 ML F atom.

II.C. Determination of absolute reaction probability

This section presents a quantitative analysis of the dependence of the flux of F and F_2 scattered from Si(100) on F_2 exposure, yielding the absolute reaction probabilities as a function of fluorine coverage. The saturation coverage is established to be 1 ML, confirming that F_2 simply decorates the highly reactive Si dangling bonds and is not able to break the silicon dimer bonds.

A fluorine molecule scattering from the silicon surface is assumed to follow one of three possible reaction channels:

Unreactive scattering (P_0) is the channel in which F_2 scatters intact from the surface into the gas phase where it is detected as either F_2^+ or F^+. The absence of F_2 adsorption at long exposures demonstrated by the thermal desorption measurements means that only unreactive scattering occurs at long exposures to F_2. Therefore, at long exposure, $\varepsilon=\infty$, the flux of unreactively scattered F_2 is equal to the incident flux of F_2. Thus, the absolute probability for unreactive scattering P_0 as a function of F_2 exposure, ε, is the ratio of the scattered F_2 flux at ε to the scattered F_2 flux at $\varepsilon=\infty$:

$$P_0(\varepsilon) = \frac{\text{scattered } F_2 \text{ flux}}{\text{incident } F_2 \text{ flux}} = \frac{I_{F_2}^{scat}(\varepsilon)}{I_{F_2}^{scat}(\infty)}. \qquad \text{(II.1)}$$

Single atom abstraction (P_1) is the channel in which one of the F atoms is adsorbed onto the surface while the complementary fluorine atom scatters into the gas phase and detected as F^+. The absolute probability for single atom abstraction P_1 as a function of ε is again determined by referencing the F atom flux to the scattered F_2 flux at long exposure and is given by:

$$P_1(\varepsilon) = \frac{\text{scattered F flux}}{\text{incident } F_2 \text{ flux}} = \frac{I_F^{scat}(\varepsilon)}{I_{F_2}^{scat}(\infty)}. \qquad \text{(II.2)}$$

Two atom adsorption (P_2) is the channel in which both fluorine atoms are adsorbed onto the surface and no scattered products are detected in the gas phase. Normalization of the three channels results in the absolute probability for two atom adsorption, P_2, is given by:

$$P_2(\varepsilon) = 1 - P_0(\varepsilon) - P_1(\varepsilon). \tag{II.3}$$

In order to calculate these probabilities, expressions for the scattered F_2 and F fluxes, $I_F^{scat}(\varepsilon)$ and $I_{F_2}^{scat}(\varepsilon)$, respectively, in terms of the measurable quantity, the signal detected by the mass spectrometer, must be obtained. The mass spectrometer signal collected at a scattering angle, θ_d, is proportional to the number density of ions produced at m/e=38 and m/e=19 upon ionization of the neutral products, F_2 and F, and are related to the scattered fluxes at θ_d by:

$$S_{38}(\varepsilon,\theta_d) = \frac{I_{F_2}^{scat}(\varepsilon,\theta_d)\sigma_{F_2\rightarrow F_2^+}T_{38}}{v_{F_2}} \text{ and} \tag{II.4}$$

$$S_{19}(\varepsilon,\theta_d) = \frac{I_{F_2}^{scat}(\varepsilon,\theta_d)\sigma_{F_2\rightarrow F^+}T_{19}}{v_{F_2}} + \frac{I_F^{scat}(\varepsilon,\theta_d)\sigma_{F\rightarrow F^+}T_{19}}{v_F}. \tag{II.5}$$

where $S(\varepsilon,\theta_d)$ is the exposure and detector angle dependent signal at the mass-to-charge ratio denoted by its subscript, σ is the appropriate electron-impact ionization cross-section at the electron energy used for the measurement, v is the average velocity of the scattered neutral indicated by its subscript, and T is the transmissivity of the ion through the quadrupole mass filter at the mass-to-charge ratio denoted by its subscript. A proportionality factor, composed of the product of the current density of bombarding electrons in the ionizer and the length of the ionization region is not included in Eqs. (II.4) and (II.5) because these instrument quantities are independent of the particles' identity and cancel in the ratios used to define the probabilities in Eqs. (II.1)-(II.3). Equation (II.5) shows that there are two contributions to the signal at m/e=19. The first contribution comes from the dissociative ionization of F_2 in the ionizer while the second

arises from the ionization of scattered F atoms.

Using Eq. (II.1), the probability for unreactive scattering at a scattering angle θ_d, $P_0(\varepsilon, \theta_d)$, can now be written in terms of the experimentally measured quantity, $S_{38}(\varepsilon, \theta_d)$, such as presented in Figure 4. Because the F_2 velocity distribution is independent of exposure as discussed in Sec. II.A, $P_0(\varepsilon, \theta_d)$ simplifies to:

$$P_0(\varepsilon,\theta_d) = \frac{S_{38}(\varepsilon,\theta_d)}{S_{38}(\infty,\theta_d)}. \tag{II.6}$$

Using Eq. (II.2), an expression for $P_1(\varepsilon, \theta_d)$ is written as the ratio of the scattered fluxes, $I_F^{scat}(\varepsilon)$ and $I_{F_2}^{scat}(\varepsilon)$, as determined from Eqs. (II.4) and (II.5). After some algebra, the ratio of transmissivities can be eliminated yielding the final form for P_1:

$$P_1(\varepsilon,\theta_s) = \left(\frac{v_F}{v_{F_2}}\right)\left(\frac{\sigma_{F_2\to F^+}}{\sigma_{F\to F^+}}\right)\left(\frac{S_{19}(\varepsilon,\theta_s)}{S_{19}(\infty,\theta_s)} - \frac{S_{38}(\varepsilon,\theta_s)}{S_{38}(\infty,\theta_s)}\right). \tag{II.7}$$

The assumption is made that only F_2 contributes to the F^+ signal at long exposure. All quantities except for $\sigma_{F\to F^+}$, can be measured with the apparatus described in Sec. II.A. The F and F_2 velocities are average values of the average velocities plotted in Figure 2, 1084±46 m/s and 419±18 m/s, respectively. Recall that both velocities were shown to be independent of exposure. The ionization cross section of F_2 to F^+, $\sigma_{F_2\to F^+}$, is 0.26±0.05 Å^2 as measured with the apparatus described in Sec. II.A by a method described elsewhere [4,6]. A literature value, 0.87±0.17 Å^2, is used as the F atom ionization cross section, $\sigma_{F\to F^+}$, at 70 eV electron energy [29]. The final term is simply the difference between the two scattered signals normalized to their respective steady state levels at long exposures. Once P_0 and P_1 have been obtained, P_2 follows by the normalization condition expressed in Eq. (II.3). The F_2 exposure is determined from the absolute flux of the incident beam. Figure 12(a)-(c) shows the probabilities of the three channels as a

function of F_2 exposure at θ_d=35°. The error bars represent propagated uncertainties of the quantities in Eqs. (II.6) and (II.7) typical of a single data set. The large uncertainty in the determination of P_1 results from the uncertainty in the literature value of $\sigma_{F\rightarrow F^+}$ whose relative error is 20% [29].

The absolute reaction probability has been determined for scattering into a given detection angle θ_d. However, the result of interest is the absolute reaction probability integrated over all detector angles, both in-plane and out-of-plane, in the hemisphere above the surface. However, integration of the probabilities given in Eqs. (II.6) and (II.7) over detection angle is obviated by the independence of the scattered F_2 and F signals as a function of exposure on θ_d in the scattering plane, as shown in Figures 5 and 6. Scattering of F_2 and F outside of the plane defined by the incident beam and the surface normal were not measured, but the independence on the in-plane detector angle θ_d suggests that a dependence on the out-of-plane angle is physically unlikely. Moreover, the lack of dependence of the scattered F_2 and F signals as a function of exposure, and hence of the reaction probabilities as a function of exposure, on azimuthal angle as shown in Figure 7, indicates that there is no significant alignment effect in the exit channel of the reaction which would lead to preferential scattering of the product along specific crystal axes and hence to anisotropic out-of-plane scattering. There is other evidence for the isotropic nature of the interaction with and scattering from this highly corrugated Si surface. For example, the independence of the reaction probabilities on incident angle, as shown in Figure 6, indicates that the reaction is non-activated with no preferential orientation of the F_2 molecule into the entrance channel. In addition, the tremendous exothermicity released in this reaction overwhelms the low incident energy and any memory of the incident trajectory, leading to a near

cosine dependence of the scattered product intensities on the angle from the surface normal. Thus, the absolute reaction probability for low energy F_2 on Si(100) at 250 K is independent of scattering angle, i.e., $P(\varepsilon)=P(\varepsilon,\theta_d)$.

Having obtained $P_1(\varepsilon)$ and $P_2(\varepsilon)$, the probabilities for adsorption of one and two fluorine atoms, respectively, as a function of exposure, the fluorine coverage as a function of exposure can be calculated. By definition of the probabilities, there will be P_1+2P_2 fluorine atoms adsorbed on the surface for each incoming F_2 molecule. Summing over all incoming F_2 molecules, the coverage, $\theta(\varepsilon)$, can be written as:

$$\theta(\varepsilon) = \int_0^{\varepsilon} I_{F_2}\left(\tfrac{1}{2}P_1(\varepsilon) + P_2(\varepsilon)\right)d\varepsilon, \qquad \text{(II.8)}$$

where I_{F_2} is the incident F_2 flux in ML F/s. Figure 12(d) shows the absolute fluorine coverage as a function of F_2 exposure. The coverage rapidly increases from a low value at initial exposures to a saturation level of 0.94±0.11 ML at exposures above 10 ML of F atoms. This plot of the fluorine coverage as a function of exposure is then used to recast the probabilities in terms of coverage, presented in Figure 13.

The above analysis along with the saturation of the thermal desorption signal in Figure 9 shows clearly that the abstraction reaction and the adsorption of F_2 on Si ceases at a coverage of 0.94 ML. The cessation of atom abstraction and adsorption at this coverage leads to the conclusion that there are about 1 ML of abstraction sites and 1 ML of adsorption sites on the Si(100) surface. In addition, the He diffraction measurements show that the saturated F overlayer has the same two-dimensional periodicity, (2x1), as the underlying Si(100) substrate. Given that the adsorption of fluorine atoms on the dangling bonds would maintain the (2x1) periodicity, the observation of the (2x1) surface unit cell for the fluorine overlayer strongly

suggests that the dangling bonds are the F atom adsorption sites. Therefore, because the number of dangling bond sites on this crystal, 1 ML, is the same as the number of adsorption and abstraction sites, it is concluded that not only are the dangling bonds the adsorption sites but that they are also the abstraction sites.

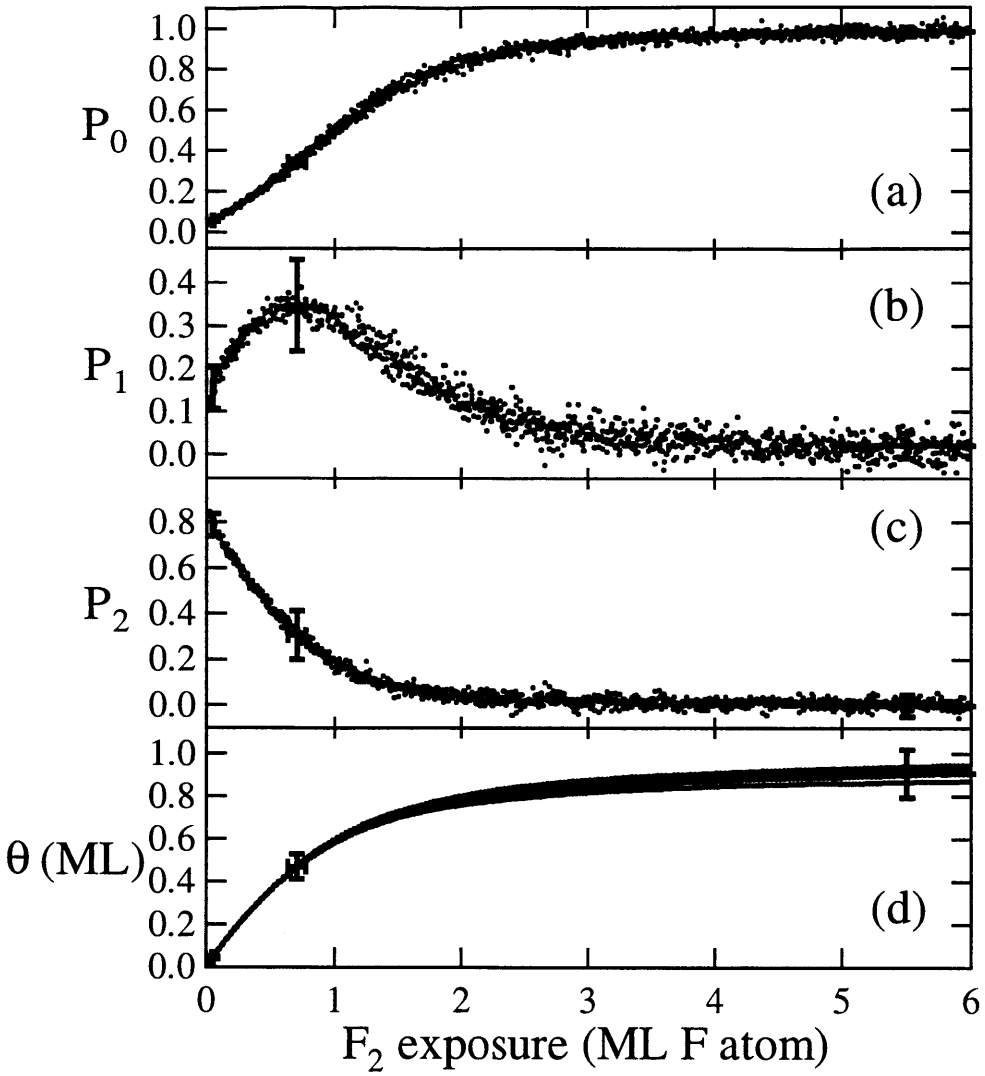

Figure 12 Reaction probabilities and fluorine coverage as a function of F_2 exposure
Reaction probability of F_2 with Si(100) as a function of F_2 exposure for (a) unreactive scattering P_0, (b) single atom abstraction P_1, (c) two atom adsorption P_2. Six data sets collected over a period of two months using two different crystals are shown. Each data set is typical of that in Figure 4. Error bars on P are propagated uncertainties typical of a single data set. Error bars on exposure reflect uncertainty in beam flux. (d) Absolute fluorine coverage as a function of F_2 exposure in ML F atom. Error bars on coverage reflect propagated uncertainties in P and beam flux typical of a single data set.

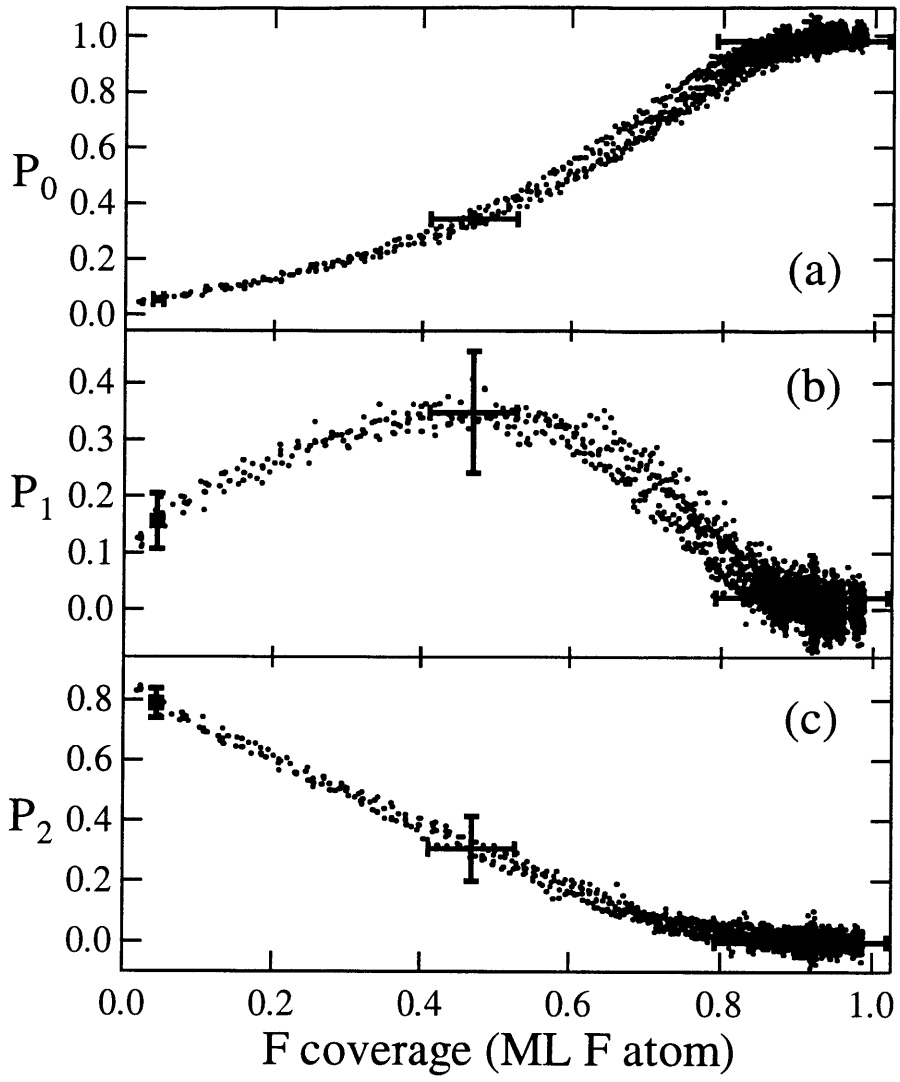

Figure 13 Reaction probabilities of F_2 with Si(100) at 250 K as a function of fluorine coverage

Reaction probability of F_2 at E_i=0.7 kcal/mol with Si(100) at 250 K as a function of fluorine coverage for P_0 unreactive scattering, P_1 single atom abstraction, and P_2 two atom adsorption. Data from Figure 12.

III. DESCRIPTION OF MODEL

Inherent in the dynamics of the interaction of F_2 with Si is the energetic allowance for the adsorption of only one F atom upon dissociation of the incident F_2 molecule. The adsorption of both F atoms, although stoichiometrically equivalent to classic dissociative chemisorption is fundamentally different in that the adsorption of both F atoms need not be a concerted process, but instead is a stepwise process. This difference is significant because it implies that a liberated F atom may subsequently interact with the surface and adsorb, even on a nonadjacent site, if it is scattered with the appropriate trajectory during the initial atom abstraction. The experiments described above only probe the interaction mechanisms that produce an observable gas phase product, i.e., F_2 molecules from unreactive scattering (P_0) or F atoms from single atom abstraction (P_1). Two atom adsorption produces no gas phase product and is only inferred from the observation that the total flux of scattered F_2 molecules and F atoms that cannot account for all of the incident F_2 flux. To provide further evidence for two atom adsorption as a stepwise dissociative chemisorption mechanism, a simple statistical model has been developed that is consistent with the experimental results presented in the previous section as well as with the experimental results of other investigators. The model provides insight regarding not only the mechanisms of two atom adsorption and single atom abstraction, but also the reactive nature of the Si(100) surface.

III.A. Probability equations

The statistical model treats the interaction of the incident F_2 molecule and its complementary F atom with four types of possible sites on the Si(100)(2x1) surface: sites that are members of filled dimers and hence necessarily occupied, the occupied and unoccupied sites

of half-filled dimers, and sites that are members of empty dimers and hence necessarily unoccupied. Occupied sites are dangling bond sites on which a fluorine atom is adsorbed. Thus, a site is distinguished not only by its fluorine occupation, but also by the occupation of its complementary surface dimer atom. The number of sites that are members of a filled dimer is denoted by θ_2, whose value ranges from zero on the clean surface to a maximum of 1 ML at the saturation coverage when every site and consequently, when every dimer is filled. The number of occupied sites that are members of a half-filled dimer is denoted by θ_1, as is the number of unoccupied sites that are members of a half-filled dimer. The value of θ_1 ranges from zero on the clean surface to a maximum of 0.5 ML when every dimer is half-filled. Finally, the number of unoccupied sites that are members of an empty dimer is denoted by $1-(2\theta_1+\theta_2)$. The factor of two in the $2\theta_1$ term arises because both the occupied and unoccupied sites on half-filled dimers decrease the number of unoccupied sites that are members of empty dimers by θ_1. The total coverage, θ, is the sum of the number of occupied sites that are members of both the half-filled and filled dimers, $\theta_1+\theta_2$.

The statistical model is based on the premise that two atom adsorption is related to single atom abstraction but is not necessarily a concerted process. Therefore, a F_2 molecule incident on a Si(100) surface proceeds through a sequential combination of up to three steps, each with two possible outcomes:

1. *Interaction of the F_2 molecule with the surface* leading to either abstraction of the first F atom from the F_2 molecule or unreactive scattering.

2. Assuming F atom abstraction, *the trajectory of the complementary F atom* leads to either direct scattering into the gas phase or the subsequent interaction of the complementary F atom with the surface.
3. Assuming the complementary F atom is not directly scattered into the gas phase, *the interaction of the F atom with the surface* leads to either adsorption or scattering of the complementary F atom.

A pictorial representation of Step 1, the initial interaction of F_2 with the four types of sites, and its two possible outcomes, abstraction and scattering, is shown in the first column of Figure 14. Cross sections A, B, B^*, C, K, M, M^*, N are defined for the two possible outcomes of the initial interaction, F atom abstraction and F_2 unreactive scattering, that can occur on the four distinct types of sites.

A ≡ Cross section for F abstraction from incident F_2 by a site in an empty dimer

B ≡ Cross section for F abstraction from incident F_2 by an unoccupied site in a half-filled dimer

B^* ≡ Cross section for F abstraction from incident F_2 by an occupied site in a half-filled dimer

C ≡ Cross section for F abstraction from incident F_2 by a site in a filled dimer

K ≡ Cross section for scattering incident F_2 by a site in an empty dimer

M ≡ Cross section for scattering incident F_2 by an unoccupied site in a half-filled dimer

M^* ≡ Cross section for scattering incident F_2 by a occupied site in a half-filled dimer

N ≡ Cross section for scattering incident F_2 by a site in a filled dimer

Relationships between the cross sections A and K, cross sections B, B^*, M and M^*, and cross sections C and N exist and are derived below. The probability of an outcome is the product of the cross section and the fraction of the total number of sites that are of a specific type of site.

Upon abstraction, the trajectory of the complementary F atom, labeled as Step 2 in Figure 14, may lead it either to scatter directly into the gas phase or to interact with the surface. A probability X is defined as the fraction of the complementary F atoms that directly scatter into the gas phase leading to single atom abstraction (P_1).

The fraction (1-X) of the complementary F atoms that do not directly scatter into the gas phase interact with the surface, label as Step 3 in Figure 14. This interaction may lead to adsorption of the F atom, resulting in two atom adsorption (P_2). If adsorption does not occur, then the F atom is scattered into the gas phase, resulting in single atom abstraction (P_1). Cross sections D, E, E^*, F, G, H, H^*, J are defined for the two possible outcomes of this step that can occur on one of the four types of sites.

D ≡ Cross section for F atom adsorption by a site in an empty dimer

E ≡ Cross section for F atom adsorption by an unoccupied site in a half-filled dimer

E^* ≡ Cross section for F atom adsorption by a occupied site in a half-filled dimer

F ≡ Cross section for F atom adsorption by a site in a filled dimer

G ≡ Cross section for scattering F atom by a site in an empty dimer

H ≡ Cross section for scattering F atom by an unoccupied site in a half-filled dimer

H^* ≡ Cross section for scattering F atom by a occupied site in a half-filled dimer

J ≡ Cross section for scattering F atom by a site in a filled pair

Again, relationships between cross sections D and G, cross sections E, E^*, H and H^*, and cross sections F and J exist and are derived below.

The probability of a specific pathway in the interaction of a F_2 molecule with the Si(100) surface is described by the product of the probabilities for the unique sequence of outcomes for the three individual steps, interaction of F_2 with Si, the trajectory of the complementary F atom, and the interaction of the complementary F atom with Si, on the four distinct sites. The probability of a specific process – two atom adsorption (P_2), single atom abstraction (P_1), and unreactive scattering (P_0) – is the sum of the probabilities for all of the pathways resulting in the adsorption of two F atoms, one F atom, and no F atoms, respectively.

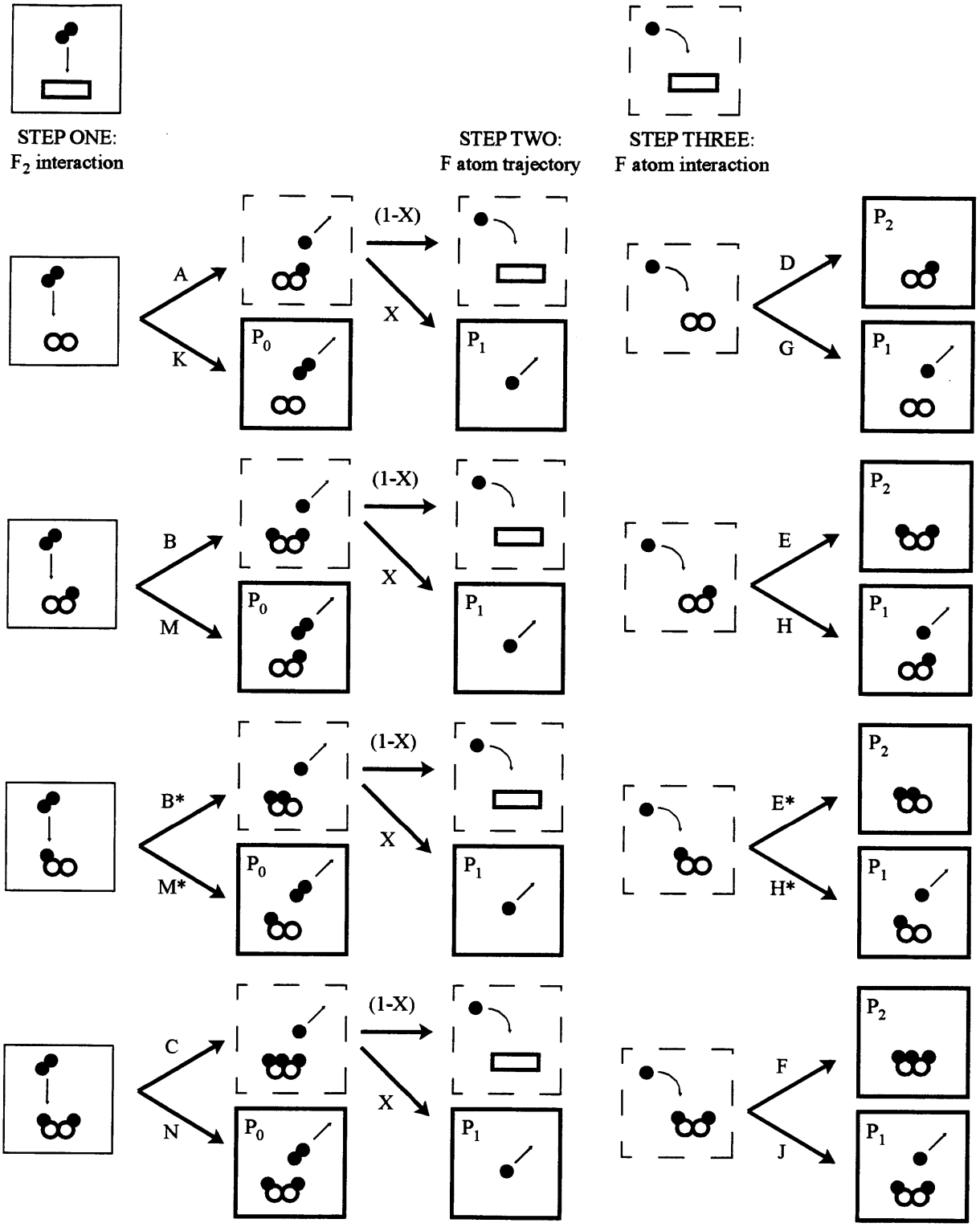

Figure 14 Pictorial representation of all possible pathways in model
Pictorial representation of model for the interaction of low energy F_2 with Si(100) at 250 K. Solid circles represent F atoms, hollow circles represent Si atoms.

Given these considerations, the probability of unreactive scattering (P_0) is the sum of the individual probabilities for the four pathways leading to unreactive scattering:

$$P_0 = K(1-(2\theta_1+\theta_2))+M\theta_1+M^*\theta_1+N\theta_2. \qquad \text{(III.1)}$$

These terms, in the order in which they are shown, represent the probability for F_2 to unreactively scatter from a site that is a member of an empty dimer, from an unoccupied site that is a member of a half-filled dimer, from an occupied site that is a member of a half-filled dimer, and from a site that is a member of a filled dimer. Because no complementary F atom is produced during unreactive scattering, there is no need to consider subsequent complementary F atom dynamics.

The probability of two atom adsorption (P_2) is the sum of the individual probabilities for the sixteen pathways leading to two atom adsorption:

$$\begin{aligned} P_2 = {} & A(1-(2\theta_1+\theta_2))(1-X)D(1-(2\theta_1+\theta_2))+A(1-(2\theta_1+\theta_2))(1-X)E\theta_1 \\ & +A(1-(2\theta_1+\theta_2))(1-X)E^*\theta_1+A(1-(2\theta_1+\theta_2))(1-X)F\theta_2 \\ & +B\theta_1(1-X)D(1-(2\theta_1+\theta_2))+B\theta_1(1-X)E\theta_1+B\theta_1(1-X)E^*\theta_1 \\ & +B\theta_1(1-X)F\theta_2+B^*\theta_1(1-X)D(1-(2\theta_1+\theta_2))+B^*\theta_1(1-X)E\theta_1 \\ & +B^*\theta_1(1-X)E^*\theta_1+B^*\theta_1(1-X)F\theta_2+C\theta_2(1-X)D(1-(2\theta_1+\theta_2)) \\ & +C\theta_2(1-X)E\theta_1+C\theta_2(1-X)E^*\theta_1+C\theta_2(1-X)F\theta_2. \end{aligned} \qquad \text{(III.2)}$$

The sixteen pathways are all of the possible combinations for the two essential outcomes, F atom abstraction and F atom adsorption, occurring at any of the four possible sites: a filled dimer site, an unoccupied or occupied site of a half-filled dimer, and an empty dimer site. For example, the first term in P_2, which constitutes the probability of the pathway involving atom abstraction on a site of an empty dimer followed by a trajectory of the complementary F atom interacting with the surface and subsequent adsorption on a site of an empty dimer, is given by the probability for abstraction on a site of an empty dimer $A(1-(2\theta_1+\theta_2))$, multiplied by the probability of an

interacting trajectory (1-X) and multiplied by the probability of adsorption of the complementary F atom on a site of an empty dimer D(1-(2θ_1+ θ_2)). Since two atom adsorption requires F atom abstraction from the F_2 molecule and the subsequent adsorption of the complementary F atom, none of the pathways resulting in two atom adsorption include the direct scattering of the complementary F atom with its probability X, an outcome that necessarily prevents adsorption of the complementary F atom.

Single atom abstraction requires F atom abstraction from the F_2 molecule, but the complementary F atom cannot adsorb to the surface. Sixteen of the pathways resulting in single atom abstraction are similar to the sixteen pathways resulting in two atom adsorption described in Eq. (III.2), except that the complementary F atom scatters from the surface instead of adsorbing onto it. However, unlike two atom adsorption, there are four additional pathways that result in single atom abstraction that include direct scattering of the complementary F atom, an outcome that necessarily results in single atom abstraction. The probability of single atom abstraction (P_1) is the sum of the individual probabilities for the twenty pathways leading to single atom abstraction:

$$\begin{aligned} P_1 = {} & A(1-(2\theta_1+\theta_2))(1-X)G(1-(2\theta_1+\theta_2))+A(1-(2\theta_1+\theta_2))(1-X)H\theta_1 \\ & +A(1-(2\theta_1+\theta_2))(1-X)H^*\theta_1+A(1-(2\theta_1+\theta_2))(1-X)J\theta_2 \\ & +B\theta_1(1-X)G(1-(2\theta_1+\theta_2))+B\theta_1(1-X)H\theta_1+B\theta_1(1-X)H^*\theta_1+B\theta_1(1-X)J\theta_2 \\ & +B^*\theta_1(1-X)G(1-(2\theta_1+\theta_2))+B^*\theta_1(1-X)H\theta_1+B^*\theta_1(1-X)H^*\theta_1 \\ & +B^*\theta_1(1-X)J\theta_2+C\theta_2(1-X)G(1-(2\theta_1+\theta_2))+C\theta_2(1-X)H\theta_1+C\theta_2(1-X)H^*\theta_1 \\ & +C\theta_2(1-X)J\theta_2+A(1-(2\theta_1+\theta_2))X+B\theta_1X+B^*\theta_1X+C\theta_2X. \end{aligned} \tag{III.3}$$

The first sixteen terms represent pathways for the two outcomes, F atom abstraction and F atom scattering upon interaction with the surface, occurring at any of the three types of sites, sites that are members of an empty dimer, a half-filled dimer, or a filled dimer. The last four terms

represent pathways for F atom abstraction on any of the four types of sites followed by direct scattering of the complementary F atom.

This statistical representation of the reaction probabilities given in Eqs. (III.1)-(III.3) assumes that both the F_2 molecule and the F atom, if produced by the initial atom abstraction, only interact one time with the surface. Physically, this assumption rules out the presence of a mobile physisorbed precursor, either intrinsic or extrinsic. In addition, this representation assumes that the cross sections are independent of coverage. The validity of these assumptions is discussed in Sec. IV.C.

The reaction probabilities given in Eqs. (III.4)-(III.6) are simplified by grouping the components of each of the three individual steps that comprise an overall pathway for the interaction of F_2 with Si(100):

$$P_2 = \left[A(1-(2\theta_1+\theta_2))+(B+B^*)\theta_1+C\theta_2\right](1-X) \times\left[D(1-(2\theta_1+\theta_2))+(E+E^*)\theta_1+F\theta_2\right], \quad \text{(III.4)}$$

$$P_1 = \left[A(1-(2\theta_1+\theta_2))+(B+B^*)\theta_1+C\theta_2\right](1-X) \times\left[G(1-(2\theta_1+\theta_2))+(H+H^*)\theta_1+J\theta_2+\left(\frac{X}{1-X}\right)\right], \quad \text{(III.5)}$$

$$P_0 = K(1-(2\theta_1+\theta_2))+(M+M^*)\theta_1+N\theta_2. \quad \text{(III.6)}$$

The reaction probabilities given in Eqs. (III.4-6) are further simplified by incorporating the experimental observation that the initial F atom abstraction cannot occur if the incident F_2 interacts with a filled site. Specifically, the experimental results show that the 1 ML of dangling bonds on the Si(100) surface are the only sites for abstraction and adsorption and that a F_2 molecule must unreactively scatter from a saturated surface so that $P_2(\theta=1\text{ ML})=0$, $P_1(\theta=1\text{ ML})=0$ and $P_0(\theta=1\text{ ML})=1$. Therefore, it is necessary that $B^*=0$ and $C=0$ in Eqs (III.4-6) leading to:

$$P_2 = [A(1-(2\theta_1+\theta_2))+B\theta_1](1-X)[D(1-(2\theta_1+\theta_2))+(E+E^*)\theta_1+F\theta_2], \quad \text{(III.7)}$$

$$P_1 = [A(1-(2\theta_1+\theta_2))+B\theta_1](1-X)\left[G(1-(2\theta_1+\theta_2))+(H+H^*)\theta_1+J\theta_2+\left(\frac{X}{1-X}\right)\right], \quad \text{(III.8)}$$

$$P_0 = K(1-(2\theta_1+\theta_2))+(M+M^*)\theta_1+N\theta_2. \quad \text{(III.9)}$$

Analogously, if the complementary F atom interacts with a filled site, then F atom adsorption cannot occur. To satisfy this assumption, it is necessary that $E^*=0$ and $F=0$ in Eqs. (III.7-8).

$$P_2 = [A(1-(2\theta_1+\theta_2))+B\theta_1](1-X)[D(1-(2\theta_1+\theta_2))+E\theta_1], \quad \text{(III.10)}$$

$$P_1 = [A(1-(2\theta_1+\theta_2))+B\theta_1](1-X)\left[G(1-(2\theta_1+\theta_2))+(H+H^*)\theta_1+\theta_2+\left(\frac{X}{1-X}\right)\right] \quad \text{(III.11)}$$

If there are only three possible channels for an incident F_2 molecule incident on a Si(100) surface, then the sum of the probabilities for the three reaction channels described by Eqs. (III.9-11) must be unity:

$$P_{total} = P_0 + P_2 + P_1 = 1. \quad \text{(III.12)}$$

In addition, the sum of the probabilities for every distinct outcome in a given step must be unity. Specifically, in the first step, the probability for any of the five distinct outcomes for either F atom abstraction from F_2 or F_2 unreactive scattering occurring must be unity.

$$P_{Step1} = A(1-(2\theta_1+\theta_2))+B\theta_1+K(1-(2\theta_1+\theta_2))+(M+M^*)\theta_1+N\theta_2 = 1. \quad \text{(III.13)}$$

Alternatively, Eq. (III.13) can be rationalized in the following manner. The first step in the interaction of F_2 with Si(100) is the F atom abstraction from F_2 or the unreactive scattering of F_2. The probability of F atom abstraction from the incident F_2 molecule is given by:

$$P_{abstraction} = [A(1-(2\theta_1+\theta_2))+B\theta_1]. \quad \text{(III.14)}$$

If the initial abstraction does occur, the resulting overall event must be either two atom adsorption (P_2) or single atom abstraction (P_1) but cannot result in unreactive scattering (P_0).

Conversely, if the initial abstraction does not occur, the incident F_2 must unreactively scatter. Therefore, the absence of the initial abstraction is the sole contribution to unreactive scattering so that:

$$P_0 = \left[K(1-(2\theta_1+\theta_2))+(M+M^*)\theta_1+N\theta_2\right]=1-\left[A(1-(2\theta_1+\theta_2))+B\theta_1\right], \quad \text{(III.15)}$$

which is equivalent to Eq. (III.13). After some algebra, Eq. (III.15) becomes,

$$(K+A-1)+(M+M^*+B-2A-2K)\theta_1+(N-K-A)\theta_2=0, \quad \text{(III.16)}$$

resulting in a system of three equations:

$$\begin{aligned} K+A-1&=0\\ M+M^*+B-2A-2K&=0\\ N-K-A&=0. \end{aligned} \quad \text{(III.17)}$$

These equalities constrain the cross sections K relative to A, as well as M+M^* relative to B:

$$K=1-A, \quad \text{(III.18)}$$

$$M+M^*=2-B. \quad \text{(III.19)}$$

The equality also yields the value of cross section N,

$$N=1. \quad \text{(III.20)}$$

These relationships exist because the normalization requirement also holds for a given type of site. Because of the normalization relationships, the cross section K and the sum of cross sections M + M^* are justifiably eliminated from the model.

In an analogous manner, the sum of the probabilities for the eight distinct outcomes for either F atom adsorption or F atom scattering of Step 3 in Figure 14, must be unity:

$$P_{Step\,3}=D(1-(2\theta_1+\theta_2))+E\theta_1+G(1-(2\theta_1+\theta_2))+(H+H^*)\theta_1+J\theta_2=1. \quad \text{(III.21)}$$

After some algebra, Eq. (III.21) becomes,

$$(D+G-1)+(E+H+H^*-2D-2G)\theta_1+(J-D-G)\theta_2=0, \quad \text{(III.22)}$$

resulting in a system of three equations:

$$\begin{aligned} D+G-1&=1 \\ E+H+H^*-2D-2G&=0 \\ J-D-G&=0. \end{aligned} \tag{III.23}$$

These equalities constrain the cross sections G relative to D, as well as H+H* relative to E:

$$G=1-D, \tag{III.24}$$

$$H+H^*=2-E. \tag{III.25}$$

The equality also yields the value of cross section J,

$$J=1. \tag{III.26}$$

Because of the normalization relationships, the cross sections G and H+H* are justifiably eliminated from the model. Substituting Eqs. (III.24-26) into Eqs. (III.10) and (III.11) yields,

$$P_2=[A(1-(2\theta_1+\theta_2))+B\theta_1](1-X)[D(1-(2\theta_1+\theta_2))+E\theta_1], \tag{III.27}$$

$$P_1=[A(1-(2\theta_1+\theta_2))+B\theta_1](1-X)\left[1-[D(1-(2\theta_1+\theta_2))+E\theta_1+\theta_2]+\left(\frac{X}{1-X}\right)\right]. \tag{III.28}$$

Redistributing the (1-X) term and incorporating it into the cross sections D and E allows the probability term X to be eliminated from the probability equations:

$$P_2=[A(1-(2\theta_1+\theta_2))+B\theta_1][D'(1-(2\theta_1+\theta_2))+E'\theta_1], \tag{III.29}$$

$$P_1=[A(1-(2\theta_1+\theta_2))+B\theta_1][1-[D'(1-(2\theta_1+\theta_2))+E'\theta_1]], \tag{III.30}$$

$$P_0=1-[A(1-(2\theta_1+\theta_2))+B\theta_1], \tag{III.31}$$

where the new cross sections D´ and E´ are related to the original cross sections D and E by:

$$D'\equiv D(1-X), \tag{III.32}$$

$$E'\equiv E(1-X). \tag{III.33}$$

The reaction probability equations can alternatively be defined in terms of G and H+H*. However, in this case, the probability term X cannot be eliminated (see Sec. IV.B.1).

III.B. Coverage equations

The solution of Eqs. (III.29)-(III-31) for the three probabilities depends on the knowledge of the two types of coverage as a function of F_2 exposure. The two types of coverage are not distinguishable based on the experimental results described above. Instead, the simplifying assumption is made that the two types of coverage develop as a result of scattering from random sites. In addition, it is assumed that there is no diffusion or desorption of adsorbed F atoms. The diffusion constraint eliminates any inhomogeneity in the spatial distribution of adsorbates on the surface that might arise from the islanding or clustering of adsorbates. Therefore, the global coverage is truly representative of the local adsorbate density in the vicinity of the random site of the interaction. The desorption constraint eliminates the need to consider concurrent adsorption and desorption processes. These assumptions are physically reasonable given the Si-F bond strength of about 150 kcal/mol [30,31]. In general, desorption barriers are equivalent to the surface-adsorbate bond strength, and adsorbate diffusion barriers are on the order of 5-20% of the surface-adsorbate bond strength [32] which, in this case, are both much greater than kT. In addition, the desorption of F atoms as fluorosilanes, i.e., the removal of fluorine as etch product, is not observed to occur in the interaction of low energy F_2 with Si(100) at 250 K.

The equations describing the coverage are developed in a manner analogous to the actual development of the coverage during the exposure of the Si(100) surface to F_2. Starting from a clean surface, the initial infinitesimal fluorine coverage arises from the number of F atoms adsorbed via a statistical distribution of pathways at zero coverage over an infinitesimal exposure range. The coverage increases by iteratively considering the statistical distribution of pathways at the new coverage. Mathematically, the coverage is the integral over exposure of the product

of the incident F_2 flux and the probability for the each relevant reaction pathway weighted by the number of F atoms adsorbed along each pathway. Thus, the half-filled coverage, θ_1, is the sum of contributions from the pathways leading to two atom adsorption (P_2) and single atom abstraction (P_1) that create half-filled dimers minus the contributions from the pathways that destroy half-filled dimers by creating filled dimers:

$$\begin{aligned}\theta_1 = \tfrac{1}{2} I_{F_2} \int \{ & 2A(1-(2\theta_1+\theta_2))D'(1-(2\theta_1+\theta_2)) \\ & + A(1-(2\theta_1+\theta_2))[1-[D'(1-(2\theta_1+\theta_2))+E'\theta_1]] \\ & - 2B\theta_1 E'\theta_1 - B\theta_1[1-[D'(1-(2\theta_1+\theta_2))+E'\theta_1]]\},\end{aligned} \tag{III.34}$$

which simplifies to:

$$\begin{aligned}\theta_1 = \tfrac{1}{2} I_{F_2} \int \{ & A(1-(2\theta_1+\theta_2))[1+D'(1-(2\theta_1+\theta_2))-E'\theta_1] \\ & - B\theta_1[1-D'(1-(2\theta_1+\theta_2))+E'\theta_1]\}.\end{aligned} \tag{III.35}$$

The filled coverage, θ_2, is the sum of the contributions from two atom adsorption (P_2) and single atom abstraction (P_1) to create filled dimers:

$$\begin{aligned}\theta_2 = I_{F_2} \int \{ & A(1-(2\theta_1+\theta_2))E'\theta_1 + B\theta_1 D'(1-(2\theta_1+\theta_2)) \\ & + 2B\theta_1 E'\theta_1 + B\theta_1[1-[D'(1-(2\theta_1+\theta_2))+E'\theta_1]]\},\end{aligned} \tag{III.36}$$

which simplifies to:

$$\theta_2 = I_{F_2} \int \{A(1-(2\theta_1+\theta_2))E'\theta_1 + B\theta_1(1+E'\theta_1)\}. \tag{III.37}$$

The total coverage, an experimentally determined quantity, is the sum of the two types of coverage:

$$\begin{aligned}\theta = I_{F_2} \int \{ & \tfrac{1}{2}\{A(1-(2\theta_1+\theta_2))[1+D'(1-(2\theta_1+\theta_2))-E'\theta_1]\} \\ & - \tfrac{1}{2}\{B\theta_1[1-D'(1-(2\theta_1+\theta_2))+E'\theta_1]\} \\ & + \{A(1-(2\theta_1+\theta_2))E'\theta_1 + B\theta_1(1+E'\theta_1)\}\},\end{aligned} \tag{III.38}$$

which simplifies to:

$$\theta = \tfrac{1}{2} I_{F_2} \int [A(1-(2\theta_1+\theta_2)) + B\theta_1][1+D'(1-(2\theta_1+\theta_2))+E'\theta_1]. \tag{III.39}$$

To check the validity of the coverage equations for θ_1 and θ_2, the total coverage must equal the integral of the product of the sum of the weighted probabilities and the incident flux:

$$\theta = I_{F_2}\int P_2 + \tfrac{1}{2}P_1 = \tfrac{1}{2}I_{F_2}\int [A(1-(2\theta_1+\theta_2))+B\theta_1][1+[D'(1-(2\theta_1+\theta_2))+E'\theta_1]]. \quad \text{(III.40)}$$

III.C. Fitting algorithm and measure of the goodness of fit

There are four unique probability factors, A, B, D′, and E′ in the three equations for the reaction probabilities. The values of two of the factors can be determined from the experimental data in the limit of zero coverage:

$$P_2(\theta=0) = AD' = 0.83\pm0.03, \quad \text{(III.41)}$$

$$P_1(\theta=0) = A(1-D') = 0.13\pm0.03, \quad \text{(III.42)}$$

$$P_0(\theta=0) = 1-A = 0.04\pm0.03. \quad \text{(III.43)}$$

Therefore,

$$A = 0.96\pm0.03, \quad \text{(III.44)}$$

$$D' = 0.87\pm0.04. \quad \text{(III.45)}$$

Thus, there are two parameters, cross sections B and E′, that can be adjusted to fit the model to the experimental data. The best fit values are B=1.68±0.06 and E′=1.03±0.14, where the uncertainties represent the standard deviation of the fitting parameters and are described in more detail in Appendix A. The probabilities are determined by numerically solving the system of coupled differential equations for the two types of coverage, θ_1 and θ_2, described by Eqs. (III.35) and (III.37), respectively, and substituting these solutions into the equations for the three reaction probabilities described by Eqs. (III.29-31). Figure 15 is a plot of the three reaction probabilities as well as the coverage derived from the best fit of the model to the experimental data shown in Figure 13 as a function of F_2 exposure. Figure 16 is a plot of the reaction probabilities in Figure 15(a)-(c) as a function of fluorine coverage which is shown in Figure 15(d). Because the

incident F_2 flux, and therefore the F_2 exposure over a fixed integration time, varied from data set to data set, the reaction probabilities and coverage determined from each of the six data sets shown in Figure 13 are interpolated over a common exposure range (0-15 ML F) and interval (0.1 ML F) using linear interpolation. The data shown in Figures 15 and 16 are the average value of the reaction probabilities and coverage at each exposure. The model is best fit to this experimental data that has been interpolated and averaged using the Levenberg-Marquardt least squares nonlinear fitting algorithm (Appendix A).

The goodness of fit is determined by a chi square function that is defined as the sum of the individual chi square values of the two independent functions, the probability of unreactive scattering (P_0) and the probability of single atom abstraction (P_1):

$$\chi^2 = \sum_{i=1}^{10}\left[\left(\frac{P_0^{obs}(\varepsilon_i) - P_0^{exp}(\varepsilon_i)}{\sigma_{P_0}(\varepsilon_i)}\right)^2 + \left(\frac{P_1^{obs}(\varepsilon_i) - P_1^{exp}(\varepsilon_i)}{\sigma_{P_1}(\varepsilon_i)}\right)^2\right]. \qquad \text{(III.46)}$$

The uncertainties in P_0 and P_1, denoted σ_{P_0} and σ_{P_1}, are representative of the uncertainties for a single set. The chi square function is limited to the first 1 ML F exposure. A chi square value of 3.4 is obtained for B=1.68 and E′=1.03. A search over the two dimensional phase space performed by randomly selecting starting values for B and E′ ranging from 0-200% of the best fit values consistently converged at the best fit values confirming that the best fit corresponded to a global minimum in the chi square function. Over the exposure range defined by the summation in the chi square function, there are twenty degrees of freedom corresponding to the values for P_0 and P_1 at each of the ten exposures. The minimum chi square value is significantly less than the number of degrees of freedom, satisfying the standard criterion for the appropriateness of using a certain model to describe a given set of data [33]. However, the data and the fit to the data do

not match well at longer exposure, which is outside of the range of the chi square function. Using the above criterion, the model indeed does not describe the data well at high exposures and coverages. The discrepancy between the model and the data at high exposure is discussed below.

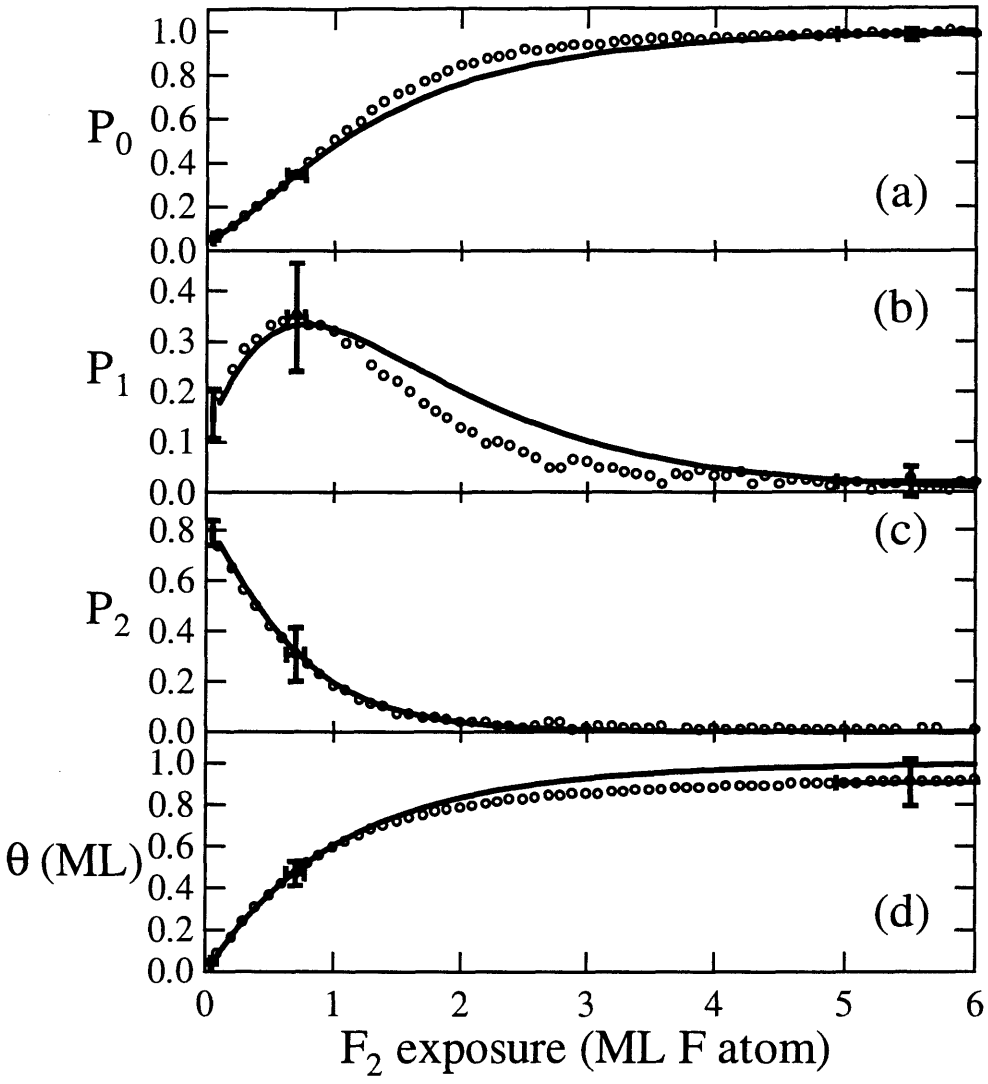

Figure 15 Reaction probabilities and coverage predicted by model as function of F_2 exposure

Reaction probability of F_2 with Si(100) as a function of F_2 exposure derived from the best fit of the model [solid line] to the experimental data [circles] for (a) unreactive scattering P_0, (b) single atom abstraction P_1, (c) two atom adsorption P_2. (d) Absolute fluorine coverage as a function of F_2 exposure. The parameters for the model are A=0.96, B=1.68, D′=0.87, and E′=1.03. The experimental data is the average of the six sets of data shown in Figure 13 after interpolating the data to a common exposure interval of 0.1 ML F.

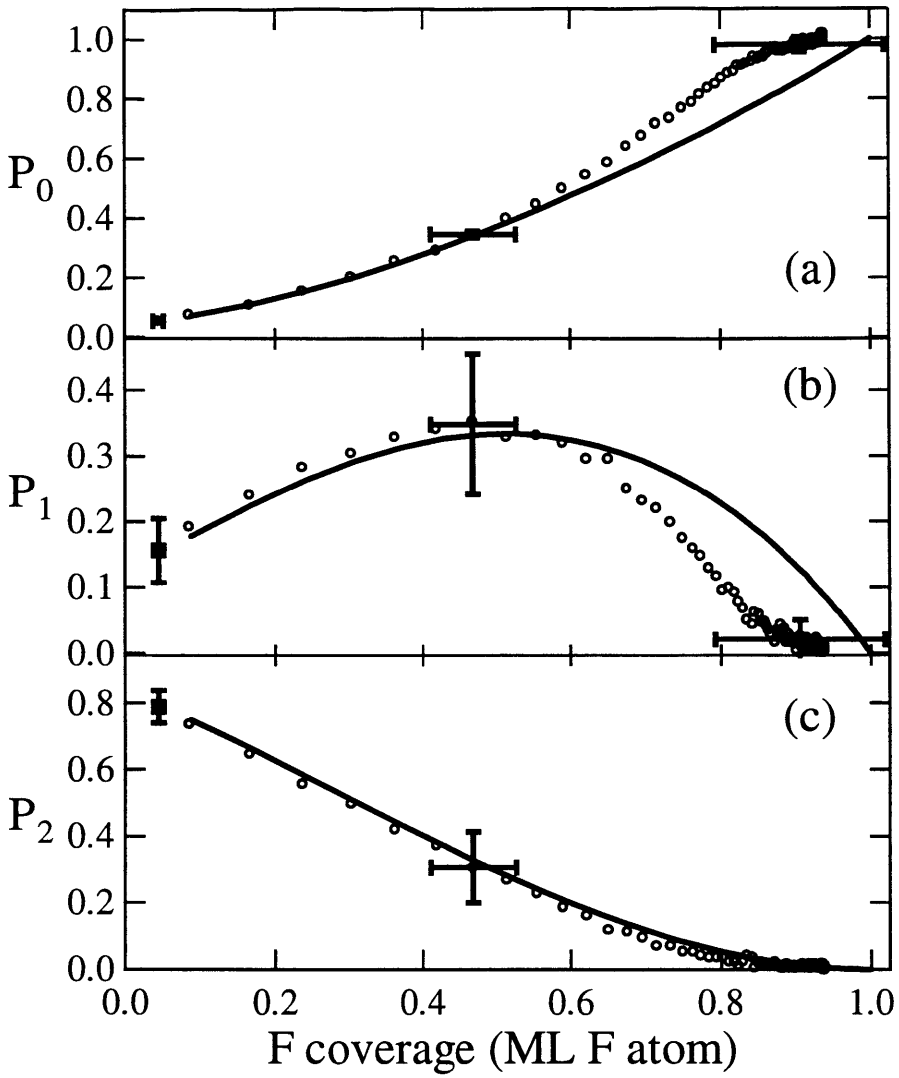

Figure 16 Reaction probabilities predicted by model as a function of fluorine coverage
Reaction probability of F_2 with Si(100) as a function of fluorine coverage derived from the best fit of the model [solid line] to the experimental data [circles] for (a) unreactive scattering P_0, (b) single atom abstraction P_1, (c) two atom adsorption P_2. The fit and the data are from Figure 15.

IV. DISCUSSION

The model provides a reasonably accurate description of the kinetics of the interaction of low energy F_2 with Si(100) at 250 K. The model is based on two premises. First, the two dissociative chemisorption channels, single atom abstraction and two atom adsorption, are both comprised of two distinct steps. The initial step, the abstraction and adsorption of the first F atom from the incident F_2 molecule, is common to both channels while the second step, the adsorption or scattering of the complementary F atom is independent of the abstraction and adsorption of the first F atom because the energy liberated by one Si-F bond is sufficient to overcome the bond energy in the incident F_2 molecule. There is no thermodynamic driving force requiring the adsorption of the second F atom. Second, the reactivity of a dangling bond site is dependent not only on its occupancy, but on the occupancy of the complementary atom in the dimer on the Si(100)(2x1) surface. This premise is physically based on the knowledge that the two atoms comprising a dimer are the only surface atoms that are directly bonded to each other on the surface so it might be expected that the adsorption of a F atom on one of them will affect the reactivity of the complementary Si atom in the dimer. The purpose of the discussion is to provide further evidence for the physical reasonableness and plausibility of the model and to gain insight into the dynamics of the interaction of F_2 with Si(100).

IV.A. Physical implications of model

IV.A.1. Total cross sections for reaction

A cross section is common concept in gas phase scattering dynamics and represents the "target area" that one particle presents to another particle that leads to a specific scattering event. It is a valuable quantity because it describes the likelihood of a reaction in terms of collision

trajectories. A small cross section implies that there must be a "head-on" collision for the scattering event to occur, whereas a large cross section implies that there are attractive forces that bring the colliding particles together even if the two particles do not appear to be on a course for collision.

The absolute cross section is related to the rate of a reaction by the concentration and velocity of the reactants. For the prototypical gas phase reaction A+B→C, the rate of production of C is given by:

$$\frac{dn_C}{dt} = \iint_{V_A,V_B} v\sigma n_A f(v_A) n_B f(v_B) dv_A dv_B . \qquad \text{(IV.1)}$$

where v is the relative velocity (v_A-v_B) between A and B, σ is the total cross section for reaction, and n_x, v_x, $f(v_x)$, are the number density, velocity, and velocity distribution of particle X. In the case of F_2 interacting with Si, the Si is stationary so the relative velocity v is equivalent to the velocity of F_2, v_{F_2}. In addition, the velocity distribution of F_2 in a supersonic beam is approximately monoenergetic so the integration over F_2 velocity can be ignored. Therefore, by analogy to a gas phase scattering event, the rate of unreactive scattering from a site of a filled dimer is:

$$\text{rate } N = v_{F_2} \sigma_N n_{F_2} n_{Si}^{\text{filled dimer}} . \qquad \text{(IV.2)}$$

Note that the product of the velocity and the number density of F_2 is simply the flux of F_2,

$$\text{rate } N = I_{F_2} \sigma_N n_{Si}^{\text{filled dimer}} . \qquad \text{(IV.3)}$$

The cross sections A, B, D′, and E′ determined from the fit of this model to the data and the cross sections K, M+M*, N, G, H+H*, and J, determined from relationships to the independent cross sections, are related to their gas phase analogs σ_A, σ_B, σ_D, σ_E, σ_K, $\sigma_M+\sigma_{M*}$, σ_N, σ_G, $\sigma_H+\sigma_{H*}$, and σ_J, respectively. For example, the probability of unreactive scattering from a site of a filled

dimer is the product of the cross section N and the fraction of the total sites that are members of filled dimers:

$$P_{unreactive}^{filled\ dimer} = N\left(\frac{n_{Si}^{filled\ dimer}}{n_{Si}^{total}}\right). \qquad (IV.4)$$

The rate of unreactive scattering on a site on a filled dimer is simply the product of the probability of the outcome and the flux of incident F_2 molecules.

$$\text{rate of unreactive scattering} = I_{F_2} P_{unreactive}^{filled\ dimer} = I_{F_2} N\left(\frac{n_{Si}^{filled\ dimer}}{n_{Si}^{total}}\right). \qquad (IV.5)$$

A comparison of Eqs. (IV.5) with Eq. (IV.3) yields a relationship between the cross section N and its gas phase analog σ_N:

$$\sigma_N = \frac{N}{n_{Si}^{total}}. \qquad (IV.6)$$

Equivalent relationships are obtained for all of the cross sections in the model.

The quantity, n_{Si}^{total}, is the two dimensional density of sites on the Si(100) surface. Based on a unit cell lattice spacing of 3.84 Å, it has a value of $n_{Si}^{total}=6.78\text{x}10^{14}$ cm^{-2}. The inverse of this quantity, $1/n_{Si}^{total}=14.7\text{x}10^{-16}$ cm^2, is the cross sectional area of a Si(100) surface site. Given that a molecule incident on a macroscopic surface must collide with it, σ_N must have at least this value, assuming that a molecule collides or interacts with a single site. In the development of the model, the cross section N for unreactive scattering of a F_2 molecule from a filled dimer site is determined to be equal to one which yields a value of $14.7\text{x}10^{-16}$ cm^2 for σ_N. This approximation for σ_N effectively treats the collision radius of F_2 (0.92 Å) [34] as small compared to the radius of a surface site, 2.2 Å, as calculated from its cross sectional area, $14.7\text{x}10^{-16}$ cm^2. Similarly the cross section J for unreactive scattering of a F atom from a filled dimer site is determined to be equal to one which yields a value of $14.7\text{x}10^{-16}$ cm^2 for σ_J. Again, this approximation treats the

collision radius of a F atom as small compared to the radius of the surface site. Therefore, the cross sections σ_N and σ_J represent the statistical probability of colliding with the appropriate site.

In an analogous manner, Eq. (IV.6) yields values for the cross section for F atom abstraction from a F_2 molecule by a site in an empty dimer, σ_A, is 14.0×10^{-16} cm^2 and by a site in a half-filled dimer, σ_B, is 24.7×10^{-16} cm^2. The cross section for adsorption of the complementary F atom on a site in an empty dimer, $\sigma_{D'}$, is 12.8×10^{-16} cm^2 and by a site in a half-filled dimer, $\sigma_{E'}$, is 15.1×10^{-16} cm^2. Although these cross sections do not reflect accurate absolute values, their values relative to the cross section of a surface site and their values relative to each other do reveal the relative reactivities of the different sites and different processes in the interaction of F_2 with Si(100).

IV.A.2. Initial F atom abstraction

The first step in both single atom abstraction and two atom adsorption is the abstraction of a F atom from the incident F_2 molecule. This initial abstraction can only occur on an empty site as shown by the experimental results. The good agreement between the model and the data indicates that the reactivity of a given site is dependent on the occupation of its complementary dimer atom. Specifically, the cross sections for F atom abstraction from a F_2 molecule by an unoccupied site in a half-filled dimer, σ_B, is 24.7×10^{-16} cm^2 and that by a site in an empty dimer, σ_A, is 14.0×10^{-16} cm^2. The large values of both cross sections compared to the cross sectional area of a surface site, 14.7×10^{-16} cm^2, suggest that there is no significant energetic barrier to the dissociative chemisorption of a F_2 molecule on a Si dangling bond, in agreement with the experimental observation. In addition, σ_B is larger than the cross sectional area of a surface site by almost a factor of two. Its larger value implies that the empty site on the half-filled dimer is

much more reactive than expected from simple statistical considerations and that the interaction potential between the unoccupied Si dimer atom and the F_2 molecule is attractive. Furthermore, σ_B is larger than σ_A also by almost a factor of two, implying that the dangling bond associated with a half-filled dimer is more reactive than that of an empty dimer. The specific site reactivity is discussed further in Section IV.A.3.

After the initial abstraction occurs, the fate of the complementary F atom is still unknown. However, regardless of the outcome, dissociative chemisorption has occurred.

IV.A.3. Neighbor independent single atom abstraction

Single atom abstraction occurs if the complementary F atom does not adsorb to the surface, but remains a gas phase F atom. Figure 17 shows two limiting scenarios for the trajectory of the F atom. If the initial abstraction occurs with the F_2 molecular bond axis in a perpendicular approach geometry with respect to the surface plane (Figure 17(a)), the exothermicity will propel the F atom away from the surface, giving no opportunity for the F atom to interact with it. This mechanism for single atom abstraction is termed "neighbor independent" because the complementary F atom scatters into the gas phase regardless of the occupancy of the neighboring sites. This direct scattering into the gas phase is described by the probability X. The value of X cannot be uniquely determined because of its relationship to the other cross sections, but an upper bound can be determined. The description of the probability of single atom abstraction by Eq. (III.30) is purely mathematical without significant physical meaning in that it is, by virtue of the normalization of the total probability, the probability of neither unreactive scattering nor two atom adsorption occurring. However, the probability of single atom abstraction can be described with more physical meaning if it is presented in terms

of cross sections, G´ and H´, which are related to the probability of the complementary F atom unreactively scattering from a site on an empty dimer and a half-filled dimer, respectively:

$$P_2 = [A(1-(2\theta_1+\theta_2))+B\theta_1][1-[G'(1-(2\theta_1+\theta_2))+H'\theta_1+(1-X)\theta_2+X]], \quad \text{(IV.7)}$$

$$P_1 = [A(1-(2\theta_1+\theta_2))+B\theta_1][G'(1-(2\theta_1+\theta_2))+H'\theta_1+(1-X)\theta_2+X], \quad \text{(IV.8)}$$

where the cross sections G´ and H´ are related to the original factors G and H+H* by:

$$\begin{aligned} G' &\equiv G(1-X) \\ H' &\equiv (H+H^*)(1-X). \end{aligned} \quad \text{(IV.9)}$$

In the limit that the cross section G´ for unreactive scattering of a F atom from a site on an empty dimer is vanishingly small, the probability of single atom abstraction at zero coverage simplifies to:

$$P_1(\theta=0) = AX = 0.13 \pm 0.03. \quad \text{(IV.10)}$$

Therefore, if A=0.96±0.03, then X=0.13±0.03 is the upper bound for the probability of direct F atom scattering. The above physical picture suggests that the value of X is proportional to the solid angle of molecular orientations leading to direct scattering relative to the 2π steradians of the hemisphere above the surface. From purely geometric considerations, the F_2 molecular axis would have to lie within 11° of the surface normal for single atom abstraction to occur via the direct F atom scattering mechanism.

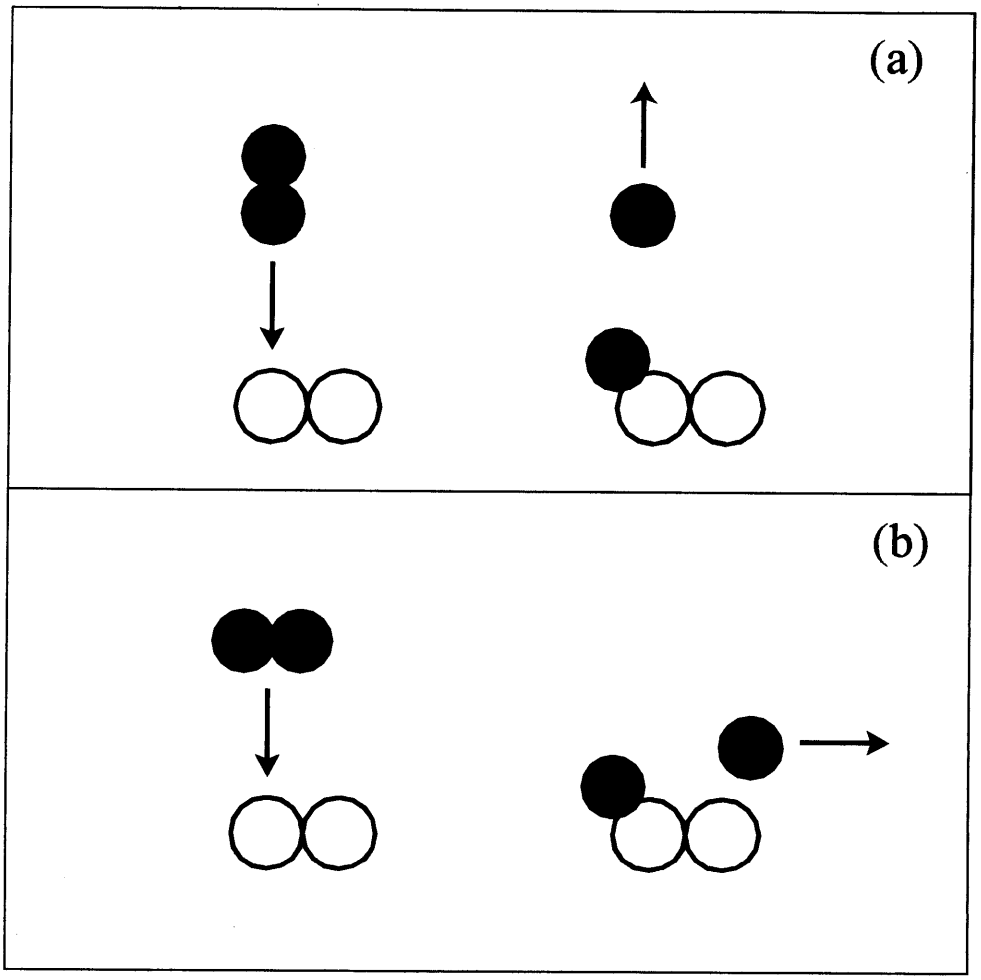

Figure 17 Pictorial representation of perpendicular and parallel approach geometries
Pictorial representation of (a) perpendicular and (b) parallel approach geometries in the interaction of the incident F_2 molecule with the Si surface.

IV.A.4. Neighbor-dependent single atom abstraction and two atom adsorption

On the other hand, if the initial abstraction occurs with the F_2 molecule in a parallel approach geometry (Figure 17(b)), the complementary F atom will scatter along the surface. Because the Si surface is so corrugated, the F atom will probably have only one interaction with the surface. If this interaction occurs at an occupied site, the F atom will be scattered into the gas phase leading to single atom abstraction. However, if this interaction occurs at an unoccupied site, the F atom may either scatter into the gas phase or adsorb on the surface leading to single atom abstraction or two atom adsorption, respectively.

The cross section for F atom adsorption by an unoccupied site in a half-filled dimer, $\sigma_{D'}$, is 15.1×10^{-16} cm^2 and that by a site in an empty dimer, $\sigma_{E'}$, is 12.8×10^{-16} cm^2. Like the initial F atom abstraction from the incident F_2 molecule, the values of both cross sections are large with respect to the cross sectional area of a surface site, 14.7×10^{-16} cm^2 suggesting that there is no significant energetic barrier to adsorption of a F atom on a Si dangling bond. In fact, the large values of $\sigma_{D'}$ and $\sigma_{E'}$ suggest that the F atom will almost always adsorb if it interacts with an empty site leading to two atom adsorption. This mechanism for single atom abstraction is termed "neighbor dependent" because it is dependent on the occupancy of the neighboring sites. It is this mechanism that is responsible for the nonmonotonic parabolic coverage dependence of the probability for single atom abstraction and represents the competition between needing an empty site for the initial F atom abstraction from the incident F_2 and an occupied site to prevent the complementary F atom adsorption.

Therefore, at low coverage (θ<0.5 ML), the probability of single atom abstraction is always lower than the probability of two atom adsorption because the number of empty sites for

F atom adsorption outnumbers the number of filled sites for F atom scattering (and the probability of neighbor independent single atom abstraction is negligible). Conversely, at high coverage (θ<0.5 ML), single atom abstraction is the dominant reactive channel. This qualitative observation based on the model is in accordance with the experimental results even at high coverage where the model cannot quantitatively describe the data well. The observation that two atom adsorption is the dominant channel at low coverage is in stark contrast to the conclusions of previous experimental and theoretical investigations which suggested that single atom abstraction was the dominant channel.

The measurements described above in Sec. II do not reveal any information regarding the site for adsorption of the complementary F atom in two atom adsorption. Its presence is only inferred from the insufficient flux into the other two channels, single atom abstraction and unreactive scattering, which are directly measured. Kummel and coworkers used scanning tunneling microscopy (STM) to probe the interaction of F_2 with Si(111) [35]. They attributed isolated adsorbates to single atom abstraction and two adjacent adsorbates to two atom adsorption. Their interpretation led to the conclusion that single atom abstraction is the dominant channel at low coverage. This result is in stark contrast to the result described above that showed two atom adsorption to be the dominant channel at low coverage. However, the two experiments probed the interactions of F_2 with different planes of the Si surface, which could account for the discrepancy in the results. The reactivity of the different planes of the Si surface will be discussed below with regard to the reactivity of different sites. However, the interpretation of STM images is questionable if two atom adsorption is indeed not constrained to occur on adjacent sites. Similar difficulties arise in the interpretation of STM experiments of O_2

on Al(111) that isolated adsorbed oxygen atoms resulted from the hot atom motion upon dissociation chemisorption [36]. This system will be discussed further in Sec. IV.C. In general, the use of STM alone to deduce reaction mechanisms is controversial because of the extremely long timescale of the experimental measurement relative to the event being probed.

Molecular dynamics simulations by Carter and coworkers using the WWC potential to describe the interaction of F_2 with Si(100), have suggested that two atom adsorption occurs preferentially, although not exclusively, across adjacent dimer rows [16]. This occurs in the simulations because the F_2 molecule tends to align with the Si dangling bond during the initial F atom abstraction so the complementary F atom is ejected in the direction of the adjacent dimer row. Indeed, the simulations also showed that the F atoms arising from single atom abstraction are preferentially ejected along the Si-F bond axis with an average velocity of ~2000 m/s preventing the F atoms from subsequently interacting with the surface and allowing for two atom adsorption. This theoretical prediction is in complete disagreement with the experimental observation of a cosinelike angular distribution of F atoms (Figure 8) with an average velocity of only 1084±46 m/s (Figure 3). Although the molecular dynamics simulations of Carter and coworkers correctly predict the presence of single atom abstraction, they do not accurately describe the dynamics of the interaction. Thus, the WWC potential is an inaccurate representation of the interaction between F_2 and Si.

IV.A.5. Surface site reactivity

IV.A.5.a. Nondifferentiation of sites in model

One of the fundamental assumptions in the development of the model is that the adsorption sites are distinguishable by the occupation of the complementary dimer atom. The

reactivity of the empty site(s) on the two types of dimers, empty and half-filled, is allowed to be different. The effect of not differentiating between the reactivity of empty and half-filled dimers can be probed by restricting the cross sections for F atom abstraction from an empty site on an empty dimer and a half-filled dimer to be equal, i.e., B=A, as well as constraining the probability factors for F atom adsorption from an empty site on an empty dimer and a half-filled dimer to be equal, i.e., E′= D′. Incorporating these equalities into Eqs. (III.27), (III.28), and (III.29) yields simplified equations for P_2, P_1, and P_0, respectively:

$$P_2 = AD'(1-\theta)^2, \tag{IV.11}$$

$$P_1 = A(1-\theta)[1-D'(1-\theta)], \tag{IV.12}$$

$$P_0 = 1-[A(1-\theta)]. \tag{IV.13}$$

These probability equations lead to simplified coverage equations (cf. Eqs. (III.28) and (III.29)):

$$\theta_1 = \tfrac{1}{2} I_{F_2} \int A(1-\theta) + AD'(1-\theta)^2 - 2A\theta_1(1+D'(1-\theta)), \tag{IV.14}$$

$$\theta_2 = \tfrac{1}{2} I_{F_2} \int A\theta_1(1+D'(1-\theta)). \tag{IV.15}$$

There are no adjustable parameters in the modified model because the two cross sections, A and D′, are both determined from the experimental results. The system of coupled differential equations, Eqs. (IV.14 and IV.15), can be solved numerically and these solutions can be substituted into Eqs. (IV.11), (IV.12), and (IV.13) to determine the reaction probabilities.

An interesting result arises from substituting the relationship between probability factors D and G in Eq. (III.25) with the modified factors D′ and G′ described by Eqs. (III.32) and (IV.9) into Eq. (IV.12):

$$P_1 = A(G'+X)(1-\theta) + AD'\theta(1-\theta). \tag{IV.16}$$

This form for P_1 as well as the form for P_2 are exactly analogous to the forms for P_1 and P_2 in an earlier statistical model that describe the probability of two atom adsorption and single atom abstraction [2,5,6].

$$P_2 = S_2(1-\theta)^2 \text{ and} \tag{IV.17}$$

$$P_1 = S_1^{ni}(1-\theta)+S_1^{nd}\theta(1-\theta), \tag{IV.18}$$

where S_2, S_1^{ni}, and S_1^{nd} are the proportionality constants for two atom adsorption, "neighbor independent" atom abstraction, and "neighbor dependent" atom abstraction. Neighbor independent atom abstraction is exactly analogous to the perpendicular approach geometry shown in Figure 17(a) while neighbor dependent atom abstraction and two atom adsorption are analogous to the parallel approach geometry shown in Figure 17(b), the only difference being the scattering or adsorption of the complementary F atom, respectively. Comparison of the probability factors in Eqs. (IV.11) and (IV.16) with those in Eqs. (IV.17) and (IV.18) yields relationships between the proportionality constants of the modified model with the cross sections of the original model:

$$S_2 = S_1^{nd} = AD', \tag{IV.19}$$

$$S_1^{ni} = A(G'+X). \tag{IV.20}$$

The most significant result is that proportionality constants for two atom adsorption and neighbor dependent single atom abstraction are identical. This constraint was not considered in the earlier model because two atom adsorption and single atom abstraction were not treated as related processes. However, in the subsequent interaction of the complementary F atom with the surface, the scattering event must contribute either to two atom adsorption or single atom

abstraction. Thus, the two processes are intimately related by the necessity for the normalization of the total probability for the F atom to either be scattered or adsorbed.

The proportionality constants can be determined from the experimentally measured probabilities at zero coverage:

$$P_2(\theta = 0) = AD' = S_2 = 0.83 \pm 0.03 . \quad \text{(IV.21)}$$

$$P_1(\theta = 0) = A(G' + X) = S_1^{ni} = 0.13 \pm 0.03 . \quad \text{(IV.22)}$$

From Eq. (IV.19),

$$S_1^{nd} = AD' = S_2 = 0.83 . \quad \text{(IV.23)}$$

The constants of the modified model for two atom adsorption S_2 and neighbor independent single atom abstraction S_1^{ni} are equivalent to what had been previously determined. However, the neighbor dependent constant S_1^{nd}=0.83 is much lower than the value derived solely from the maximum in the experimental value of P_1, S_1^{nd}=1.13. Figure 18(a)-(c) is a comparison of the reaction probabilities as a function of coverage derived from the modified model and the experimental results. The modified model does not describe the data well. The chi square value, as defined in Eq. (III.44), is 1012 which is orders of magnitude greater than the original model.

In particular the modified model is unable to describe the probability of unreactive scattering, which according to Eq. (IV.13), is linear with respect to coverage, unlike the data which is distinctly nonlinear with respect to coverage. The contribution of P_0 to the chi square function (the first term in Eq. (III.46)) is 1009 for the modified model compared to a value of 3.1 for the original model. Unreactive scattering is the process that results when F atom abstraction from the F_2 molecule does not occur. Since F atom abstraction simply requires one empty site, a linear dependence on the number of empty sites would be expected for reactive scattering. On

the other hand, a linear dependence on the number of filled sites, i.e., the coverage, would be expected for unreactive scattering. Therefore, the unexpected nonlinearity of the experimental data for the probability of unreactive scattering suggests that the reactivity is not described so simply.

However, the modified model describes the probability of single atom abstraction about as well as the original model. The contribution of P_1 to the chi square function (the second term in Eq. (III.46)) is 3.1 for the modified model compared to a value of 0.25 for the original model. Both values are much less than 20, the number of degrees of freedom, and therefore are reasonably accurate descriptions of the data over the 0-1 ML F exposure range. Both models successfully describe the probability of single atom abstraction because the kinetics are driven by the competition between empty sites for the F atom abstraction and filled sites to prevent F atom adsorption leading to a parabolic dependence of the single atom abstraction probability on coverage.

On the contrary, the model does not accurately describe the probability of two atom adsorption, a value that is dependent on the probability of the other two reaction channels. In particular, the modified model predicts the standard Langmuirian coverage dependence that is quadratic in the fraction of empty sites, i.e., $(1-\theta)^2$, whereas the data are essentially linear with respect to the number of sites except at high coverages. On the other hand, the original model is able to accurately describe the probability of two atom adsorption. It is a mathematical necessity that the probability of two atom adsorption be essentially quadratic in the number of empty sites because this process requires the adsorption of two atoms on two empty sites. Thus, every term in Eq. (III.2) is the product of two terms that are related to the number of empty sites. However,

the differentiation of sites allows the unoccupied sites in empty and half-filled dimers to contribute unequally to two atom adsorption resulting in an overall reaction probability that is quasilinear as opposed to quadratic with respect to the number of empty sites. This is the reason the modified model gives a description similar to the original model of single atom abstraction, but not for two atom adsorption. Unlike single atom abstraction which requires filled sites, which are all equally unreactive, to prevent F atom adsorption, two atom adsorption requires empty sites, which are not equally reactive, for F atom adsorption.

The differentiation between the reactivity of the empty and half-filled dimers yields a dramatic improvement in the goodness of fit of the model to the experimental data, especially with regard to the probability of unreactive scattering and two atom adsorption. Although the improvement could be simply a natural consequence of the original model having two more adjustable parameters than the modified model, it will be shown in the next section, that there is a physical basis for the differentiation of sites on the Si(100) surface.

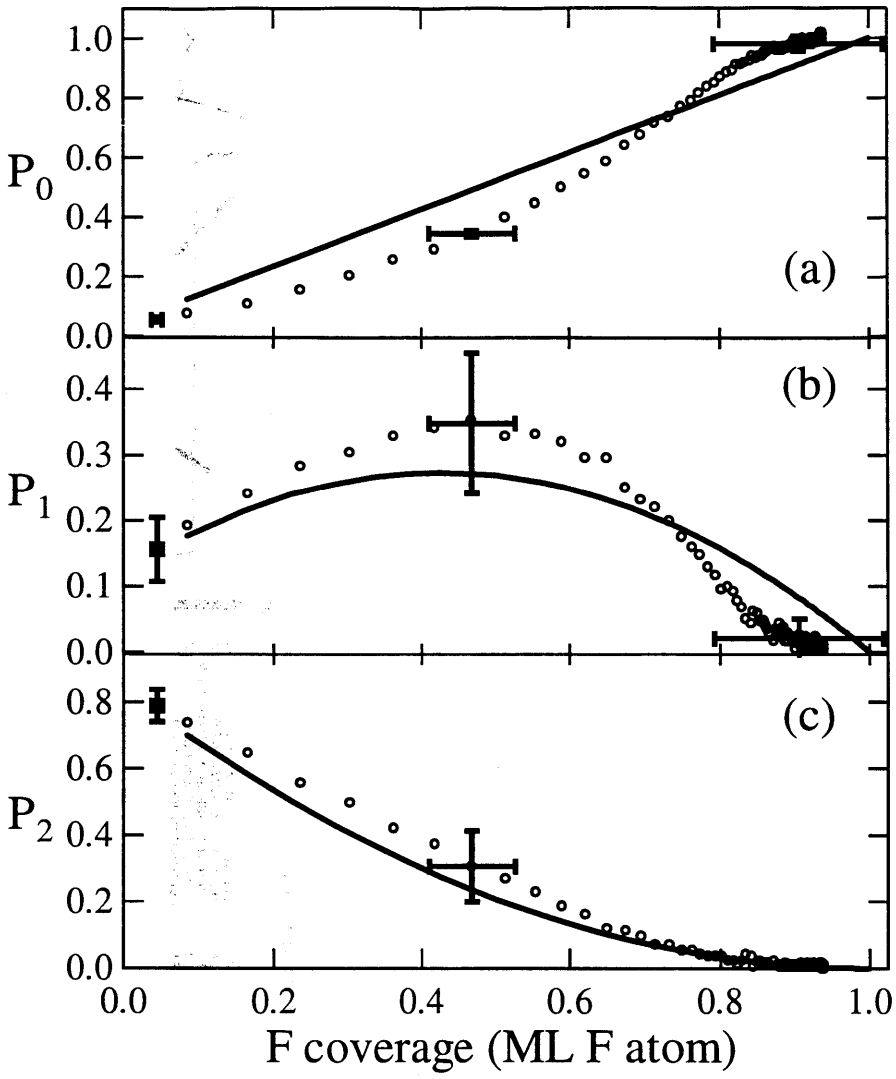

Figure 18 Reaction probabilities predicted by model with no site differentiation as a function of fluorine coverage

Reaction probability of F_2 with Si(100) as a function of fluorine coverage derived from the modified model [solid line] with no adjustable parameters to the experimental data [circles] for (a) unreactive scattering P_0, (b) single atom abstraction P_1, (c) two atom adsorption P_2. The data are from Figure 15.

IV.A.5.b. Dimer pairing energy

The unreconstructed Si(100) surface consists of Si atoms that are sp^3-coordinated to two Si atoms below the surface. The remaining two valence electrons each occupy one of the remaining two sp^3 orbitals of the tetrahedron that project into the vacuum. These singly occupied orbitals are the dangling bonds. The dimerization that occurs in the (2x1) reconstruction of the Si(100) surface is primarily a sigma interaction between one pair of dangling bonds from the two surface Si atoms. The remaining two dangling bonds interact weakly through a π interaction [37]. The magnitude of this π interaction is the subject of controversy.

The enhanced reactivity of an empty site in a half-filled dimer relative to an empty dimer can be understood in terms of the stability of the Si dimer. The dimer is destabilized when one of the dangling bonds reacts because there is the loss of the stabilizing π interaction between the two dangling bonds. The unusual first order recombinative desorption kinetics of H_2 from Si(100) has been attributed to the pairing of H atoms on Si dimers to overcome the destabilization of the Si dimer π interaction [38,39,40,41]. Models for the kinetics of thermal desorption of H_2 from Si(100) suggest that the driving force behind the pairing of H atoms to completely fill a dimer site is the π-bond stabilization of the unoccupied Si—Si dimers [38,39]. In addition, STM measurements by Boland [40,41] on the H-Si(100) system show that when H atoms adsorb on the Si(100)(2x1) surface, they tend to occupy both sites on a single dimer rather than a single site on two different dimers. Thus, if a H atom binds on an empty dimer, there is a loss of the π-bond stabilization, whereas if it binds on a half-filled dimer, there is no increase in the total energy. Estimates of the π-bond stabilization range from a few kcal/mol [38,39] based

on the modeling of the thermal desorption kinetics to 18 kcal/mol based on the STM results [40]. The effect is not limited to the interaction of hydrogen with Si(100). STM measurements have suggested that O_2 preferentially dissociatively chemisorbs at the empty sites of half-filled dimers on hydrogen terminated Si(100) [42] and that Cl_2 preferentially dissociatively chemisorbs onto adjacent sites within a single empty dimer on Si(100) [43].

An interesting experiment amenable to the experimental technique described above in Section II would be to measure the reaction probabilities of F_2 incident on Si(111)(7x7). On the Si(111)(7x7) surface each surface atom has, at most, one dangling bond, but there are no dimers and therefore, no strong interactions between surface atoms. In addition, the nearest neighbors on Si(111) are separated by at least 6.9 A, much larger than the dimer bond distance of 2.3 A on Si(100). If the dependence of the reaction probabilities on coverage of F_2 with the Si(100) surface is a direct consequence of the differences in the reactivity of the empty and half-filled dimers, then the coverage dependence of the reaction probabilities on Si(111), which has no surface dimers, ought to be different from the results presented in Sec. II.

Kummel and coworkers examined the coverage dependence of the sticking coefficient of F_2 on both Si(100) and Si(111) using the molecular beam reflectivity method of King and Wells [44]. No remarkable differences between the two surface planes were noted. The sticking coefficient was observed to have a linear dependence on coverage for both surface planes. However, the sticking coefficient is the probability of not unreactively scattering, i.e., $1-P_0$ or, equivalently, P_1+P_2. They did not observe single atom abstraction because their experimental apparatus could not detect F atoms. Their calculation of the sticking coefficient is based on several assumptions regarding wall reactions as well as calibrations to experimental and

theoretical data. Consequently, the determination of the sticking coefficient as well as the coverage, which is determined by integration of the sticking coefficient, are questionable. Therefore, it is difficult to make any conclusions based on the observed similarity of the reactivities of the two Si surface planes. Regardless, the observation that the sticking coefficient of F_2 obeys a linear dependence on coverage on both Si(100) and Si(111) could be accidental. For example, if atom abstraction is dominant on Si(111) as suggested by the interpretation of STM results by Kummel and coworkers, where the surface Si atoms are separated by large distances relative to the F_2 bond length, then a linear dependence on the coverage would be expected. However, these interpretations are based on measurements of the sticking coefficient as well as the STM measurements, neither of which yield unambiguous results. The definitive experiment to determine the role of the surface structure in the dynamics of the interaction of F_2 with Si would be to use the method described in this chapter to directly measure the flux of the scattered products from both surfaces and determine the reaction probability of single atom abstraction and two atom adsorption.

IV.A.5.c. Molecular steering

Recently there have been many experimental [45,46] and theoretical [47, 48, 49] investigations of a phenomenon termed molecular steering in which the incident molecule is oriented by the gas-surface interaction potential along a more favorable trajectory to reaction than expected from a random orientation. This effect is expected to be accentuated in molecular beam experiments because the supersonic expansion causes extreme rotational cooling (T_{rot}~5 K) of the molecules in the beam making them more susceptible to rotation by external forces, i.e, the gas-surface interaction potential. It is suggested above that the cross section B>1 for F atom

abstraction from F_2 incident on Si(100) is representative of an attractive gas-surface interaction potential because the cross section is larger than the cross sectional area of a site on the Si(100) surface. Although the evidence for molecular steering in the interaction of F_2 with Si(100) is certainly not conclusive, it is consistent with the experimental results.

Consideration of the experimental results on other systems involving the interactions of halogen molecules with silicon lends further support for molecular steering in the interaction of F_2 with Si(100). Kummel and coworkers observed preferential adsorption of iodine relative to chlorine in the reaction of ICl with Si(111) using STM and Auger [50]. The surface is enriched in I relative to Cl by a factor of 2.1-2.8 depending on the technique used to measure the contributions to the coverage. They suggest that because the initial sticking coefficient of ICl is 0.89±0.07, the preferential I adsorption cannot be attributed simply to the enhanced reactivity of the I-end relative to the Cl-end because if this were the case, then the maximum sticking coefficient would be ~0.7 assuming an isotropic distribution of the incident ICl orientation relative to the surface. In other words, if the interaction of the I-end with the surface always leads to adsorption of I, then the maximum sticking coefficient of the I atom would be 0.5 because the I-end is directed towards the surface in half of the collisions. Because the surface is enriched in I relative to Cl by a factor of 2.1-2.8, the sticking coefficient of Cl would be lower than that of I by a factor of 2.1-2.8. Thus, the maximum sticking coefficient of the Cl atom is ~0.2 and the total sticking coefficient of ICl is ~0.7. Instead, they claim that the ICl molecule is oriented by the interaction potential with the Si surface into an I-end configuration. Kummel and coworkers observed a similar effect with I_2Cl_6 [51], but did not with IBr [52].

IV.B. Limitations of model

Although the model offers a good description of the kinetics of the interaction of F_2 with Si(100) as well as a physically intuitive picture of this gas-surface interaction, a few assumptions were made in the development of the model that warrant further discussion.

One of the major limitations of the model is that the saturation coverage of F on Si is defined to be 1 ML, the number of dangling bonds, or equivalently, the number of reactive sites as well as the number of adsorption sites, on the Si(100) surface. The experimental results show that the saturation coverage is indeed about 1 ML, but the measured value is only 0.94±0.11 ML. There are two possible reasons for the low saturation coverage. First, the uncertainty in the experimental measurement does not preclude the value from being 1 ML. In fact, the largest source of error is the literature value for the F atom ionization cross section, $\sigma_{F\rightarrow F^+}$, which has a relative uncertainty of 20%. Because the probability of single atom abstraction (P_1) is directly proportional to $\sigma_{F\rightarrow F^+}$ and the probability of two atom adsorption (P_2) is directly related to P_1, if the true value of $\sigma_{F\rightarrow F^+}$ is 15% lower than the reported value, the saturation coverage increases to 1 ML. Second, the presence of defects on the surface that eliminate dimer atoms, and hence eliminate dangling bonds, might lead to a decrease in the total number of available adsorption sites. Scanning tunneling microscope images of clean Si(100) surfaces have shown defect densities on the order of a few percent [41].

While the model could have been modified by redefining the saturation coverage, θ_{sat}, to be less than 1 ML, this modification would have created an additional variable, θ_{sat}, for which there was no *a priori* justification. Regardless, the values of P_1 and P_2 decay towards zero as the coverage approaches θ_{sat} far more rapidly than predicted by the model and maintain values near

zero beyond a coverage at which there are still 0.05 ML unoccupied sites on the surface. There are two possible causes of this divergence of the data from the model. First, the true saturation coverage may be higher than 1 ML so that the final 0.05 ML of sites that are eventually occupied are defect sites that are much less accessible than surface dangling bonds. Given the uncertainty of the measurement, this is a plausible explanation. Second, at a near saturation coverage, the remaining unoccupied surface dangling bonds may be less accessible because of steric effects or less reactive because of electronic effects than expected because of the effects of neighboring adsorbates.

The absence of any effect from neighboring adsorbates other than the complementary surface atom of the dimer pair is another significant limitation of the model. The effect of neighboring adsorbates could be incorporated into the model by incorporating a coverage dependence into the probability factors. Although this modification of the probability factors certainly would be a more accurate description of reality, the additional complexity only diminishes the physical insight gained from the simplicity of the model.

Finally, the statistical basis of the model is founded on the assumption that adsorption sites are accessed randomly by the incident F_2 molecules and that there is no diffusion either prior to adsorption, i.e., as a physisorbed precursor, or subsequent to adsorption, i.e., as a chemisorbed adsorbate. In the presence of diffusive motion the concentration of adsorbates on the surface might not be necessarily homogeneous such that the global coverage would not be representative of the local environment. This simplifying assumption is justified by STM images of Si(111) at low fluorine coverage [35] which show random fluorine adsorption sites with no significant islanding or clustering of adsorbates. In addition repeated imaging of the fluorinated surface

shows no significant adsorbate motion, through either diffusion or desorption. Sholl [53] has examined the effect of adsorbate interactions as well as the possibility of a physisorbed precursor mechanism using Monte Carlo simulations that incorporate a model similar to the earlier model (i.e., model with no site differentiation) described above in Sec. IV.A.3.a. A comparison of these simulations with the experimental results presented above in Sec. II suggests that both adsorbate interactions as well as a precursor mechanism have no significant, if any, contributions to the kinetics of the interaction of F_2 with Si.

IV.C. Atom abstraction in other gas-surface systems

Atom abstraction is not unique to the interactions of halogens with silicon. If the energy released in forming one surface-adsorbate bond is sufficient to compensate for the energy required to break the bond of the incident molecule, then abstraction by the surface is possible. An interesting candidate for atom abstraction is the interaction of O_2 with Al(111), although observation of isolated adsorbed atomic oxygen atoms on Al(111) using STM has been interpreted as evidence for hot atom motion of the two atoms resulting from a classic dissociative chemisorption event [36]. Hot atom motion arises from the release of exothermicity into parallel translational motion of the two atoms away from each other [54,55,56]. The atoms remain bound to the surface but travel along the surface until they dissipate enough energy to be trapped at a chemisorption site. Although this interpretation is plausible, especially considering subsequent work on O_2 on Pt(111) [57] and on Ag(110) [58] where energetic considerations necessitate the adsorption of both atoms, the results on Al(111) can also be explained by oxygen atom abstraction [2,59]. Unfortunately, the use of STM as the sole probe of dynamics of such a fast nature inevitably leads to ambiguity because the end result of each mechanism is likely to be

indistinguishable. Both atom abstraction and hot atom motion are dissociative chemisorption processes in which the two fragments separate from each other and lead independent existences. However, in hot atom motion, which arises from classic dissociative chemisorption, both atoms are and remain bound to the surface during their motion parallel to the surface because the exothermicity is insufficient to allow one or both to escape from the surface. In contrast, the complementary atom in atom abstraction is not initially bound to the surface and may move parallel to the surface for some distance before encountering an adsorption site. In either case, the hot atom or the abstracted atom will likely appear to a STM observation at some distance from its partner.

Earlier work on other gas-surface systems has yielded indirect observations consistent with atom abstraction. Lunsford and coworkers observed methyl radical production upon passing methane over a MgO surface [60] implying hydrogen atom abstraction by the MgO surface. White and coworkers also observed methyl radical production upon dissociative chemisorption of methyl bromide on potassium doped Ag surface [61]. Bent and coworkers also observed methyl radical production upon thermal desorption of molecularly adsorbed methyl iodide on a Cu surface [62,63]. Kasemo and coworkers have suggested chlorine atom abstraction in the Cl_2/K system [59].

V. CONCLUSION

F_2 interacts with Si(100) via two novel dissociative chemisorption mechanisms called single atom abstraction and two atom adsorption in which one and two F atoms adsorb to the surface, respectively. The distinguishing feature of single atom abstraction and two atom adsorption from classic dissociative chemisorption is that only one surface-adsorbate bond is necessary to liberate sufficient energy to cleave the incident molecular bond. As a consequence, the fate of the complementary F atom is not necessarily as an adsorbate on the surface as it is in classic dissociative chemisorption in which the two fragments of the cleaved molecule adsorb to the surface in a concerted process. The complementary F atom may scatter into the gas phase leading to single atom abstraction, or it may subsequently interact with the surface and adsorb leading to two atom adsorption.

The kinetics of the interaction of F_2 with Si(100) cannot be described by traditional gas-surface kinetics models. Instead, a statistical model is able to describe the kinetics of single atom abstraction and two atom adsorption that is based on the premise that single atom abstraction and two atom adsorption share a common initial mechanism, F atom abstraction, and that the four distinct types of sites, sites on empty dimers and filled dimers as well as unoccupied and occupied sites on half-filled dimers, interact differently with the incident F_2 molecule and scattered F atom. The model describes the data remarkably well, and the results are consistent with a stepwise mechanism in which the initial atom abstraction is central to both single atom abstraction and two atom adsorption. This result is expected since there is no thermodynamic driving force requiring the adsorption of the second F atom so its fate is independent of that of the initially abstracted F atom, a distinct difference from classic dissociative chemisorption

which is necessarily a concerted process in which both fragments must adsorb to the surface. The results of the model suggest that the fate of the complementary F atom is determined, in part, by the orientation of the incident F_2 molecular axis with respect to the surface. If the incident F_2 is oriented perpendicular to the surface, the complementary F atom will likely be ejected away from the surface making two atom adsorption impossible. This mechanism is termed neighbor-independent" because the fate of the complementary F atom is independent of the occupancy of the other sites on the surface. At zero coverage, it is this mechanism that yields the nonzero probability for single atom abstraction. On the other hand, if the incident F_2 is oriented parallel to the surface, the complementary F atom will likely interact with the surface. If the F atom interacts with an unoccupied site, adsorption may occur. This mechanism is termed "neighbor-dependent" because the occupancy of the site with which the F atom interacts determines whether the overall result is single atom abstraction or two atom adsorption. It is the competition between the need for an unoccupied site for the initial atom abstraction, and the subsequent need for an occupied site to prevent adsorption of the complementary F atom that yields the unusual coverage dependence of the probability of single atom abstraction which is signified by a maximum likelihood at 0.5 ML coverage.

The results of the model also suggest that the unoccupied sites on half-filled dimers are substantially more reactive than the unoccupied sites on empty dimers. A plausible explanation is that the remaining unoccupied dangling bond in a half-filled dimer is energetically less stable and, therefore, more reactive due to the absence of the π interaction that exists between the two unoccupied dangling bonds in an empty dimer. The necessity for differentiation of the reactivity of the distinct surface sites is demonstrated by the poor ability of the model to describe the data

when there is no differentiation of sites. Finally, the total reaction probability is near unity at zero coverage which indicates that there is no barrier to reaction. The results of the model suggest that the unoccupied sites on the half-filled dimer are so reactive that they are able to attract the incident F_2 molecule from a distance extending beyond the cross sectional area of the site itself. These results are consistent with the phenomenon of molecular steering in which the incident molecules are aligned into a favorable orientation for reaction.

Atom abstraction is not unique to the interaction of F_2 with Si(100). Atom abstraction ought to be present in any gas-surface system in which the energy liberated by the formation of a single surface-adsorbate bond is sufficient to cleave the incident molecular bond. Although no previous experimental investigation has provided direct evidence of atom abstraction, several investigations have provided experimental evidence that is consistent with the presence of atom abstraction. Despite the dearth of experimental evidence demonstrating atom abstraction, this gas-surface mechanism may have significant implications in important chemical processes like heterogeneous catalysis, chemical vapor deposition, and semiconductor etching. The possibility of atom abstraction ought to be considered in reaction systems in which atom abstraction is energetically favorable, especially in situations in which the production of radical atoms and molecules may have a significant effect on the rest of the system.

In the next chapter, an investigation of the interaction of XeF_2 with Si(100), a model semiconductor etching system, is presented. The energetics of the interaction of XeF_2 with Si(100) are similar to the energetics of F_2 with Si(100). Therefore, F atom abstraction ought to be present. Indeed, despite dramatic differences in the reactivity of XeF_2 and F_2 with Si, F atom abstraction is present.

REFERENCES

1. D.D. Eley and E.K. Rideal, *Nature* **146**, 401 (1940). D.D. Eley and E.K. Rideal, *Proc. Roy. Soc. London* **178**, 429 (1941). D.D. Eley, *Proc. Roy. Soc. London* **178**, 452 (1941).
2. S.T. Ceyer, *Proceedings of the R.A. Welch Foundation Conference on Chemical Research XXXVIII: Chemical Dynamics of Transient Species* (R.A. Welch Foundation, Houston, 1994).
3. Y.L. Li, D.P. Pullman, J.J. Yang, A.A. Tsekouras, D.B. Gosalvez, K.B. Laughlin, Z. Zhang, M.T. Schulberg, D.J. Gladstone, and S.T. Ceyer, *Phys. Rev. Lett.* **74**, 2603 (1995).
4. M.R. Tate, D. Gosalvez-Blanco, D.P. Pullman, A.A. Tsekouras, Y.L. Li, J.J. Yang, K.B. Laughlin, S.C. Eckman, M.F. Bertino, and S.T. Ceyer, *J. Chem. Phys.*, in press.
5. J.J. Yang, Ph.D. thesis, Massachusetts Institute of Technology, 1993.
6. D. Gosalvez-Blanco, Ph.D. thesis, Massachusetts Institute of Technology, 1997.
7. H.F. Winters and J.W. Coburn, *Surf. Sci. Rep.* **14**, 161 (1992).
8. J.R. Engstrom, M.M. Nelson, and T. Engel, *Phys. Rev. B* **37**, 6563 (1988).
9. J.R. Engstrom, M.M. Nelson, and T. Engel, *Surf. Sci.* **215**, 437 (1989).
10. E.W. Kuipers, A. Vardi, A. Danon, and A. Amirav, *Phys. Rev. Lett.* **66**, 116 (1991).
11. C.T. Rettner, *Phys. Rev. Lett.* **69**, 383 (1992). C.T. Rettner and D.J. Auerbach, *Science* **263**, 365 (1994). C.T. Rettner, *J. Chem. Phys.* **101**, 1529 (1994). C.T. Rettner and D.J. Auerbach, *Phys. Rev. Lett.* **74**, 4551 (1995). C.T. Rettner and D.J. Auerbach, *Surf. Sci.* **357**, 602 (1996). C.T. Rettner, D.J. Auerbach, and J. Lee, *J. Chem. Phys.* **105**, 10115 (1996).
12. F.H. Stillinger and T.A. Weber, *Phys. Rev. Lett.* **62**, 2144 (1989). T.A. Weber and F.H. Stillinger, *J. Chem. Phys.* **92**, 6239 (1990).
13. C.J. Wu and E.A. Carter, *Phys. Rev. B* **45**, 9065 (1992).
14. P.C. Weakliem, C.J. Wu and E.A. Carter, *Phys. Rev. Lett.* **69**, 200 (1992).
15. P.C. Weakliem and E.A. Carter, *J. Chem. Phys.* **98**, 737 (1993).
16. L.E. Carter, S. Khodabandeh, P.C. Weakliem, and E.A. Carter, *J. Chem. Phys.* **100**, 2277 (1994).
17. L.E. Carter and E.A. Carter, *J. Phys. Chem.* **100**, 873 (1996).
18. L.E. Carter and E.A. Carter, *J. Vac. Sci. Tech. A* **12**, 2235 (1994).
19. L.E. Carter and E.A. Carter, *Surf. Sci.* **323**, 39 (1995).
20. T.A. Schoolcraft and B.J. Garrison, *J. Vac. Sci. Tech. A* **8**, 3496 (1990). T.A Schoolcraft, A.M. Diehl, A.B. Steel, and B.J. Garrison, *J. Vac. Sci. Tech. A* **13**, 1861 (1995).
21. S.T. Ceyer, D.J. Gladstone, M. McGonigal, and M.T. Schulberg, *Physical Methods of Chemistry*, edited by B.W. Rossiter and R.C. Baetzold (Wiley, New York, 1993), 2nd ed., Vol. IXA, p. 383.
22. D.J. Gladstone, Ph.D. thesis, Massachusetts Institute of Technology, 1989.
23. M. McGonigal, Ph.D. thesis, Massachusetts Institute of Technology, 1989.
24. M.T. Schulberg, Ph.D. thesis, Massachusetts Institute of Technology, 1990.
25. A. Ishizaka and Y. Shiraki, *J. Electrochem. Soc.* **133**, 666 (1986).
26. The original energy resolution calculation given in Ref. 23 on p. 41 is incorrect by a factor of two. The correct formula for the energy resolution is $\Delta E/E = 2(\ell_{\text{ionizer}}/L_{\text{neutral}})$.
27. M.J. Cardillo and G.E. Becker, *Phys. Rev. B* **21**, 1497 (1980).
28. H.F. Winters and F.A. Houle, *J. Appl. Phys.* **54**, 1218 (1983).
29. T.R. Hayes, R.C. Wetzel, and R.S. Freund, *Phys. Rev. A* **35**, 578 (1987).

30. R. Walsh, *Acc. Chem. Res.* **14**, 246 (1981).
31. C.J. Wu and E.A. Carter, *J. Am. Chem. Soc.* **113**, 9061 (1991).
32. A. Zangwill, *Physics at Surfaces*, (Cambridge University Press, Cambridge, 1988), 379.
33. P.R. Bevington and D.K. Robinson, *Data Reduction and Error Analysis for the Physical Sciences*, 2nd ed., (McGraw-Hill, New York, 1992), 195.
34. J.O. Hirschfelder, C.F. Curtiss, and R.B. Bird, *Molecular Theory of Gases and Liquids* (Wiley, New York, 1964), 1111.
35. J.A. Jensen, C. Yan, and A.C. Kummel, *Science* **267**, 493 (1995).
36. H. Brune, J. Wintterlin, R.J. Behm, and G. Ertl, *Phys. Rev. Lett.* **68**, 624 (1992). H. Brune, J. Wintterlin, J. Trost, G. Ertl, J. Wiechers, and R.J. Behm, *J. Chem. Phys.* **99**, 2128 (1993).
37. J.A. Appelbaum, G.A. Baraff, and D.R. Hamann, *Phys. Rev. B* **14**, 588 (1976).
38. M.C. Flowers, N.B.H. Jonathan, A. Morris, and S. Wright, *J. Chem. Phys.* **108**, 3342 (1998).
39. M.P. D'Evelyn, Y.L. Yang, and L.F. Sutcu, *J. Chem. Phys.* **96**, 852 (1991).
40. J.J. Boland, *Phys. Rev. Lett.* **67**, 1539 (1991).
41. J.J. Boland, *Adv. Phys.* **42**, 129 (1993).
42. H. Kajiyama, S. Heike, T. Hitosugi, and T. Hashizume, *Jap. J. Appl. Phys.* **37**, L1350 (1998).
43. I. Lyubinetsky, Z. Dohnálek, W.J. Choyke, and J.T. Yates, *Phys. Rev. B* **58**, 7950 (1998).
44. E.R. Behringer, H.C. Flaum, D.J.D. Sullivan, D.P. Masson, E.J. Lanzendorf, and A.C. Kummel, *J. Phys. Chem.* **99**, 12863 (1995). E.R. Behringer, H.C. Flaum, and A.C. Kummel, *J. Phys. Chem.* **99**, 5532 (1995).
45. M. Beutl, M. Riedler, K.D. Rendulic, *Chem. Phys. Lett.* **247**, 249 (1995).
46. M. Gostein and G.O. Sitz, *J. Chem. Phys.* **106**, 7378 (1997).
47. A. Gross, S. Wilke, and M. Scheffler, *Phys. Rev. Lett.* **75**, 2718 (1995).
48. M. Kay, G.R. Darling, S. Holloway, J.A. White, and D.M. Bird, *Chem. Phys. Lett.* **245**, 311 (1995).
49. G.R. Darling, M. Kay, and S. Holloway, *Surf. Sci.* **400**, 314 (1998).
50. Y. Liu, D.P. Masson, and A.C. Kummel, *Science* **276**, 1681 (1997).
51. Y. Liu, P.R. Taylor, and A.C. Kummel, *J. Chem. Phys.* **109**, 5714 (1998).
52. Y. Liu, A.J. Komrowski, P.R. Taylor, and A.C. Kummel, *J. Chem. Phys.* **109**, 2467 (1998).
53. D.S. Sholl, *J. Chem. Phys.* **106**, 289 (1997).
54. B. Kasemo and J. Harris, *Surf. Sci.* **105**, L281 (1981).
55. S. Caratzoulas, B. Jackson, and M. Persson, *J. Chem. Phys.* **107**, 6420 (1997). D. Shalashilin and B. Jackson, *J. Chem. Phys.* **109**, 2856 (1998).
56. S.L. Tang, J.D. Beckerle, M.B. Lee, and S.T. Ceyer, *J. Chem. Phys.* **84**, 6488 (1986).
57. J. Wintterlin, R. Schuster, and G. Ertl, *Phys. Rev. Lett.* **77**, 123 (1996).
58. J.V. Barth, T. Zambelli, J. Wintterlin, and G. Ertl, *Chem. Phys. Lett.* **270**, 152 (1997).
59. J. Strömquist, L. Hellberg, B. Kasemo, and B.I. Lundqvist, *Surf. Sci.* **352-354**, 435 (1996).
60. D.J. Driscoll, W. Martir, J.-X. Wang, and J.H. Lunsford, *J. Am. Chem. Soc.* **107**, 58 (1985).
61. X.-L. Zhou, S.R. Coon, and J.M. White, *J. Chem. Phys.* **94**, 1613 (1991).
62. J.-L. Lin and B.E. Bent, *J. Am. Chem. Soc.* **115**, 2849 (1993).
63. P.W. Kash, D.-H. Sun, M. Xi, G.W. Flynn, and B.E. Bent, *J. Phys. Chem.* **100**, 16621 (1996) and references therein.

Chapter 2: The Interaction of XeF_2 with Si(100)

I. INTRODUCTION

The detailed dynamics of the interaction of F_2 with Si(100) are described in Chapter 1. A novel mechanism for dissociative chemisorption called single atom abstraction is identified in which only a single surface-adsorbate bond is formed while the complementary atom is scattered into the gas phase. In addition to single atom abstraction, a mechanism similar to classic dissociative chemisorption called two atom adsorption is indirectly identified in which both atoms are adsorbed to the surface. Dissociative chemisorption via atom abstraction ought to be present in any gas-surface system in which the energy liberated in forming a single surface-adsorbate bond is greater than the energy necessary to break the bond of the incident molecule. Xenon difluoride (XeF_2) is an excellent candidate for dissociative chemisorption on Si via atom abstraction given its similar chemical structure and thermodynamics to molecular fluorine. In addition to understanding the novel gas-surface mechanism of atom abstraction, the disparate reactivity of these two similar compounds with silicon is of fundamental significance and their use as model etchants in semiconductor etching is of great applied importance.

I.A. Previous Investigations of the Reactivity of XeF_2 with Si

The etching of semiconductors is essential to the microelectronics industry and the fabrication of the ubiquitous "microchip". Semiconductor etching is a marvel of engineering, but it is not well understood. The model system is the reaction of atomic fluorine with elemental silicon. However, fluorine atoms do not come in a bottle. Although true atomic fluorine sources exist, the experimental difficulties have led many investigators to seek simpler alternative sources of fluorine.

The ability of XeF_2 to etch silicon spontaneously under ambient conditions was first shown by Winters and Coburn twenty years ago [1]. Since this discovery, several investigators have sought to understand the way in which XeF_2 reacts with silicon [2]. The reactivity of this noble gas compound with silicon is similar to that of atomic fluorine, a comparison that has led to the popular notion that XeF_2 is simply a convenient source of fluorine atoms. However, despite its unusual chemical nature, XeF_2 is a very stable molecule. In fact, it is more stable than F_2, a compound that does not etch silicon spontaneously under similar conditions. Thus, XeF_2 is indeed not just a source of fluorine atoms! Many investigators have acknowledged the different reactivity of XeF_2, F, and F_2 with silicon, but there is no direct evidence to support any explanation for the disparity in reactivity.

Because of its practical importance in the microelectronics industry, many investigations have focused on the etch rate of silicon by XeF_2 and the identification of the silicon etch products [1,3,4,5]. The absolute etch rates are strongly dependent on the exact conditions, i.e., XeF_2 flux, surface temperature, surface structure. The probability that a single XeF_2 molecule leads to the desorption of a single silicon atom is on the order of 10^{-4}-10^{-2}. Under ambient conditions, the magnitude of the silicon etch rate by xenon difluoride is lower than that of F [3] by an order of magnitude but about three to four orders of magnitude higher than that of F_2 [1].

The surface temperature dependence of the etch rate of silicon by XeF_2 is unusual. Under ambient XeF_2 vapor pressure conditions (~1 torr), Ibbotson *et al* [4] determined that at surface temperatures above 450 K, the etch rate increases monotonically with temperature as expected for normal Arrhenius behavior, whereas at surface temperatures below 400 K, the etch rate actually increases monotonically with decreasing temperature suggestive of a negative activation

energy. Under ultrahigh vacuum (UHV) conditions, Vugts *et al* [6] also measured a nonmonotonic temperature dependence similar to the high pressure study of Ibbotson *et al.* However, at the very low surface temperatures (150 K) below those obtainable by Ibbotson *et al*, they observed XeF_2 condensation leading to surface passivation and no etching. In gas-surface systems, this non-Arrhenius behavior is typically attributed to a physisorbed precursor mechanism [7].

Similar to other fluorine etchants, the major etch product arising from reaction with XeF_2 at low surface temperatures (T_s<600 K) is fully fluorine-coordinated silicon, tetrafluorosilane (SiF_4) [1,3,4,8,9,10,11]. Time-of-flight measurements using incident beam modulation showed that SiF_4 does not desorb entirely in thermal equilibrium with the surface, but instead the SiF_4 desorbs with a bimodal distribution suggesting that etch product desorption is not simply the evaporation of volatile silicon compounds [9]. Other investigations have shown minor etch products including radicals like SiF [8], SiF_2 [3,4,8], SiF_3 [8,9,11], as well as higher fully coordinated fluorosilanes like Si_2F_6 [9,11], but there is disagreement in the literature regarding the relative abundances. Similar to the reaction of F atoms with Si, SiF_2 is the most abundant of the minor etch products [4,10,12]. In one of the first realizations that XeF_2 was not simply a source of F atoms [4], evidence against this simple analogy was that the relative abundance of SiF_2 is less from XeF_2 than F atoms. Mitchell *et al* [12] measured the chemiluminescence arising from the reaction of XeF_2 with Si and the reaction of F with Si under ambient conditions and attributed a diffuse visible feature centered around 500 nm to emission from electronically excited SiF_3 arising from gas phase reaction of desorbing SiF_2 with the incident XeF_2 molecule or F atom. In addition, the reaction with XeF_2 showed a distinct feature at 350 nm arising from

emission from the excimer B state of XeF, the product of the gas phase reaction. Analogous to the interactions of F and F_2 with Si, SiF_2 is a major etch product of the interaction of XeF_2 with Si at high surface temperatures (T_s>600 K) in agreement with thermal desorption measurements that show significant SiF_2 desorption around 800 K.

To better understand the etching mechanism, many investigations have focused on the characterization of the silicon surface structure arising from exposure to XeF_2 [13,14,15,16,17,18,19,20,21,22,23,24,25,26,27]. X-ray photoelectron spectroscopy (XPS) is the most common experimental probe of fluorinated silicon [13-23]. Based on the analysis of the shifts of the Si 2p core levels with increasing fluorine coordination, a distribution of SiF_x (x=1,2,3) have been observed. McFeely and coworkers [14-16] studied the fluorinated silicon surface at low XeF_2 exposures prior to the onset of significant etching. Low energy electron diffraction (LEED) of Si(100) showed that the characteristic (2x1) reconstruction persists upon the initial interaction of XeF_2 suggesting that the dangling bonds are the sites of the initial adsorption of fluorine from XeF_2 analogous to the interaction of F_2 with Si(100). XPS and electron energy loss spectroscopy (EELS) confirmed that the predominant surface species is SiF. Higher XeF_2 exposures cause the coverage to increase beyond the 1 ML F. XPS measurements suggest that a diffuse structure of fluorinated silicon chains forms. The total fluorine coverage saturates at about 1.6 ML for both Si(100) and Si(111) and consists of mostly SiF, especially on Si(100), with the remaining fluorine divided evenly between SiF_2 and SiF_3. At very high XeF_2 exposures [17-22], there is a shift in the population to increasingly fluorinated surface Si atoms. Other spectroscopic techniques like photon stimulated desorption (PSD) [24,25], infrared reflection absorption spectroscopy (IRAS) [26], and second harmonic generation (SHG) [27]

have been utilized to characterize the fluorinated surface structure. These results are all in reasonable agreement with the results from the XPS investigations discussed above. An interesting investigation by Chuang using infrared chemiluminescence showed emission from vibrationally excited surface species [28]. The surface temperature was not sufficiently high to account for the vibrational excitation indicating that the excitation arose from the reaction of XeF_2 with Si.

In addition to studies of the effects of XeF_2 on the Si surface structure, the effects of the Si surface composition, i.e., dopant type and concentration, on the XeF_2 reactivity have also been probed [11,29]. Winters and coworkers [2,29] determined that etching was enhanced in heavily n-doped silicon and inhibited in heavily p-doped silicon. They proposed a simple model for halogen etching based on the Mott-Cabrera theory of oxide formation.

Because of its relevance to plasma etching, a number of investigations have sought to incorporate additional energetic particles to better mimic the plasma environment. Many investigations have focused on the enhancement of XeF_2 reactivity with coincident ions [30,31,32,33,34,35] and photons [36,37,38,39,40,41,42]. Winters and coworkers [30,31] measured a significant enhancement of the Si etch rate with coincident ions. The enhancement was dramatically greater than the sum of the etch rates from either XeF_2 or ions alone. This phenomenon is known as chemical sputtering. In addition, they showed that unlike F atoms, XeF_2 could not etch SiO_2 except in the presence of coincident charged particle (i.e., ion or electron) bombardment.

Interestingly, the practical use of XeF_2 as a Si etchant has been recently popularized by the materials science and engineering community in the fabrication of microelectromechanical

systems (MEMS). Because of its extremely high selectivity towards silicon relative to silicon dioxide (SiO_2), aluminum, and photoresist, xenon difluoride is considered an ideal isotropic etchant for bulk micromachining [43].

I.B. Detailed Dynamics of the Interaction of XeF_2 with Si(100)

Despite the wealth of information on the XeF_2/Si gas-surface system regarding the etch rate, the etch products, the surface structure, as well as the effects of a variety of enhancements, the dynamics of the interaction of XeF_2 with Si are still not well understood. Most importantly, there is no direct evidence to support any resolution of the apparent contradiction of energetic considerations and the reactivity of XeF_2, F, and F_2.

The focus of the investigation described in this chapter is to probe the dynamics of the interaction of XeF_2 with Si. The experiments with XeF_2 directly parallel those with F_2 described in Chapter 1, and the results of these experiments will be compared with the results of the experiments on the interaction of F_2 with Si. Briefly, recall that F_2 incident on Si proceeds through one of three channels: single atom abstraction (P_1) or two atom adsorption (P_2), two dissociative chemisorption mechanisms in which only one or both fluorine atoms are adsorbed onto the surface, respectively, or unreactive scattering (P_0). F_2 reacts exclusively with the Si dangling bonds; no Si-Si dimer bonds or lattice bonds are broken. When all of the Si dangling bonds are fluorinated, the reaction ceases. On a clean Si surface, F_2 is extremely reactive ($P_{total}=1-P_0=0.95$) and the most probable channel is two atom adsorption ($P_2=0.83$). However, as the surface is fluorinated, the probability of single atom abstraction increases at the expense of two atom adsorption reaching a maximum ($P_{1,max}=0.35$) at 0.5 ML coverage. The unusual coverage dependence of single atom abstraction was described by a competition for a single

empty site for the initial atom abstraction and an occupied site for preventing two atom adsorption. Beyond 0.5 ML, the probability of both single atom abstraction and two atom adsorption decrease to zero as all of the Si dangling bonds are occupied and the fluorine coverage approaches 1 ML.

Based on the similar chemical structure and thermodynamics of XeF_2 and F_2, similarities in their interaction with Si are expected. Namely, three channels are expected to be available for a XeF_2 molecule incident on the Si surface: single atom abstraction, two atom adsorption and unreactive scattering. The presence of xenon in XeF_2 offers a wonderful opportunity to probe the dynamics of two atom adsorption through observation of the scattered product. Unlike F_2 two atom adsorption in which there is no scattered product, the Xe atom is an inert atomic witness of XeF_2 two atom adsorption. Thus, the energetics of the scattered Xe atom ought to yield valuable insight into the possibly stepwise mechanism of two atom adsorption, a dissociative chemisorption mechanism that is fundamentally different from the necessarily concerted mechanism of classic dissociative chemisorption despite the product of the two mechanisms being stoichiometrically identical.

This chapter presents a detailed comprehensive investigation of the interaction of XeF_2 with Si(100). Section II describes the experimental apparatus with particular emphasis on the production and maintenance of the XeF_2 molecular beam. Section III presents the experimental results and is divided into three subsections. Section III.A considers the exposure dependence of the flux of scattered products from the interaction of XeF_2 with Si(100). Section III.B considers the fluorine coverage as a function of exposure to XeF_2 using helium diffraction and thermal desorption to probe the fluorine adlayer. Section III.C considers the velocity and angular

distributions of the scattered products as a function of exposure to XeF_2 for coverages ranging from the clean Si surface to the steady state etching regime. Section IV is a discussion of the results. The discussion considers previous work from this laboratory on the interaction of F_2 with Si(100) as well as work from other laboratories on the interactions of F_2 and XeF_2 with Si.

II. EXPERIMENTAL

The experimental apparatus has been described in detail [44,45,46,47]. Briefly the apparatus consists of two supersonic molecular beam sources coupled to an ultrahigh vacuum (UHV) chamber (base pressure=$5x10^{-11}$ torr) containing the silicon crystal and a triply-differentially pumped line-of-sight rotatable quadrupole mass spectrometer as well as an ion sputtering gun, a cylindrical mirror electrostatic analyzer for Auger electron spectroscopy and a mass spectrometer for residual gas analysis.

II.A. Xenon difluoride molecular beam

II.A.1. Xenon difluoride

Xenon difluoride is a solid at ambient temperature and pressure. While XeF_2 is stable at room temperature, it is a strong oxidizer and readily hydrolyzes in the presence of water to form Xe and HF. Therefore, special care must be taken in handling XeF_2 to minimize its decomposition. The enhanced awareness of the susceptibility of XeF_2 to decompose has led to the recent development of a careful protocol for handling XeF_2 in this laboratory which is described below. The results described in this chapter span this change in protocol. Namely, the high energy XeF_2 experiments were all performed prior to the modification whereas all of the low energy XeF_2 experiments have been performed since the modification. Although the possible presence of free Xe in the molecular beam should be considered, especially in the high energy XeF_2 experiments, the majority of the results are not affected by free Xe in the molecular beam because it simply scatters *unreactively* from the surface. The only adverse effect is the measurement of the signal at m/e=129, which corresponds to Xe^+ that arises from scattered Xe. If there is no XeF_2 decomposition, the signal at m/e=129 that is attributable to Xe is solely that

which arises from the reactive interaction with Si. However, if there is decomposition, the Xe signal has contributions from both the *unreactive* scattering of Xe in the molecular beam and the *reactive* scattering of Xe that arises from the interaction of XeF_2 with Si. Finally, despite the enhanced awareness of the possibility of XeF_2 decomposition and the change in protocol for handling XeF_2, there is no conclusive evidence that XeF_2 decomposition was present in the molecular beam in any of the experiments described in this chapter.

The new protocol for handling XeF_2 focuses on the avoidance of any contact with the ambient atmosphere. Xenon difluoride (99% by F ion titration, Lancaster Synthesis) is manufactured, packed and stored under an inert nitrogen environment. The solid XeF_2 is stored in a clean, valved stainless steel vessel that has been baked to 400 K under vacuum on the gas handling manifold to remove any residual water prior to adding the solid XeF_2. The stainless steel vessel is removed from the gas manifold, and the solid XeF_2 is transferred from the manufacturer's sealed container to the stainless steel vessel in a dry nitrogen glove box. The stainless steel vessel is subsequently attached to the gas manifold. The manifold is baked to 400 K overnight to remove any residual water vapor prior to opening the XeF_2 container.

In addition to the initial setup of the solid XeF_2 vessel, the gas manifold must be passivated prior to each molecular beam expansion. The ratio of the mass spectrometer signals at m/e=129 (Xe^+) and m/e=167 (XeF_2^+) of the incident XeF_2 beam ought to be constant and equal to the XeF_2 cracking ratio that arises from ionizer fragmentation if there is no passivation. This ratio is higher than normal during the initial expansion indicating that a fraction of the XeF_2 decomposes to produce free Xe during the initial expansion in a baked manifold. In addition, it has been observed that the ratio increases after the XeF_2 has been present for prolonged periods

greater than one hour in the manifold leading to the nozzle and within the nozzle itself indicating the accumulation of free Xe. Thus, prior to starting the experiments for the day, the XeF_2 beam is expanded through the nozzle for a period of 15 minutes, the XeF_2 is pumped out of the manifold, and the process of expanding the XeF_2 through the nozzle and pumping out the manifold is repeated. Prior to each experiment, the XeF_2 is expanded for two minutes to ensure that the XeF_2 flux has stabilized. In between experiments, the XeF_2 is pumped out of the manifold to prevent the accumulation of free Xe.

It is difficult to determine the extent of Xe contamination, if any, in the XeF_2 molecular beam with the present experimental apparatus because the sole diagnostic technique is electron bombardment ionization quadrupole mass spectrometry. Because the ionization process is not selective and commonly leads to fragmentation of the parent neutral molecules into daughter ions, both Xe and XeF_2 are detected at m/e=129 which corresponds to Xe^+. Time-of-flight measurements of the incident beam at m/e=129 cannot reveal any contribution from free Xe since the Xe and XeF_2 in the molecular beam will travel at identical velocities in a supersonic expansion as well as in a quasi-effusive expansion which is described below. The most valuable measurement is the ratio of the mass spectrometer signal at m/e=129 to the signal at m/e=167 of the incident molecular beam, which in the absence of free Xe is equivalent to the XeF_2 cracking ratio. This ratio is constant after the initial passivation. Therefore, the ratio of the flux of Xe to the flux of XeF_2 is constant implying that there is either no free Xe in the molecular beam or the relative flux of free Xe in the molecular beam is constant. However, without the knowledge of the absolute cracking ratio of XeF_2, the quantitative amount of free Xe in the molecular beam cannot be directly determined.

One method for determining the upper bound for the extent of Xe contamination is by comparison of the mass spectra of similar molecular beams of Xe and XeF_2. Figure 1(a) shows a plot of the mass spectrum of a Xe molecular beam formed under quasi-effusive expansion conditions of 5 torr stagnation pressure and a room temperature nozzle of 50 mm orifice diameter. The relevant signals are the clusters around m/e=64.5 and m/e=129 corresponding to Xe^{2+} and Xe^{+}, respectively. Figure 1(b) shows a plot of the mass spectrum of a XeF_2 molecular beam formed under identical quasi-effusive expansion conditions to the Xe molecular beam described above. Note that the ratio of the Xe^{2+} signal to the Xe^{+} signal is dramatically lower for the XeF_2 molecular beam. Assuming that all of the Xe^{2+} in the XeF_2 molecular beam arises from Xe contamination, the fraction of the Xe^{+} signal that can be attributed to Xe, based on the ratio of the Xe^{2+} signal to the Xe^{+} signal in the Xe molecular beam, is 0.32. This number is not representative of the fraction of the molecular beam that is Xe relative to XeF_2 because the ionization cross sections of the two processes, $\sigma_{Xe \rightarrow Xe^{+}}$ and $\sigma_{XeF_2 \rightarrow Xe^{+}}$, have not been considered in this analysis. However, it is important to reiterate that the presence of free Xe, if any, in the XeF_2 molecular beam only affects the measurement of the scattered products at m/e=129 that arise from the interaction of XeF_2 with Si. The free Xe does not affect the interaction of XeF_2 with Si.

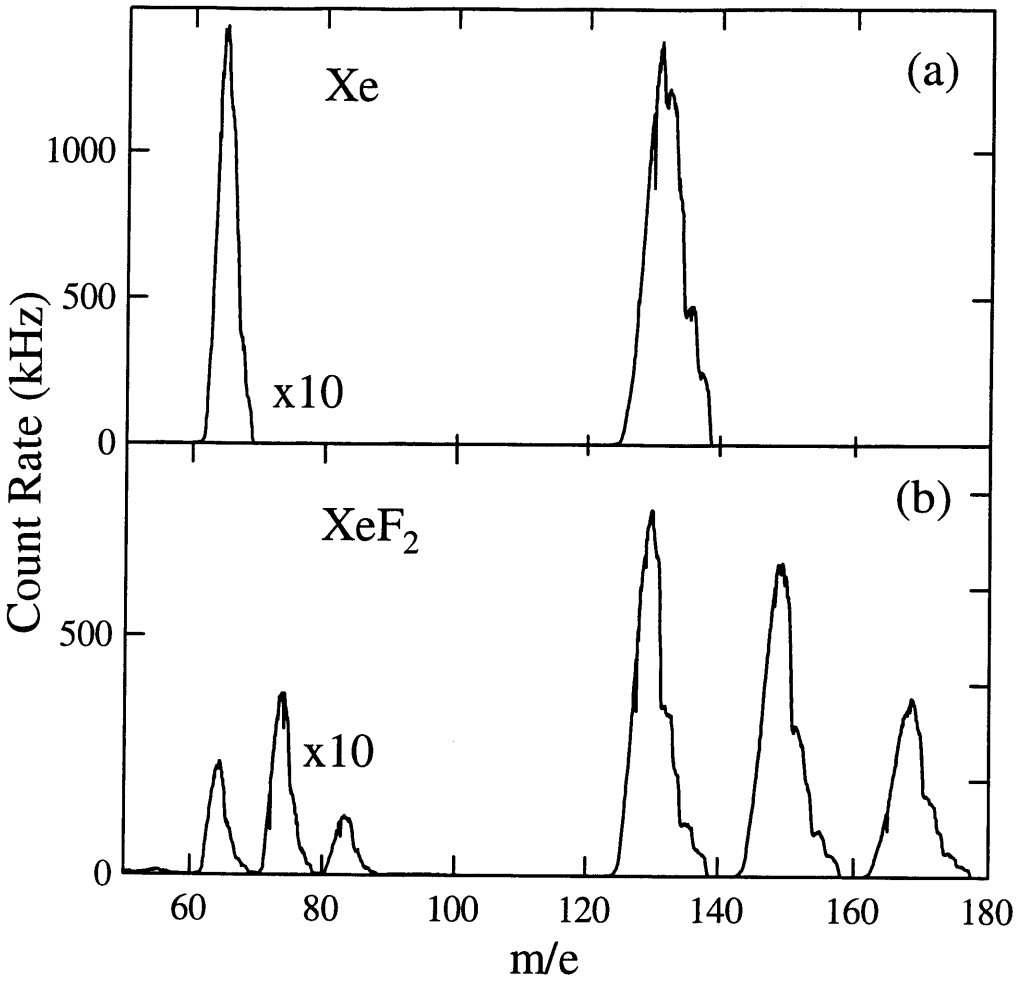

Figure 1 Mass spectra of Xe and XeF_2 molecular beams
Mass spectra of quasi-effusive molecular beams of (a) Xe and (b) XeF_2. The doubly-charged ion signal centered around m/e=64.5 (as well as m/e=74 and m/e=83.5 for XeF_2) is multiplied by a factor of ten.

II.A.2. Supersonic molecular beam: high energy XeF_2 (E_i=6.3 kcal/mol)

In the experiments described in this chapter, the standard molecular beam is a supersonic expansion of XeF_2 seeded in Ar (99.9995%, Spectra Gases). Typical expansion conditions of 400 torr stagnation pressure with a room temperature nozzle of 50 μm orifice diameter yield a nearly monoenergetic beam ($\Delta E/E$=0.17, resolution limited) as determined from the velocity distribution of the incident beam measured using a time-of-flight (TOF) technique. Figure 2(a) shows the TOF distribution of a supersonic molecular beam expansion of 0.25% XeF_2/Ar. The average velocity and translational energy of XeF_2 in these mixtures is v_{avg}=559±24 m/s and E_i=6.3±0.5 kcal/mol, respectively, where the major contribution to the uncertainties is the length of the flight path due to the finite length of the ionization region. The incident energy of the XeF_2 molecular beam is much greater than kT at room temperature (0.6 kcal/mol). The large incident energy is a consequence of the large mass of XeF_2 which precludes the use of a heavy inert carrier gas to lower the XeF_2 energy. Although the use of Kr or Xe as a carrier gas would substantially lower the incident energy relative to using Ar, the signals from unreactively scattered Kr and Xe interfere with and overwhelm the signals from the scattered products of the interaction of XeF_2 with Si. A supersonic expansion of neat XeF_2 would yield the lowest incident energy, but the low vapor pressure of XeF_2 at room temperature (~ 5 torr) precludes the production of a monoenergetic flux of particles afforded by a truly supersonic expansion. Despite the high energy of the supersonic expansion of XeF_2, the experiments described below show that the effect of incident energy on the interaction of XeF_2 with Si is minimal.

II.A.3. Quasi-effusive molecular beam: low energy XeF_2 (E_i=1.8 kcal/mol)

Because one of the goals of this investigation is to compare the results of the XeF_2 experiments with those of the F_2 experiments described in Chapter 1, the incident energy of XeF_2 ideally ought to be similar to the low energy F_2 (0.7 kcal/mol) described in the previous chapter. Although the use of effusive molecular beams is generally shunned in favor of supersonic molecular beams in gas scattering experiments, the large mass and low vapor pressure of XeF_2 necessitated the use of expansion conditions that are more effusive than supersonic in order to attain sufficiently low incident energies.

The criterion for a supersonic molecular beam expansion is that the mean free path λ of the gas at a stagnation pressure P_{stag} behind the nozzle is much less than the diameter of the nozzle orifice d_{nozzle}. If λ is much greater than d_{nozzle}, then the molecular beam expansion will be effusive. Depending on the expansion conditions, the average translational energy of XeF_2 can range from 2kT (1.2 kcal/mol at 300 K) for an ideal effusive expansion to (7/2)kT (2.1 kcal/mol at 300 K) for an ideal supersonic expansion (i.e., total translational and rotational relaxation) of a gas of linear molecules.

The vapor pressure is about 4.5 torr at 298 K and is strongly temperature dependent ranging from 3-6.5 torr around room temperature (293-303 K) [48]. Therefore, the solid XeF_2 vessel is submerged in constant temperature water bath maintained at 30° C to ensure a constant stagnation pressure and hence a constant molecular beam flux. In addition, the gas manifold is gently warmed with resistive heating tapes to avoid XeF_2 condensation in the manifold. With a vapor pressure of 5 torr, the mean free path λ of XeF_2 is about 5 μ. Although this mean free path is much less than the nozzle diameter d_{nozzle}=50 μ, meeting the criterion for a supersonic

expansion ($\lambda<d_{nozzle}$), the incident beam is quasi-effusive with a broad distribution and an average velocity and translational energy of v_{avg}=285 m/s and E_i=1.8 kcal/mol, respectively. Figure 2(b) shows a TOF distribution of a neat XeF_2 molecular beam. The simulated TOF spectra for the limiting cases of an ideal supersonic expansion ($\Delta E/E$=0.17, resolution limited) and an ideal effusive expansion are superimposed for comparison. An unfortunate consequence of this quasi-effusive molecular beam expansion is that the energy distribution is extremely broad ($\Delta E/E$=1.2) unlike the nearly monoenergetic distribution ($\Delta E/E$=0.17, resolution limited) afforded by a supersonic molecular beam expansion. Figure 2(c) shows the energy distributions of XeF_2 in the supersonic molecular beam and the quasi-effusive molecular beam, which will be referred to throughout this chapter as high energy XeF_2 and low energy XeF_2, respectively.

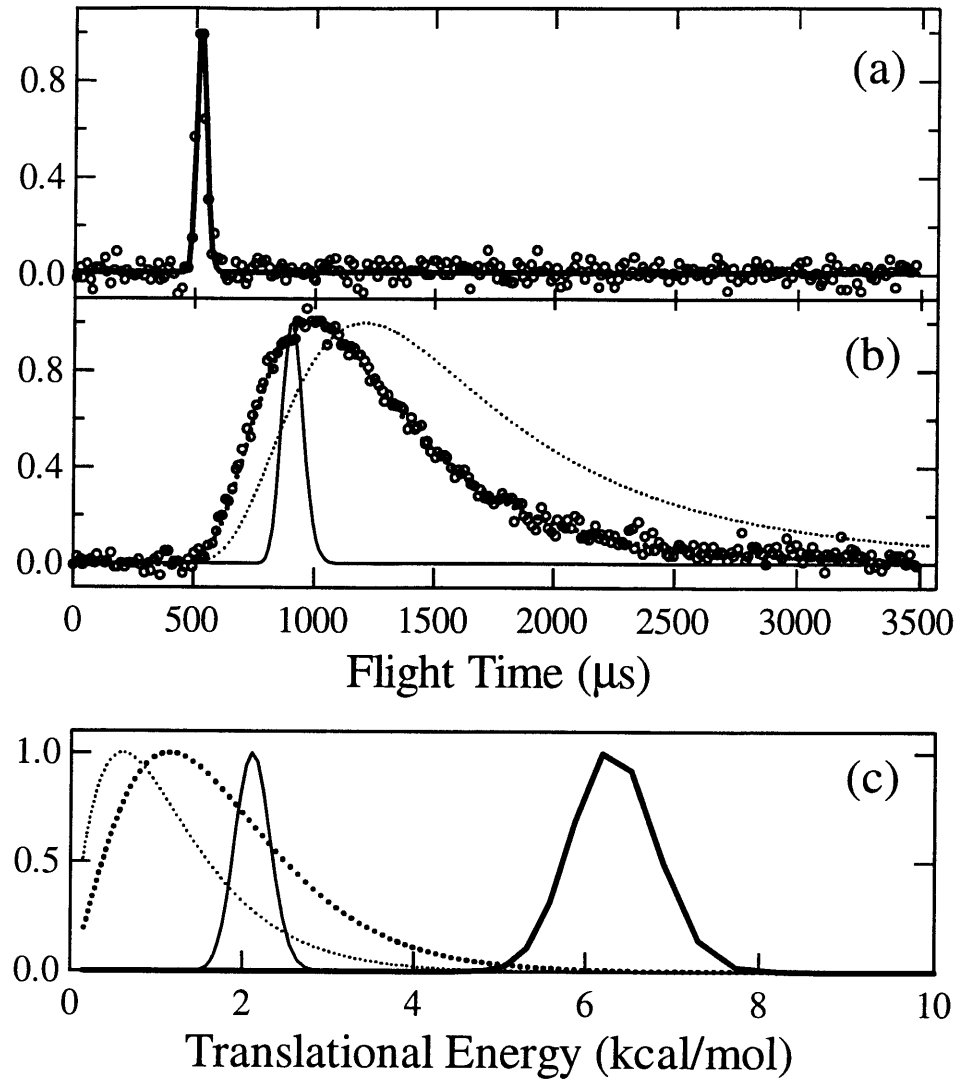

Figure 2 TOF distributions of high and low energy XeF_2 molecular beams
(a) TOF spectrum of supersonic molecular beam expansion of 0.25% XeF_2/Ar. Thick solid line shows fit to the data of the Maxwell-Boltzmann function described in Eq. (II.1) of Sec. II.D. (b) TOF spectrum of quasi-effusive molecular beam expansion of neat XeF_2. Thick dashed line shows fit to the data of the function described in (a). Time-of-flight spectra of ideal supersonic (thin solid line) and effusive (thin dashed line) molecular beam expansions of neat XeF_2 are superimposed for comparison. The width of the ideal supersonic expansion is limited by the instrument resolution. (c) Kinetic energy distribution of supersonic molecular beam of 0.25% XeF_2/Ar (thick solid line) and quasi-effusive molecular beam of neat XeF_2 (thick dashed line). Kinetic energy distributions of ideal supersonic expansion (thin solid line) and ideal effusive expansion (thin dashed line) of neat XeF_2 are superimposed for comparison.

II.B. Silicon crystal

The crystal is mounted between two Ta clamps that are attached to the manipulator. The crystal is mounted such that the crystal face is flush with the Ta brackets to preclude its shadowing by the brackets. The crystal normal can be rotated in the scattering plane defined by the axes of the two molecular beams and the detector. The axis of crystal rotation is perpendicular to and intercepts the intersection of these three axes. The crystal can be cooled to 125 K with liquid N_2 and heated resistively to ~1100 K. Its temperature is measured via a W-5%Re/W-26%Re thermocouple spot welded to a thin Ta tab in thermal contact with the back of the crystal. As with the experiments described in Chapter 1, the surface temperature is held constant at 250 K during XeF_2 exposure.

The Si crystal is cut along the (100) plane. Both lightly n-type and p-type doped Si with resistivities of 8-12 Ω cm have been used. No differences in reactivity, based on the probabilities for reaction versus XeF_2 exposure, have been observed for the two types of doping. The Si crystal is cleaned by a wet etching procedure [49] prior to installation into the vacuum chamber. The crystal is sputtered with 1.5 keV Ar^+ and subsequently annealed to ~1100 K. This process is repeated until C and O contamination are below the 1% sensitivity limit of Auger electron spectroscopy. No metal contamination, such as W, Ta, Cu, Ni, is observed. The crystal is typically mounted such that the scattering plane, defined by the beams, crystal normal and detector, is along the (10) direction of the crystal surface. Helium diffraction confirms the (2x1) periodicity of the reconstructed Si(100) surface. A brief anneal of the crystal to about 1100 K after each XeF_2 exposure removes all the fluorine and results in recovery of the 2x1 periodicity of the surface. The crystal is sputtered and annealed after about ten exposures to XeF_2 to ensure

surface cleanliness and order. The crystal is replaced when an etch spot becomes visible, typically after several months of experiments. No difference in reactivity is observed over the lifetime of the crystal.

II.C. Detection scheme

Primary measurements are made with a triply differentially pumped, rotatable quadrupole mass spectrometer with electron bombardment ionization. Unlike previous experiments in this laboratory which detected particles with mass-to-charge ratios primarily under m/e=50, this experiment requires the detection of particles primarily in the range m/e=100-200 to detect Xe, XeF, and XeF_2, but still requires detection of particles below m/e=50. This wide range of mass-to-charge ratios requires the appropriate tuning of the electrostatic lenses of the ionizer to optimally focus the ions into the entrance of the quadrupole mass filter. There are five electrostatic lens parameters: the ion energy E_{ion} which defines the energy of the ion into the entrance of the quadrupole, the negative extractor voltage V_{ext} which attracts the positive ions out of the region of ion formation, and a set of three lenses, L_1, L_2 and L_3, which focus the ions into the entrance of the quadrupole. In general, the larger the mass-to-charge ratio, the greater the magnitude of the voltages. To simplify the tuning algorithm, the set of three lenses are treated as an einzel lens (L_1=L_3) with the outer lenses grounded (L_1=L_3=0) [50]. The remaining three parameters, E_{ion}, V_{ext}, and L_2, are adjusted iteratively to maximize the signal arising from the particles traveling along the line-of-sight of the detector axis as opposed to the background. Time-of-flight measurements of the incident molecular beam are utilized to determine the ratio of signal detected at flight times corresponding to the narrow velocity distribution of the

molecular beam relative to the signal detected at all times in the baseline. The optimal ionizer settings for low and high mass-to-charge ratios are given in Table 1.

Table 1 Optimal ionizer settings for low and high mass ranges.

Parameter	Low mass (m/e=0-50)	High mass (m/e=100+)
Ion energy (E_{ion})	25 V	45 V
Extractor voltage (V_{ext})	-250 V	-250 V
Lens 1 (L_1)	0 V	0 V
Lens 2 (L_2)	-60 V	-300 V
Lens 3 (L_3)	0 V	0 V

Ions of a specific mass-to-charge ratio pass through a quadrupole mass filter to the detector. The resolution of the quadrupole mass filter is low (ΔM=1.7 FWHM) to maximize the transmissivity of ions through the quadrupole, especially the high mass-to-charge ratio Xe compounds which are strongly discriminated against at higher resolution. The one exception is the detection of signal at m/e=19 when using the supersonic molecular beam seeded in Ar which requires high resolution (ΔM=0.7 FWHM) in order to minimize interference from the signal present at m/e=20 arising doubly ionized ^{40}Ar carrier gas.

A channeltron electron multiplier is used to detect the ions. The detector rotates about the center point of the intersection of the incident beam and the crystal normal. The angular range is 35°-180° with respect to the incident beam. The solid angle subtended by the detector is

5.8×10^{-4} sr. The angular resolution in the scattering plane is 3.52°. The rotation of the crystal and detector allow for a wide range of incident and detection angles.

II.D. Measurement and analysis of time-of-flight distribution

A pseudorandom chopper wheel with 255 slots and spinning at 280 Hz at the entrance of the detector allows for measurements of the velocity distribution of both the incident beam as well as the scattered products using a cross correlation TOF technique. The neutral flight path is 29.3±1.27 cm. The energy resolution is limited to $\Delta E/E=0.17$ because of the uncertainty in the path length that is a result of the finite length of the ionization region.

In the majority of the experiments presented in this chapter, TOF distributions of the scattered products are measured over successive exposure intervals which correspond to different coverage ranges to probe the coverage dependence of the TOF distribution. The TOF distribution is measured at a single mass and a single detector angle over the entire exposure range. The data acquisition program controls the entire process described below. The molecular beam flag is opened to expose the surface to XeF_2. TOF signal is collected over the exposure interval which is generally 10 s in the high energy XeF_2 experiments or 2 s in the low energy XeF_2 experiments. The molecular beam flag is subsequently closed while the TOF signal is stored on the microcomputer. The process repeats with the opening of the molecular beam flag for the next exposure interval and continues until the entire exposure is complete. At the end of the last exposure interval, the molecular beam flag is closed and the crystal is briefly annealed to ~1100 K to desorb the fluorine and recover a well-ordered surface.

The TOF distributions are fit to a Maxwell-Boltzmann function F(t):

$$F(t) = \sum_{\text{i components}} A_i t^{-4} \exp\left[-\left(\frac{m_i}{2kT_i}\right)\left(\left(\frac{L}{t}\right) - v_{f,i}\right)^2\right], \qquad \text{(II.1)}$$

where for each of the i components, A_i is the normalization constant, m is the neutral mass, L is the neutral flight path length, and $v_{f,i}$ and T_i are the flow velocity and temperature, respectively, which describe the center and width of the velocity distribution. Three parameters are derived from the fit to the TOF distribution: relative flux, average velocity, and average translational energy. The relative flux is the integral of the velocity-weighted TOF distribution:

$$I = \int_0^\infty t^{-1} F(t) dt . \qquad \text{(II.2)}$$

The TOF distribution is multiplied by the velocity, which is inversely proportional to the flight time, to transform the mass spectrometer signal, which is proportional to the number density, into a value that is proportional to the flux. Based on the velocity-weighted TOF distribution, the average velocity and energy are given by:

$$v = \frac{\int_0^\infty \left(\frac{L}{t^2}\right) F(t) dt}{\int_0^\infty t^{-1} F(t) dt}, \qquad \text{(II.3)}$$

$$E = \frac{\int_0^\infty \frac{1}{2} m \left(\frac{L^2}{t^3}\right) F(t) dt}{\int_0^\infty t^{-1} F(t) dt} \qquad \text{(II.4)}$$

The uncertainty in all three of these parameters is given by the propagation of the uncertainties in all of the fit parameters, namely A, v_f, and T, as well as the uncertainty of the flight path length L due to the finite length of the ionization region. The effect of the flight path length is the dominant contribution to the uncertainty of the average velocity and energy. Thus, the uncertainty in the average velocity and energy are generally on the order of ±4% and ±9%,

respectively, because the velocity is proportional to L and the energy is proportional to L^2. Unless noted, the uncertainties of the average velocity and energy determined from a single TOF distribution always represent the standard deviation of the average value.

III. RESULTS

Before presenting the experimental results of this investigation, there are a few noteworthy observations to consider when comparing the interactions of XeF_2 and F_2 with Si(100). Recall that in the interaction of F_2 with Si(100), there are only three possible distinguishable reaction pathways – two atom adsorption, single atom abstraction and unreactive scattering – of which only the latter two channels can be directly observed by mass spectrometric detection of the scattered F atom and F_2 molecule, respectively. In addition, no etching is observed to occur within the detection limit of the measurement ($\sim 10^{-5}$ ML/s).

The first observation is that scattered Xe can arise from two possible sources other than two atom adsorption. The product of single atom abstraction, XeF, is very weakly bound by only 3 kcal/mol [51]. Considering the large exothermicity of the reaction (90 kcal/mol), the subsequent dissociation of excited XeF prior to detection would not only inhibit direct observation of single atom abstraction, but also complicate the observation of Xe arising from two atom adsorption in the interaction of XeF_2 with Si. In addition, the presence of any free Xe in the incident XeF_2 molecular beam would scatter *unreactively* and obscure the observation of *reactively* scattered Xe arising from the interaction of XeF_2 with Si.

The second observation is that XeF_2 is a much better etchant of Si than F_2. Since etching is the removal of Si, the surface structure of the Si, which remains intact throughout the interaction with low energy F_2, will inevitably change upon interaction of XeF_2 with Si if etching does occur. Unlike the interaction of F_2 with Si(100), which was restricted to the interaction with the dangling bonds of the surface Si atoms, the interaction of XeF_2 with Si(100) necessarily requires the cleavage of Si lattice bonds for etching to occur.

This investigation of the interactions of XeF_2 with Si focuses on two distinct energy regimes. The majority of the experimental results are based on the use of a supersonic expansion of high energy XeF_2 (E_i=6.3 kcal/mol). The reason for the use of high energy XeF_2 is that it provides a high intensity monoenergetic flux of XeF_2. In these high energy XeF_2 experiments, the molecular beam is incident at θ_i=35°, in contrast to the low energy F_2 experiments in which the molecular beam was commonly directed at normal incidence, θ_i=0°, to the Si surface. The reason for the use of θ_i=35° is that it allows for the detection of the scattered products in the entire forward region in the scattering plane. The measurement of the angular distribution of the scattered products yields substantial information regarding the dynamics of XeF_2 with Si.

However, one of the goals of this investigation is to compare the dynamics of the interaction of XeF_2 with Si to that of F_2. Although comparisons can be made between the high energy XeF_2 experiments and the low energy F_2 experiments, the effects of incident angle and energy are not necessarily insignificant. Therefore, the remaining experiments are based on the use of a quasi-effusive expansion of low energy XeF_2 (E_i=1.8 kcal/mol) directed at normal incidence to the Si surface. Although the incident energy is more than twice the incident energy of low energy F_2 used in the investigation described in Chapter 1, it has been shown from an investigation of the dynamics of the interaction of F_2 with Si(100) at E_i=1.4 kcal/mol that incident energy does not have a significant effect on the interaction at these low energies [52]. In fact, an investigation of the fluorinated surface structure using thermal desorption and He diffraction has shown that incident F_2 energy does not have a significant effect until the incident normal energy exceeds 4 kcal/mol [54]. Thus, the low energy XeF_2 beam ought to have sufficiently low incident energy to make a comparison with low energy F_2. Because of the low

signal intensities, the experiments are limited to a single detector angle, θ_i=35°. Although there are significant differences between the dynamics of the scattered products arising from the interaction of low and high energy XeF_2 with Si, the similarities are remarkable considering the threefold difference in incident energy.

The presentation of experimental results is divided into three sections. In Sec. III.A the scattered products of the interaction of XeF_2 with Si(100) are identified and the intensity of their signals as a function of XeF_2 exposure as well as scattering geometry are measured. These results provide a foundation for the rest of the experimental results. Sec. III.B presents the evolution of the fluorine overlayer on the Si surface as a function of XeF_2 exposure as determined by thermal desorption and helium diffraction measurements. These results show that despite the complexity caused by the presence of etching, the interaction of XeF_2 with Si(100) at fluorine coverages below 1 ML is remarkably similar to the interaction of F_2 with Si(100) in that it is primarily the dangling bonds that are the reactive sites. Thus, the interaction of XeF_2 with Si(100) at coverages below 1 ML can be approximated as the fluorination of the Si dangling bonds. Finally, the velocity distributions of the scattered products are presented in Sec. III.C as a function of both XeF_2 exposure and scattering geometry. The goal of this section is to compare the dynamics of the scattered products from the interactions of XeF_2 with Si(100) to that of F_2 with Si(100) in order to better understand the mechanism of atom abstraction, as it relates to both single atom abstraction and two atom adsorption, as well as gain insight into the mechanism of Si etching.

III.A. Exposure dependence of scattered products

The simplest experiment is to identify the scattered product signals and measure the intensity of the individual signals as a function of XeF_2 exposure. At a surface temperature of 250 K, the surface temperature for all of the experiments in this investigation, there are five distinct detectable ions at m/e=167, m/e=148, m/e=129, m/e=19, and m/e=85. However, the ions do not necessarily have a unique correspondence to neutral particles because of fragmentation during electron bombardment ionization. The signal at m/e=167 arises solely from $^{129}XeF_2$, which is one of the most abundant isotopes. The m/e=148 signal arises from two possible neutrals: $^{129}XeF_2$ and ^{129}XeF. The m/e=129 signal arises from three possible neutrals: $^{129}XeF_2$, ^{129}XeF, and ^{129}Xe. The m/e=19 signal arises from several neutrals: XeF_2, XeF, and F. In the case of high energy XeF_2, which is seeded in Ar, there is an additional minor, but not insignificant, contribution of $^{38}Ar^{2+}$ to the signal at m/e=19. The m/e=85 signal arises from the cracking of SiF_4 to SiF_3^+. At an electron energy of 70 eV, SiF_4 fragments almost exclusively to SiF_3^+. Analysis of the mass spectrum of the incident XeF_2 beam in Figure 1(b) shows that the signal from $^{132}XeF_2^{2+}$ at m/e=85 is about 1% of the signal from $^{129}XeF_2^+$ at m/e=167.

Knowledge of the relative fragmentation of the neutral particles into ions allows for the isolation of the neutral particle of interest. The fragmentation pattern or cracking ratio is typically determined by measuring the mass spectrum of a pure source of the particle of interest (i.e., without any particles that might be detected at the same mass-to-charge ratio as the particle of interest) directed into the detector under conditions (i.e., particle flux, ionizer and quadrupole configuration) that are identical to those of the experiment of interest. The fragmentation pattern of XeF_2 can be determined from a mass spectrum of the incident quasi-effusive neat XeF_2

molecular beam described in Sec. II.A.3. The mass spectra of XeF_2 seeded in Ar and Kr are complicated by a minor, but not insignificant, contribution from van der Waals complexes $Xe\cdots Ar^+$ and $Kr\cdots Kr^+$, respectively [53]. Figure 1(b) shows the mass spectrum of a neat XeF_2 molecular beam. The cracking ratio of XeF_2 is 2.4:1.9:1.0 into the three fragments Xe^+, XeF^+, and XeF_2^+, respectively. However, the cracking ratio of XeF is difficult to determine because there is no method for creating pure source of XeF without either the interference from a stable parent molecule like XeF_2 or decomposition product like Xe. Therefore, only a limiting value for the cracking ratio of XeF, which is necessary to remove the contribution of XeF to the Xe^+ signal, can be determined indirectly from the results presented below. The maximum fragmentation ratio for the ionization of XeF to Xe^+ relative to XeF^+ is about 8.

III.A.1. High incident energy (E_i=6.3 kcal/mol)

Figures 3-6 show plots of the signal intensities as a function of high energy XeF_2 exposure at m/e=85, 167, 148, 129, and 19 which represent the products scattered from Si(100) at 250 K. The measurement is for a scattering geometry in which the XeF_2 beam is 35° from the surface normal, θ_i=35°, and the detector is positioned along the surface normal, θ_d=0°. The signals are collected almost simultaneously during a single XeF_2 exposure by cycling the quadrupole mass filter between the four mass-to-charge ratios at a rate of 10 Hz. Signal is collected beginning 5 ms after each switch to account for the finite switching time of the quadrupole power supply. The incident XeF_2 flux is low enough that the 2 Hz sampling rate per ion provides sufficient time resolution to observe the kinetics of the reaction. The system has reached a steady state by the end of the XeF_2 exposure.

Figure 3 shows a plot of the signal intensity at m/e=85 as a function of high energy XeF_2 exposure which corresponds to SiF_3^+ arising from the etch product SiF_4. The signal intensity remains zero or near zero throughout the initial XeF_2 exposure. After sufficient exposure to XeF_2, which will be shown in the following section to correspond to about 1 ML fluorine coverage, there is a dramatic increase in the intensity of the signal with further XeF_2 exposure. The m/e=85 signal attains a constant intensity level corresponding to the steady state etching regime.

Figure 4(a) shows a plot of the signal intensities at m/e=148 and m/e=167 as a function of XeF_2 exposure. The m/e=167 signal corresponds to unreactively scattered XeF_2 and is multiplied by the XeF_2 cracking ratio to show the contribution to the m/e=148 signal. The evolution of the intensity of this unreactive signal with XeF_2 exposure is similar to that of the etch product signal. The signal intensity is distinctly nonzero and remarkably insensitive to the initial exposure to XeF_2 considering that the coverage ranges from 0-0.6 ML F (Sec. III.B.1). This is in stark contrast to the unreactively scattered F_2 which showed a strong dependence on coverage related to the number of available sites. The signal intensity increases by almost an order of magnitude to reach a steady state level at a similar XeF_2 exposure as the m/e=85 signal.

The signal at m/e=148 has two possible contributions: unreactively scattered XeF_2 and XeF arising from F atom abstraction. The exposure dependence of the m/e=148 and m/e=167 signals are similar because the major contribution to the m/e=148 signal is unreactively scattered XeF_2, but there is a significant contribution from XeF, the product of single atom abstraction, especially during the initial XeF_2 exposure. Figure 4(b) shows a plot of the XeF contribution as a function of XeF_2 exposure determined by point-by-point subtraction of the m/e=167 signal

multiplied by the XeF_2 cracking ratio from the m/e=148 signal. Similar to the interaction of F_2 with Si(100), the XeF signal attains a maximum at nonzero XeF_2 exposure, but in stark contrast to the F atom signal which is directly related to the probability of single atom abstraction, the maximum XeF signal is attained at a coverage of about 1 ML, not 0.5 ML as determined by thermal desorption measurements described in Sec. III.B.1. However, it is important to note that the XeF signal shown in Figure 4(b) is not necessarily directly related to the probability of single atom abstraction because the velocity and angular distribution of the scattered XeF have not been taken into account. This apparent difference in the coverage dependence of the single atom abstraction probability in the interactions of XeF_2 and F_2 with Si will be discussed in Sec. IV.B.1

Figure 5 shows a plot of the signal intensity at m/e=129 as a function of XeF_2 exposure. The m/e=129 signal corresponds to Xe^+ and has several contributions. First, there is ionizer fragmentation of unreactively scattered XeF_2 as well as XeF from single atom abstraction. Second, there ought to be Xe from two atom adsorption. In addition to these three obvious contributions to the Xe^+ signal, there are the two contributions mentioned in the beginning of Sec. III. First, because the exothermicity of single atom abstraction is extremely large with respect to the bond strength of XeF, the gas phase product of single atom abstraction, if only a small fraction of the energy liberated in the reaction is coupled into the internal energy of the XeF molecule, the XeF molecule will dissociate into a Xe atom and a F atom. Second, because XeF_2 is susceptible to decomposition in the presence of water, the magnitude of the free Xe component in the XeF_2 molecular beam is unknown. Altogether there are five possible contributions to signal at m/e=129, and the contribution of none of them is known.

Under these circumstances of less than perfect knowledge, there are two methods for unraveling the various contributions to the measured signals. First, measurement of the signal intensities of the scattered products as a function of XeF_2 exposure under a wide variety of conditions (i.e., scattering geometry, surface temperature, incident energy) can yield a large library of experimental data that may include results in which certain contributions are minimized or eliminated completely. Recognition of relationships and patterns among the measured signals within this library of data leads to a self-consistent separation of the contributions using optimized scaling factors instead of directly measuring the cracking ratios. This self-consistent method has been employed to identify the XeF signal arising from single atom abstraction in the interaction of high energy XeF_2 with Si(100) [53]. Second, measurement of the velocity distributions of the scattered products using a time-of-flight technique can separate the various contributions based on their velocity distributions, which ought to be different since each product arises from a different interaction with the surface. This time-of-flight method has been successfully employed to identify and characterize the F atom signal arising from single atom abstraction in the interaction of F_2 with Si(100) [53,54,55,56]. The time-of-flight method will be employed in Sec. III.C to identify and characterize the scattered products of the interaction of XeF_2 with Si(100).

Figure 6 shows a plot of the signal intensity at m/e=19 as a function of XeF_2 exposure. The m/e=19 signal corresponds to primarily to F^+ as well as $^{38}Ar^{2+}$ from the carrier gas. There are several contributions to the F^+ signal: cracking of unreactively scattered XeF_2, XeF from single atom abstraction, and SiF_4 etch product as well as F atoms arising from the dissociation of XeF and doubly ionized ^{38}Ar carrier gas. In principle, the contributions from XeF_2 and SiF_4 can

be separated by subtracting the signals at m/e=167 and m/e=85 multiplied by the XeF_2 cracking ratio and the SiF_4 cracking ratio, respectively. The contribution from ^{38}Ar can be separated by subtracting the signal at m/e=40, which corresponds to ^{40}Ar, multiplied by both the ratio of the isotopic abundances of the two isotopes and the ratio of the cross sections for single and double ionization of Ar. The contribution from XeF cannot be separated because the XeF cracking ratio is unknown. Because the contributions to the signal at m/e=19 cannot be separated, the exposure dependence of the signal intensity is not valuable by itself. In Sec. III.C, the contributions to the signal at m/e=19 will be separated and better characterized using the time-of-flight method described above.

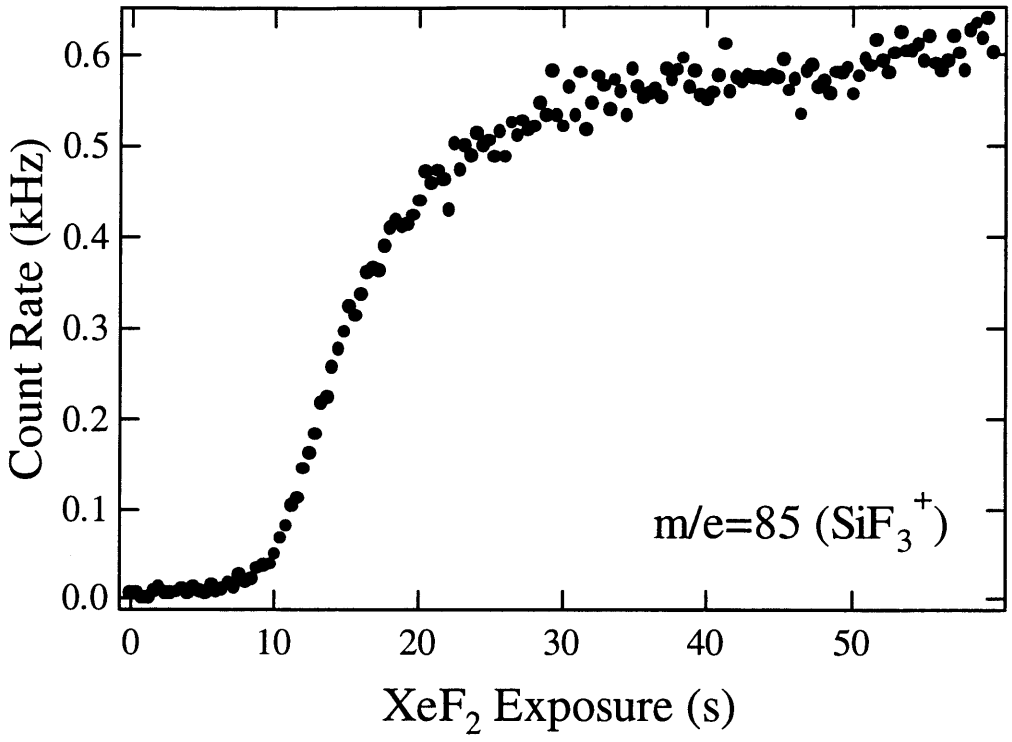

Figure 3 High energy XeF_2 exposure dependence of scattered SiF_3^+ signal
Signal at m/e=85 as a function of high energy XeF_2 exposure at θ_i=35°, θ_d=0° and T_s=250 K. Note that the high energy XeF_2 incident flux in Figures 3-6 is approximately a factor of two greater than the flux in all of the other high energy XeF_2 experiments shown in this thesis because the molecular beam nozzle in these experiments had an orifice diameter of ~75 μm. The current molecular beam nozzle has an orifice diameter of ~50 μm and has been used in all of the other experiments presented in this chapter.

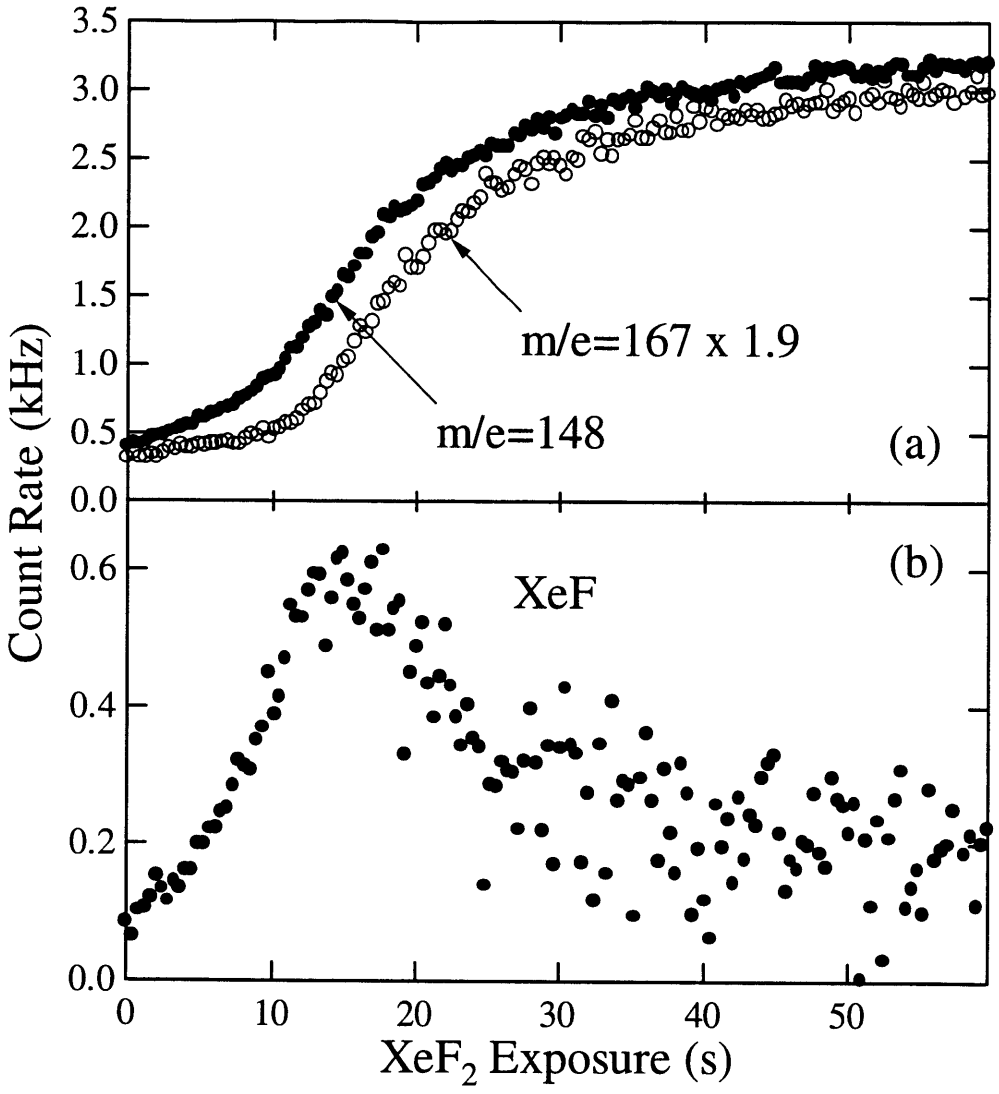

Figure 4 High energy XeF_2 exposure dependence of scattered XeF^+ and XeF_2^+ signals
(a) Signal at m/e=148 and m/e=167 multiplied by XeF_2 cracking ratio as a function of high energy XeF_2 exposure at θ_i=35°, θ_d=0° and T_s=250 K. (b) Net scattered XeF signal calculated by point-by-point subtraction of m/e=167 signal multiplied by XeF_2 cracking ratio from m/e=148 signal in (a). Note that the high energy XeF_2 incident flux in this experiment is approximately a factor of two greater than the flux in all of the other high energy XeF_2 experiments (see Figure 3 caption).

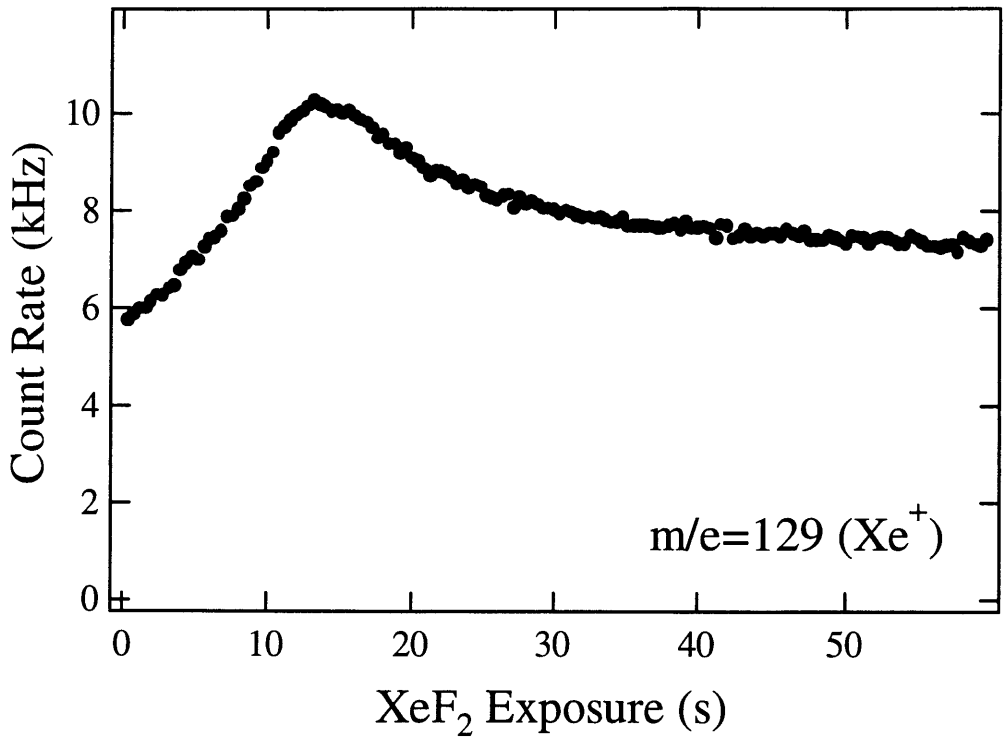

Figure 5 High energy XeF_2 exposure dependence of scattered Xe^+ signal
Signal at m/e=129 as a function of high energy XeF_2 exposure at θ_i=35°, θ_d=0° and T_s=250 K. Note that the high energy XeF_2 incident flux in this experiment is approximately a factor of two greater than the flux in all of the other high energy XeF_2 experiments (see Figure 3 caption).

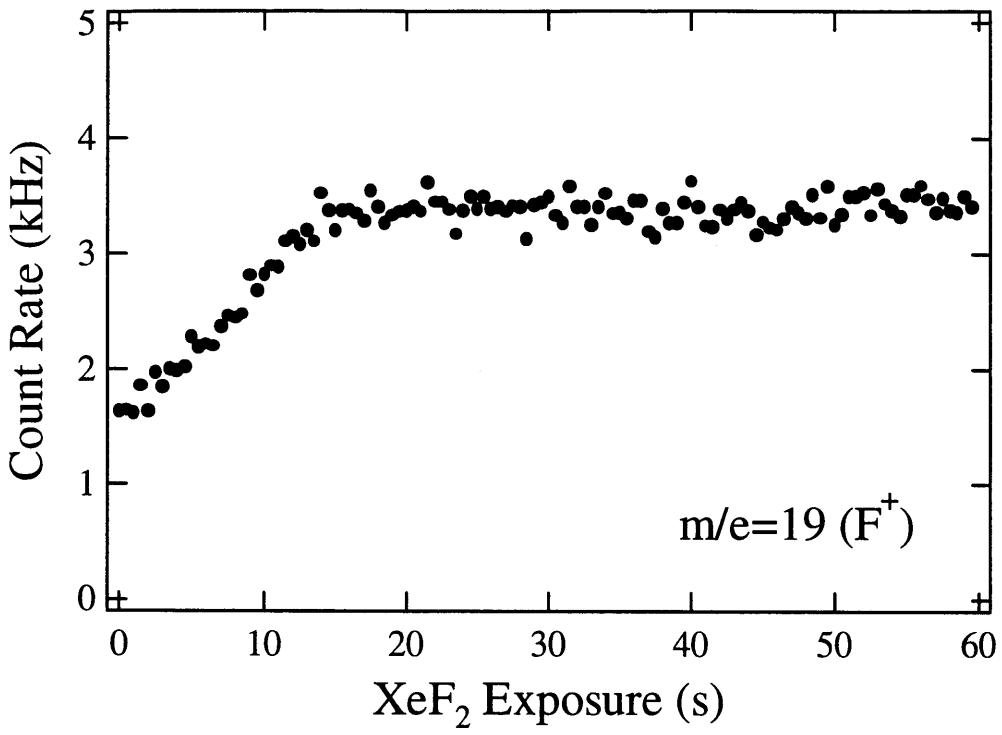

Figure 6 High energy XeF_2 exposure dependence of scattered F^+ signal
Signal at m/e=19 as a function of high energy XeF_2 exposure at θ_i=35°, θ_d=0° and T_s=250 K. Note that the high energy XeF_2 incident flux in this experiment is approximately a factor of two greater than the flux in all of the other high energy XeF_2 experiments (see Figure 3 caption).

III.A.2. Low incident energy (E_i=1.8 kcal/mol)

Figures 7-10 show plots of the signal intensities as a function of low energy XeF_2 exposure at m/e=85, 167, 148, 129, and 19 which represent the products scattered from Si(100) at 250 K. The measurement is for a scattering geometry in which the XeF_2 beam is normal to the surface, θ_i=0°, and the detector is positioned at 35° from the surface normal, θ_d=35°. The scattering geometry is different from that used in the high energy XeF_2 experiments described above, because the low energy XeF_2 experiments are to be compared with the low energy F_2 experiments which were performed at normal incidence. Although it will become apparent that incident angle does not significantly affect the dynamics of the interaction of XeF_2 with Si, the different detection angle has a profound effect on the measured signal intensities. The angular distribution of the scattered products will be considered further in Sec. III.C. The system has reached a steady state by the end of the low energy XeF_2 exposure. Although the relative incident flux of the low and high energy XeF_2 beams is unknown, it is apparent by comparison of the exposure dependence of the scattered signal intensities that the order of magnitude of the two fluxes are the same. This is reasonable since the partial pressure of XeF_2 in the stagnation region behind the nozzle, which is approximately proportional to the incident flux on the crystal surface, is 5 torr and 1 torr in the low and high energy XeF_2 beams, respectively. Of course, the angular distribution of the supersonic and quasi-effusive molecular beams as well as the area of the crystal that is imaged by the molecular beam must be considered to determine the relative flux of the low and high energy XeF_2 beams.

Figure 7 shows a plot of the signal intensity at m/e=85, which corresponds to SiF_3^+ arising from the etch product SiF_4, as a function of low energy XeF_2 exposure. Similar to the

high energy XeF_2 exposure dependence of the intensity this signal (cf. Figure 3), the intensity remains zero or near zero throughout the initial XeF_2 exposure and subsequently increases to a steady state level.

Figure 8 shows plots of the signal intensities at (a) m/e=167 and (b) m/e=148 as a function of low energy XeF_2 exposure. The signal at m/e=167 which corresponds to unreactively scattered XeF_2 is multiplied by the XeF_2 cracking ratio to show the contribution to the signal at m/e=148. Plots of the signal intensity at m/e=167 and m/e=148 as a function of high energy XeF_2 exposure at an identical scattering geometry, θ_i=0° and θ_d=35°, are superimposed for comparison. In Figures 8-9, the signals arising from scattering high energy XeF_2 has been scaled by a universal scaling factor such that the steady state signal level at m/e=129 matches the steady state signal level from the scattering of low energy XeF_2. In addition, the exposure was scaled by a universal factor such that the maximum in the m/e=129 signal is similar for both high and low energy XeF_2. This scaling assumes that the signal intensities at m/e=129 arise from similar dynamics for both low and high energy XeF_2. The validity of this assumption will be examined further below. Figure 8(c) shows a plot of the XeF contribution as a function of XeF_2 exposure determined by point-by-point subtraction of the m/e=167 signal multiplied by the XeF_2 cracking ratio from the m/e=148 signal. The exposure dependence and the relative intensity of the signals at m/e=167 and m/e=148 are remarkably similar for both low and high energy XeF_2.

Figure 9 shows a plot of the signal intensity at m/e=129 as a function of low energy XeF_2 exposure. Analogous to Figure 8, a plot of the signal intensity at m/e=129 as a function of high energy XeF_2 exposure at an identical scattering geometry is superimposed for comparison. By

definition of the universal scaling factor, the exposure dependence and intensity of the signal at m/e=129 is similar for both low and high energy XeF_2.

Figure 10 shows a plot of the signal intensity at m/e=19 as a function of low energy XeF_2 exposure. There are several contributions to the F^+ signal: cracking of unreactively scattered XeF_2, XeF from single atom abstraction, and SiF_4 etch product as well as F atoms arising from the dissociation of XeF. Similar to the high energy XeF_2 exposure dependence of the intensity this signal (cf. Figure 6), the signal intensity increases monotonically from a nonzero value to a steady state level. Despite scaling the exposure of low energy XeF_2 to that of high energy XeF_2, the low energy exposure necessary to reach a steady state level is about two times longer than it is upon exposure to high energy XeF_2. However, it is important to note that the detection angle is different in the two experiments.

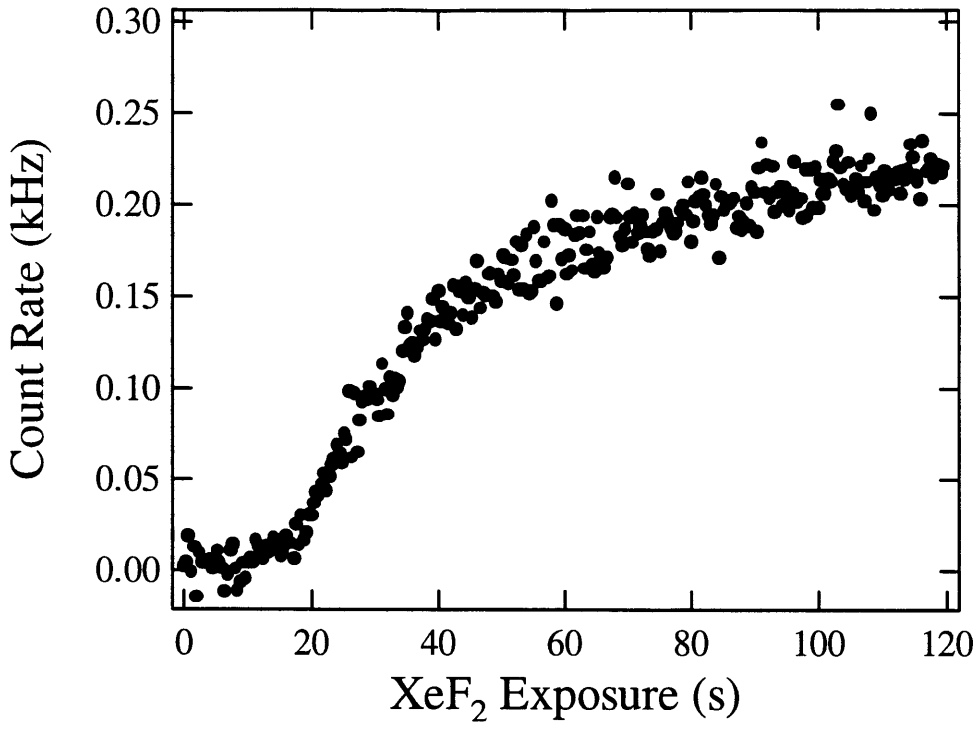

Figure 7 Low energy XeF_2 exposure dependence of scattered SiF_3^+ signal
Signal at m/e=85 as a function of low energy XeF_2 exposure (solid circles) at θ_i=0°, θ_d=35° and T_s=250 K.

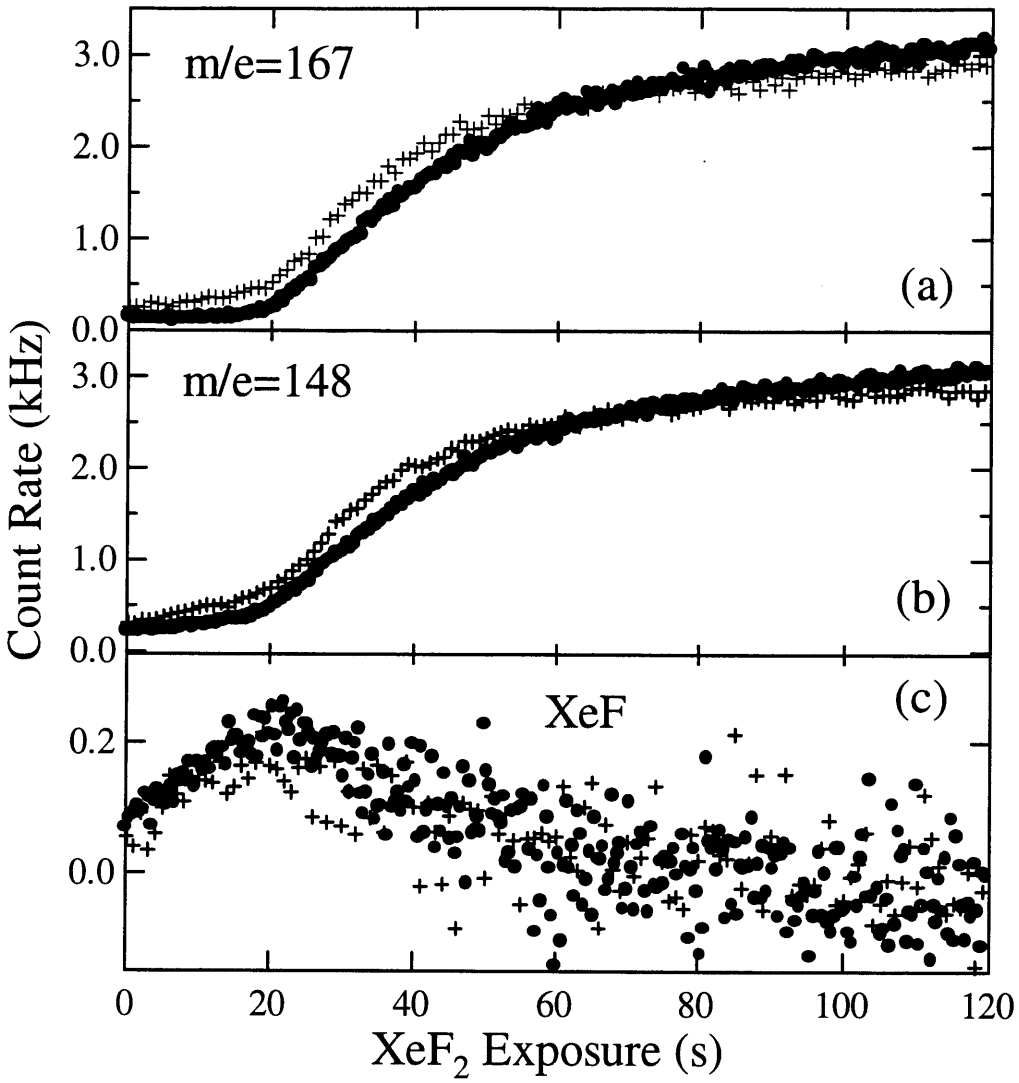

Figure 8 Low energy XeF_2 exposure dependence of scattered XeF^+ and XeF_2^+ signals
(a) Signal at m/e=167 multiplied by XeF_2 cracking ratio and (b) m/e=148 as a function of low energy XeF_2 exposure (solid circles) at θ_i=0°, θ_d=35° and T_s=250 K. (c) Net scattered XeF signal calculated by point-by-point subtraction of m/e=167 signal multiplied by XeF_2 cracking ratio in (a) from m/e=148 signal in (b). Identical signals as a function of high energy XeF_2 exposure (crosses) at θ_i=0°, θ_d=35° and T_s=250 K are superimposed for comparison. A universal scaling factor is used to account for differences in flux and detector sensitivity in Figures 8-9.

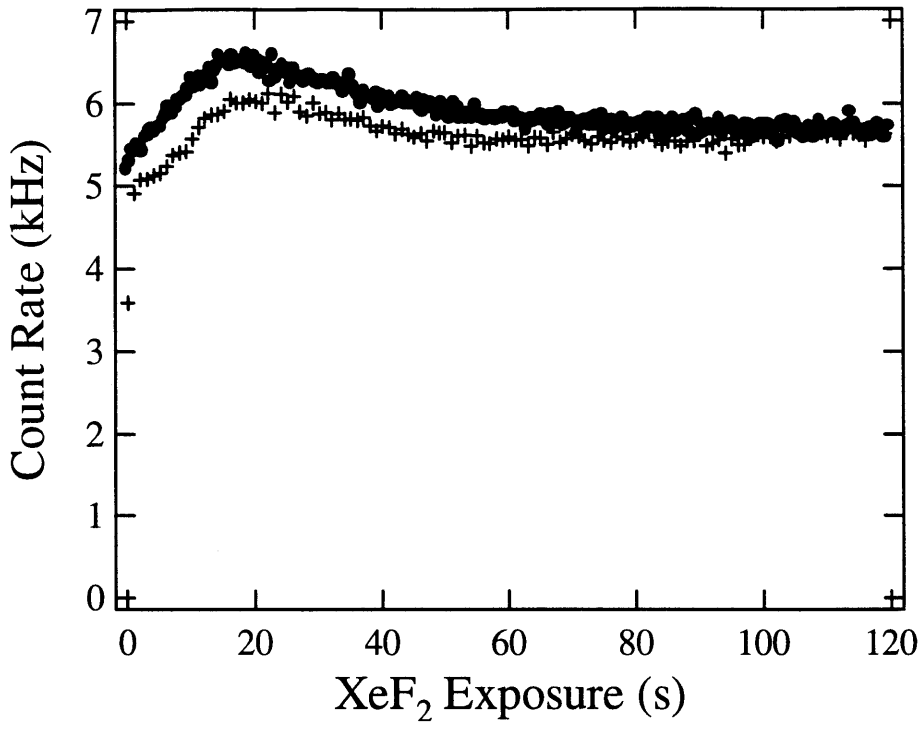

Figure 9 Low energy XeF_2 exposure dependence of scattered Xe^+ signal
Signal at m/e=129 as a function of low energy XeF_2 exposure (solid circles) at θ_i=0°, θ_d=35° and T_s=250 K. Signal at m/e=129 as a function of high energy XeF_2 exposure (crosses) at θ_i=0°, θ_d=35° and T_s=250 K is superimposed for comparison. A universal scaling factor is used to match the high energy signal to the low energy signal at m/e=129 to account for differences in flux and detector sensitivity in Figures 8-9.

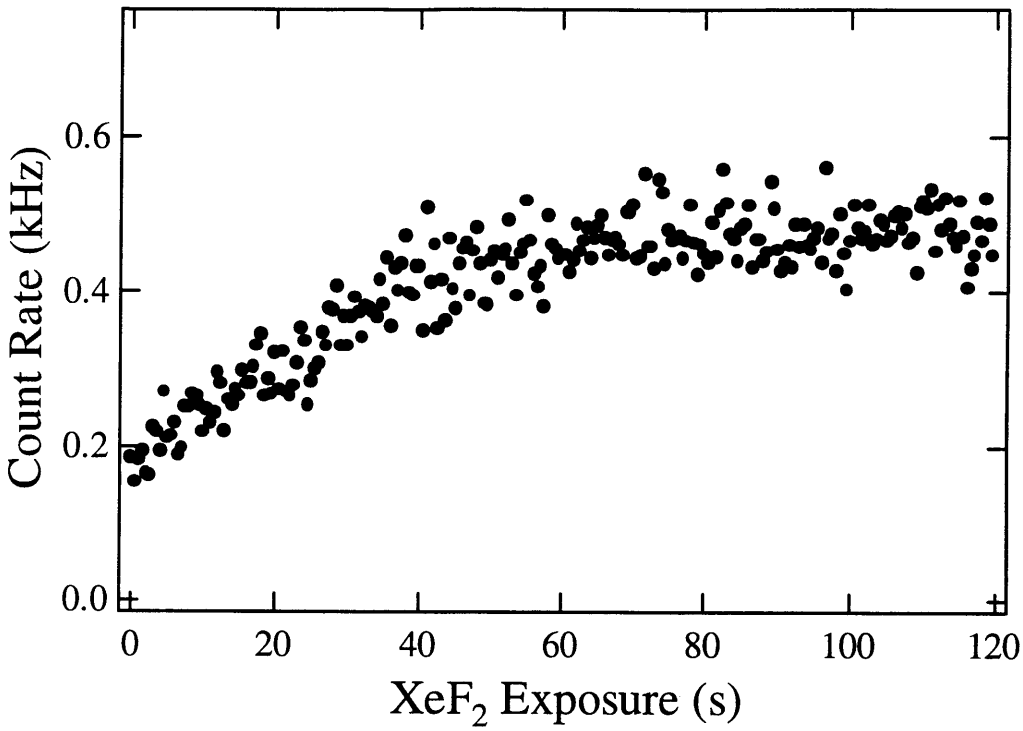

Figure 10 Low energy XeF_2 exposure dependence of scattered F^+ signal
Signal at m/e=19 as a function of low energy XeF_2 exposure (solid circles) at θ_i=0°, θ_d=35° and T_s=250 K.

III.A.3. Summary of exposure dependence of scattered products

The results presented above suggest that surprising similarities and distinct differences exist between the interaction of XeF_2 with Si(100) and that of F_2. The products of the two dissociative chemisorption channels, single atom abstraction and two atom adsorption, are present in the interaction of XeF_2 with Si. However, the dependence of the scattered products on XeF_2 exposure, especially the unreactively scattered XeF_2 and the scattered XeF arising from single atom abstraction, are distinctly different from the exposure dependence of their analogs, F_2 and F atom, in the interaction of F_2 with Si. In agreement with previous investigations, the interaction of XeF_2 with Si leads to the production of gas phase SiF_4, the product of etching. However, the production of etch product does not occur upon initial exposure to XeF_2, suggesting that XeF_2 interacts primarily with the Si dangling bonds during the initial exposure. Of course, at higher XeF_2 exposures, interaction with the rest of the Si lattice must occur for etching to occur. In the next section, the focus of the investigation shifts to probing the structure of the fluorine overlayer on the surface as a function of XeF_2 exposure using thermal desorption and He diffraction. The focus of the investigation will return to the identification and characterization of the scattered products of the interaction of XeF_2 with Si(100) in Sec. III.C using a time-of-flight technique to measure the velocity distribution of the scattered products.

III.B. Exposure dependence of Si surface structure

III.B.1.a. Thermal desorption

The crystal, at a temperature of 250 K, is exposed to high energy XeF_2 at normal incidence, subsequently rotated so that the surface normal is along the axis of the differentially pumped mass spectrometer detector and then heated at a rate of 5 K/s from 250-1000 K. The desorption of multiple species is monitored essentially simultaneously by switching, at a rate of 10 Hz, the mass to which the quadrupole is tuned. Figure 11 shows a superposition of thermal desorption spectra at m/e=66 and m/e=85 after three different exposures to F_2 and XeF_2. In the first case (circles in Figure 11), the thermal desorption spectra were measured after a sufficiently long F_2 exposure to correspond to the steady state regime in which the reaction ceases. The signals at m/e=66 and m/e=85 correspond to SiF_2^+ and SiF_3^+ and arise from SiF_2 and SiF_4, respectively. Comparison of thermal desorption features at m/e=66, m/e=85, as well as m/e=104, which corresponds to SiF_4^+, shows that there is little or no SiF_3 contribution to the SiF_3^+ signal and little or no SiF_4 contribution to the SiF_2^+ signal, in agreement with previous results [57]. The major thermal desorption product, SiF_2, is observed as a single feature centered around 800 K. The minor product, SiF_4, desorbs as two broad features around 550 and 700 K. Recall that the fluorine coverage is essentially 1 ML after the cessation of the reaction of F_2 with Si(100). In the second case (crosses on Figure 11), the thermal desorption spectra were measured after a sufficiently long high energy XeF_2 exposure to correspond to 1 ML fluorine coverage based on a quantitative comparison of the integrated thermal desorption fluorine yield described below. The XeF_2 exposure is not sufficiently long to produce any significant etch product. The thermal desorption features after the F_2 and XeF_2 exposures are identical with

respect to their shape and intensity, suggesting that the initial fluorine overlayers formed by exposure to F_2 and XeF_2 are identical. To test the possibility that XeF_2 disrupts the Si surface creating new adsorption sites, in the third case (squares on Figure 11), the thermal desorption spectra were measured after a XeF_2 exposure identical to the previous case with a subsequent long exposure to F_2. No etch product was observed to evolve during the F_2 exposure. Again the thermal desorption features after the consecutive XeF_2 and F_2 exposures are identical providing further evidence that the Si surface is not disrupted by the initial interaction with XeF_2. However, at longer XeF_2 exposures, additional fluorine is incorporated onto the surface leading to the evolution of etch product as was shown in Sec. III.A.

Figure 12(a) shows the total integrated thermal desorption fluorine yield as a function of XeF_2 exposure. The integrated yield is the sum of the integrated yields of SiF_2^+ and SiF_3^+ after scaling them for the relative detection sensitivities of the two signals and the factor of two more fluorine atoms that SiF_4 has relative to SiF_2. The different velocity and angular distributions of the desorbing SiF_2 and SiF_4 species as well as their relative ionization cross sections and quadrupole transmissions are taken into account in this determination of their relative yield [53,54]. The absolute coverage is determined by referencing the integrated thermal desorption yield after exposure to XeF_2 to the integrated thermal desorption yield after a sufficiently long F_2 exposure to reach the steady state regime which is known to correspond to a fluorine coverage of 1 ML. Figure 12(b)-(c) show the contributions of SiF_2 and SiF_4, respectively, to the total integrated thermal desorption fluorine yield. The fluorine coverage increases nearly linearly with XeF_2 exposure to 1 ML. The fluorine coverage continues to increase beyond 1 ML until it reaches a steady state level of 1.7 ML when the rate of adsorption of fluorine is equal to the rate

of desorption of fluorine due to etching. Note that the contribution of SiF_4 to the total fluorine coverage is negligible until the coverage exceeds 1 ML and only accounts for 12% of the total fluorine coverage in the steady state regime. The thermal desorption measurements provide evidence that the initial interaction of XeF_2 with Si(100) is similar to the interaction of F_2 with Si(100) in that the fluorine overlayer consists of similar species, which in the case of the interaction of F_2 with Si corresponded to adsorption on the dangling bonds. However, thermal desorption yields are not the most sensitive measurements of overlayer structure. He diffraction is much more sensitive to the surface periodicity and can provide more compelling evidence that the interaction of XeF_2 with Si(100) at coverages below 1 ML is with the dangling bonds.

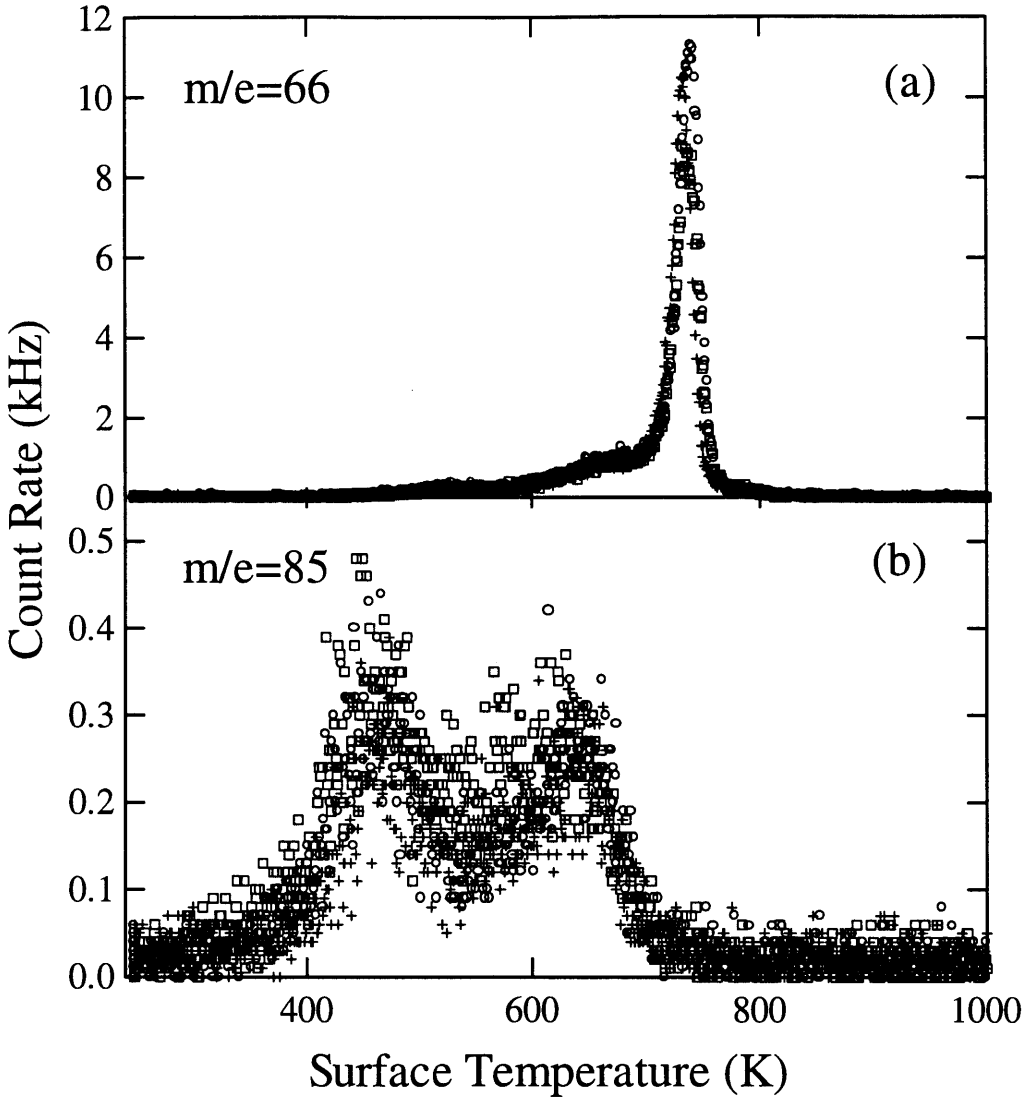

Figure 11 Thermal desorption spectra of Si(100) after exposure to F_2 and XeF_2
Thermal desorption spectra at (a) m/e=66 and (b) m/e=85 after 1. a F_2 exposure of 40 ML F (circles), 2. a 30 s high energy XeF_2 exposure (crosses), and 3. a 30 s high energy XeF_2 exposure with a subsequent F_2 exposure of 40 ML F (squares).

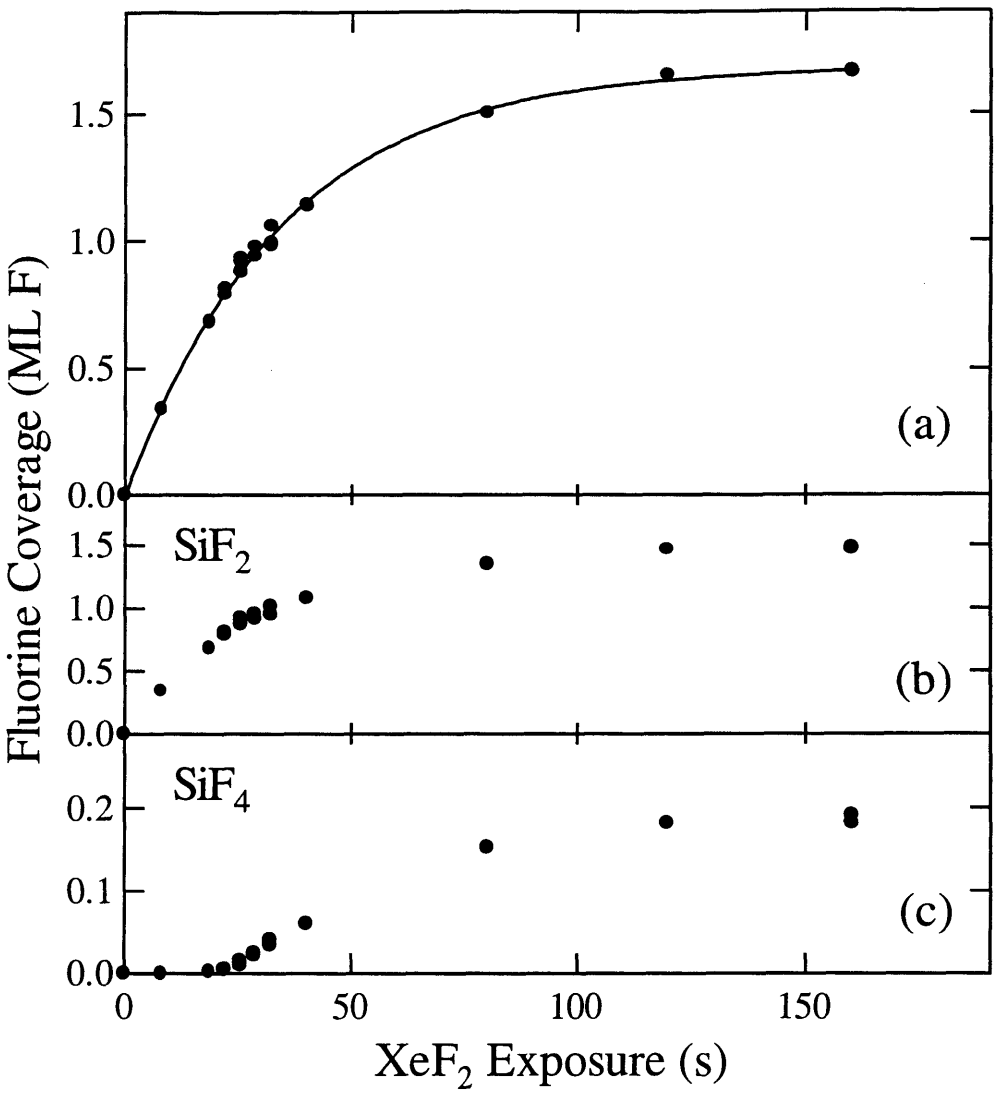

Figure 12 Fluorine coverage as a function of XeF_2 exposure
(a) Fluorine coverage as a function of high energy XeF_2 exposure determined from the integrated thermal desorption yield after high energy XeF_2 exposure calibrated to the integrated thermal desorption yield after a sufficiently long exposure to F_2 to yield 1 ML F. Fluorine coverage attributable to adsorbed fluorine that desorbs as (b) SiF_2 and (c) SiF_4 when the crystal temperature is increased from 250-1000 K.

III.B.2. Helium diffraction

Si(100) reconstructs forming rows of surface Si dimers resulting in one partially-filled molecular orbital or dangling bond projecting into the vacuum for each surface Si atom and yielding a (2x1) periodicity that is observable by He diffraction [58]. These dangling bonds, which effectively are radical sites and hence very reactive species, are logical sites for F atom abstraction and adsorption. Analogous to the He diffraction experiments that probe the interaction of F_2 with Si(100), the goal here is to identify the site of F adsorption and, most importantly in the case of XeF_2 interacting with Si, to determine the extent of Si-Si bond cleavage, if any, prior to the evolution of etch product when surface order is inevitably lost due to the removal of Si. While He diffraction cannot directly identify the F adsorption site, it can reveal the prevailing periodicity to determine which periodic structures have been disrupted upon F adsorption, thereby providing supporting evidence for the dangling bonds as the F atom adsorption sites in the interaction of XeF_2 with Si(100)(2x1).

A mixture of He seeded in Ar is expanded to produce a He beam that has an average velocity of 766±65 (FWHM) m/s as determined from TOF measurements. The average wavelength of the incident He is 1.31±0.11 (FWHM) Å, which is comparable to the surface unit cell dimensions of 3.84 Å and 7.68 Å. The beam is incident at θ_i=20° and is modulated at 150 Hz with a tuning fork to allow for background subtraction. The detector is rotated in steps of 0.5° from 15°-55° with respect to the surface normal in the forward scattering direction.

Figure 13(a) shows a plot of the scattered He intensity as a function of the scattering angle, θ_d, measured from the surface normal of a clean Si(100) surface at 250 K. The features are broad because of the low angular resolution of the detector that is necessary to obtain

sufficient sensitivity to detect reactive species which typically scatter with very low fluxes. However, three primary features of the diffraction spectrum indicative of the (2x1) periodicity are apparent. These features are a specular peak arising from overall order and smoothness, a half order peak at θ_d=31° arising from diffraction perpendicular to the rows, and a first order peak at θ_d=43° arising from diffraction parallel to the dimer rows. Figure 13(b) shows helium diffraction from a Si(100) surface at 250 K after a sufficiently long exposure to F_2 so as to reach the steady state regime in which the reaction ceases. Although the intensities of the features are changed upon fluorination, the (2x1) periodicity persists. The identical two-dimensional unit cells of the fluorine overlayer and the Si(100) surface strongly suggests that each dangling bond serves as an adsorption site for one F atom. More importantly, the persistence of the half order feature indicates that no Si lattice bonds, not even the s Si dimer bonds, are broken upon reaction with F_2. There is no etching of the Si surface nor is the surface disordered upon reaction with F_2. Figure 13(c) shows helium diffraction from a Si(100) surface at 250 K after sufficient exposure to XeF_2, to reach a fluorine coverage of 1 ML. The diffraction spectrum is identical to the diffraction spectrum of the ordered F-Si(100) surface. Despite its superior etching ability, XeF_2 interacts with Si in a similar fashion to F_2 during the initial fluorination. Considering that the fluorination of the Si dangling bonds is so facile, this is not surprising. However, contrary to early speculation [22], XeF_2 does not induce significant disorder on the partially-fluorinated Si surface creating reactive sites and causing etching.

The previous experiment provides a snapshot of the fluorine overlayer at a single coverage, 1 ML. However, from the thermal desorption measurements, it was apparent that during a continuous XeF_2 exposure the fluorine coverage on Si(100) increases beyond 1 ML. To

understand the surface periodicity as the surface overlayer evolves, helium diffraction feature intensities were monitored as a function of XeF_2 exposure providing a movie of the evolution of periodicity of the fluorine overlayer. This experiment utilizes the two molecular beam sources to simultaneously expose the surface to the reactant molecules and diffract He from the surface. The XeF_2 beam is incident at θ_i=35° and the He beam is incident at θ_i=55°. The detector is positioned at θ_d=55° in the forward scattering direction which corresponds to the specular angle of the scattered He beam. As a demonstration of the technique, Figure 14(a) shows a plot of the specularly scattered He intensity as a function of F_2 exposure. The intensity of the specular feature decays rapidly as surface order is lost due to the random adsorption of fluorine on the surface, but recovers completely after all of the dangling bonds are fluorinated and the reaction ceases. Figure 14(b) shows a plot of the specularly scattered He intensity as a function of XeF_2 exposure. Similar to the experiment with F_2, the intensity of the specular feature decays rapidly and then recovers almost completely around 1 ML F coverage. However, the reaction of XeF_2 with the Si surface continues and the intensity of the specular feature decays monotonically as the surface order is lost due to further fluorination and etching.

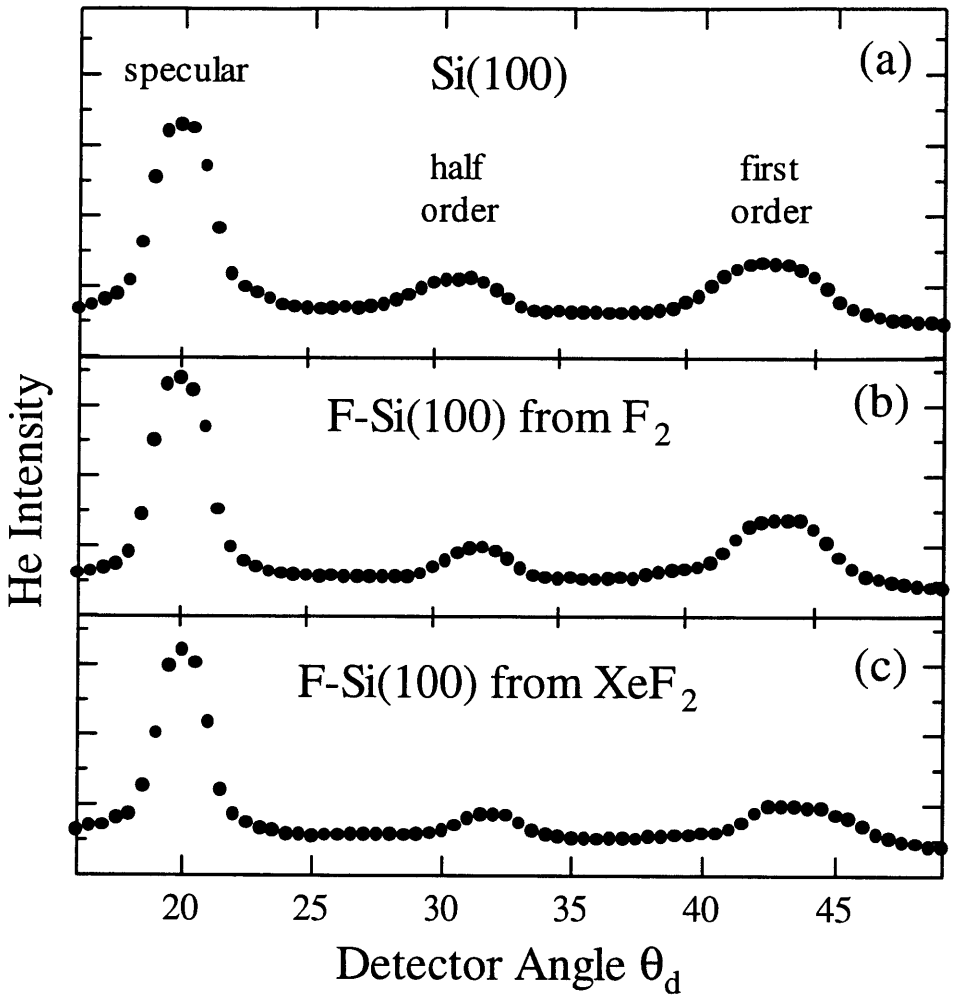

Figure 13 He diffraction from clean and fluorinated Si(100)
Helium signal scattered from Si(100) at 250 K and at θ_i=20 as a function of detector angle θ_d. (a) clean surface, (b) after low energy F_2 exposure of 20 ML F, (c) after 30 s high energy XeF_2 exposure.

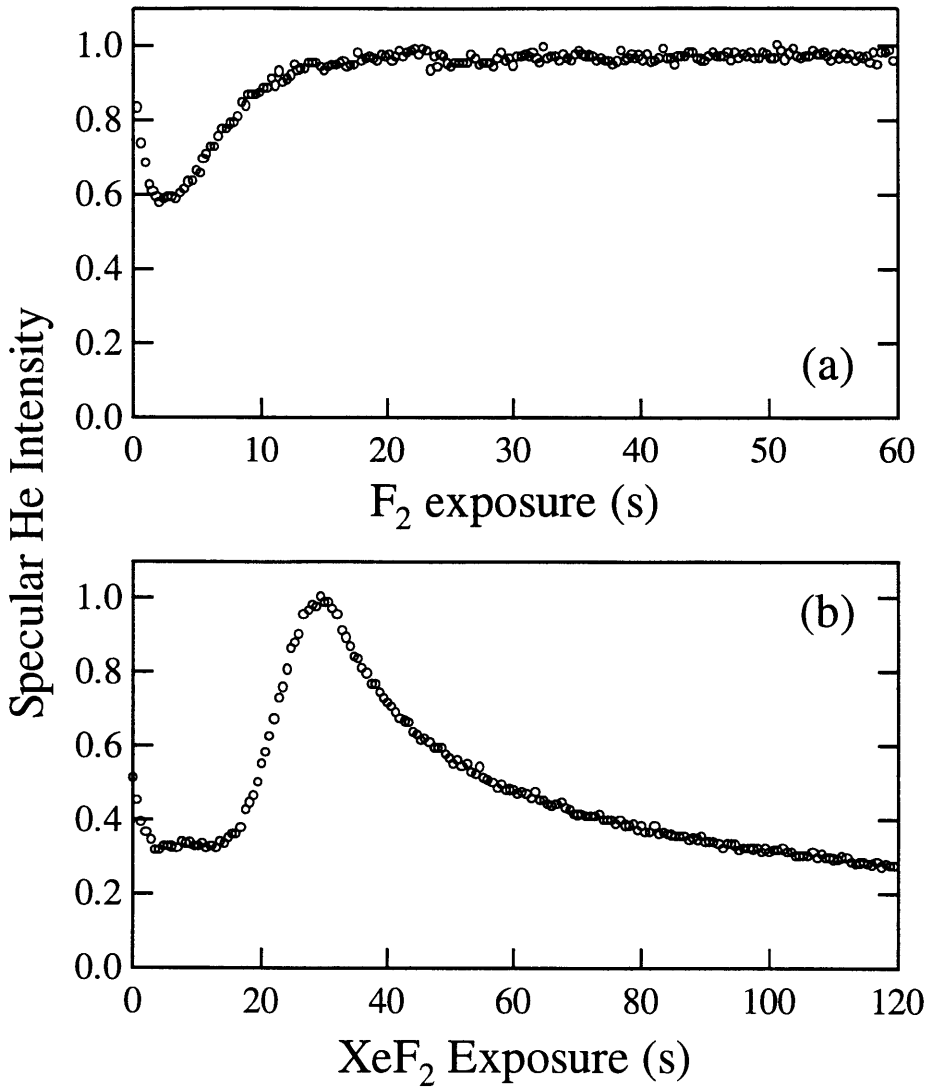

Figure 14 Specular He diffraction signal from Si(100) as a function of F_2 and XeF_2 exposure

Helium signal scattered at the specular angle from Si(100) at 250 K as a function of exposure to (a) low energy F_2 and (b) high energy XeF_2. The F_2 and XeF_2 beams are incident at θ_i=35° and the He beam is incident at θ_i=55°. The detector is positioned at θ_d=55°.

III.B.3. Summary of exposure dependence of Si surface structure

Together, the thermal desorption and helium diffraction results provide evidence that the interactions of XeF_2 and Si(100) at fluorine coverages below 1 ML are remarkably similar to the interactions of F_2 with Si(100). The absence of significant SiF_4 thermal desorption product, which has been suggested to indicate surface disorder [59], at coverages below 1 ML and the complete recovery of the (2x1) periodicity of the Si(100) surface after sufficient exposure to XeF_2 to yield 1 ML fluorine coverage suggest that the initial reaction of XeF_2 is limited to the dangling bonds. Not until almost all of the dangling bonds are fluorinated is XeF_2 able to destroy the surface via further fluorination which requires the breaking of Si lattice bonds and subsequently lead to etching. It is not surprising that the dangling bonds are the most reactive species to XeF_2 nor is it surprising that etching does not occur until the surface is fully fluorinated since additional fluorine must adsorb to the surface Si atoms beyond simply occupying the dangling bond in order to cleave Si lattice bonds to the bulk. The remarkable observation is that until all of the dangling bonds are fluorinated, the interactions of XeF_2 and F_2 with Si(100) are essentially identical, but once the initial fluorination is complete, XeF_2 continues to react with the Si surface while F_2 ceases to react. To better understand the differences between the interactions of XeF_2 and F_2 with Si(100), requires a closer examination of the scattered products.

III.C. Velocity distribution of scattered products as a function of detector angle and XeF_2 exposure

The scattered products of the interaction of XeF_2 with Si(100) at 250 K are identified in Sec. III.A, and the intensity of the signals are measured as a function of exposure to high and low energy XeF_2. Five distinct species are scattered in the interaction of XeF_2 with Si: 1. unreactively scattered XeF_2, 2. XeF arising from single atom abstraction, 3. F atoms arising from the dissociation of XeF produced in single atom abstraction, 4. Xe arising from two atom adsorption, XeF dissociation, as well as the unreactive scattering of free Xe in the XeF_2 molecular beam, and 5. SiF_4, the etch product. Although the exposure dependence of the signal intensities attributable to these five species has been measured, the fragmentation of different neutral species in the ionization region to a common ion obscures the relationship between the signal intensity and the scattered flux which is directly related to the reaction probability. In principle, the contributions from the distinct neutral species could be separated with knowledge of the fragmentation pattern or cracking ratio of the ionization of each neutral species to its parent ion relative to its daughter ion fragments. Although the majority of the cracking ratios are unknown, a self-consistent analysis of an extensive library of data similar to that presented in Sec. III.A has had reasonable success separating the contributions of the various neutral species [53]. However, the three distinct sources of scattered Xe makes it impossible to distinguish the contributions from these distinct scattering mechanisms to the exposure dependence of the signal intensity at m/e=129.

A better method for separating the contributions to the measured signals discussed in Sec. III.A is to measure the TOF distributions of the scattered products. Because the scattered

products arise from different interactions with the surface, it is likely that the individual contributions will have different velocity distributions. In addition to separating the contributions to the mass spectrometer signal, the measurement of the TOF distributions of the scattered products is essential for determining the kinetics as well as probing the dynamics of the interaction of XeF_2 with Si.

The TOF distributions of the scattered product signals that are present in the initial fluorination of Si(100) upon exposure to high and low energy XeF_2 are presented in this section. The results focus on the initial fluorination, defined as fluorine coverages below 1 ML, to best compare these results to those of the interaction of F_2 with Si(100). This section is divided into four subsections which correspond the four scattered product signals that are present during the initial fluorination. The TOF distribution of the signal at m/e=85 which corresponds to the etch product, SiF_4, is not presented because it is not prevalent at coverages below 1 ML F. The TOF distributions at m/e=167 are presented in Sec. III.C.1. In principle, these results are the simplest because the signal corresponds solely to unreactively scattered XeF_2. The dynamics of the unreactively scattered XeF_2 yields significant insight into the dynamics of the *reaction* of XeF_2 with Si. The TOF distributions at m/e=148 are shown in Sec III.C.2. The TOF distribution of the product of single atom abstraction, XeF, is isolated, and in the case of high energy XeF_2 exposure, the angular distribution of the scattered XeF flux is also measured. The angular distribution of scattered XeF is profoundly different from that of the F atoms scattered as a result of single atom abstraction in the interaction of F_2 with Si. The TOF distributions at m/e=19 are presented in Sec. III.C.3. The TOF distribution of scattered F atoms is isolated providing direct evidence for XeF dissociation. Finally, the TOF distributions at m/e=129 are presented in Sec.

III.C.4. Because the magnitude of none of the contributions to the signal at m/e=129 is known, several approximations are made in order to unravel the myriad contributions to the signal at m/e=129.

III.C.1. m/e=167

III.C.1.a. High incident energy XeF_2 (E_i=6.3 kcal/mol)

Figure 15 shows a TOF distribution of the products at m/e=167 that are scattered as a result of the interaction of XeF_2 at E_i=6.3 kcal/mol with Si(100) at 250 K. The signal at m/e=167 corresponds to $^{129}XeF_2^+$ which arises solely from unreactively scattered XeF_2. The TOF distribution shown in Figure 15 is for a single scattering geometry in which the XeF_2 beam is incident at 35° from the surface normal, θ_i=35°, and the detector is positioned along the surface normal, θ_d=0°. The TOF distribution is signal averaged over a 40 s exposure to high energy XeF_2 that corresponds to a fluorine coverage range of 0-1.1 ML determined by quantitative comparison of the integrated thermal desorption yields after the XeF_2 exposure to those after exposure to low energy F_2 which is known to yield a coverage of 1 ML F. Figure 16 shows a plot of the fluorine coverage as a function of high energy XeF_2 exposure.

The velocity distribution of the unreactively scattered XeF_2 is bimodal, a common observation in the scattering of hyperthermal particles from a surface [60]. The narrow fast feature at short flight times corresponds to particles scattering via a direct-inelastic (DI) mechanism. In DI scattering, the interaction between the particle and the surface can be described as a single binary collision or a series of collisions. The particle transfers only a fraction of its energy to the surface and retains memory of its incident trajectory preferentially scattering anisotropically along the specular scattering angle. On the other hand, the broad slow

feature at longer flight times corresponds to particles scattering via a trapping-desorption (TD) mechanism. In TD scattering, the interaction between the particle and the surface can be described as the physisorption of the particle to the surface with subsequent thermal equilibration between the particle and the surface. The particle desorbs from the surface with a thermal velocity distribution when the thermal energy fluctuations are sufficient to overcome the physisorption potential well between the particle and the surface. The particle effectively transfers all of its energy to the surface and retains no memory of its incident trajectory.

Two velocity distributions are fit to the two components of the TOF distribution in a stepwise manner. The TD component is determined first because the velocity distribution is only dependent on the surface temperature. A Maxwell-Boltzmann velocity distribution for XeF_2 at a temperature of 250 K, the surface temperature, describes the TD component. This velocity distribution is fit to the part of the TOF spectrum that does not contain a significant contribution from the DI component. The regions of the TOF spectrum that are largely free of the DI component encompass flight times greater than 1250 μs as well as all flight times less than 500 μs. The shortest flight times are included because of the cyclic nature of the time axis in TOF measurements modulated with a mechanical chopper wheel. When the period of one chopper cycle (3570 μs) is shorter than the flight time of the slowest particles ($v<82$ m/s), these slow particles are detected at the beginning of the subsequent cycle of the chopper wheel which corresponds to very short flight times, and hence artificially fast velocities, in the TOF measurement. The TD component is then subtracted from the TOF distribution and the remaining signal is attributed entirely to the DI component. The DI component is fit to a one component Maxwell-Boltzmann function F(t) (Eq. (II.1)) where the flow velocity and

temperature, which describe the average velocity and width of the distribution, are free parameters. For the TOF distribution shown in Figure 15, the average velocity and energy of the DI component are 390±18 m/s and 3.2±0.3 kcal/mol, respectively. For comparison, the average velocity and energy of the TD component are 213±9 m/s and 1.0±0.1 kcal/mol, respectively.

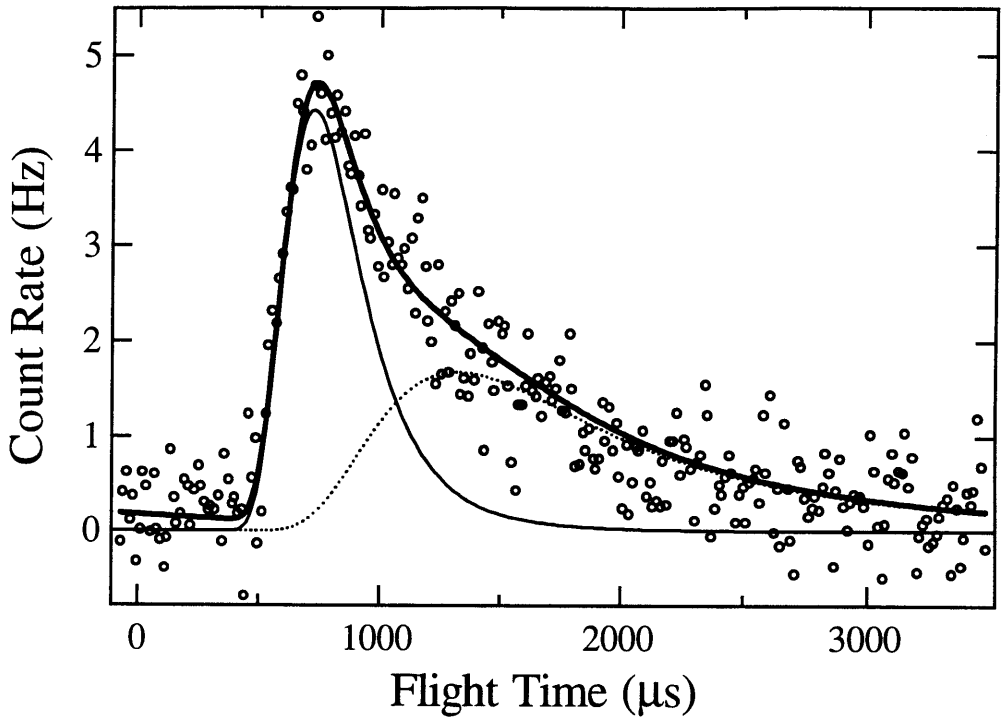

Figure 15 TOF distribution of scattered products at m/e=167
TOF spectrum of signal at m/e=167 scattered along the surface normal, θ_d=0°, from Si(100) at 250 K upon exposure to high energy XeF_2 at θ_i=35°. Thick solid line shows a least squares fit of a two component velocity distribution. The fast component (thin solid line) at short flight times corresponds to direct-inelastic (DI) scattering and is described by a Maxwell-Boltzmann function F(t) described by Eq. (II.1) in Sec. II.D. The slow component (dashed line) at long flight times corresponds to trapping-desorption (TD) and is described by a Maxwell-Boltzmann function F(t) with v_f=0 and T=250 K. Spectrum is averaged over XeF_2 exposure corresponding to a fluorine coverage range of 0-1.1 ML F. Average velocities of the two distributions are v_{DI}=389±18 m/s and v_{TD}=213±9 m/s.

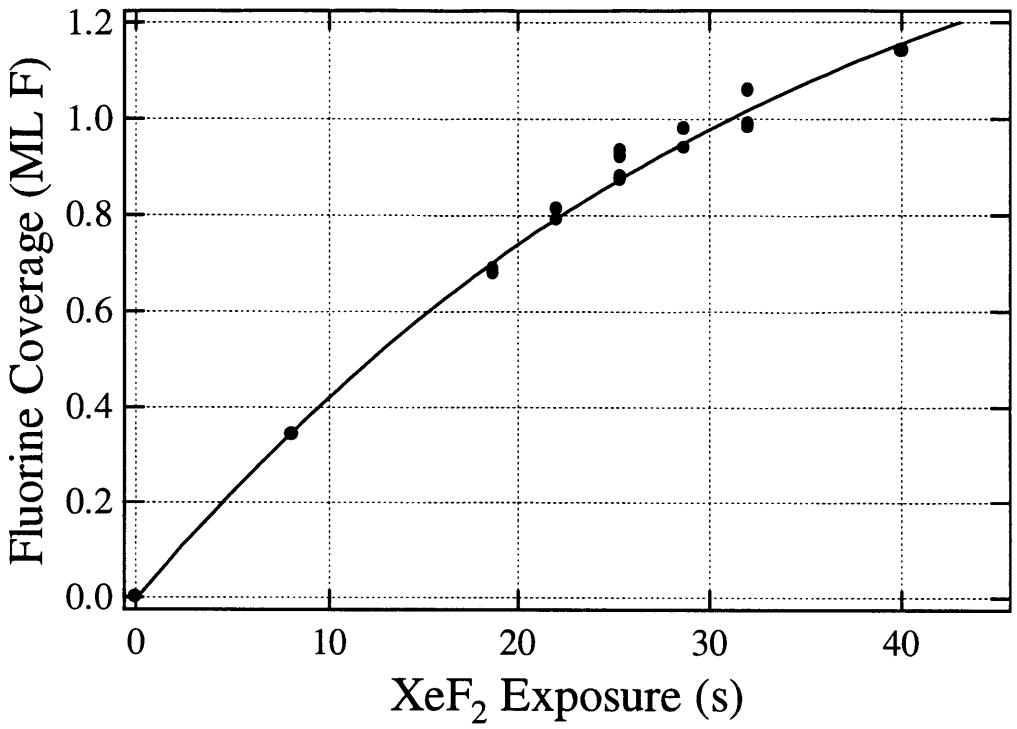

Figure 16 Fluorine coverage as a function of XeF_2 exposure for TOF distribution measurements

Expanded plot of total fluorine yield from Si(100) as a function of XeF_2 exposure shown in Figure 12.

The TOF distribution shown in Figure 15 is for a single scattering geometry in which the high energy XeF_2 is incident at θ_i=35° and the detector is positioned along the surface normal, θ_d=0°. In addition, the TOF distribution has been signal averaged over a long XeF_2 exposure that corresponds to a coverage range of 0-1.1 ML. The TOF distributions may not represent the true velocity distributions at all scattering geometries and for all coverages if they are sensitive to scattering geometry and fluorine coverage. To test the sensitivity of the TOF distributions of scattered XeF_2 to scattering geometry, TOF distributions at m/e=167 are measured at several detection angles, θ_d, spanning the entire forward scattering region in the scattering plane. To test the sensitivity of the TOF distribution to fluorine coverage, TOF distributions are signal averaged over shorter 10 s XeF_2 exposure intervals that correspond to the approximate fluorine coverage ranges: 0-0.4 ML F, 0.4-0.7 ML F, 0.7-0.9 ML F, and 0.9-1.1 ML F (cf. Figure 16).

Figure 17 shows the TOF distributions of the products at m/e=167 scattered into nine detection angles, θ_d, from the interaction of high energy XeF_2 at θ_i=35°. The TOF distributions are signal averaged over a coverage range of 0-0.4 ML F. The results shown in Figures 18-20 are measured under identical conditions to those in Figure 17 except that the TOF distributions are signal averaged over coverage ranges of 0.4-0.7 ML F, 0.7-0.9 ML F, and 0.9-1.1 ML F, respectively. Analogous to the analysis of the TOF distribution shown in Figure 15, two velocity distributions are fit to the two components of the TOF distribution, corresponding to DI and TD scattering, in a stepwise manner.

Figure 21 shows the angular distribution of the flux of XeF_2 scattered unreactively from Si(100) via DI scattering and TD scattering over four ranges of coverage due to XeF_2 exposure. The flux plotted in Figure 21 is calculated by integrating the velocity-weighted TOF distributions

shown in Figures 17-20. The angular distributions of the DI and TD scattered fluxes are in agreement with previous investigations of unreactive gas-surface scattering [60]. The XeF_2 DI angular distribution is anisotropic with a broad lobe centered around θ_d=40°, a detection angle that is near the specular scattering angle, because the DI scattered XeF_2 retains memory of its incident trajectory. The XeF_2 TD angular distribution is isotropic and cosinelike since the TD scattered XeF_2 has no memory of its incident trajectory. The remarkable observation is that the flux into the DI scattering is reasonably insensitive to coverage, whereas the flux into TD scattering increases dramatically at coverages greater than 0.6 ML F. This dramatic shift in the branching between DI scattering and TD scattering provides insight into the reactivity of XeF_2 and will be discussed further in Sec. IV.A

The shape of the TOF distribution of the DI component is insensitive to scattering geometry and fluorine coverage. Figure 22 shows a plot of the average translational energy of the DI component of the unreactively scattered XeF_2. The translational energy and the full width at half of the maximum of the distribution (FWHM) are 3.4±0.2 kcal/mol and 2.9±0.2 kcal/mol, respectively, averaged over all nine detection angles and four coverage ranges. The uncertainties represent the standard deviations of the average of the average energy and of the FWHM of the distributions. The incident energy is 6.3 kcal/mol, so about half of the translational energy of XeF_2 is transferred to the Si surface or to the internal energy of the XeF_2 molecule on average in a DI scattering event. This value is in agreement with the energy transfer of Xe, Kr, and Ar scattered from Si(100) via DI scattering at similar incident energies [61]. Therefore, within the uncertainty of the TOF measurement, XeF_2 scatters like an atom without internal degrees of

freedom. That is, rotation and vibration do not play a significant role in the energy transfer occurring during this unreactive gas-surface interaction.

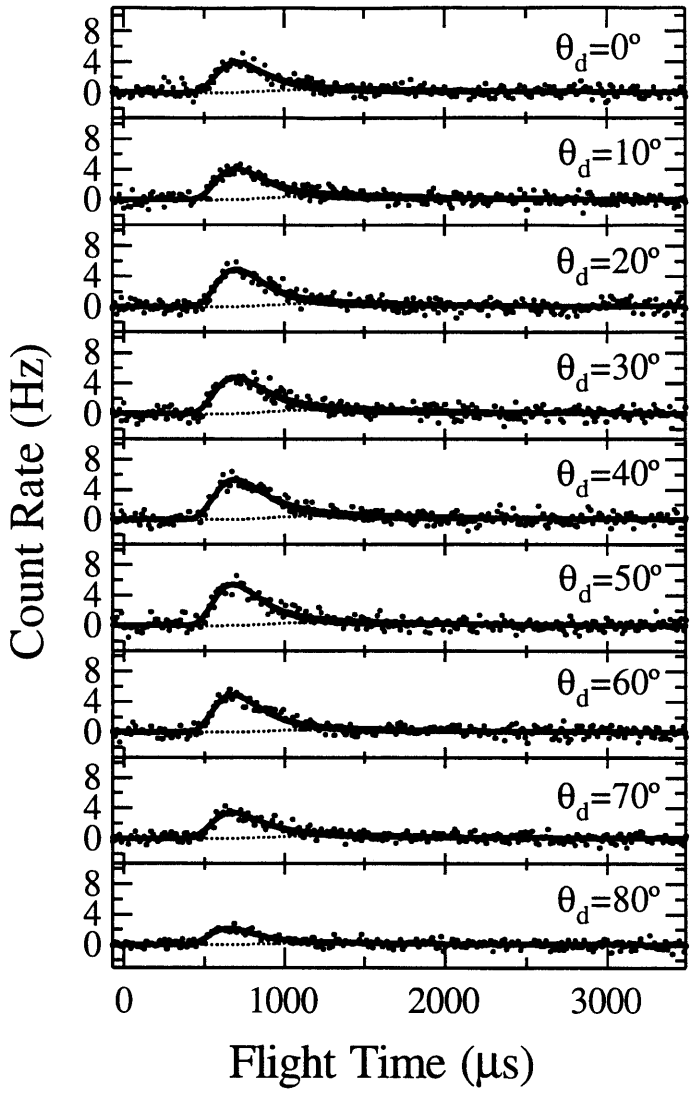

Figure 17 TOF distribution of scattered products at m/e=167 as a function of detector angle over a coverage range of 0-0.4 ML F

TOF spectra at m/e=167 measured at nine detector angles θ_d and T_s=250 K upon exposure to high energy XeF_2 at θ_i=35°. Thick solid line shows a least squares fit of a two component velocity distribution to the data. The fast component (thin solid line) at short flight times corresponds to DI scattering and the slow component (dashed line) at long flight times corresponds to trapping-desorption TD scattering. Spectra are averaged over a 10 s high energy XeF_2 exposure corresponding to a fluorine coverage range of 0-0.4 ML F. Over this coverage range, the plot of the fast component (thin solid line) is indistinguishable from the total distribution (thick solid line).

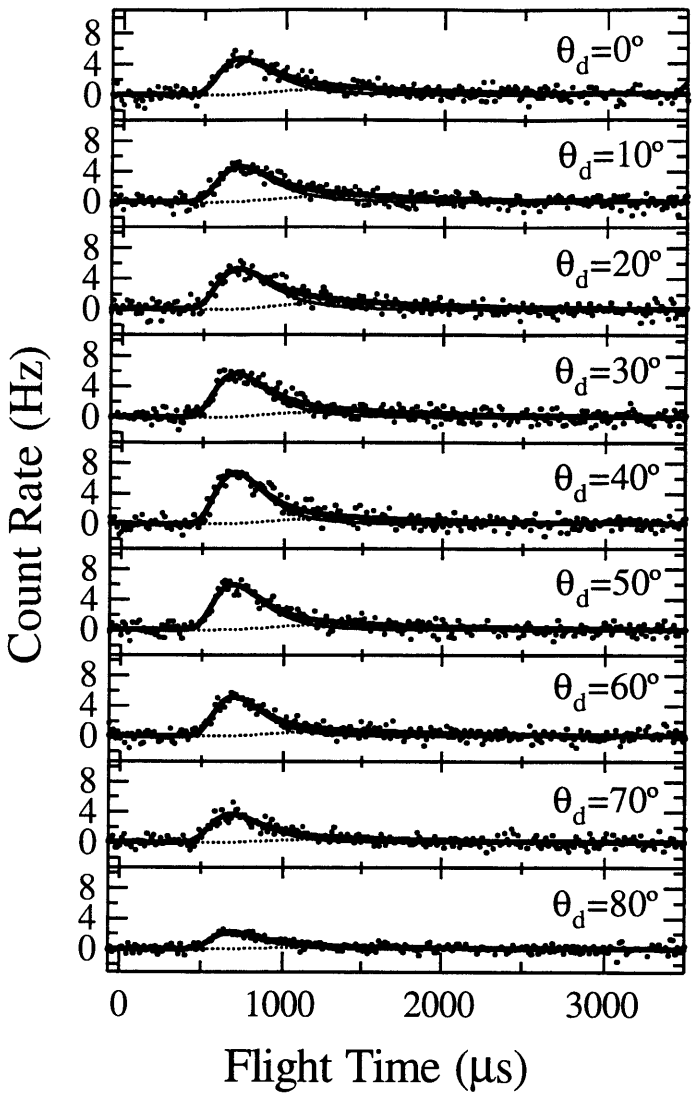

Figure 18 TOF distribution of scattered products at m/e=167 as a function of detector angle over a coverage range of 0.4-0.7 ML F

TOF spectra at m/e=167 measured at nine detector angles θ_d and T_s=250 K upon exposure to high energy XeF_2 at θ_i=35°. Thick solid line shows a least squares fit of a two component velocity distribution to the data. The fast component (thin solid line) at short flight times corresponds to DI scattering and the slow component (dashed line) at long flight times corresponds to trapping-desorption TD scattering. Spectra are averaged over a 10 s high energy XeF_2 exposure corresponding to a fluorine coverage range of 0.4-0.7 ML F. Over this coverage range, the plot of the fast component (thin solid line) is indistinguishable from the total distribution (thick solid line).

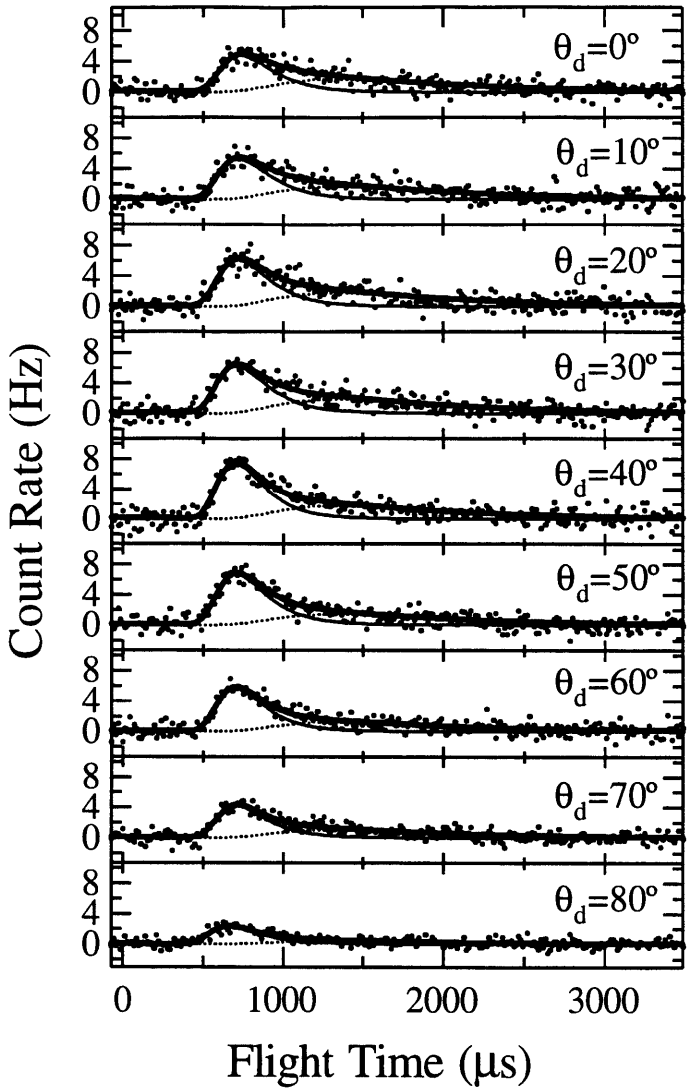

Figure 19 TOF distribution of scattered products at m/e=167 as a function of detector angle over a coverage range of 0.7-0.9 ML F

TOF spectra at m/e=167 measured at nine detector angles θ_d and T_s=250 K upon exposure to high energy XeF_2 at θ_i=35°. Thick solid line shows a least squares fit of a two component velocity distribution to the data. The fast component (thin solid line) at short flight times corresponds to DI scattering and the slow component (dashed line) at long flight times corresponds to trapping-desorption TD scattering. Spectra are averaged over a 10 s high energy XeF_2 exposure corresponding to a fluorine coverage range of 0.7-0.9 ML F.

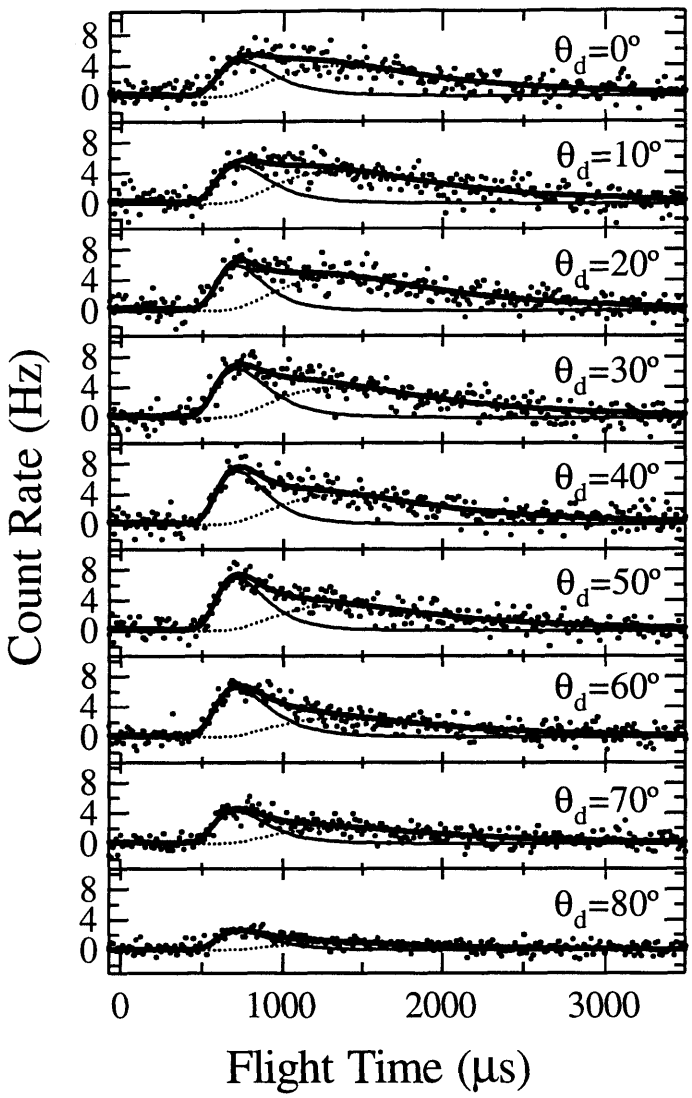

Figure 20 TOF distribution of scattered products at m/e=167 as a function of detector angle over a coverage range of 0.9-1.1 ML F

TOF spectra at m/e=167 measured at nine detector angles θ_d and T_s=250 K upon exposure to high energy XeF_2 at θ_i=35°. Thick solid line shows a least squares fit of a two component velocity distribution to the data. The fast component (thin solid line) at short flight times corresponds to DI scattering and the slow component (dashed line) at long flight times corresponds to trapping-desorption TD scattering. Spectra are averaged over a 10 s high energy XeF_2 exposure corresponding to a fluorine coverage range of 0.9-1.1 ML F.

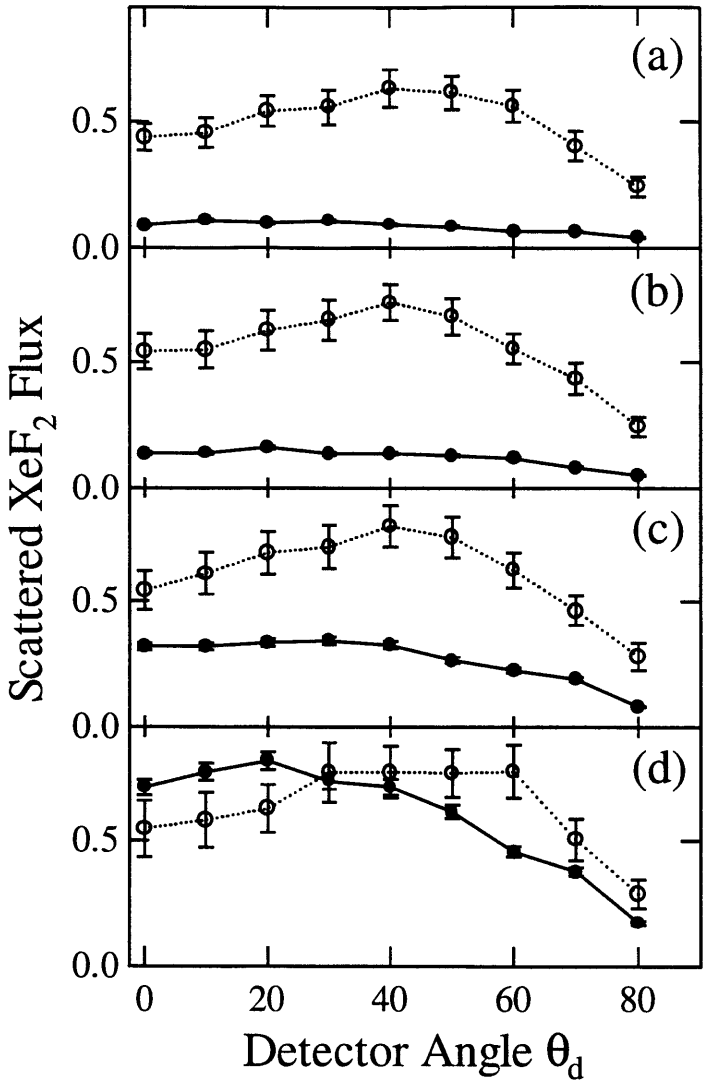

Figure 21 Angular distribution of flux of XeF_2 scattered from Si(100)
Scattered flux of XeF_2 determined from velocity-weighted integration of the fit to the TOF distribution at m/e=167 attributable to DI scattering (hollow circles) and TD scattering (solid circles) as a function of detector angle over successive 10 s high energy XeF_2 exposure intervals corresponding to coverage ranges of (a) 0-0.4 ML F, (b) 0.4-0.7 ML F, (c) 0.7-0.9 ML F, and (d) 0.9-1.1 ML F. Error bars represent uncertainty of the integral of the velocity-weighted fit to the TOF distributions (Sec. II.D) in Figures 17-20.

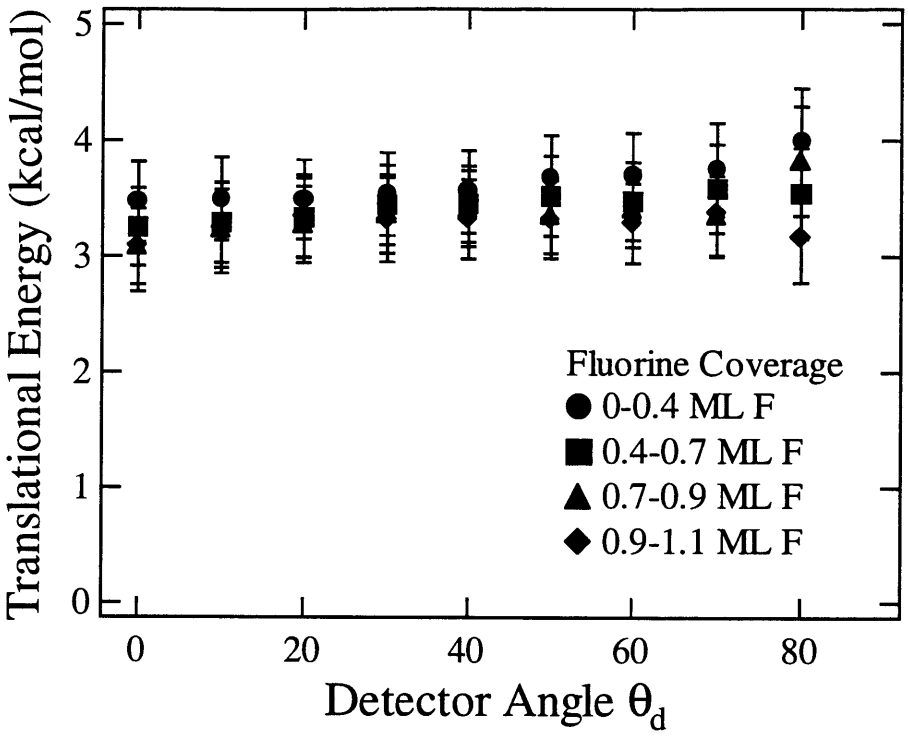

Figure 22 Translational energy of F atom scattered from Si(100) as a function of detector angle

Average translational energy of unreactively scattered XeF_2 via DI scattering as a result of exposure to high energy XeF_2 as a function of detector angle over four different fluorine coverage ranges. The average translational energy is determined from the velocity-weighted TOF distributions shown in Figures 17-20. Error bars represent the uncertainty of the determination of the average translational energy (Sec. II.D) from the fits to the TOF distributions in Figures 17-20.

III.C.1.b. Low incident energy XeF_2 (E_i=1.8 kcal/mol)

The TOF distributions described above are all for scattering high energy XeF_2 at E_i=6.3 kcal/mol. To better compare the dynamics of the interaction of XeF_2 with Si(100) with the dynamics of the interaction of F_2 with Si(100) described in Chapter 1, TOF distributions of the products at m/e=167 scattered from the interaction of low energy XeF_2 at E_i=1.8 kcal/mol with Si(100). Figure 23 shows a TOF distribution of the products at m/e=167 that are scattered from the interaction of low energy XeF_2 from Si(100) at 250 K. The TOF distribution is for a scattering geometry in which the incident XeF_2 is at θ_i=0° and the detector is positioned at θ_d=35°. The TOF distribution is signal averaged over a 24 s exposure to low energy XeF_2. Based on the similarity of the relative exposure dependence of the scattered products for high and low energy XeF_2, in particular the point of onset of significant etching, this length of exposure to XeF_2 is presumed to correspond to a fluorine coverage range of 0-1.1 ML. Assuming that the coverage ranges are similar, the unreactively scattered flux upon exposure to low energy XeF_2 is five times lower than that of high energy XeF_2, based on comparison of the integrals of the velocity weighted TOF distributions into the same detection angle. The lower flux of unreactively scattered XeF_2 suggests that the low energy XeF_2 is more reactive than the high energy XeF_2.

Analogous to the TOF distributions of unreactively scattered XeF_2 from the interaction of high energy XeF_2 with Si, the TOF distribution in Figure 23 is comprised of two components, which are attributed to DI and TD scattering. The fits to the two contributions are superimposed on the TOF distribution in Figure 23. The distinction between DI and TD scattering is more difficult to discern because the velocity distribution of the incident beam is similar to that of the

thermal distribution from the surface. The average velocity and translational energy of the DI component are 343±32 m/s and 2.5±0.5 kcal/mol, respectively. The average energy of the DI component is larger than the average energy of the incident beam (1.8 kcal/mol) not because the XeF_2 is gaining substantial energy from the collision with the surface, but because the width of the energy distribution of the incident beam is so large.

Analogous to the TOF distributions of XeF_2 unreactively scattering as a result of the interaction of high energy XeF_2 with Si, TOF distributions at m/e=167 have been signal averaged over shorter 6 s exposures to low energy XeF_2 to probe the exposure dependence of the unreactively scattered XeF_2. Figure 24 shows the TOF distributions of the scattered products at m/e=167 over four successive 6 s exposures to low energy XeF_2. Despite extensive signal averaging, the extremely low intensity of the signal at m/e=167 in combination with the broad TOF distribution yield a TOF distribution with low signal-to-noise. The data are shown for the sake of completeness, and will be necessary in subsequent sections to determine the contribution of unreactively scattered XeF_2 to the other signals because of fragmentation in the ionization region.

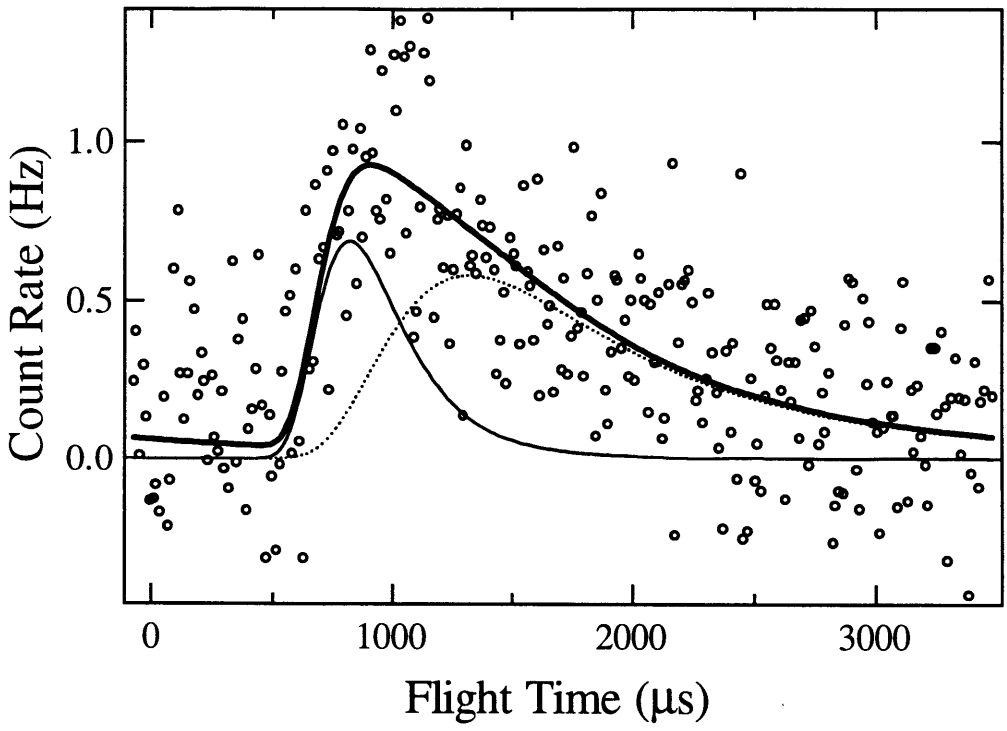

Figure 23 TOF distribution of scattered products at m/e=167 upon exposure to low energy XeF_2

TOF spectrum of signal at m/e=167 scattered at θ_d=35°, from Si(100) at 250 K upon exposure to low energy XeF_2 at θ_i=0°. Thick solid line shows a least squares fit of a two component velocity distribution to the data. The fast component (thin solid line) at short flight times corresponds to DI scattering and the slow component (dashed line) at long flight times corresponds to TD scattering. Spectrum is averaged over XeF_2 exposure corresponding to a fluorine coverage range of 0-1.1 ML F. Average velocities of the two distributions are v_{DI}=343±32 m/s and v_{TD}=213±9 m/s.

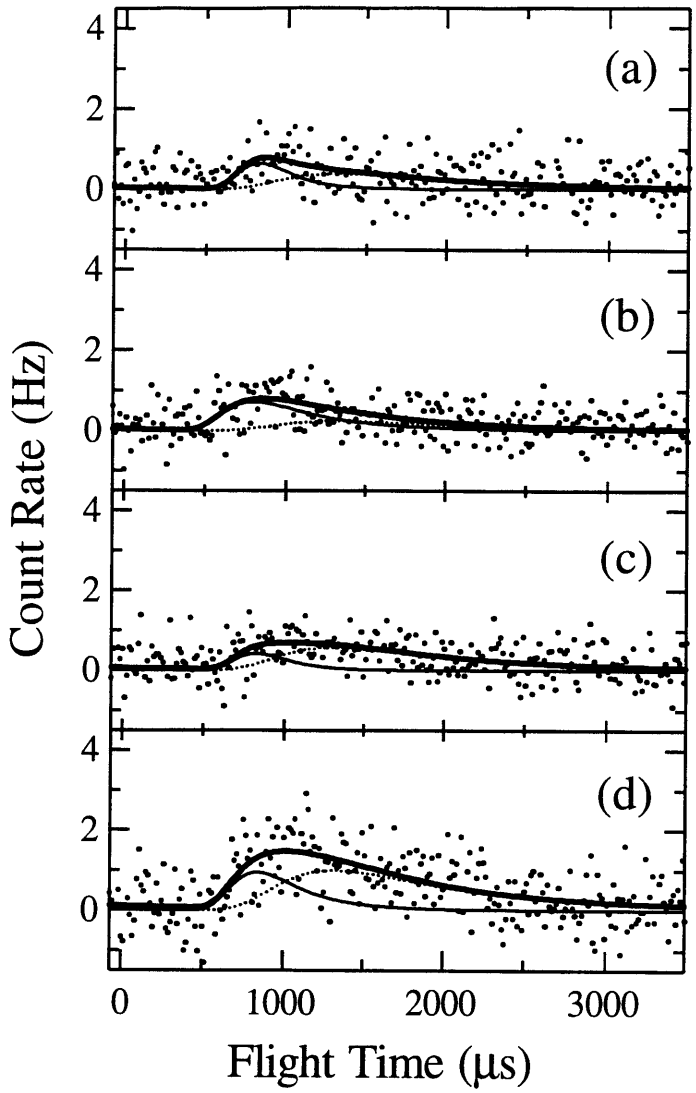

Figure 24 TOF distribution of scattered products at m/e=167 upon exposure to low energy XeF_2 as a function of coverage

TOF spectra of signal at m/e=167 scattered at θ_d=35°, from Si(100) at 250 K upon exposure to low energy XeF_2 at θ_i=0°. Thick solid lines show a least squares fit of a two component velocity distribution. The fast component (thin solid lines) at short flight times corresponds to DI scattering and the slow component (thin dashed lines) at long flight times corresponds to TD scattering. Spectra are averaged over successive 6 s low energy XeF_2 exposures corresponding to coverage ranges of (a) 0-0.4 ML F, (b) 0.4-0.7 ML F, (c) 0.7-0.9 ML F, and (d) 0.9-1.1 ML F.

III.C.2. m/e=148

III.C.2.a. High incident energy XeF_2 (E_i=6.3 kcal/mol)

Figure 25(a) shows a TOF distribution of the products at m/e=148 that are scattered as a result of the interaction of XeF_2 at E_i=6.3 kcal/mol with Si(100) at 250 K. The TOF distribution is for a scattering geometry in which the XeF_2 beam is 35° from the surface normal, θ_i=35°, and the detector is positioned along the surface normal, θ_d=0°. The TOF distribution is signal averaged over a 40 s exposure to high energy XeF_2 that corresponds to a fluorine coverage range of 0-1.1 ML. The signal at m/e=148 corresponds to $^{129}XeF^+$ which arises from XeF, the product of single atom abstraction, as well as unreactively scattered XeF_2 that fragments in the ionizer. The characteristic bimodal velocity distribution of XeF_2 is apparent in the TOF distribution. The XeF_2 TOF distribution shown in Figure 15 is multiplied by the XeF_2 cracking ratio and superimposed onto the TOF distribution at m/e=148 in Figure 25(a). Figure 25(b) shows the result of subtracting the XeF_2 contribution from the m/e=148 signal. The narrow fast feature corresponds to XeF scattering from single atom abstraction. The average velocity and energy of the scattered XeF are 620±27 m/s and 7.8±0.7 kcal/mol, respectively.

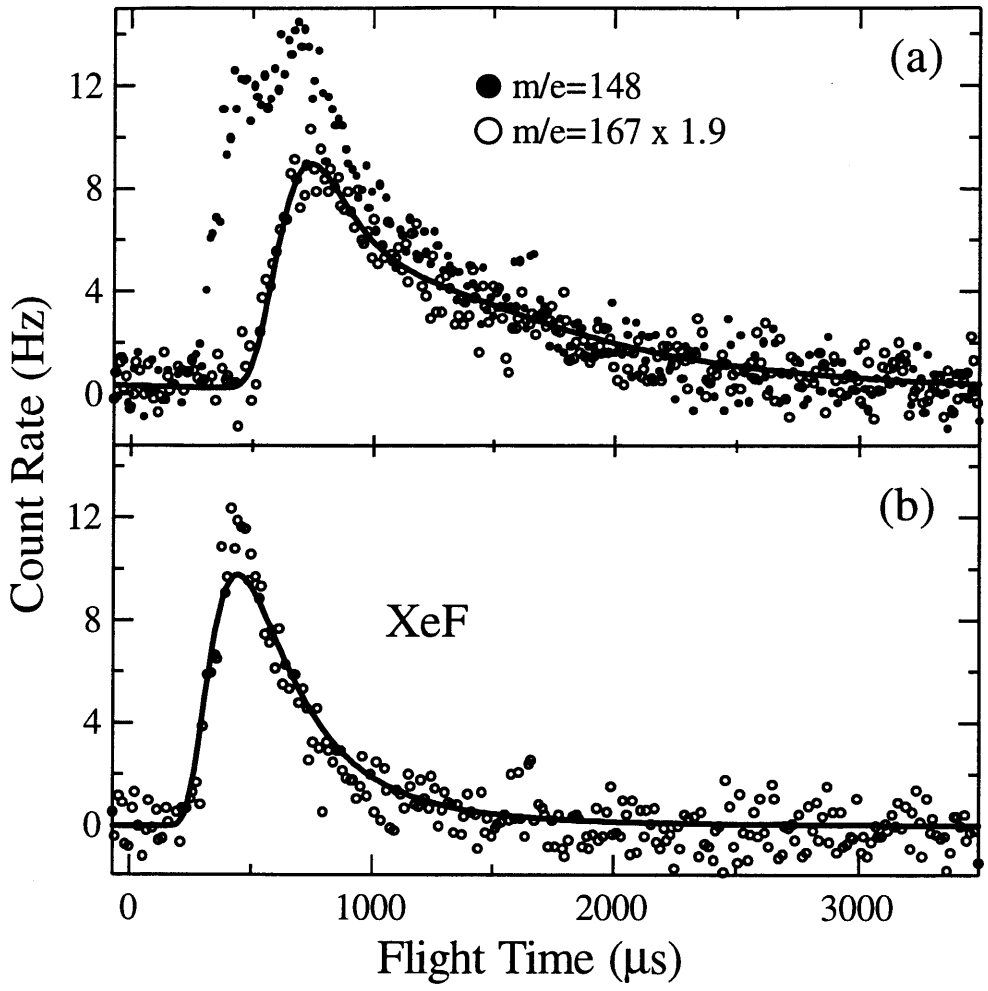

Figure 25 TOF distribution of scattered products at m/e=148
(a) TOF spectra at m/e=167 multiplied by the XeF_2 cracking ratio and at m/e=148 measured at θ_d=0° and T_s=250 K upon exposure to high energy XeF_2 at θ_i=35°. The solid line in (a) shows the fit to the TOF distribution at m/e=167 multiplied by the XeF_2 cracking ratio. (b) Net scattered XeF TOF distribution obtained by point-by-point subtraction of m/e=167 signal multiplied by XeF_2 cracking ratio from m/e=148 signal in (a). The solid line in (b) shows a fit to the data of a single component Maxwell-Boltzmann function F(t) described in Sec. II.D. Spectra are averaged over XeF_2 exposure corresponding to a fluorine coverage range of 0-1.1 ML F. Average velocity of the XeF distribution is v_{XeF}=620±27 m/s.

Analogous to the TOF measurements at m/e=167 presented in Sec. III.C.1, TOF distributions at m/e=148 have been measured at nine detection angles, θ_d, spanning the entire forward scattering region in the scattering plane and signal averaged over four successive 10 s XeF_2 exposure intervals. Figure 26 shows the TOF distributions of the products at m/e=148 scattered into nine detection angles, θ_d, from the interaction of high energy XeF_2 at θ_i=35°. The TOF distribution of the scattered products at m/e=167 are multiplied by the XeF_2 cracking ratio and superimposed for comparison. The TOF distributions are signal averaged over a coverage range of 0-0.4 ML F. The results shown in Figures 28, 30, and 32 are measured under identical conditions to those in Figure 26 except that the TOF distributions are signal averaged over coverage ranges of 0.4-0.7 ML F, 0.7-0.9 ML F, and 0.9-1.1 ML F, respectively.

Like the analysis of the TOF distribution shown in Figure 25, the contribution from XeF_2 is separated from the TOF distributions at m/e=148 by subtracting the TOF distribution at m/e=167 multiplied by the XeF_2 cracking ratio to reveal the TOF distribution of XeF arising from single atom abstraction. Figures 27, 29, 31, and 33 show these TOF distributions of the scattered XeF into the nine detection angles over the coverage ranges of 0-0.4 ML F, 0.4-0.7 ML F, 0.7-0.9 ML F, and 0.9-1.1 ML F, respectively. The most remarkable feature of the TOF distributions of scattered XeF is the strong dependence of the scattered flux on detector angle as well as fluorine coverage. Figure 34 shows the angular distribution of the flux of XeF scattered from Si(100) over the four successive high energy XeF_2 exposures corresponding to increasingly high ranges of fluorine coverage. The flux of scattered XeF is defined as the integral of the velocity-weighted TOF distribution of scattered XeF. Over a coverage range 0-0.7 ML F (Figure 34(a)-(b)), the angular distribution is broad and essentially isotropic. However, at higher

coverages when the system has progressed beyond the initial fluorination stage, the angular distribution becomes increasingly directed along the surface normal. Essentially no XeF is observed at detector angles greater than 50°. The anisotropy of the XeF angular distribution is remarkable given that in the interaction of F_2 with Si(100), the F atom angular distribution arising from single atom abstraction is isotropic and cosinelike over the entire fluorine coverage range (cf. Figure 8 in Chapter 1).

Although the average translational energy of the scattered XeF is independent of detector angle over most of the angular distribution, the translational energy of the scattered XeF is strongly dependent on the fluorine coverage. Figure 35 is a plot of the average translational energy of the scattered XeF as a function of detector angle over the four different coverage ranges due to exposure to high energy XeF_2. Values are not shown for the average translational energy at detector angles $\theta_d>50°$ for coverages greater than 0.7 ML F because of the extremely low signal intensity of the scattered XeF. The translational energy of the scattered XeF is reasonably insensitive to detector angle, but there is a noticeable shift to lower energy with coverage. Figure 36 is a plot of the average translational energy of the scattered XeF averaged over the nine detection angles spanning the entire forward scattering region in the scattering plane. The translational energy of the scattered XeF decreases substantially with coverage during the initial fluorination from a maximum around 10 kcal/mol at low fluorine coverage, leveling off around 6 kcal/mol at a coverage of about 1 ML F. The strong coverage dependence of the translational energy of the reactively scattered products is in stark contrast to the translational energy of the scattered F atoms in the interaction of F_2 with Si which is independent of coverage.

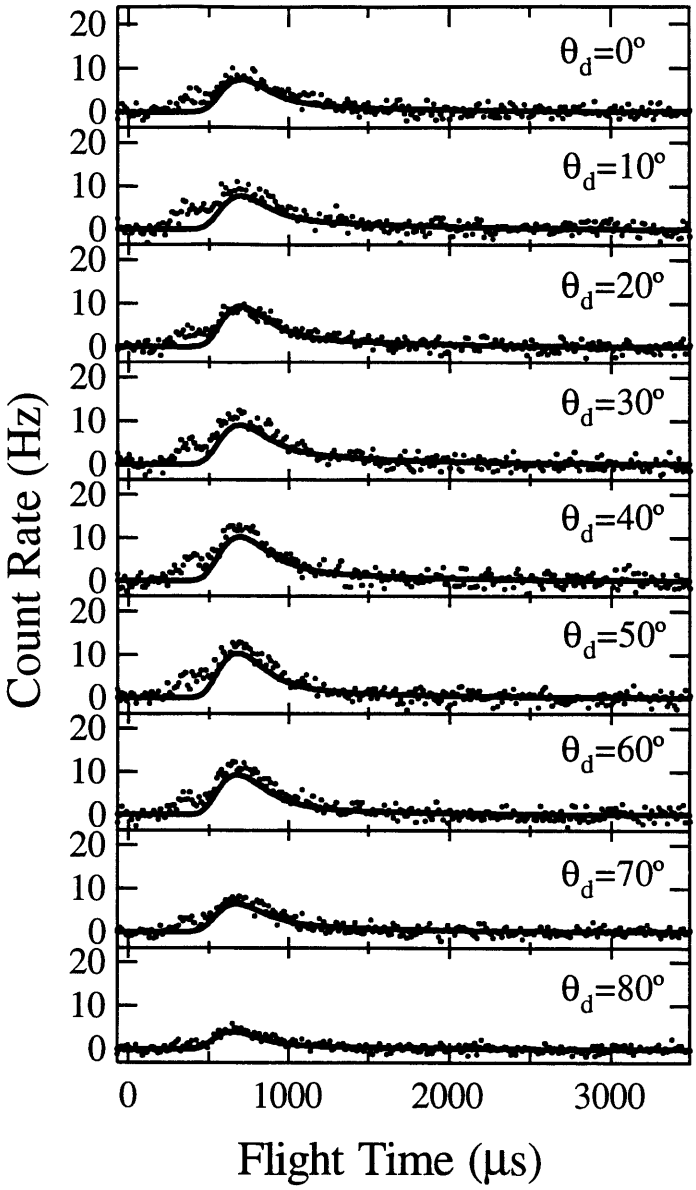

Figure 26 TOF distribution of scattered products at m/e=148 as a function of detector angle over a coverage range of 0-0.4 ML F

TOF spectra at m/e=148 measured at nine detector angles θ_d and T_s=250 K upon exposure to high energy XeF_2 at θ_i=35°. The solid lines show the fits to the TOF distributions at m/e=167 multiplied by the XeF_2 cracking ratio (fits to data in Figure 17) and represents the contribution from unreactively scattered XeF_2 to the m/e=148 signal. Spectra are averaged over a 10 s high energy XeF_2 exposure corresponding to a fluorine coverage range of 0-0.4 ML F.

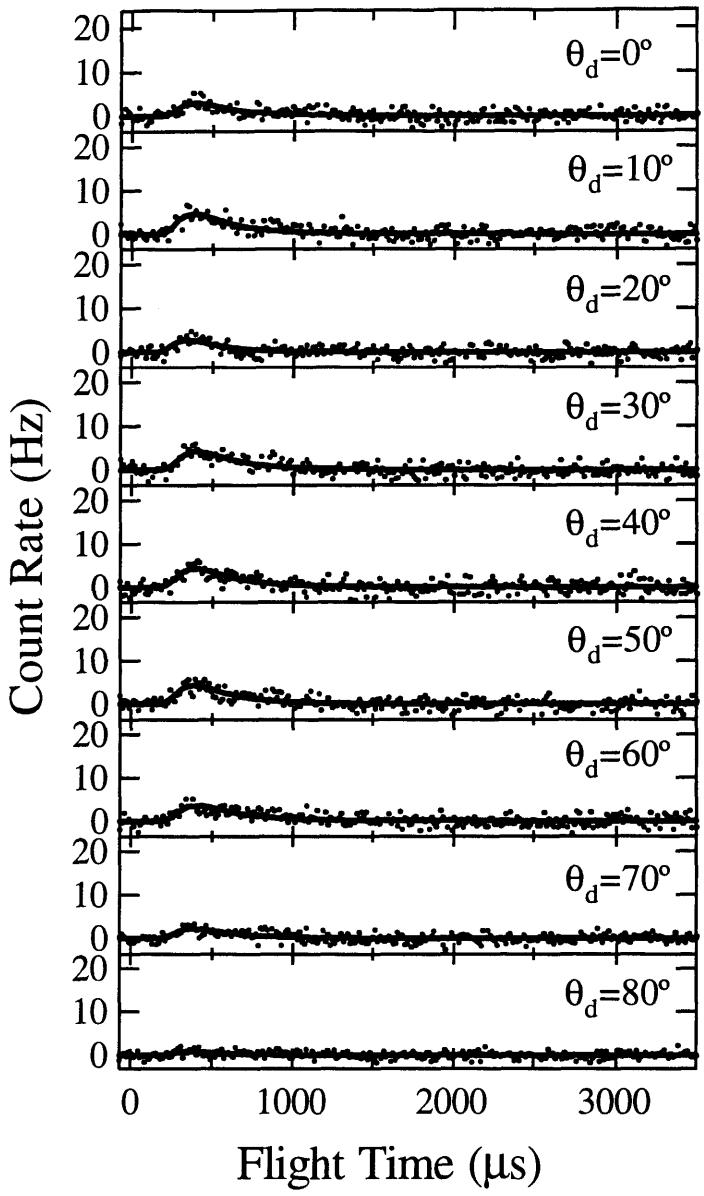

Figure 27 TOF distribution of scattered XeF as a function of detector angle over a coverage range of 0-0.4 ML F

TOF spectra of scattered XeF measured at nine detector angles θ_d and T_s=250 K upon exposure to high energy XeF_2 at θ_i=35°. Net scattered XeF TOF distribution obtained by point-by-point subtraction of m/e=167 signal in Figure 17 multiplied by XeF_2 cracking ratio from m/e=148 signal in Figure 26. The solid lines show the fits to the data of a single component Maxwell-Boltzmann function F(t) described in Sec. II.D. Spectra are averaged over XeF_2 exposure corresponding to a fluorine coverage range of 0-0.4 ML F.

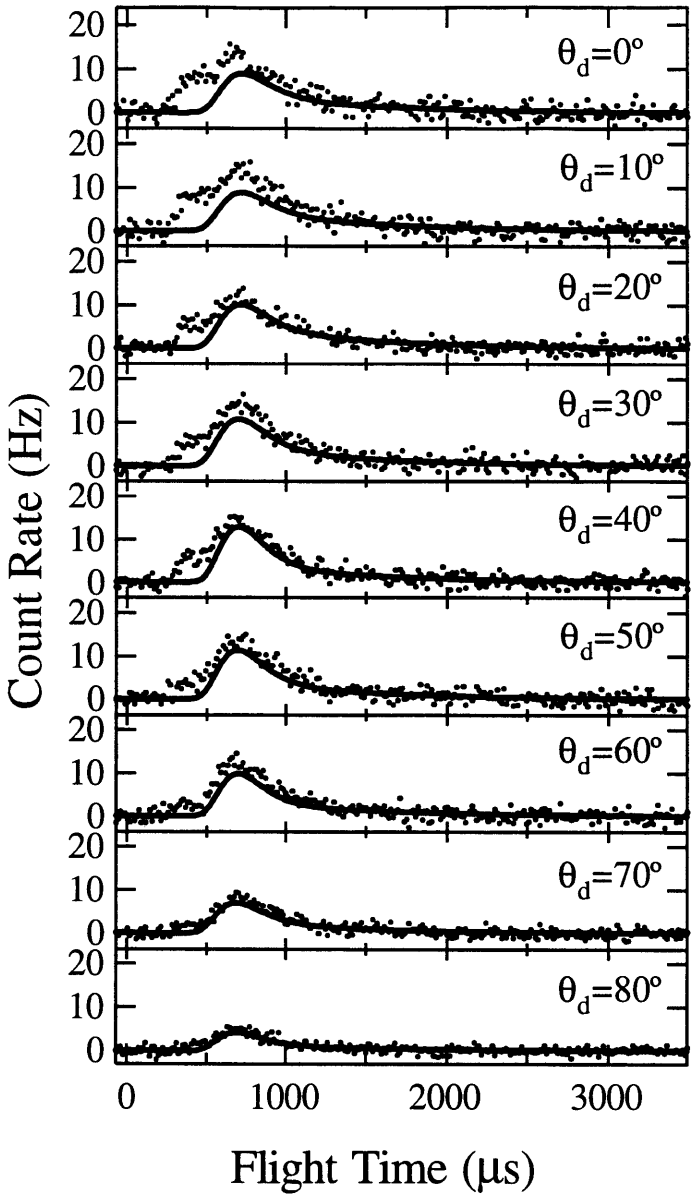

Figure 28 TOF distribution of scattered products at m/e=148 as a function of detector angle over a coverage range of 0.4-0.7 ML F

TOF spectra at m/e=148 measured at nine detector angles θ_d and T_s=250 K upon exposure to high energy XeF_2 at θ_i=35°. The solid lines show the fits to the TOF distributions at m/e=167 multiplied by the XeF_2 cracking ratio (fits to data in Figure 18) and represents the contribution from unreactively scattered XeF_2 to the m/e=148 signal. Spectra are averaged over a 10 s high energy XeF_2 exposure corresponding to a fluorine coverage range of 0.4-0.7 ML F.

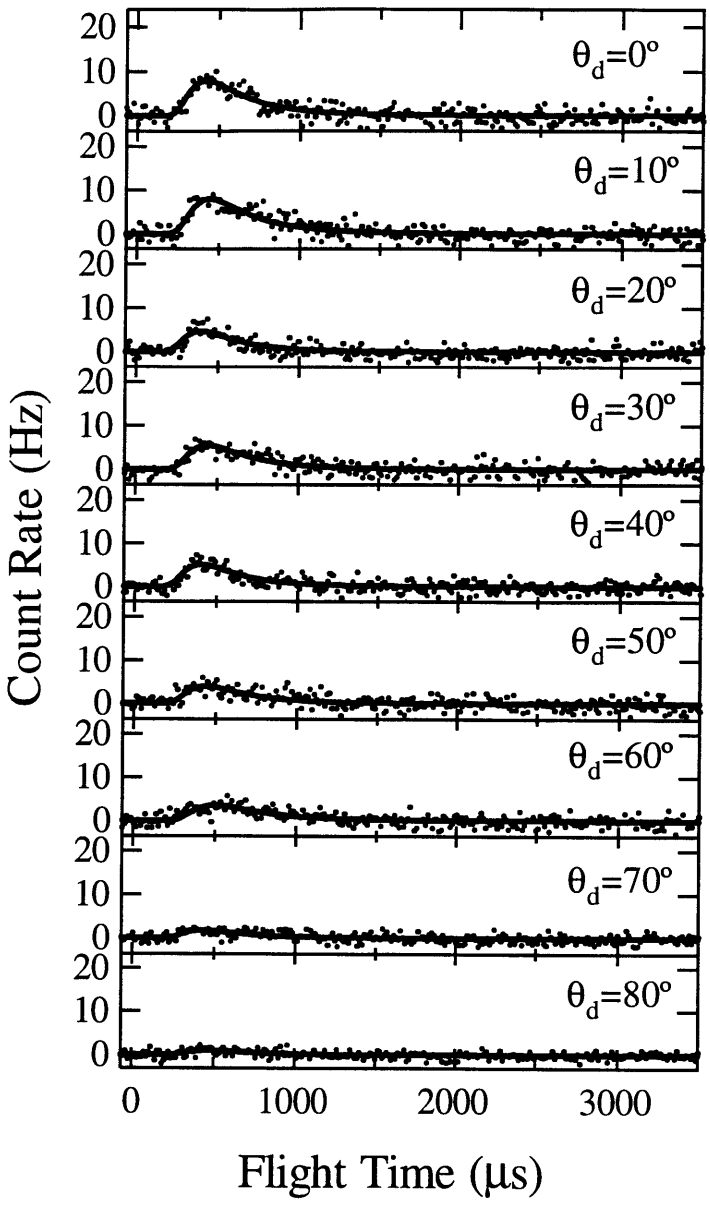

Figure 29 TOF distribution of scattered XeF as a function of detector angle over a coverage range of 0.4-0.7 ML F

TOF spectra of scattered XeF measured at nine detector angles θ_d and T_s=250 K upon exposure to high energy XeF_2 at θ_i=35°. Net scattered XeF TOF distribution obtained by point-by-point subtraction of m/e=167 signal in Figure 18 multiplied by XeF_2 cracking ratio from m/e=148 signal in Figure 28. The solid lines show the fits to the data of a single component Maxwell-Boltzmann function F(t) described in Sec. II.D. Spectra are averaged over XeF_2 exposure corresponding to a fluorine coverage range of 0.4-0.7 ML F.

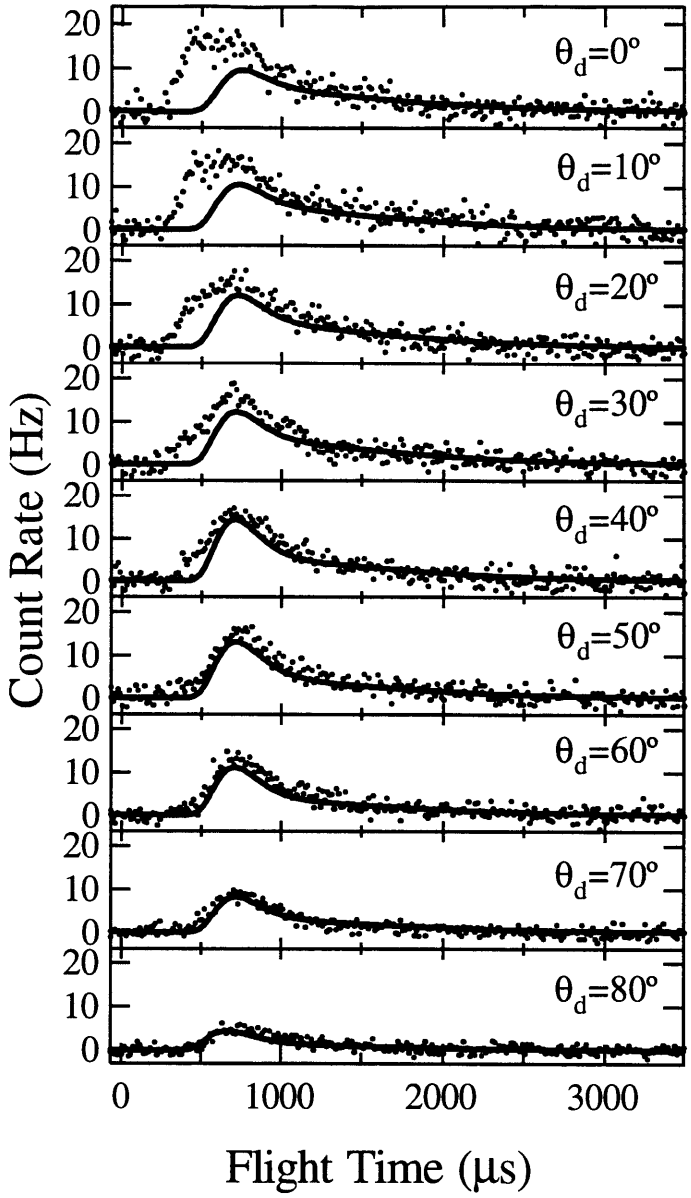

Figure 30 TOF distribution of scattered products at m/e=148 as a function of detector angle over a coverage range of 0.7-0.9 ML F

TOF spectra at m/e=148 measured at nine detector angles θ_d and T_s=250 K upon exposure to high energy XeF_2 at θ_i=35°. The solid lines show the fits to the TOF distributions at m/e=167 multiplied by the XeF_2 cracking ratio (fits to data in Figure 19) and represents the contribution from unreactively scattered XeF_2 to the m/e=148 signal. Spectra are averaged over a 10 s high energy XeF_2 exposure corresponding to a fluorine coverage range of 0.7-0.9 ML F.

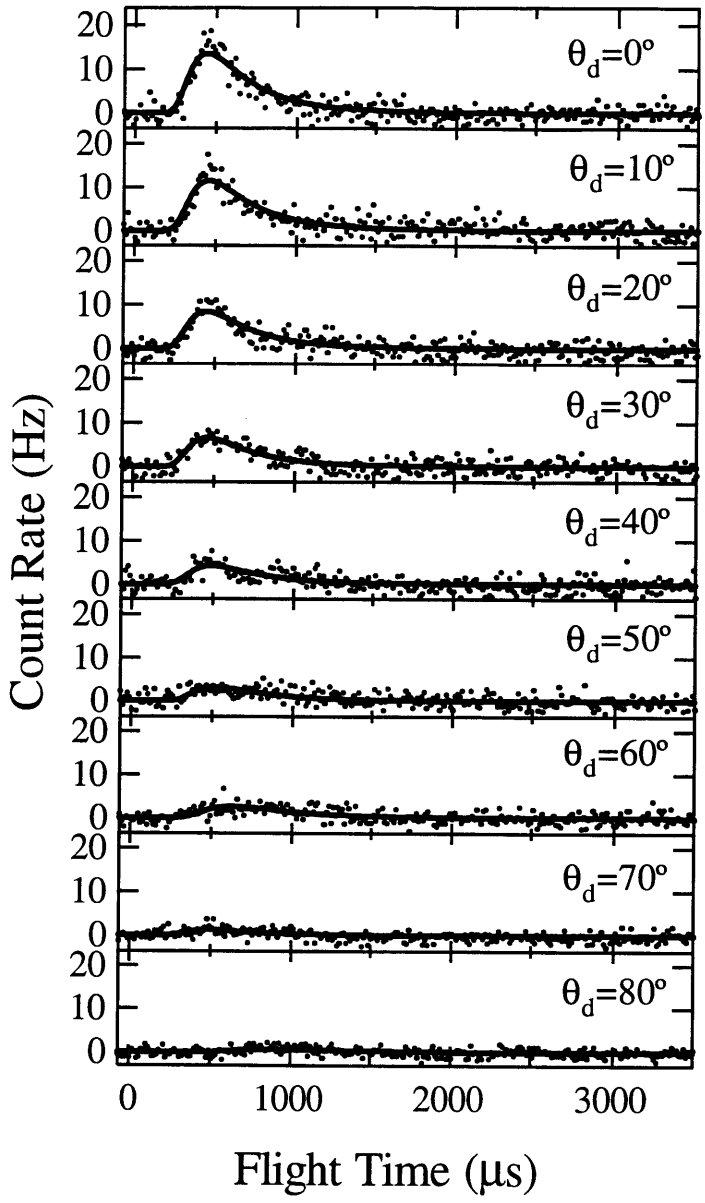

Figure 31 TOF distribution of scattered XeF as a function of detector angle over a coverage range of 0.7-0.9 ML F

TOF spectra of scattered XeF measured at nine detector angles θ_d and T_s=250 K upon exposure to high energy XeF_2 at θ_i=35°. Net scattered XeF TOF distribution obtained by point-by-point subtraction of m/e=167 signal in Figure 19 multiplied by XeF_2 cracking ratio from m/e=148 signal in Figure 30. The solid lines show the fits to the data of a single component Maxwell-Boltzmann function F(t) described in Sec. II.D. Spectra are averaged over XeF_2 exposure corresponding to a fluorine coverage range of 0.7-0.9 ML F.

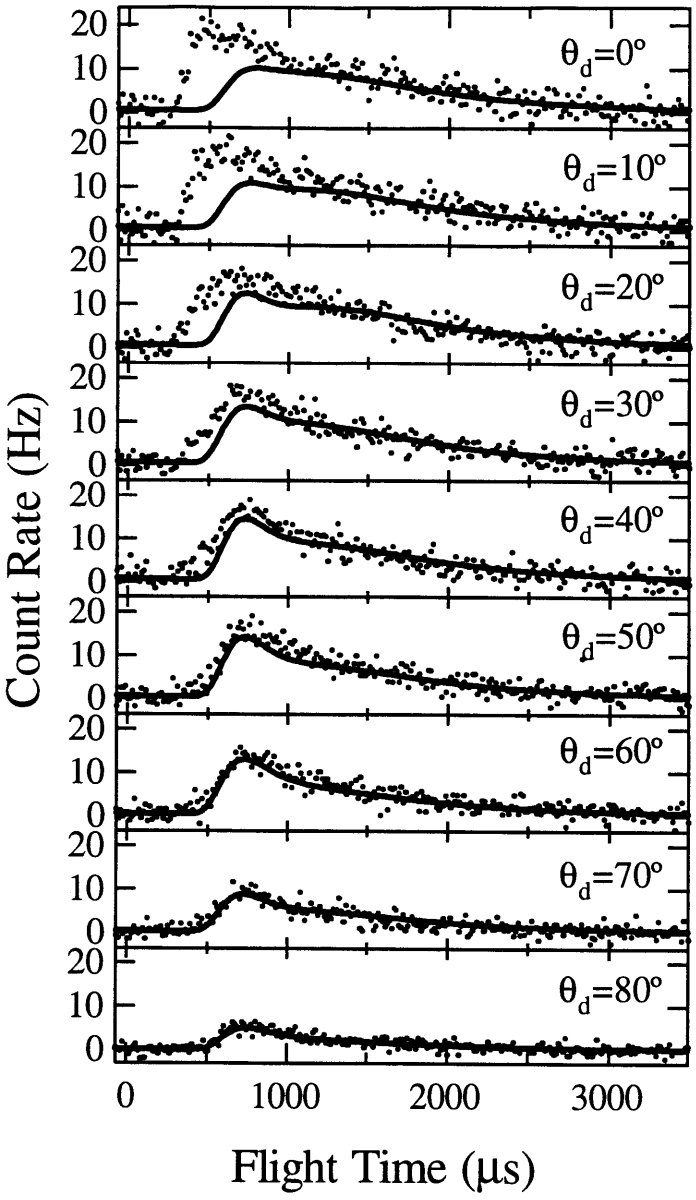

Figure 32 TOF distribution of scattered products at m/e=148 as a function of detector angle over a coverage range of 0.9-1.1 ML F

TOF spectra at m/e=148 measured at nine detector angles θ_d and T_s=250 K upon exposure to high energy XeF_2 at θ_i=35°. The solid lines show the fits to the TOF distributions at m/e=167 multiplied by the XeF_2 cracking ratio (fits to data in Figure 20) and represents the contribution from unreactively scattered XeF_2 to the m/e=148 signal. Spectra are averaged over a 10 s high energy XeF_2 exposure corresponding to a fluorine coverage range of 0.9-1.1 ML F.

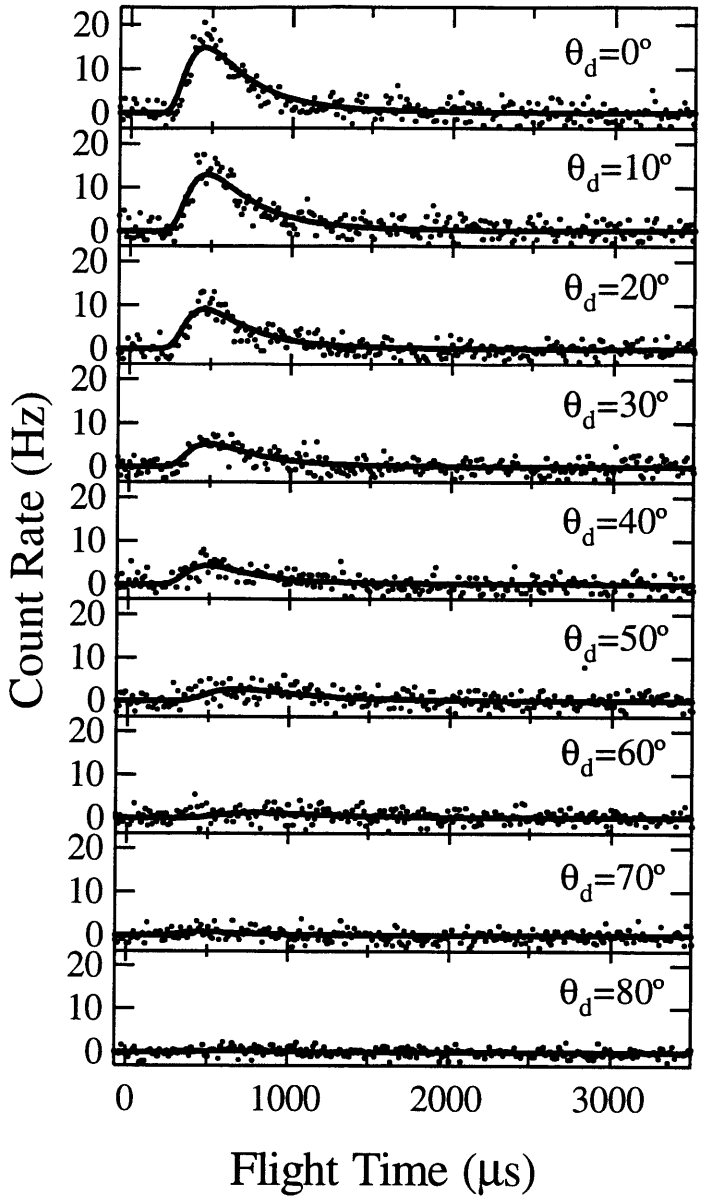

Figure 33 TOF distribution of scattered XeF as a function of detector angle over a coverage range of 0.9-1.1 ML F

TOF spectra of scattered XeF measured at nine detector angles θ_d and T_s=250 K upon exposure to high energy XeF_2 at θ_i=35°. Net scattered XeF TOF distribution obtained by point-by-point subtraction of m/e=167 signal in Figure 20 multiplied by XeF_2 cracking ratio from m/e=148 signal in Figure 32. The solid lines show the fits to the data of a single component Maxwell-Boltzmann function F(t) described in Sec. II.D. Spectra are averaged over XeF_2 exposure corresponding to a fluorine coverage range of 0.9-1.1 ML F.

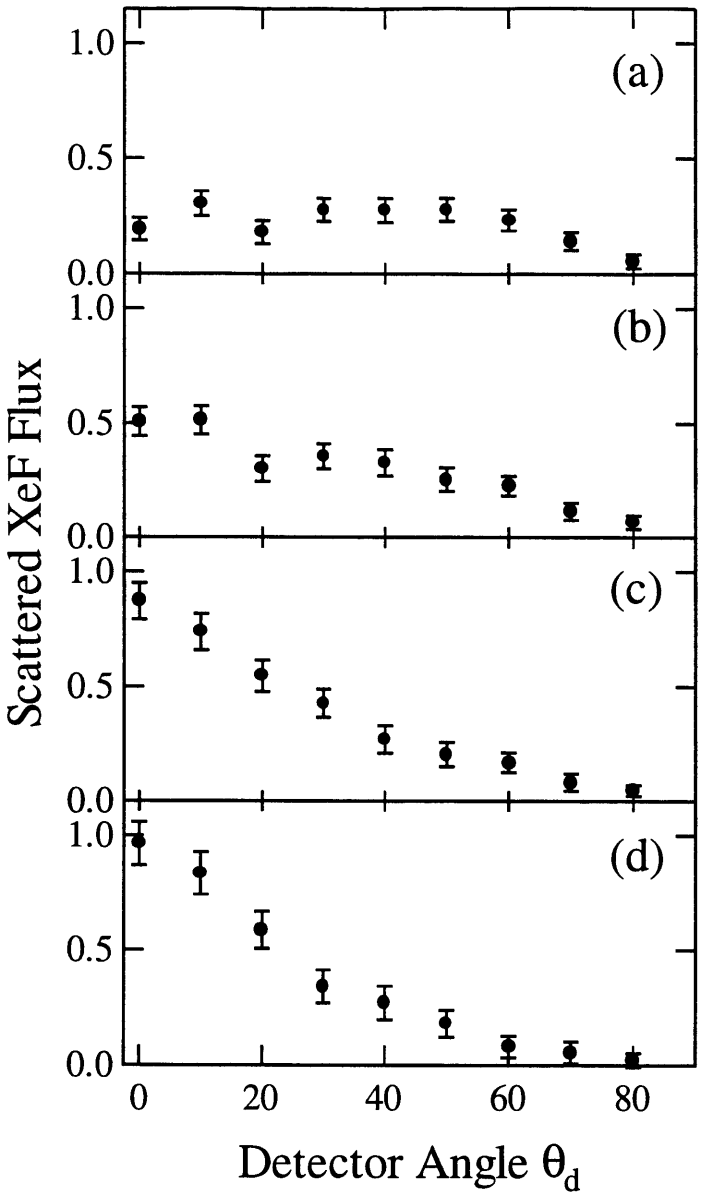

Figure 34 Angular distribution of flux of XeF scattered from Si(100)
Flux of scattered XeF as a function of detector angle determined by integration of velocity-weighted TOF distributions of scattered XeF shown in Figures 27, 29, 31, 33 over a sequence of 10 s exposures to high energy XeF_2 which corresponds to coverage ranges of (a) 0-0.4 ML F, (b) 0.4-0.7 ML F, (c) 0.7-0.9 ML F, and (d) 0.9-1.1 ML F. Error bars represent the uncertainty of integral of the velocity-weighted fit to the TOF distributions (Sec. II.D).

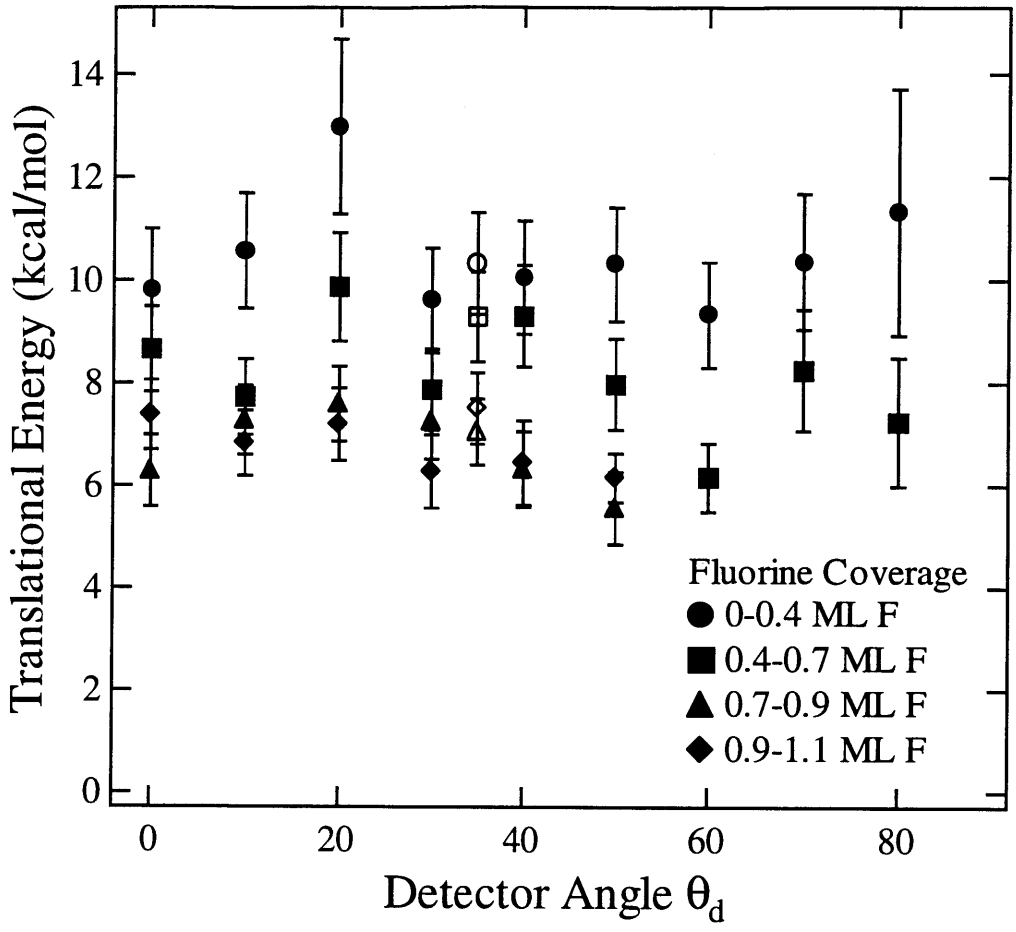

Figure 35 Translational energy of XeF scattered from Si(100) as a function of detector angle

Average translational energy of scattered XeF as a result of exposure to high energy XeF_2 (solid symbols) and low energy XeF_2 (hollow symbols) as a function of detector angle over four different fluorine coverage ranges. The average translational energy is determined from the velocity-weighted TOF distributions shown in Figures 27, 29, 31, and 33. Error bars represent the uncertainty of the determination of the average translational energy (Sec. II.D) from the fits to the TOF distributions in Figures 27, 29, 31, 33. The translational energy of the scattered XeF into detector angles θ_d>50° at coverages greater than 0.7 ML F are not shown because the uncertainty of these values resulting from extremely low signal intensity.

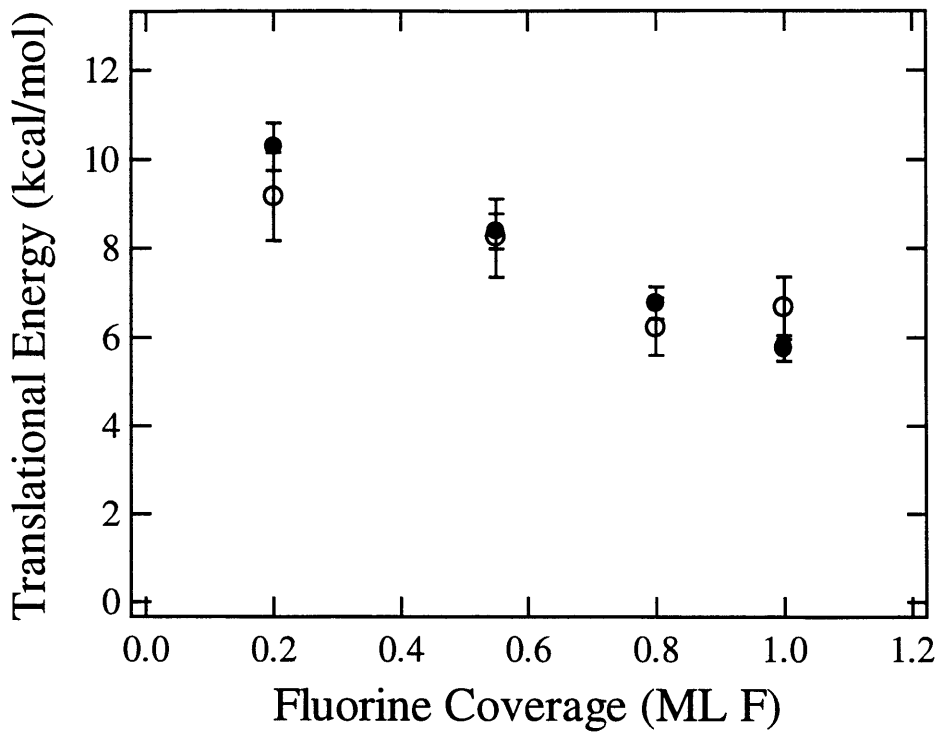

Figure 36 Coverage dependence of translational energy of scattered XeF
The average translational energy of the fast feature in the TOF distribution of scattered XeF. The solid circles correspond to high energy XeF_2; the hollow circles correspond to low energy XeF_2. Error bars for high energy XeF_2 represent the standard deviation of the average of measurements at nine detection angles spanning the entire forward scattering region in the scattering plane. Error bars for low energy XeF_2 represent the uncertainty of the determination of the average translational energy from the fits to the TOF distributions in Figure 39.

III.C.2.b. Low incident energy XeF_2 (E_i=1.8 kcal/mol)

Figure 37(a) shows a TOF distribution of the products at m/e=148 that are scattered from the interaction of low energy XeF_2 from Si(100) at 250 K. The TOF distribution is for a scattering geometry in which the incident XeF_2 is at θ_i=0° and the detector is positioned at θ_d=35°. The TOF distribution is signal averaged over an exposure to low energy XeF_2 that corresponds to a fluorine coverage range of 0-1.2 ML. The TOF distribution of the products at m/e=167, which corresponds to unreactively scattered XeF_2, is multiplied by the XeF_2 cracking ratio and superimposed onto the TOF distribution at m/e=148 in Figure 37(a). Figure 37(b) shows the result of subtracting the XeF_2 contribution from the m/e=148 signal. The single fast feature corresponds to XeF scattering from single atom abstraction. The average velocity and energy of the XeF are 639±28 m/s and 7.4±0.6 kcal/mol, respectively. Recall that the average velocity and energy of the XeF arising from single atom abstraction from high energy XeF_2 are 620±27 m/s and 7.8±0.7 kcal/mol, respectively. Thus, the velocity distribution of XeF arising from single atom abstraction is reasonably insensitive to incident energy over the range 1.8-6.3 kcal/mol.

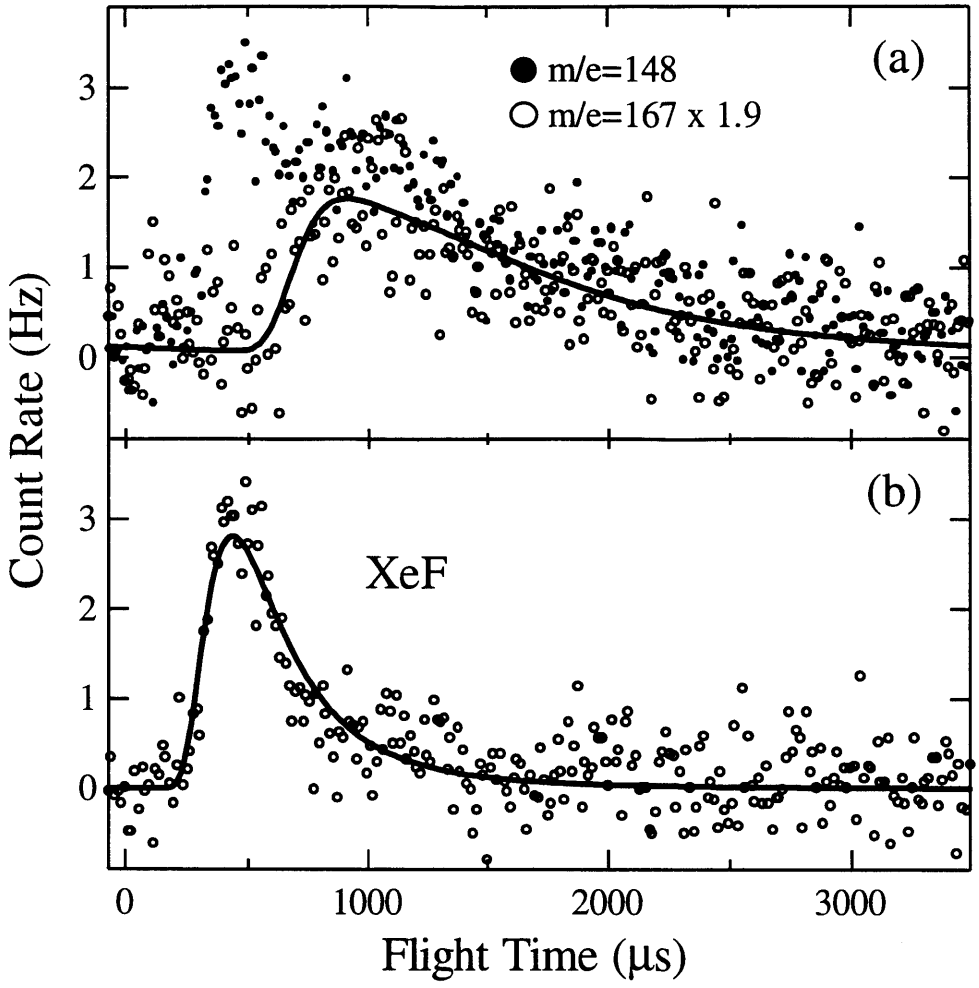

Figure 37 TOF distribution of scattered products at m/e=148 with low energy XeF_2
(a) TOF spectra at m/e=167 multiplied by the XeF_2 cracking ratio and at m/e=148 measured at θ_d=35° and T_s=250 K upon exposure to low energy XeF_2 at θ_i=0°. The solid line in (a) shows the fit to the TOF distribution at m/e=167 multiplied by the XeF_2 cracking ratio. (b) Net scattered XeF TOF distribution obtained by point-by-point subtraction of m/e=167 signal multiplied by XeF_2 cracking ratio from m/e=148 signal in (a). The solid line in (b) shows the fit to the data of a single component Maxwell-Boltzmann function F(t) described in Sec. II.D. Spectra are averaged over XeF_2 exposure corresponding to a fluorine coverage range of 0-1.1 ML F. Average velocity of the XeF distribution is v_{XeF}=639±28 m/s.

The TOF distribution in Figure 37 is signal averaged over a 24 s exposure to low energy XeF_2. To test the exposure dependence of the scattered XeF, TOF distributions have been signal averaged over shorter exposures to low energy XeF_2. Figure 38 shows the TOF distributions at m/e=148 signal averaged over four successive 6 s exposures to low energy XeF_2. The TOF distributions of the scattered products at m/e=167 are multiplied by the XeF_2 cracking ratio and superimposed to show the contribution from unreactively scattered XeF_2. Figure 39 shows the TOF distributions of scattered XeF arising from single atom abstraction, which are determined by subtracting the TOF distributions at m/e=167 multiplied by the XeF_2 cracking ratio.

Two features of the low energy XeF_2 exposure dependence of the TOF distribution of scattered XeF shown in Figure 39 are reminiscent of that of the high energy XeF_2 exposure. First, at a detector angle of θ_d=35°, the flux of scattered XeF increases slightly, attains a maximum, and decays slightly over the coverage range 0-1.1 ML F. Second, not only are the shapes of the TOF distribution of scattered XeF arising from exposure to low energy XeF_2 similar to that upon exposure to high energy XeF_2, but the average translational energy of XeF scattered from the interaction of low energy XeF_2 with Si also similarly decreases as a function of fluorine coverage. The average translational energy is superimposed for comparison in Figure 36.

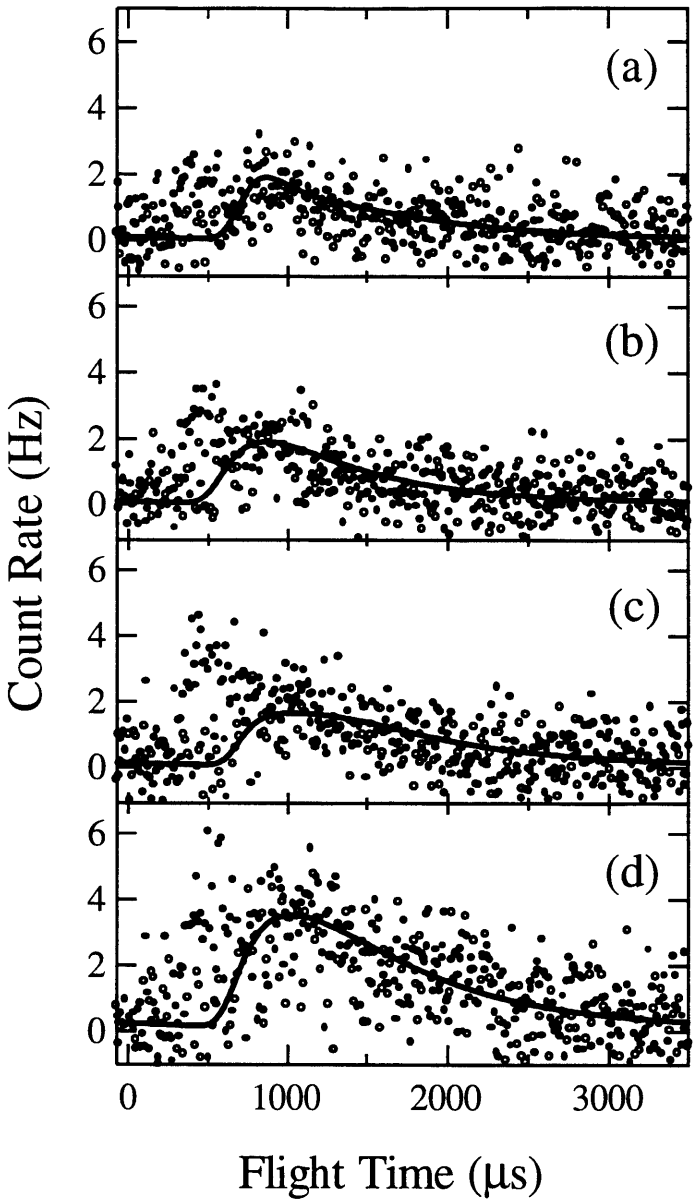

Figure 38 TOF distribution of scattered products at m/e=148 upon exposure to low energy XeF_2 as a function of coverage

TOF spectra at m/e=167 multiplied by the XeF_2 cracking ratio and at m/e=148 measured at at θ_d=35° and T_s=250 K upon exposure to low energy XeF_2 at θ_i=0°. Thick solid line shows a fit to the TOF distribution at m/e=167 multiplied by the XeF_2 cracking ratio. Spectra are averaged over successive 6 s low energy XeF_2 exposures corresponding to coverage ranges of (a) 0-0.4 ML F, (b) 0.4-0.7 ML F, (c) 0.7-0.9 ML F, and (d) 0.9-1.1 ML F.

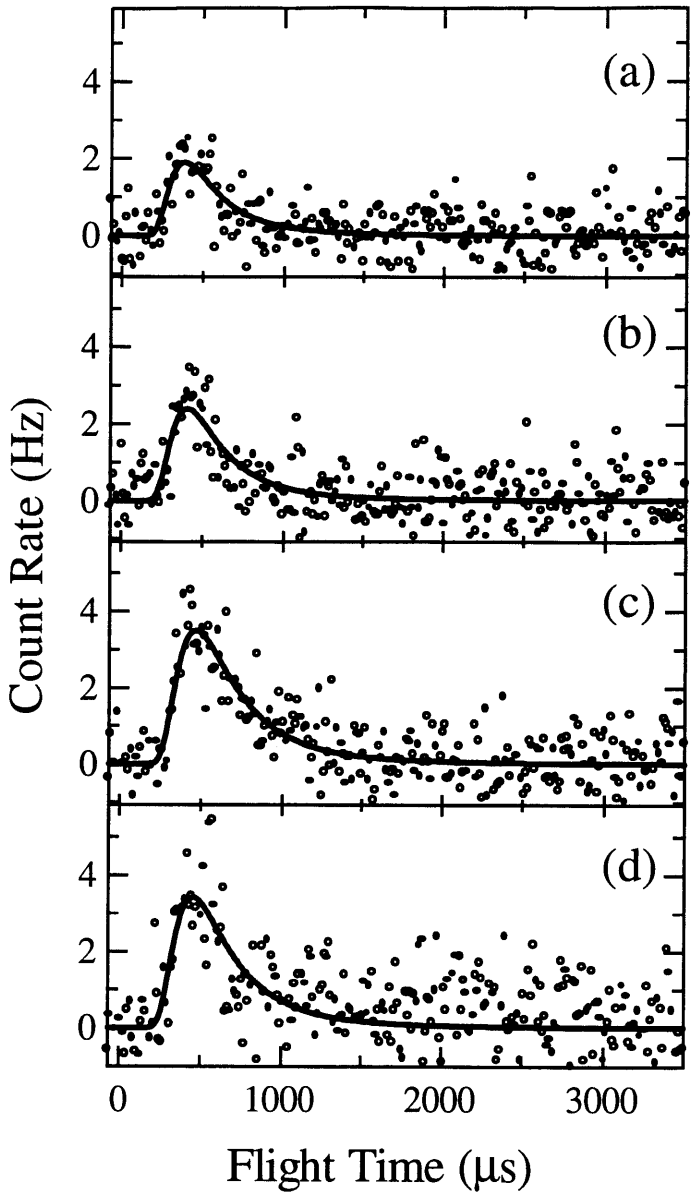

Figure 39 TOF distribution of scattered XeF upon exposure to low energy XeF_2 as a function of coverage

TOF spectra of scattered XeF measured at θ_d=35° and T_s=250 K upon exposure to low energy XeF_2 at θ_i=0°. Net scattered XeF TOF distributions obtained by point-by-point subtraction of m/e=167 signal multiplied by XeF_2 cracking ratio from m/e=148 signal in Figure 38. The solid lines show the fits to the data of a single component Maxwell-Boltzmann function F(t) described in Sec. II.D. Spectra are averaged over successive 6 s low energy XeF_2 exposures corresponding to coverage ranges of (a) 0-0.4 ML F, (b) 0.4-0.7 ML F, (c) 0.7-0.9 ML F, and (d) 0.9-1.1 ML F.

III.C.3. m/e=19

III.C.3.a. High incident energy XeF_2 (E_i=6.3 kcal/mol)

It is likely that the XeF produced as a result of single atom abstraction will dissociate if just a small fraction of the tremendous exothermicity of the reaction (90 kcal/mol) is channeled into the internal energy of the weakly bound XeF (3 kcal/mol). However, the presence of signal at m/e=148 that is attributable to scattered XeF shows that some of the XeF that is produced from the interaction of XeF_2 with Si does escape into the gas phase intact. To test the possibility that some of the XeF does indeed dissociate, the TOF distribution of scattered products at m/e=19 are measured. Figure 40(a) shows a TOF distribution of the products at m/e=19 that are scattered from the interaction of XeF_2 at E_i=6.3 kcal/mol with Si(100) at 250 K. The TOF distribution is for a scattering geometry in which the XeF_2 beam is 35° from the surface normal, θ_i=35°, and the detector is positioned along the surface normal, θ_d=0°. The TOF distribution is signal averaged over an exposure to high energy XeF_2 that corresponds to a fluorine coverage range of 0-1.1 ML. The signal at m/e=19 corresponds to F^+ which arises from F atoms, as well as from XeF_2 and XeF that fragment in the ionizer. In addition, there is a contribution from $^{38}Ar^{2+}$ which arises from the Ar carrier gas.

The TOF distribution of the scattered products at m/e=19 is distinctly bimodal. The slower feature is comprised of several contributions and matches well with the TOF distributions of scattered XeF, XeF_2, and Ar. The XeF_2 cracking ratio ($\sigma_{XeF_2 \rightarrow F^+} / \sigma_{XeF_2 \rightarrow XeF_2^+}$) is 0.333 as determined from a mass spectrum of the incident XeF_2 beam. The XeF_2 TOF distribution is multiplied by this cracking ratio and superimposed onto Figure 40(a). To separate the contribution from $^{38}Ar^{2+}$, TOF distributions of unreactively scattered Ar carrier gas at m/e=40

have been measured, but are not shown here. The contribution of scattered Ar to the signal at m/e=19 is determined by multiplying the TOF distribution at m/e=40 by the ratio of the abundance of the two isotopes (0.00063) [62] and the ratio of the cross sections for single ionization and double ionization of Ar at 70 eV electron energy (0.55) [63]. The Ar TOF distribution is multiplied by this scaling factor and superimposed onto Figure 40(a). The XeF cracking ratio is unknown. However, the exact cracking ratio is not essential because the myriad contributions to the slow feature do not significantly affect the velocity distribution of the very fast feature. In addition, the slow feature is not a source of unique information since the TOF distributions of all of the contributions to the slow feature have been measured elsewhere. Without further justification, a value of 0.25 is chosen for the XeF cracking ratio because it yields a similar physically reasonable contribution to the signal at m/e=19 at all detector angles and coverage ranges as well as upon exposure to both high and low energy XeF_2. The fit to the XeF TOF distribution is multiplied by this arbitrary cracking ratio and superimposed onto Figure 40(a). Figure 40(b) shows the result of subtracting these three contributions from the m/e=19 signal. Because the contributions from all of the scattered products that crack in the ionization region and are detected at m/e=19 have been removed from the TOF distribution, the narrow very fast feature must arise from scattered F atoms. The average velocity and energy of the F atoms is 1551±68 m/s and 6.2±0.5 kcal/mol, respectively, where the major contribution to the uncertainties is the length of the flight path due to the finite length of the ionization region. This average energy is significantly higher than that of the F atoms arising from single atom abstraction in the interaction of F_2 with Si(100) which have an average energy of 3.7±0.4 kcal/mol. The F atoms must arise from the dissociation of XeF prior to ionization.

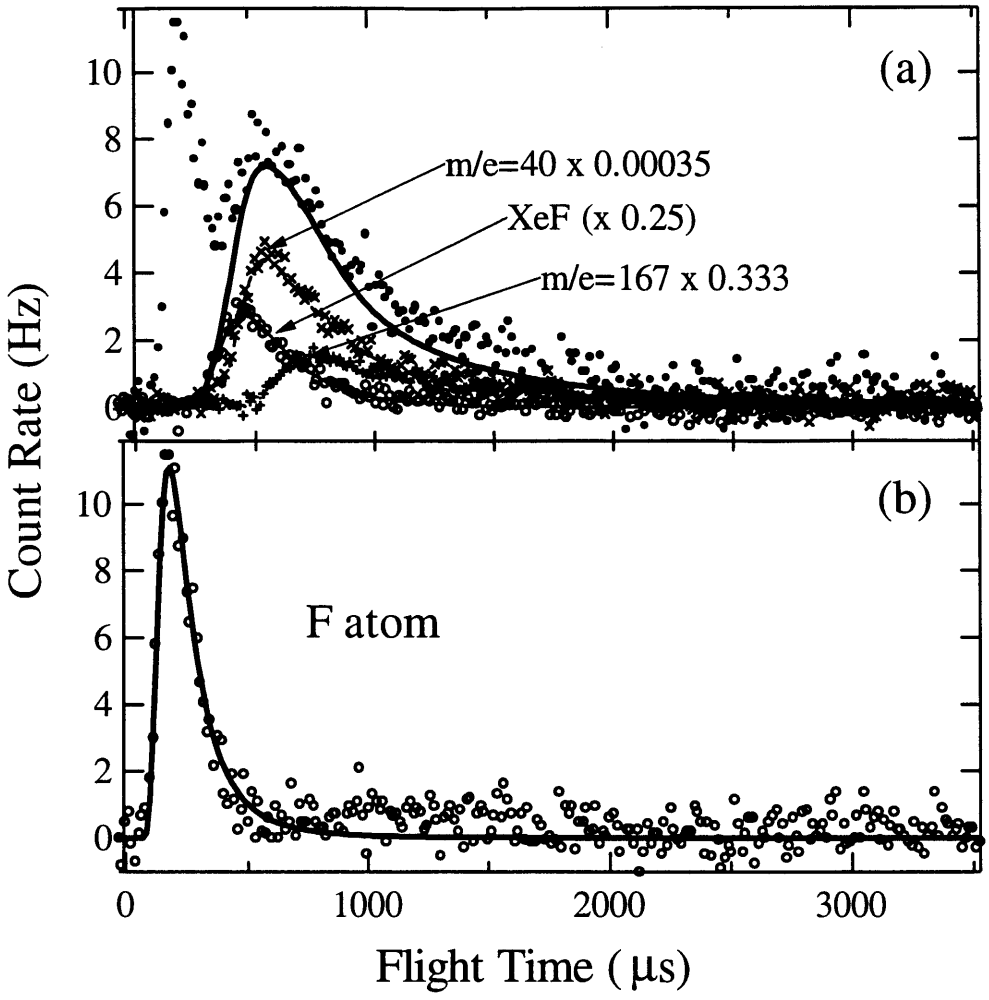

Figure 40 TOF distribution of scattered products at m/e=19
(a) TOF spectra at m/e=19 measured at θ_d=0° and T_s=250 K upon exposure to high energy XeF_2 at θ_i=35°. Signal at m/e=167 multiplied by XeF_2 cracking ratio, signal at m/e=40 multiplied by scaling factor of 0.00035 to account for isotopic abundance and ionization cross section, and XeF signal multiplied by optimal scaling factor of 0.25 are superimposed for comparison. (b) Net scattered F atom TOF distribution obtained by point-by-point subtraction of contributions from XeF_2, Ar, and XeF from m/e=19 signal in (a). Spectra are averaged over XeF_2 exposure corresponding to a fluorine coverage range of 0-1.1 ML F. Average velocity of the XeF distribution is v_{XeF}=1550±68 m/s.

Analogous to the TOF measurements at m/e=167 and m/e=148, TOF distributions at m/e=19 have been measured at several detection angles, θ_d, spanning the entire forward scattering region in the scattering plane and signal averaged over four successive 10 s XeF_2 exposure intervals. Figure 41 shows the TOF distributions of the products at m/e=19 scattered into nine detection angles, θ_d, from the interaction of high energy XeF_2 at θ_i=35°. The fits to the TOF distribution of the scattered XeF_2, Ar, and XeF are multiplied by the appropriate cracking ratio or scaling factor and superimposed for comparison. The TOF distributions are signal averaged over a coverage range of 0-0.4 ML F. The results shown in Figures 43, 45, and 47 are taken under identical conditions to those in Figure 41 except that the TOF distributions are signal averaged over coverage ranges of 0.4-0.7 ML F, 0.7-0.9 ML F, and 0.9-1.1 ML F, respectively. Analogous to the analysis of the TOF distribution shown in Figure 40, the contributions from XeF_2, XeF, and Ar are separated from the TOF distributions at m/e=19 by subtracting the respective TOF distributions multiplied by the appropriate cracking ratio or scaling factor to reveal the TOF distribution of F. Figures 42, 44, 46, and 48 show the TOF distributions of the scattered F atoms into the nine detection angles over the coverage ranges of 0-0.4 ML F, 0.4-0.7 ML F, 0.7-0.9 ML F, and 0.9-1.1 ML F, respectively. Despite the narrow angular distribution of scattered XeF, which is the source of these very fast F atoms, the angular distribution of the scattered F atoms is broad. Figure 49 shows the angular distribution of the flux of F atoms scattered from Si(100) over the four successive high energy XeF_2 exposures corresponding to increasingly higher ranges of fluorine coverage. The flux of scattered F atoms is defined as the integral of the velocity-weighted TOF distribution of scattered F atoms. Indeed, the angular distribution of the scattered F atom flux is isotropic and cosinelike over the entire fluorine

coverage range of 0-1.1 ML. The magnitude of the F atom flux increases with coverage to a maximum around 1 ML and decreases with further XeF_2 exposure. The increase is analogous to the increase in the XeF flux at detector angles near the surface normal, but the magnitude of the increase is only slight unlike the dramatic increase in the XeF flux. These apparent contradictions will be reconciled in the discussion of single atom abstraction and XeF dissociation in Sec. IV.B and IV.C.

The translational energy of the scattered F atom flux is reasonably insensitive to fluorine coverage and detector angle. Figure 50 shows a plot of the angular distribution of the average translational energy of the scattered F atom for the four coverage ranges. The average translational energy averaged over all detector angles and coverage ranges is 6.7±0.1 kcal/mol, where the uncertainty represents the standard deviation of the average of all of the measurements.

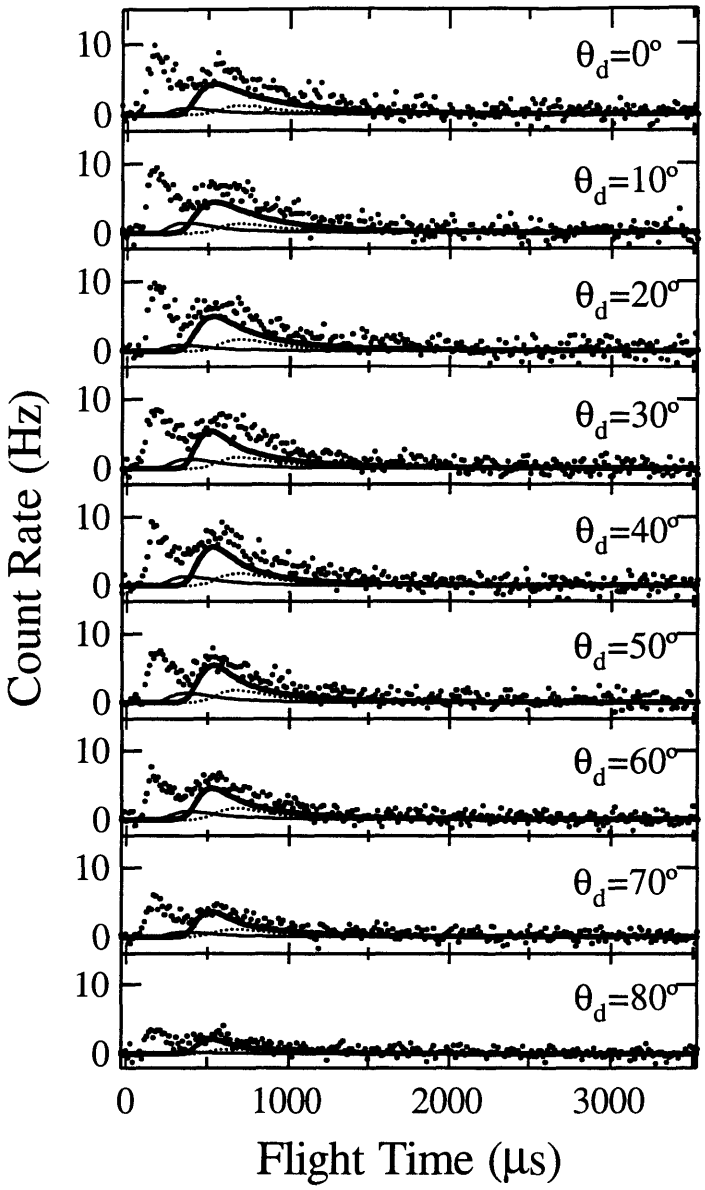

Figure 41 TOF distribution of scattered products at m/e=19 as a function of detector angle over a coverage range of 0-0.4 ML F

TOF spectra at m/e=19 measured at nine detector angles θ_d and T_s=250 K upon exposure to high energy XeF_2 at θ_i=35°. The thin dashed lines show the fits to the TOF distributions at m/e=167 multiplied by the XeF_2 cracking ratio (fits to data in Figure 17). The thin solid lines show the fits to the TOF distributions of scattered XeF multiplied by a scaling factor of 0.25 (fits to data in Figure 27). Thick solid lines show the fits to the TOF distributions at m/e=40 (data not shown) multiplied by the scaling factor of 0.00035 (see text). Spectra are averaged over a 10 s high energy XeF_2 exposure corresponding to a fluorine coverage range of 0-0.4 ML F.

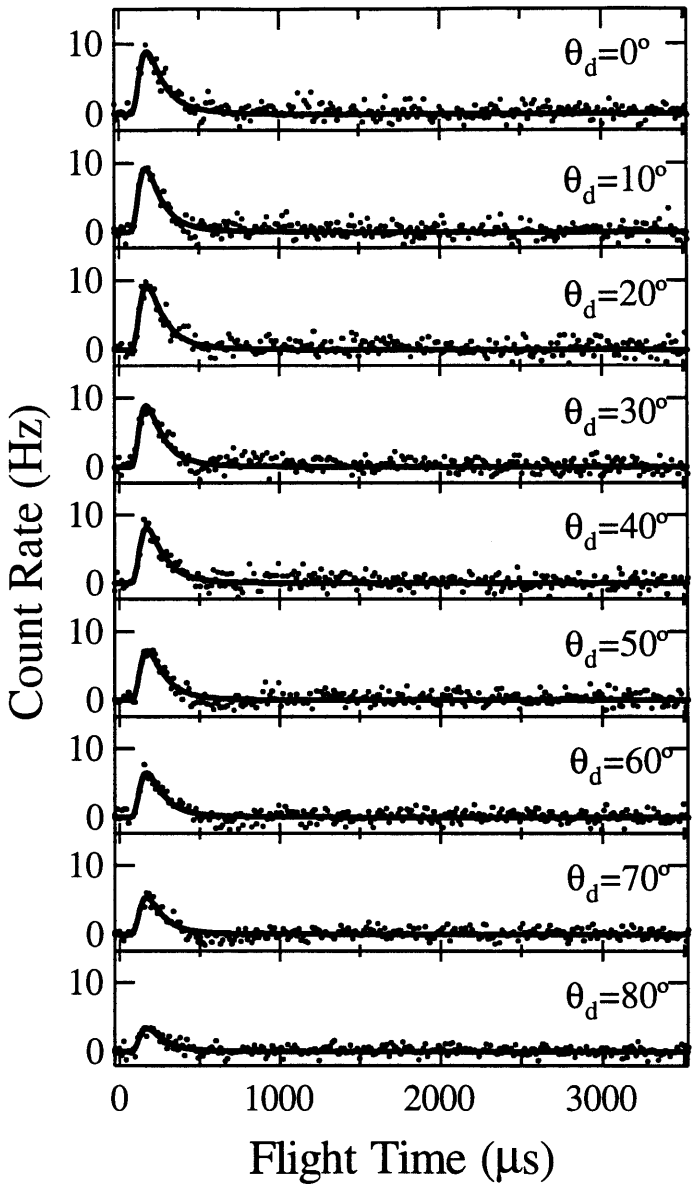

Figure 42 TOF distribution of scattered F as a function of detector angle over a coverage range of 0-0.4 ML F

TOF spectra of scattered F measured at nine detector angles θ_d and T_s=250 K upon exposure to high energy XeF_2 at θ_i=35°. Net scattered XeF TOF distribution obtained by point-by-point subtraction of contributions of the m/e=167 signal as well as the XeF signal and the $^{38}Ar^{2+}$ signal from the m/e=19 signal all shown in Figure 41. The solid lines show the fits to the data of a single component Maxwell-Boltzmann function F(t) described in Sec. II.D. Spectra are averaged over XeF_2 exposure corresponding to a fluorine coverage range of 0-0.4 ML F.

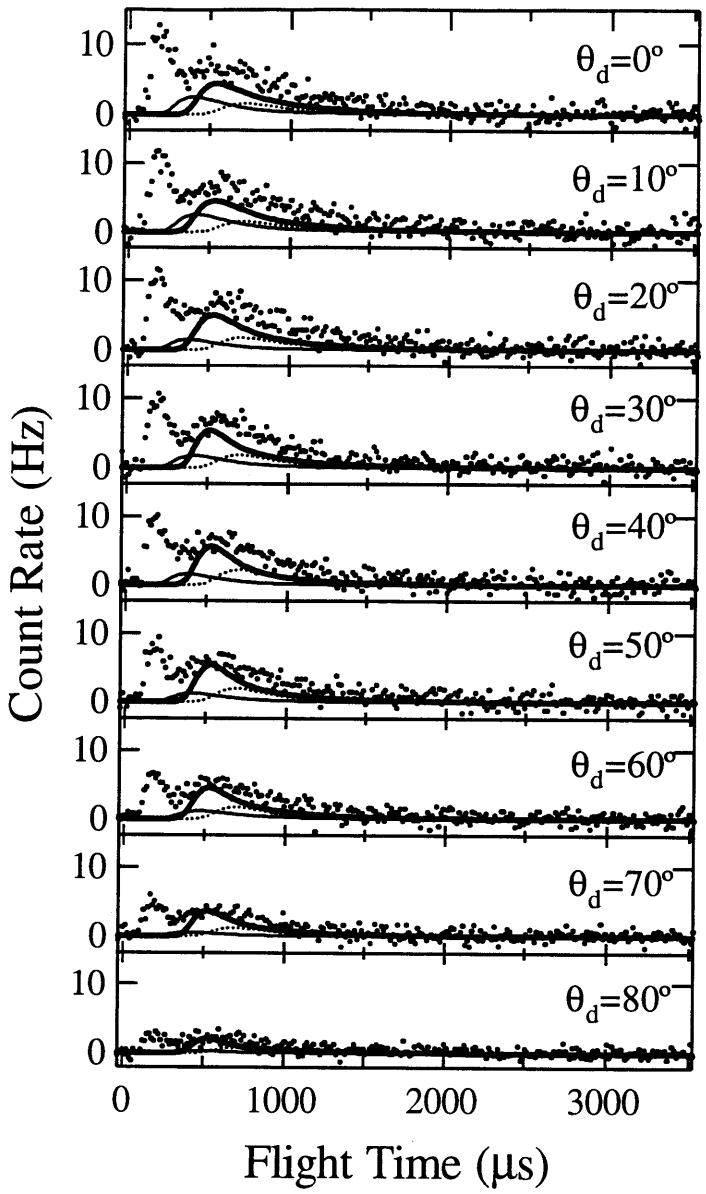

Figure 43 TOF distribution of scattered products at m/e=19 as a function of detector angle over a coverage range of 0.4-0.7 ML F

TOF spectra at m/e=19 measured at nine detector angles θ_d and T_s=250 K upon exposure to high energy XeF_2 at θ_i=35°. The thin dashed lines show the fits to the TOF distributions at m/e=167 multiplied by the XeF_2 cracking ratio (fits to data in Figure 18). The thin solid lines show the fits to the TOF distributions of scattered XeF multiplied by a scaling factor of 0.25 (fits to data in Figure 29). Thick solid lines show the fits to the TOF distributions at m/e=40 (data not shown) multiplied by the scaling factor of 0.00035 (see text). Spectra are averaged over a 10 s high energy XeF_2 exposure corresponding to a fluorine coverage range of 0.4-0.7 ML F.

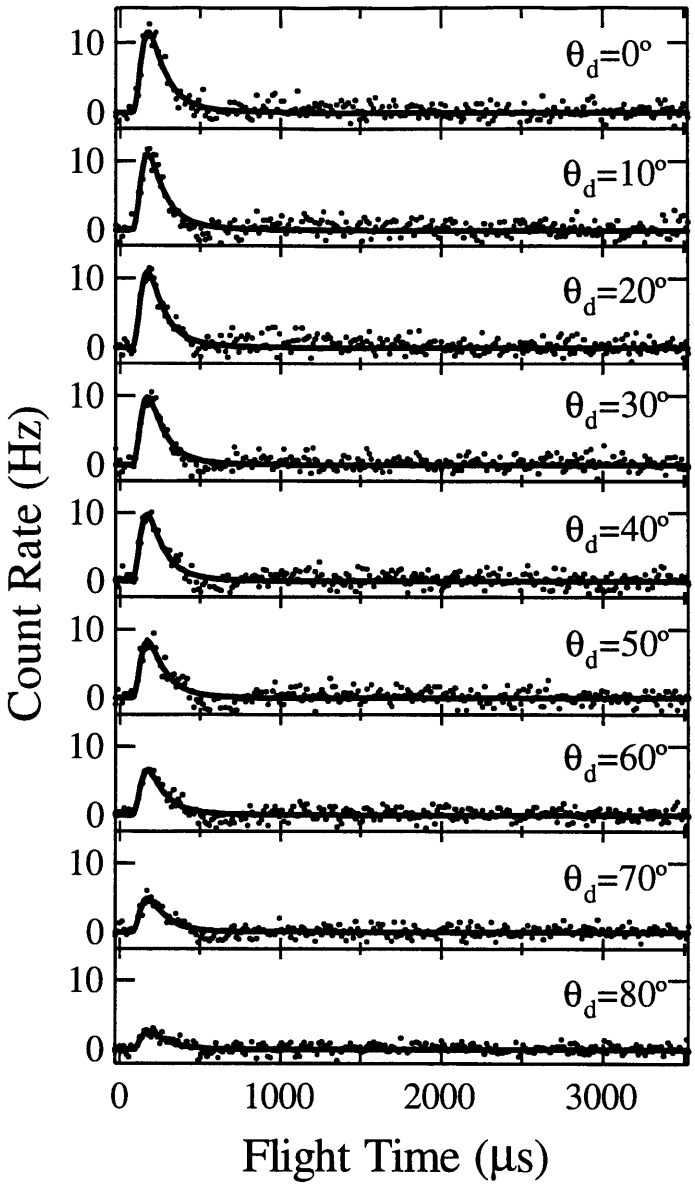

Figure 44 TOF distribution of scattered F as a function of detector angle over a coverage range of 0.4-0.7 ML F

TOF spectra of scattered F measured at nine detector angles θ_d and T_s=250 K upon exposure to high energy XeF_2 at θ_i=35°. Net scattered XeF TOF distribution obtained by point-by-point subtraction of contributions of the m/e=167 signal as well as the XeF signal and the $^{38}Ar^{2+}$ signal from the m/e=19 signal all shown in Figure 43. The solid lines show the fits to the data of a single component Maxwell-Boltzmann function F(t) described in Sec. II.D. Spectra are averaged over XeF_2 exposure corresponding to a fluorine coverage range of 0.4-0.7 ML F.

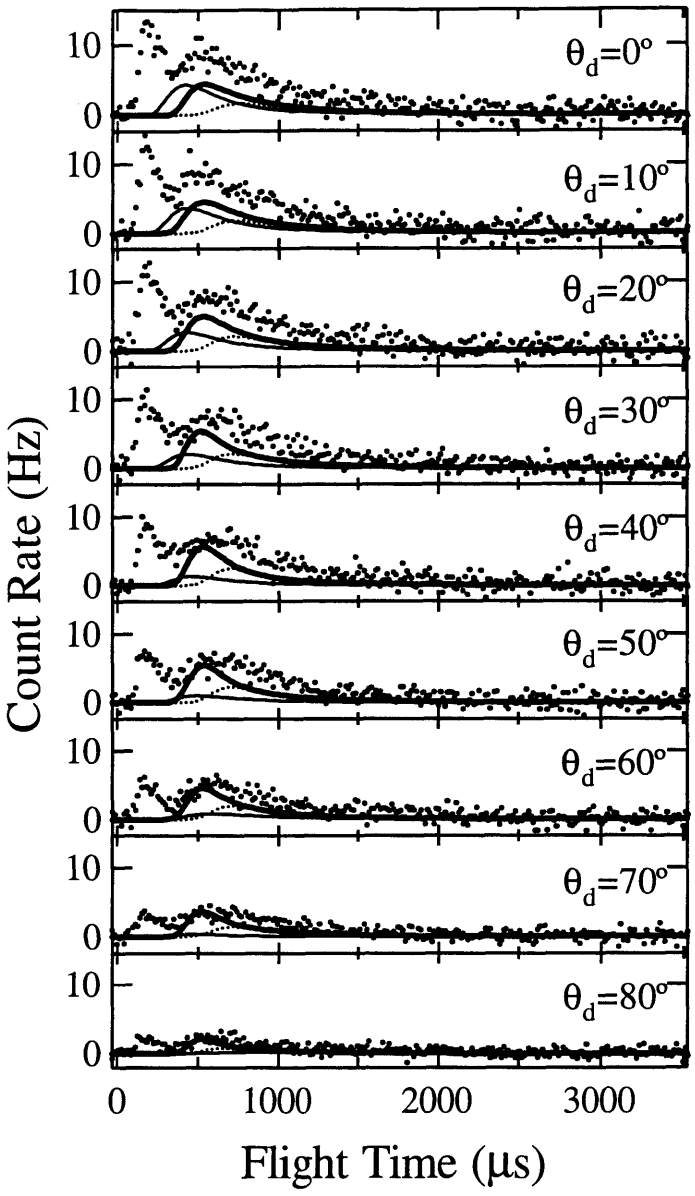

Figure 45 TOF distribution of scattered products at m/e=19 as a function of detector angle over a coverage range of 0.7-0.9 ML F

TOF spectra at m/e=19 measured at nine detector angles θ_d and T_s=250 K upon exposure to high energy XeF_2 at θ_i=35°. The thin dashed lines show the fits to the TOF distributions at m/e=167 multiplied by the XeF_2 cracking ratio (fits to data in Figure 19). The thin solid lines show the fits to the TOF distributions of scattered XeF multiplied by a scaling factor of 0.25 (fits to data in Figure 31). Thick solid lines show the fits to the TOF distributions at m/e=40 (data not shown) multiplied by the scaling factor of 0.00035 (see text). Spectra are averaged over a 10 s high energy XeF_2 exposure corresponding to a fluorine coverage range of 0.7-0.9 ML F.

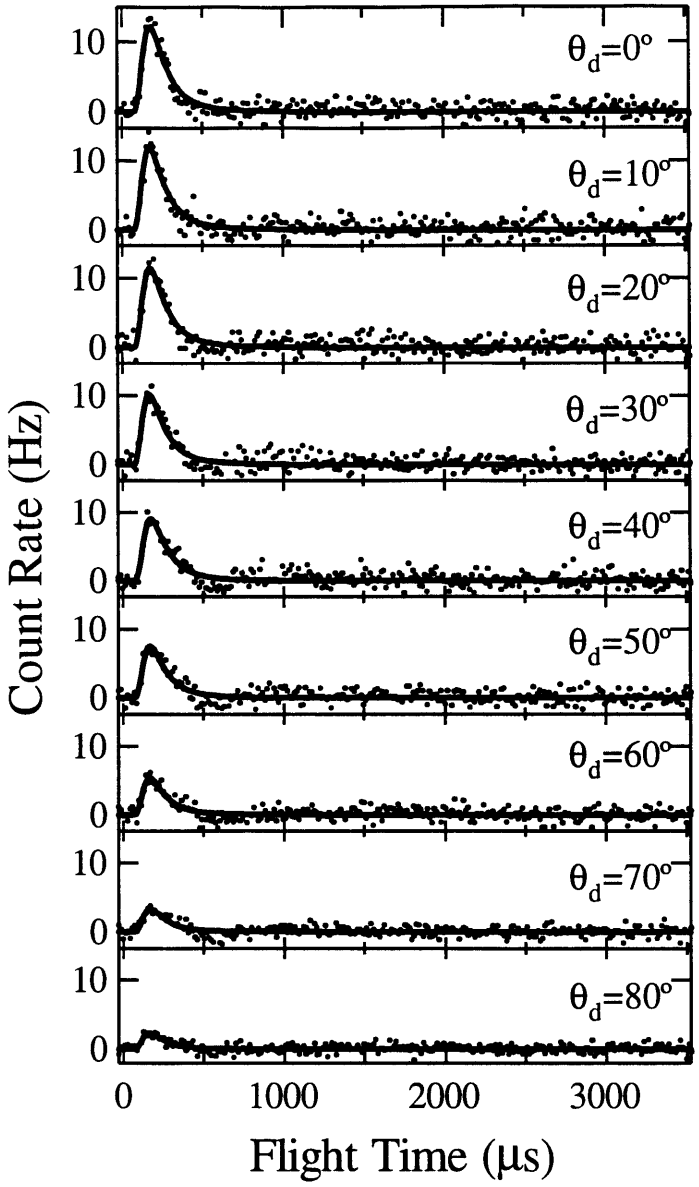

Figure 46 TOF distribution of scattered F as a function of detector angle over a coverage range of 0.7-0.9 ML F

TOF spectra of scattered F measured at nine detector angles θ_d and T_s=250 K upon exposure to high energy XeF_2 at θ_i=35°. Net scattered XeF TOF distribution obtained by point-by-point subtraction of contributions of the m/e=167 signal as well as the XeF signal and the $^{38}Ar^{2+}$ signal from the m/e=19 signal all shown in Figure 45. The solid lines show the fits to the data of a single component Maxwell-Boltzmann function F(t) described in Sec. II.D. Spectra are averaged over XeF_2 exposure corresponding to a fluorine coverage range of 0.7-0.9 ML F.

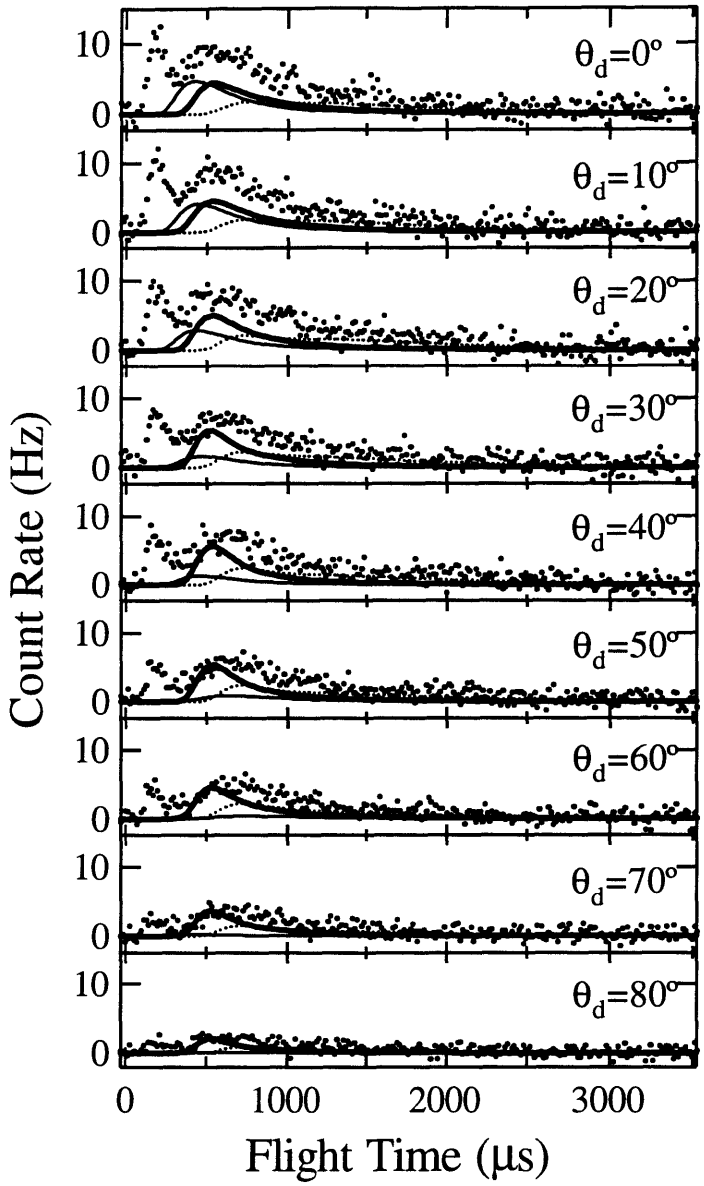

Figure 47 TOF distribution of scattered products at m/e=19 as a function of detector angle over a coverage range of 0.9-1.1 ML F

TOF spectra at m/e=19 measured at nine detector angles θ_d and T_s=250 K upon exposure to high energy XeF_2 at θ_i=35°. The thin dashed lines show the fits to the TOF distributions at m/e=167 multiplied by the XeF_2 cracking ratio (fits to data in Figure 20). The thin solid lines show the fits to the TOF distributions of scattered XeF multiplied by a scaling factor of 0.25 (fits to data in Figure 33). Thick solid lines show the fits to the TOF distributions at m/e=40 (data not shown) multiplied by the scaling factor of 0.00035 (see text). Spectra are averaged over a 10 s high energy XeF_2 exposure corresponding to a fluorine coverage range of 0.9-1.1 ML F.

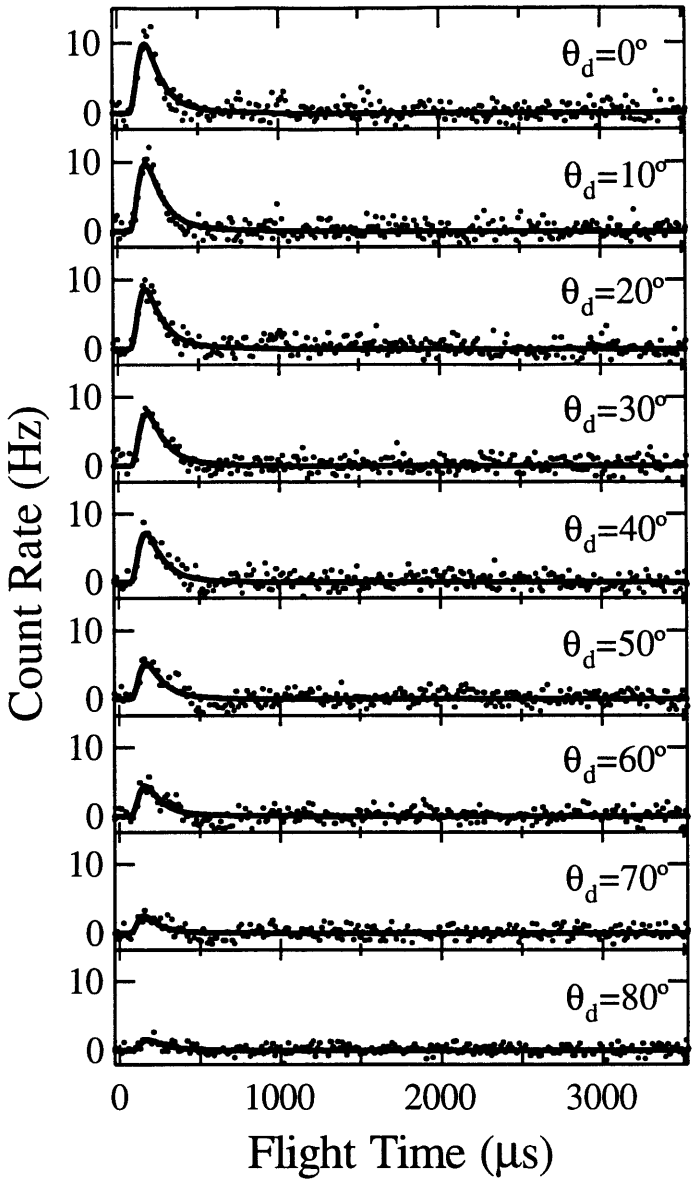

Figure 48 TOF distribution of scattered F as a function of detector angle over a coverage range of 0.9-1.1 ML F

TOF spectra of scattered F measured at nine detector angles θ_d and T_s=250 K upon exposure to high energy XeF_2 at θ_i=35°. Net scattered XeF TOF distribution obtained by point-by-point subtraction of contributions of the m/e=167 signal as well as the XeF signal and the $^{38}Ar^{2+}$ signal from the m/e=19 signal all shown in Figure 47. The solid lines show the fits to the data of a single component Maxwell-Boltzmann function F(t) described in Sec. II.D. Spectra are averaged over XeF_2 exposure corresponding to a fluorine coverage range of 0.9-1.1 ML F.

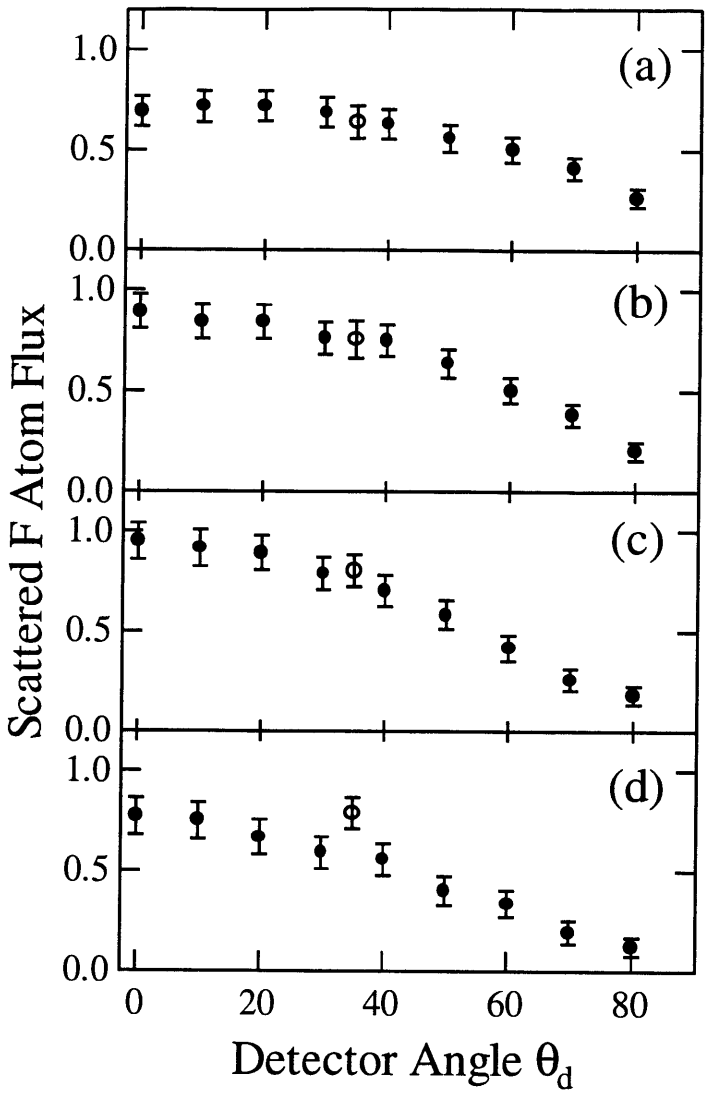

Figure 49 Angular distribution of flux of F scattered from Si(100)
Scattered flux of F atom as a function of detector angle upon exposure to high energy XeF_2 (solid circles) and low energy XeF_2 (hollow circles) at exposure intervals corresponding to coverage ranges of (a) 0-0.4 ML F, (b) 0.4-0.7 ML F, (c) 0.7-0.9 ML F, and (d) 0.9-1.1 ML F. Scattered F atom flux determined from velocity-weighted integration of the fits to the TOF distributions shown in Figures 42, 44, 46, and 48 (high energy) and Figure 53 (low energy). Error bars represent uncertainties of the integral of the velocity-weighted fit to the TOF distributions (Sec. II.D) in Figures 42, 44, 46, 48, and 53.

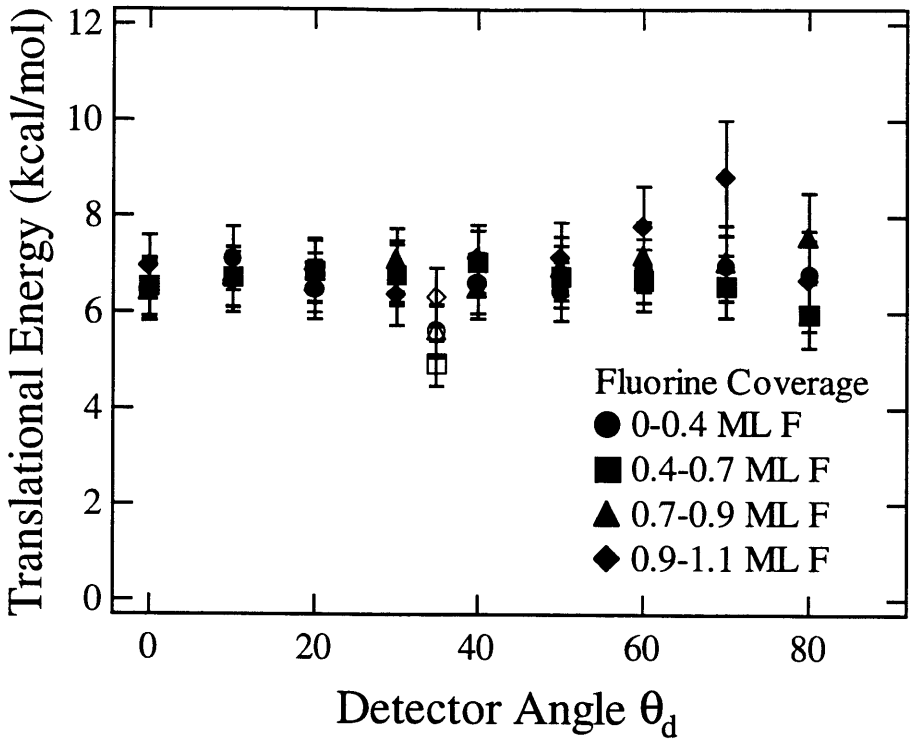

Figure 50 Translational energy of F scattered from Si(100) as a function of detector angle
Average translational energy of scattered F atom as a result of exposure to high energy XeF_2 (solid symbols) and low energy XeF_2 (hollow symbols) as a function of detector angle over four different fluorine coverage ranges. The average translational energy is determined from the velocity-weighted TOF distributions shown in Figures 42, 44, 46, 48 (high energy) and Figure 53 (low energy). Error bars represent the uncertainty of the determination of the average translational energy (Sec. II.D) from the fits to the TOF distributions in Figures 42, 44, 46, 48, and 53.

III.C.3.b. Low incident energy XeF_2 (E_i=1.8 kcal/mol)

The TOF distributions at m/e=19 described above are all for scattering high energy XeF_2. Analogous to the sets of the TOF measurements at m/e=167 and m/e=148 described in Sec. III.C.1 and Sec. III.C.2, respectively, the TOF distributions of the scattered products at m/e=19 arising from the interaction of low energy XeF_2 with Si have also been measured. This provides the opportunity for comparison between the dynamics of the interaction of XeF_2 with Si(100) with the dynamics of the interaction of F_2 with Si(100) described in Chapter 1.

Figure 51 is a plot of the TOF distributions of the products at m/e=19 that are scattered from the interaction of low energy XeF_2 from Si(100). The TOF distribution is for a scattering geometry in which the incident XeF_2 is at normal incidence, θ_i=0°, and the detector is positioned at 35° from the surface normal, θ_d=35°. The TOF distribution is signal averaged over a 24 s exposure to low energy XeF_2. The average velocity and energy of the scattered F are 1472±65 m/s and 5.6±0.5 kcal/mol, respectively. Recall that the average velocity and energy of the scattered F from the interaction of high energy XeF_2 with Si are 1551±68 m/s and 6.7±0.1 kcal/mol, respectively. Thus, although very fast F atoms are present in the interaction of XeF_2 with Si over a range of incident XeF_2 energies, the TOF distribution of F arising from the interaction of low energy XeF_2 with Si is less energetic than that arising from exposure of Si to high energy XeF_2.

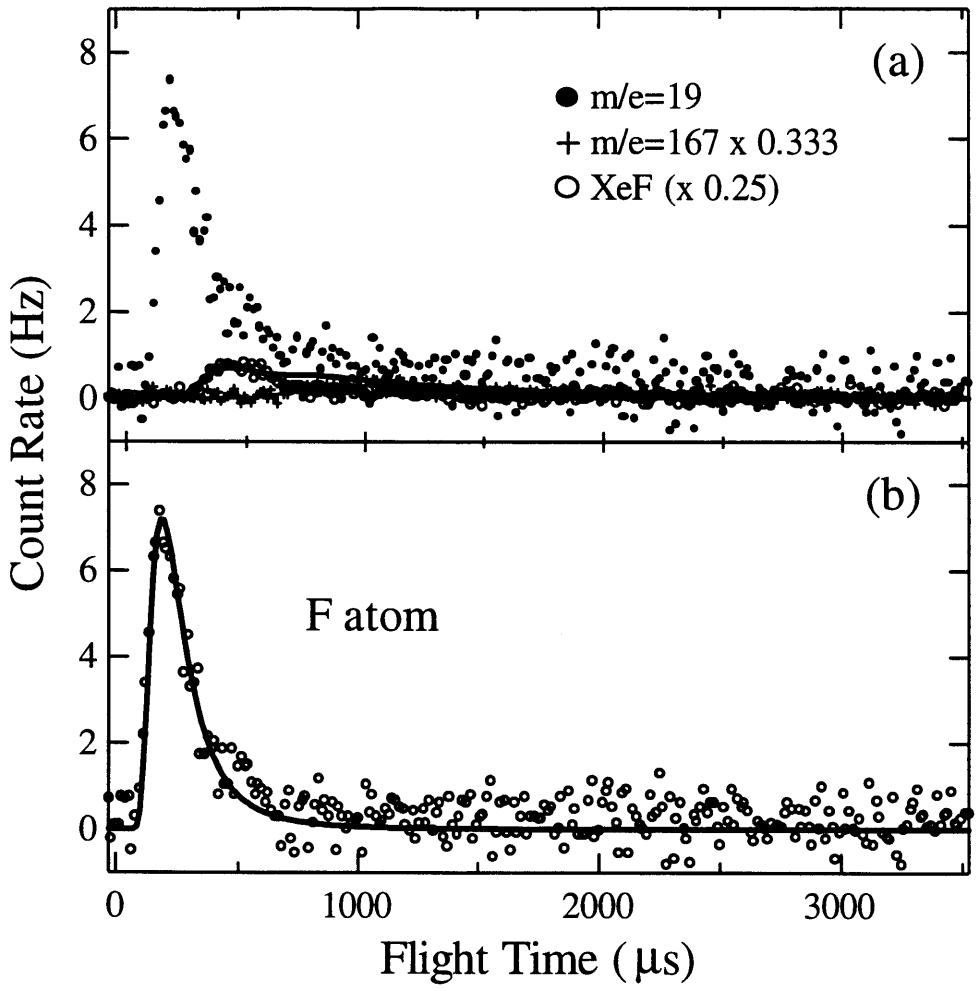

Figure 51 TOF distribution of scattered products at m/e=19 upon exposure to low energy XeF_2

(a) TOF spectra at m/e=19 measured at θ_d=35° and T_s=250 K upon exposure to high energy XeF_2 at θ_i=0°. Signal at m/e=167 multiplied by XeF_2 cracking ratio and XeF signal multiplied by optimal scaling factor of 0.25 are superimposed for comparison. (b) Net scattered F atom TOF distribution obtained by point-by-point subtraction of contributions from XeF_2 and XeF from m/e=19 signal in (a). Spectra are averaged over XeF_2 exposure corresponding to a fluorine coverage range of 0-1.2 ML F. Average velocity of the XeF distribution is v_{XeF}=1472±65 m/s.

The TOF distribution in Figure 51 is signal averaged over a 24 s exposure to low energy XeF_2. To test the exposure dependence of the scattered F, TOF distributions have been signal averaged over shorter 6 s exposures to low energy XeF_2. Figure 52 shows the TOF distributions at m/e=19 signal averaged over four successive 6 s exposures to low energy XeF_2. The TOF distributions of the scattered products at m/e=167 and m/e=148 are multiplied by the XeF_2 and XeF cracking ratios, respectively, and superimposed to show the contributions from unreactively scattered XeF_2 and XeF from single atom abstraction. Figure 53 shows the TOF distributions of scattered F atoms, which are determined by subtracting the TOF distributions at m/e=167 and m/e=148 multiplied by the XeF_2 cracking ratio and XeF scaling factor, respectively.

The scattered flux of very fast F atoms is reasonably insensitive to low energy XeF_2 exposure. The flux of scattered F atoms at θ_d=35°, defined as the integral of the velocity-weighted TOF distribution of scattered F atoms, is superimposed onto the plot of the angular distribution of scattered F atoms arising from the interaction of high energy XeF_2 with Si in Figure 49. The scattered F atom flux arising from the interaction of low energy XeF_2 is multiplied by a scaling factor such that flux of F atoms from low and high energy XeF_2 is similar at low XeF_2 exposure. Although the comparison at successive exposures is not necessarily valid because the relative flux of low and high energy XeF_2 is unknown, the flux of very fast F atoms is reasonably insensitive to fluorine coverage, increasing slightly as the XeF_2 exposure increases.

The average translational energy of the scattered F atoms from the interaction of low energy XeF_2 with Si is superimposed onto the plot of the translational energy of the scattered F atoms as a function of detector angle in Figure 50. The energy of the scattered F atoms is

reasonably insensitive to coverage, but it is distinctly lower than that of the scattered F atoms from the interaction of high energy XeF_2 with Si.

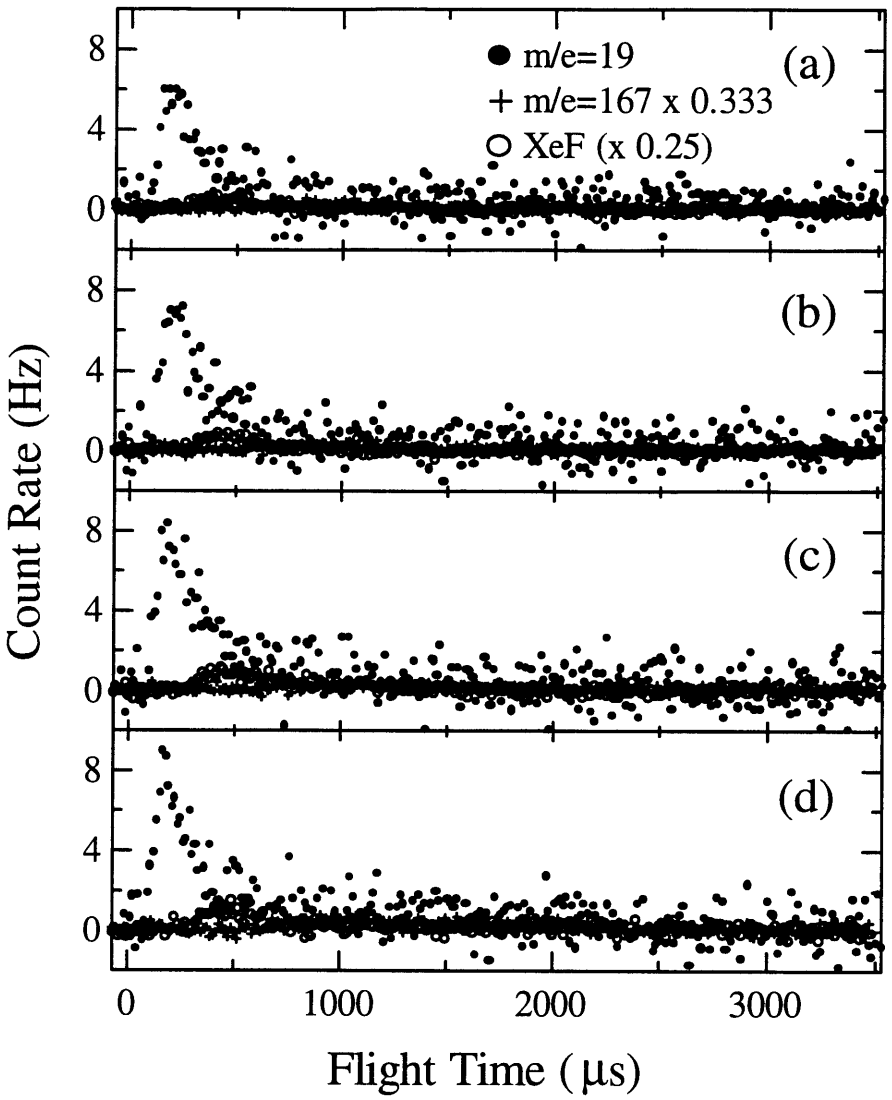

Figure 52 TOF distribution of scattered products at m/e=19 upon exposure to low energy XeF_2 as a function of coverage

TOF spectra at m/e=19 measured at θ_d=35° and T_s=250 K upon exposure to low energy XeF_2 at θ_i=0°. TOF spectra at m/e=167 multiplied by XeF_2 cracking ratio and TOF spectra of scattered XeF multiplied by optimal scaling factor of 0.25 are superimposed for comparison. Spectra are averaged over successive 6 s low energy XeF_2 exposures corresponding to coverage ranges of (a) 0-0.4 ML F, (b) 0.4-0.7 ML F, (c) 0.7-0.9 ML F, and (d) 0.9-1.1 ML F.

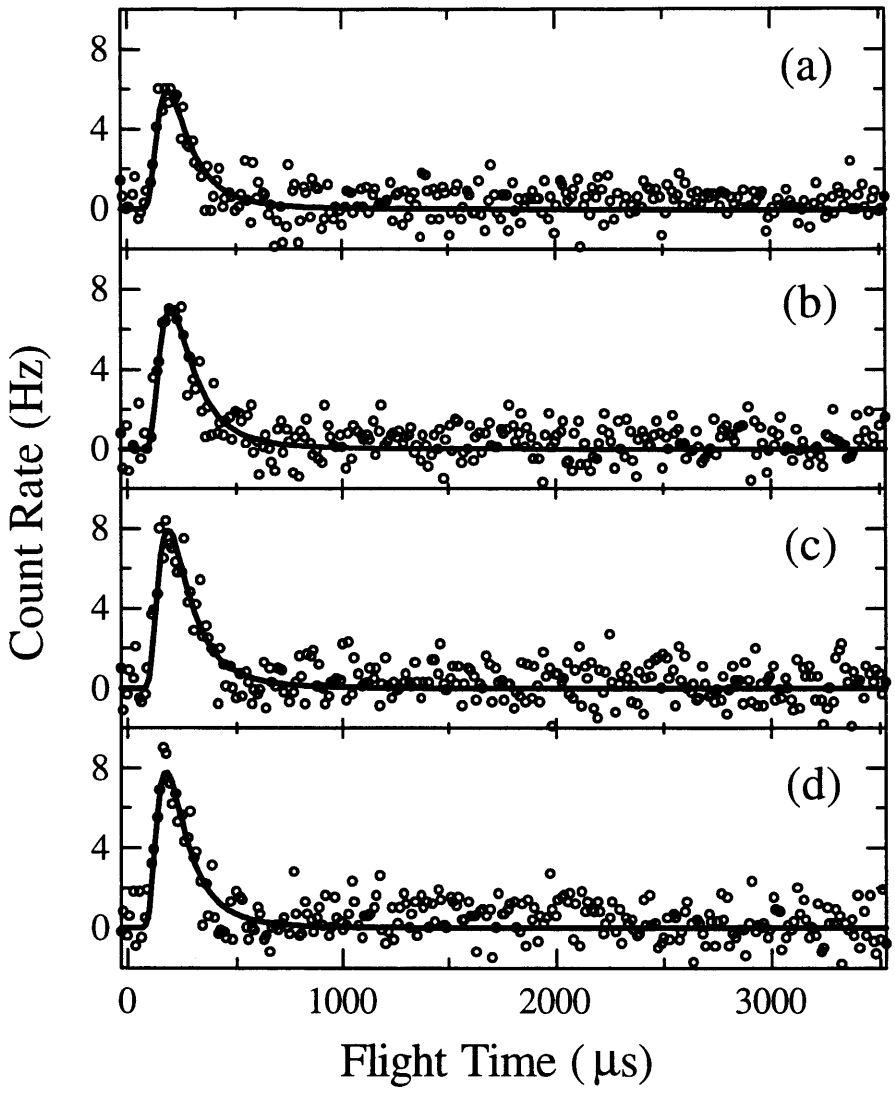

Figure 53 TOF distribution of scattered F with low energy XeF_2 as a function of coverage. TOF spectra of scattered F atom measured at θ_d=35° and T_s=250 K upon exposure to low energy XeF_2 at θ_i=0°. Net scattered F atom signal obtained by point-by-point subtraction of contributions form XeF2 and XeF from m/e=19 signal in Figure 52. Spectra are averaged over successive 6 s low energy XeF_2 exposures corresponding to coverage ranges of (a) 0-0.4 ML F, (b) 0.4-0.7 ML F, (c) 0.7-0.9 ML F, and (d) 0.9-1.1 ML F.

III.C.4. m/e=129

III.C.4.a. High incident energy XeF_2 (E_i=6.3 kcal/mol)

Figure 54 shows a TOF distribution of the products at m/e=129 that are scattered as a result of the interaction of XeF_2 at E_i=6.3 kcal/mol with Si(100) at 250 K. The TOF distribution is for a scattering geometry in which the XeF_2 beam is 35° from the surface normal, θ_i=35°, and the detector is positioned along the surface normal, θ_d=0°. The TOF distribution is signal averaged over an exposure to high energy XeF_2 that corresponds to a fluorine coverage range of 0-1.1 ML. The TOF distribution at m/e=129 is bimodal with a narrow fast feature and a broad slow feature. However, the TOF distribution is not simply comprised of only two contributions. First, there are contributions from unreactively scattered XeF_2 and XeF arising from single atom abstraction which fragment in the ionization region and are detected as Xe^+ at m/e=129. Second, there is Xe that is *reactively* scattered as a result of the interaction of XeF_2 with Si. This reactively scattered Xe may arise from the dissociation of XeF, the product of single atom abstraction, or from two atom adsorption. Finally, there may Xe that is *unreactively* scattered as a result of free Xe in the incident XeF_2 beam arising from XeF_2 decomposition. Of course, the contribution from *reactively* scattered Xe is the contribution of interest. In addition, the further separation of the two reactive Xe channels would yield significant insight into the dynamics of the interaction of XeF_2 with Si. However, because of the unknown magnitude of the myriad contributions to the signal at m/e=129, the analysis of the TOF distribution at m/e=129 is limited to considering the range of effects that the other contributions may have on the TOF distribution of Xe reactively scattered as a result of the interaction of XeF_2 with Si.

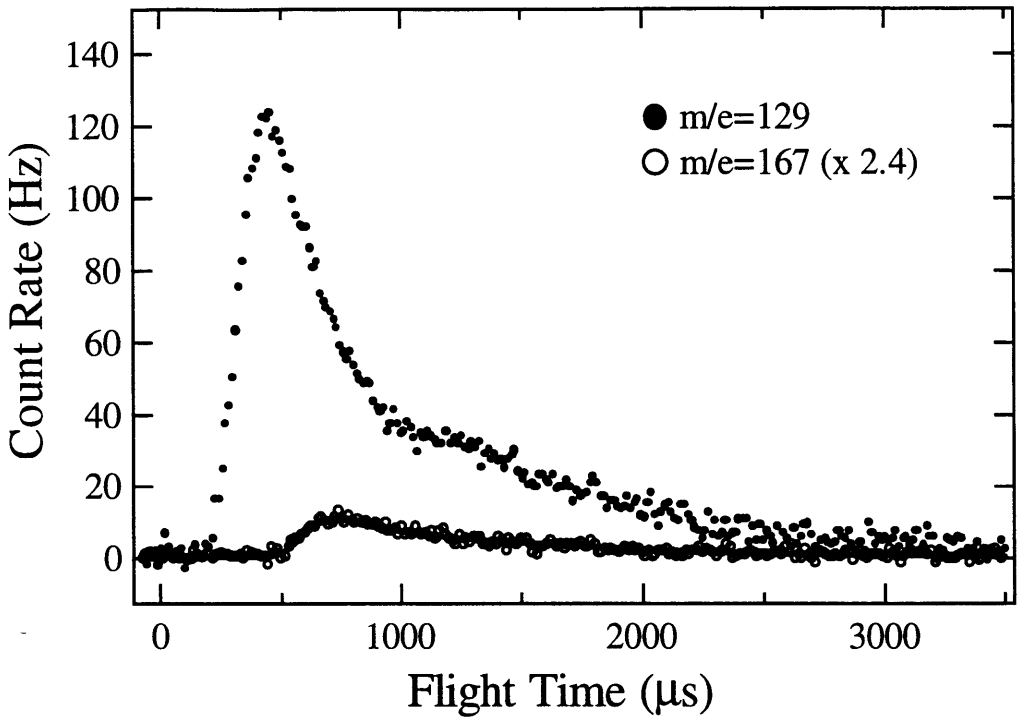

Figure 54 TOF distribution of scattered products at m/e=129
TOF spectrum at m/e=129 measured at θ_d=0° and T_s=250 K upon exposure to high energy XeF_2 at θ_i=35°. Signal at m/e=167 multiplied by maximum XeF_2 cracking ratio is superimposed to show the maximum contribution from unreactively scattered XeF_2. Solid line shows the fit to the TOF distribution given by Eq. (II.1) in Sec. II.D at m/e=167 multiplied by the maximum XeF_2 cracking ratio.

III.C.4.a.i. Determination of XeF_2 contribution to signal at m/e=129

Figure 55 is a plot of the TOF distributions of the scattered signal at m/e=129 detected along the surface normal, θ_d=0°, signal averaged over short XeF_2 exposure intervals. The contribution from unreactively scattered XeF_2 to the signal at m/e=129 is equal to the TOF distribution at m/e=167 multiplied by the XeF_2 cracking ratio, $\sigma_{XeF_2 \rightarrow Xe^+} / \sigma_{XeF_2 \rightarrow XeF_2^+}$. The ratio of the measured signal intensities at m/e=129 and m/e=167 is 2.4, but because of the unknown contribution of free Xe in the XeF_2 molecular beam, this measured ratio is only an upper limit to the XeF_2 cracking ratio. The TOF distributions at m/e=167 shown in Figures 17-20 are multiplied by this maximum XeF_2 cracking ratio and superimposed onto the TOF distributions at m/e=129 in Figures 54-55. Note that the XeF_2 contribution cannot account for all of the slow feature of the TOF distribution at m/e=129.

III.C.4.a.ii. Determination of an upper bound for XeF contribution to signal at m/e=129

The contribution from scattered XeF to the signal at m/e=129 is equal to the TOF distribution at m/e=148 that is attributed to scattered XeF multiplied by the XeF cracking ratio, $\sigma_{XeF \rightarrow Xe^+} / \sigma_{XeF \rightarrow XeF^+}$. However, the XeF cracking ratio is unknown because there is no experimentally feasible method for producing a pure source of XeF. In Figure 55 the TOF distributions of scattered XeF are multiplied by an arbitrary scaling factor of 8.0. It will be shown below that this arbitrary scaling factor must be equal to the maximum XeF cracking ratio.

Similar TOF distributions at m/e=129 have also been measured at several other detection angles, θ_d, spanning the entire forward scattering region in the scattering plane. Figure 56 shows the TOF distributions of the products at m/e=129 scattered into five detection angles, θ_d, from the interaction of high energy XeF_2 at θ_i=35°. The TOF distributions are signal averaged over a

coverage range of 0-0.4 ML F. The results shown in Figures 57, 58, and 59 are taken under identical conditions to those in Figure 56 except that the TOF distributions are signal averaged over coverage ranges of 0.4-0.7 ML F, 0.7-0.9 ML F, and 0.9-1.1 ML F, respectively. Analogous to Figure 55, the contributions from the TOF distribution of XeF_2 and XeF are superimposed for comparison.

The contribution of scattered XeF to the TOF distribution of the scattered products at m/e=129 cannot be greater than the overall signal at m/e=129. The maximum XeF cracking ratio is the largest scaling factor that the TOF distribution of scattered XeF can be multiplied by such that the contribution from scattered XeF is not greater than the overall m/e=129 signal at any detector angle or exposure interval. The scaling factor is determined by matching the signal intensities of scattered XeF to the m/e=129 signal under the conditions in which the flux of XeF relative to the signal at m/e=129 is the smallest. These conditions correspond to the maximum XeF signal which is with the detector along the surface normal at a fluorine coverage around 1 ML. It is apparent from Figure 55(d) that the maximum XeF cracking ratio is indeed 8.0.

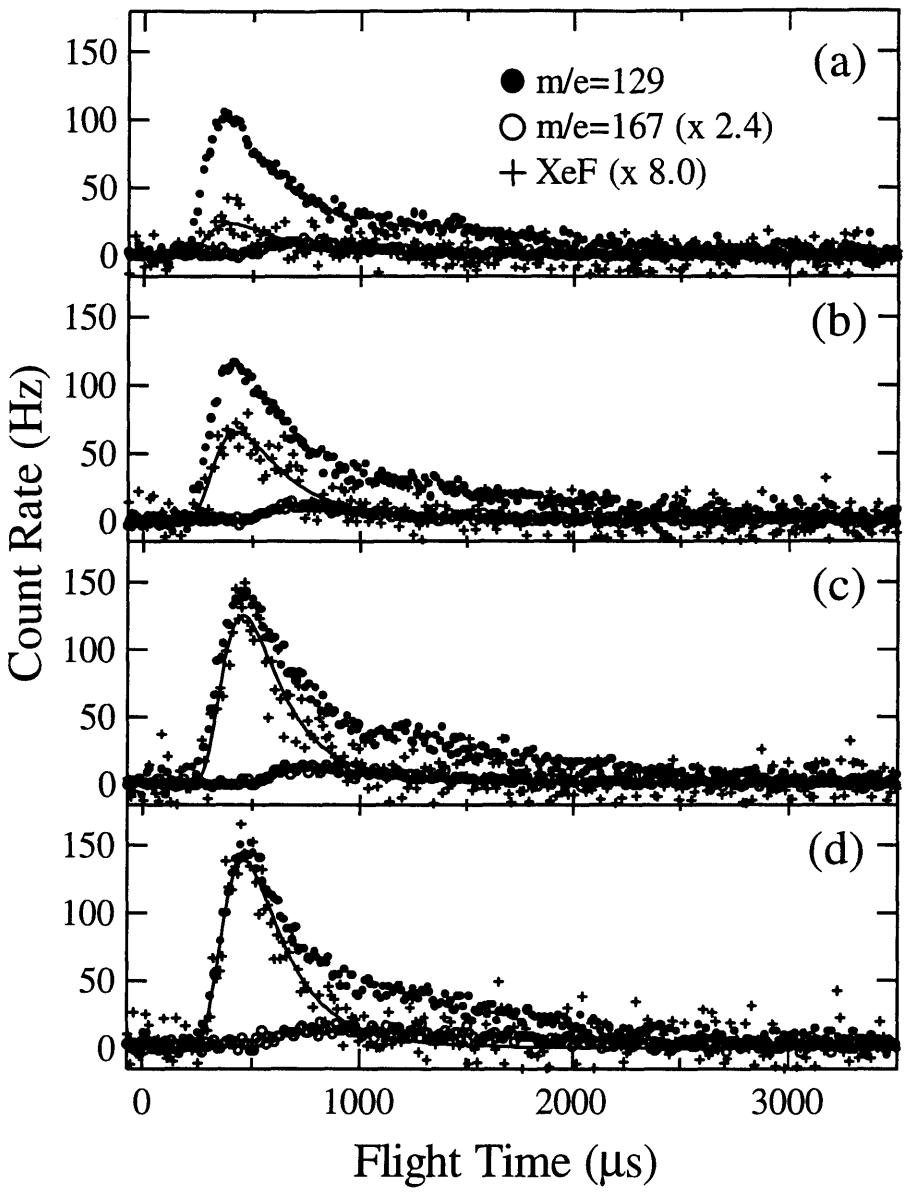

Figure 55 TOF distribution of scattered products at m/e=129 as a function of fluorine coverage

TOF spectra at m/e=129 measured at θ_d=0° and T_s=250 K upon exposure to high energy XeF_2 at θ_i=35°. Signal at m/e=167 multiplied by maximum XeF_2 cracking ratio and XeF signal multiplied by arbitrary XeF scaling factor of 8.0 are superimposed for comparison. Spectra are averaged over XeF_2 exposures corresponding to coverage ranges of (a) 0-0.4 ML F, (b) 0.4-0.7 ML F, (c) 0.7-0.9 ML F, and (d) 0.9-1.1 ML F.

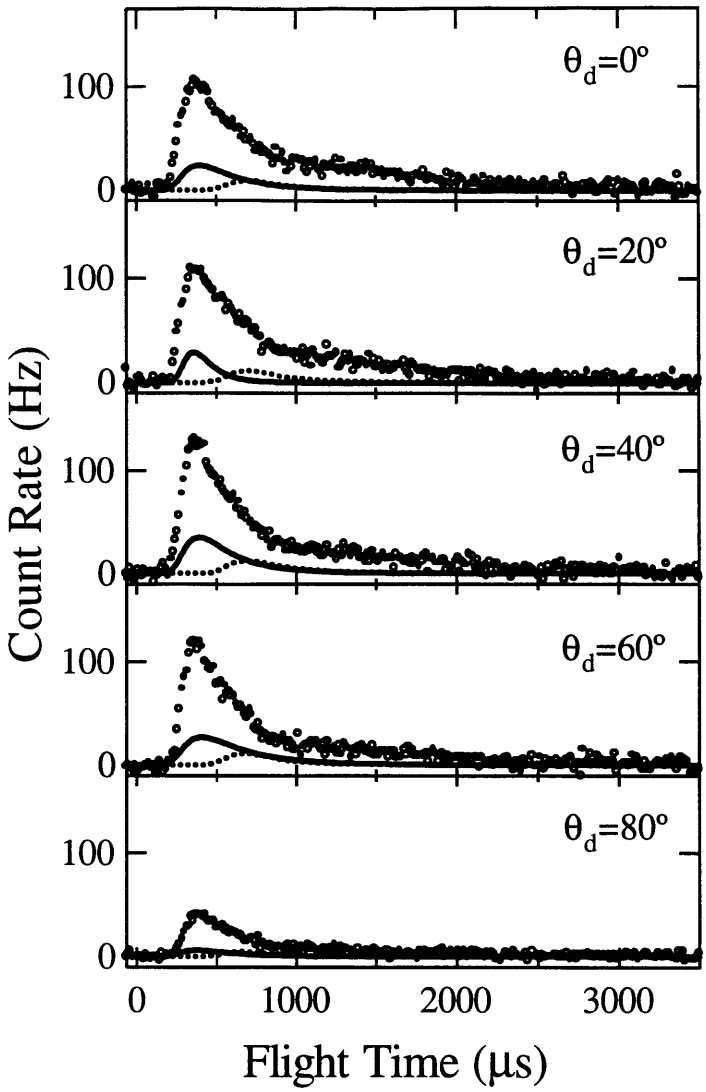

Figure 56 TOF distribution of scattered products at m/e=129 as a function of detector angle over a coverage range of 0-0.4 ML F

TOF spectra at m/e=129 measured at five detector angles θ_d and T_s=250 K upon exposure to high energy XeF_2 at θ_i=35°. The solid line shows the fit to the TOF distributions of XeF multiplied by the maximum XeF cracking ratio (fits to data in Figure 27) and represents the maximum contribution from XeF arising from single atom abstraction to the m/e=148 signal. The dashed line shows the fit to the TOF distributions at m/e=167 multiplied by the maximum XeF_2 cracking ratio (fits to data in Figure 17) and represents the maximum contribution from unreactively scattered XeF_2 to the m/e=129 signal. Spectra are averaged over a 10 s high energy XeF_2 exposure corresponding to a fluorine coverage range of 0-0.4 ML F.

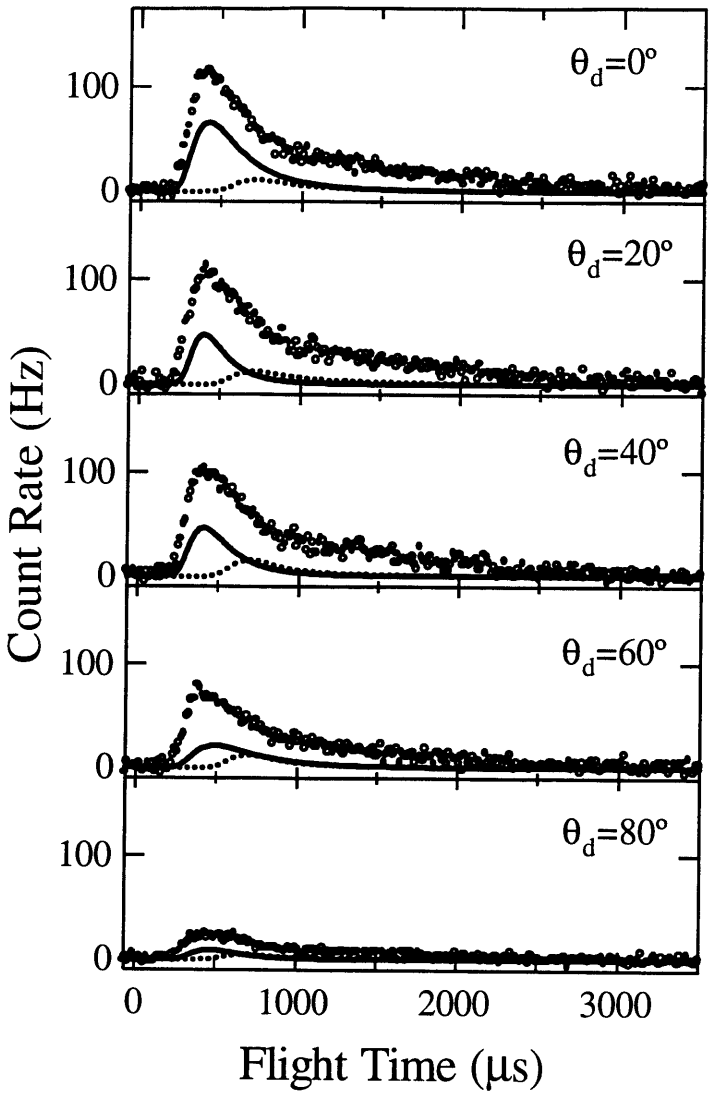

Figure 57 TOF distribution of scattered products at m/e=129 as a function of detector angle over a coverage range of 0.4-0.7 ML F

TOF spectra at m/e=129 measured at five detector angles θ_d and T_s=250 K upon exposure to high energy XeF_2 at θ_i=35°. The solid line shows the fit to the TOF distributions of XeF multiplied by the maximum XeF cracking ratio (fits to data in Figure 29) and represents the maximum contribution from XeF arising from single atom abstraction to the m/e=148 signal. The dashed line shows the fit to the TOF distributions at m/e=167 multiplied by the maximum XeF_2 cracking ratio (fits to data in Figure 18) and represents the maximum contribution from unreactively scattered XeF_2 to the m/e=129 signal. Spectra are averaged over a 10 s high energy XeF_2 exposure corresponding to a fluorine coverage range of 0.4-0.7 ML F.

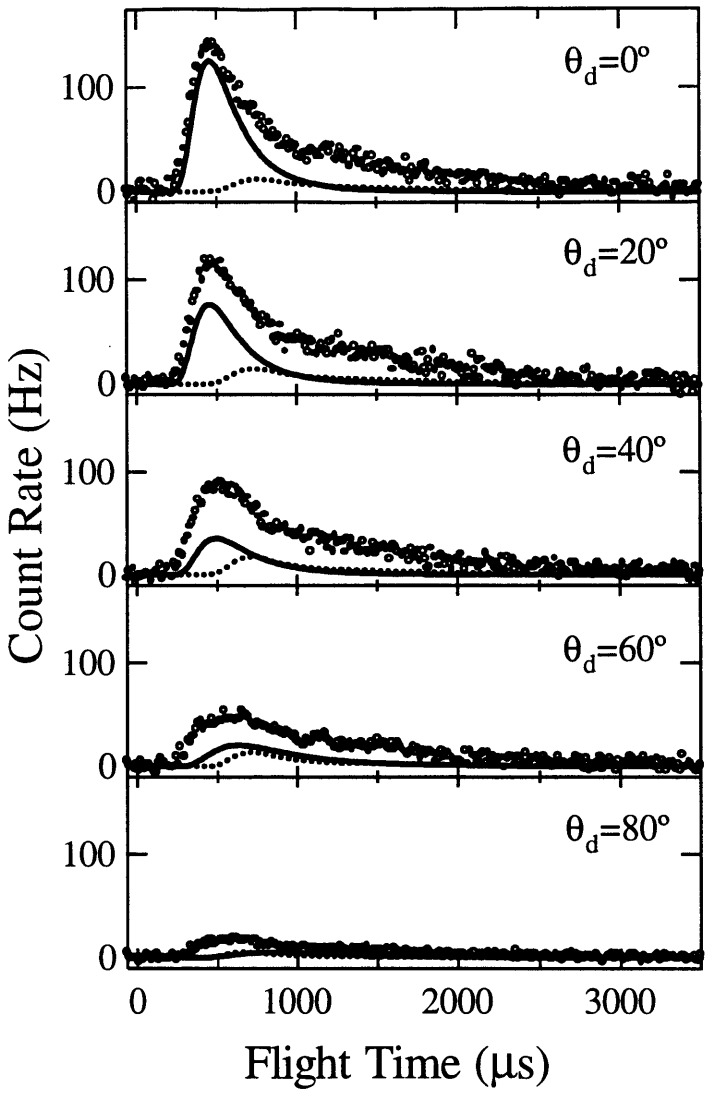

Figure 58 TOF distribution of scattered products at m/e=129 as a function of detector angle over a coverage range of 0.7-0.9 ML F

TOF spectra at m/e=129 measured at five detector angles θ_d and T_s=250 K upon exposure to high energy XeF_2 at θ_i=35°. The solid line shows the fit to the TOF distributions of XeF multiplied by the maximum XeF cracking ratio (fits to data in Figure 31) and represents the maximum contribution from XeF arising from single atom abstraction to the m/e=148 signal. The dashed line shows the fit to the TOF distributions at m/e=167 multiplied by the maximum XeF_2 cracking ratio (fits to data in Figure 19) and represents the maximum contribution from unreactively scattered XeF_2 to the m/e=129 signal. Spectra are averaged over a 10 s high energy XeF_2 exposure corresponding to a fluorine coverage range of 0.7-0.9 ML F.

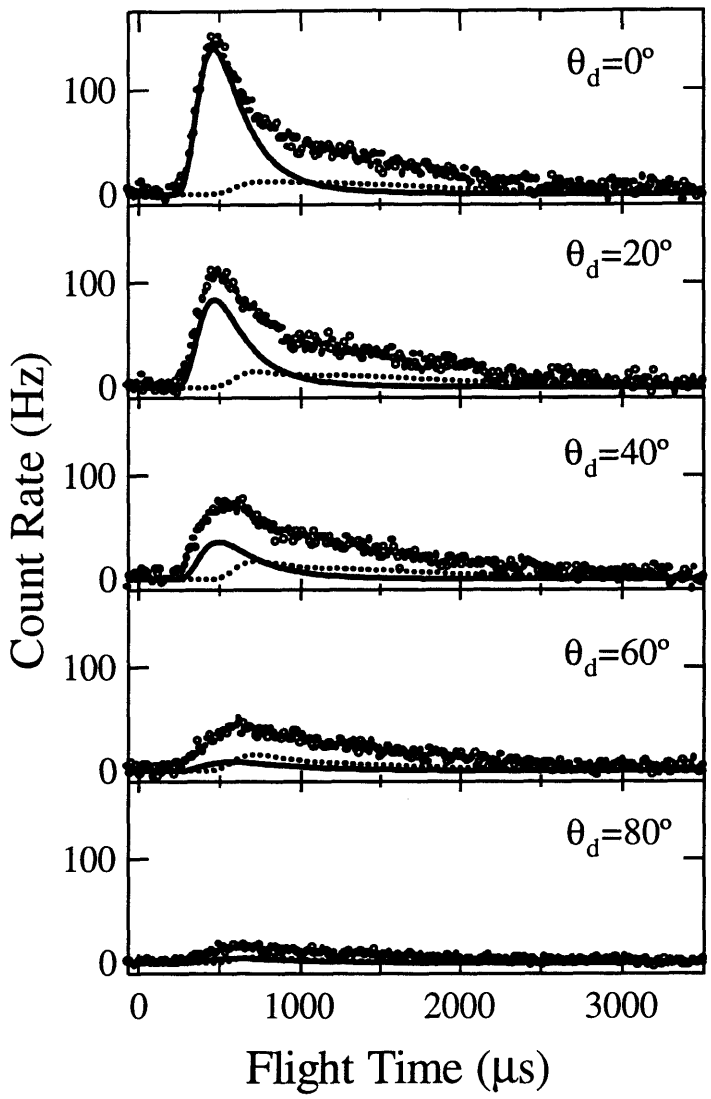

Figure 59 TOF distribution of scattered products at m/e=129 as a function of detector angle over a coverage range of 0.9-1.1 ML F

TOF spectra at m/e=129 measured at five detector angles θ_d and T_s=250 K upon exposure to high energy XeF_2 at θ_i=35°. The solid line shows the fit to the TOF distributions of XeF multiplied by the maximum XeF cracking ratio (fits to data in Figure 33) and represents the maximum contribution from XeF arising from single atom abstraction to the m/e=148 signal. The dashed line shows the fit to the TOF distributions at m/e=167 multiplied by the maximum XeF_2 cracking ratio (fits to data in Figure 20) and represents the maximum contribution from unreactively scattered XeF_2 to the m/e=129 signal. Spectra are averaged over a 10 s high energy XeF_2 exposure corresponding to a fluorine coverage range of 0.9-1.1 ML F.

III.C.4.a.iii. Identification of unreactively scattered Xe from decomposition of the XeF_2 molecular beam

The presence of a thermal feature attributable to Xe scattered from the interaction of XeF_2 with Si is unusual considering the significant energy that is liberated during F atom abstraction from either XeF_2 or XeF. The slow feature in the Xe TOF distribution may not arise from the *reactive* scattering of Xe from the interaction of XeF_2 with Si, but the *unreactive* scattering of free Xe in the incident molecular beam.

The possibility of XeF_2 decomposition in the molecular beam source is mentioned in Sec. II.A. The Xe contamination that results from XeF_2 decomposition does not adversely affect the dynamics of the interaction of XeF_2 with Si. However, it can adversely affect the measurement of the TOF distribution, the experimental probe of the dynamics, because the TOF distribution of unreactively scattered Xe may obscure the TOF distribution of Xe scattered as a result of the interaction of XeF_2 with Si.

In order to determine the effect of unreactively scattered Xe on the measurement of the TOF distribution of the scattered products at m/e=129, the high energy XeF_2 (0.25% XeF_2/Ar) molecular beam was intentionally doped with Xe (1%) so that the TOF distribution of unreactively scattered Xe could be measured as a function of XeF_2 exposure. The concentration of Xe was large enough to overwhelm the other contributions to the signal at m/e=129, but small enough not to significantly affect the molecular beam expansion. The average velocity and energy of the incident XeF_2 are 550±24 m/s and 6.1±0.5 kcal/mol, respectively, compared to 560±24 m/s and 6.3±0.5 kcal/mol for the original high energy XeF_2 beam. Figure 60 is a plot of the TOF distributions of the scattered signal at m/e=129 parameterized by fluorine coverage due

to XeF_2 exposure. The experimental conditions of these measurements are identical to the measurements shown in Figure 55, except for the intentional introduction of free Xe in the molecular beam. The data from Figure 55 are superimposed here for comparison. The insets show that the small shoulder on the TOF distributions of the scattered Xe and XeF_2 molecular beam at short flight times matches well with the TOF distributions of the scattered high energy XeF_2 molecular beam.

Time-of-flight distributions of the scattered products at m/e=129 upon simultaneous exposure to high energy Xe and XeF_2 have been measured at five detection angles, θ_d, spanning the entire forward scattering region in the scattering plane. Figure 61 shows the TOF distributions of the products at m/e=129 scattered into five detection angles, θ_d, from the simultaneous interaction of high energy Xe and XeF_2 at θ_i=35°. The TOF distributions are signal averaged over a coverage range of 0-0.4 ML F. The results shown in Figures 62, 63, and 64 are taken under identical conditions to those in Figure 61 except that the TOF distributions are signal averaged over coverage ranges of 0.4-0.7 ML F, 0.7-0.9 ML F, and 0.9-1.1 ML F, respectively. The experimental conditions for these measurements are identical to those for the measurements shown in Figures 56-59, except for the intentional introduction of free Xe in the molecular beam. The data from Figures 56-59 are superimposed onto Figures 61-64, respectively, for comparison.

It is apparent that the majority of the signal in the TOF distribution of the scattered products at m/e=129 upon simultaneous exposure to Xe and XeF_2 arises from unreactively scattered Xe. The TOF distribution of unreactively scattered Xe can be isolated by a point-by-point subtraction of the TOF distribution at m/e=129 of the scattered products shown in Figures 56-59 that arise from exposure to only high energy XeF_2. The resulting TOF distributions of

unreactively scattered Xe, which are not shown here, are bimodal with a narrow fast feature and a broad slow feature corresponding to direct-inelastic (DI) and trapping-desorption (TD) scattering mechanisms. A Maxwell-Boltzmann function is fit to each of the two components of the TOF distribution, corresponding to DI scattering and TD scattering, in a stepwise manner analogous to that described in Sec. III.C for unreactively scattered XeF_2. The fits to the DI and TD components of the unreactively scattered Xe are superimposed onto Figures 61-64.

The angular distribution of the unreactively scattered Xe flux can be determined from the integration of the velocity-weighted TOF distributions shown in Figures 61-64. Figure 65 shows a plot of the flux of Xe unreactively scattered from Si(100) via DI scattering and TD scattering as a function of detector angle over four ranges of coverage due to XeF_2 exposure. The flux of Xe unreactively scattered via DI scattering and TD scattering is remarkably insensitive to coverage which is in stark contrast to the strong coverage dependence of the TOF distributions of unreactively scattered XeF_2. The dramatic difference in the unreactive scattering of Xe and XeF_2 as a function of fluorine coverage will be discussed further in Sec. IV.A.

Although the TOF distribution of unreactively scattered Xe has been identified, the contribution, if any, to the TOF distributions of the scattered products at m/e=129 arising from the interaction of high energy XeF_2 is unknown. However, the only detrimental effect of free Xe in the molecular beam is that the TOF distribution of the unreactively scattered Xe, namely the fast DI scattering component, would obscure the fast feature in the TOF distribution at m/e=129 that arises from the reactively scattered products of the interaction of XeF_2 with Si. The use of a low energy XeF_2 beam can minimize this interference by decreasing the intensity of the DI scattering component of the unreactively scattered Xe and shifting it to lower velocities and

hence longer flight times in the TOF distribution at m/e=129. The TOF distributions of the reactively scattered products of the interaction between XeF_2 and Si are not affected by the lower energy of the incident XeF_2 because of the large amount of energy liberated in the exothermic process of F atom abstraction. Indeed, the TOF distribution of the product of single atom abstraction, XeF, is shown in Sec. III.C.2.b to be identical for both low and high energy XeF_2. Assuming that two atom adsorption and single atom abstraction are related processes in the interaction of XeF_2 with Si, an assumption based on one of the main conclusions of the experimental and theoretical study of the interaction between F_2 and Si(100) presented in Chapter 1, the TOF distribution of the product of two atom adsorption, Xe, should also be insensitive to the energy of the incident XeF_2 in the range of 1.8-6.3 kcal/mol.

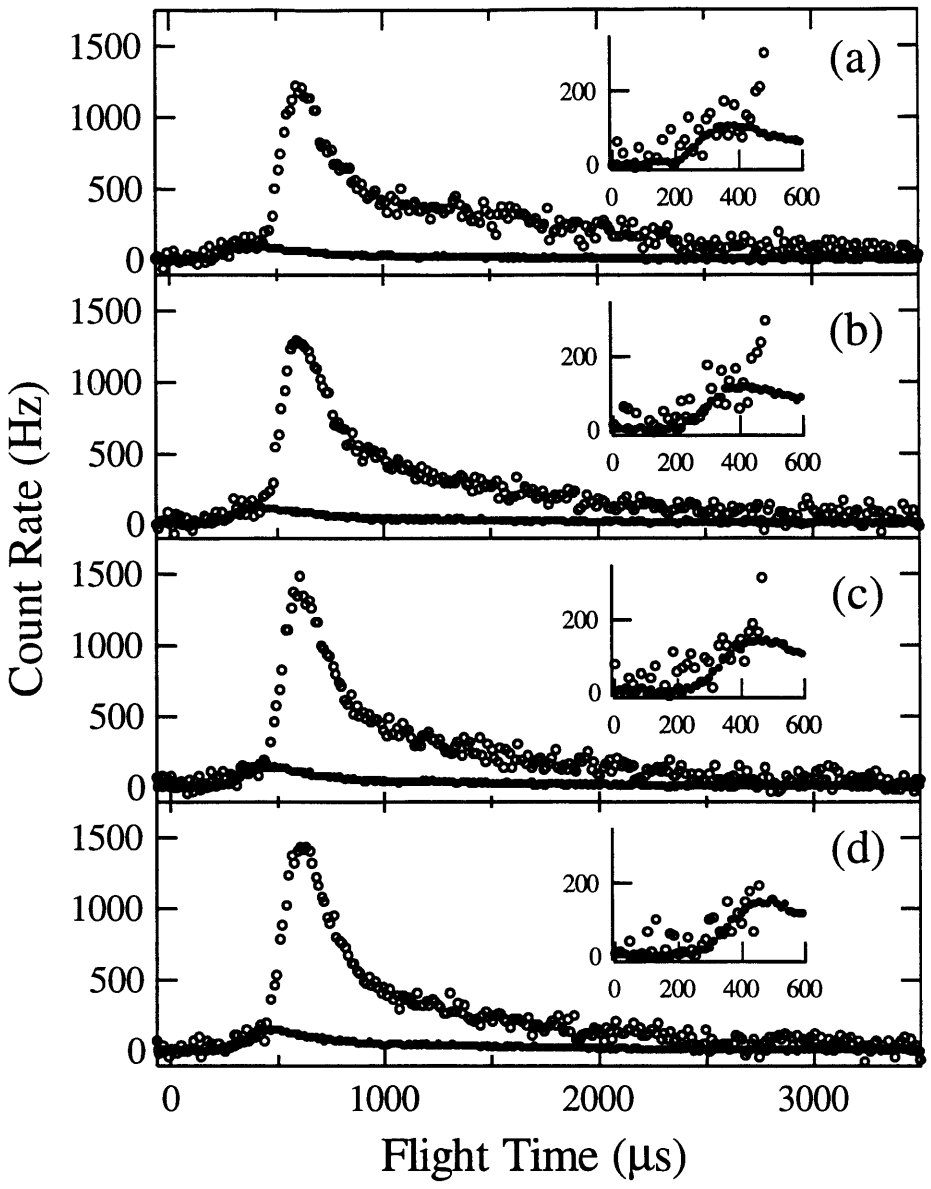

Figure 60 TOF distributions of scattered products at m/e=129 as a function of coverage upon exposure to high energy Xe and XeF_2

TOF spectra at m/e=129 measured at θ_d=0° and T_s=250 K upon exposure to high energy XeF_2 (solid circles) and simultaneous exposure to high energy XeF_2 and Xe (hollow circles) at θ_i=35°. Spectra are averaged over XeF_2 exposures corresponding to coverage ranges of (a) 0-0.4 ML F, (b) 0.4-0.7 ML F, (c) 0.7-0.9 ML F, and (d) 0.9-1.1 ML F. The insets are enlargements of the fast part of the TOF spectra to show the presence of reactively scattered Xe in the TOF distribution of the signal at m/e=129 arising from the simultaneous exposure to high energy XeF_2 and Xe.

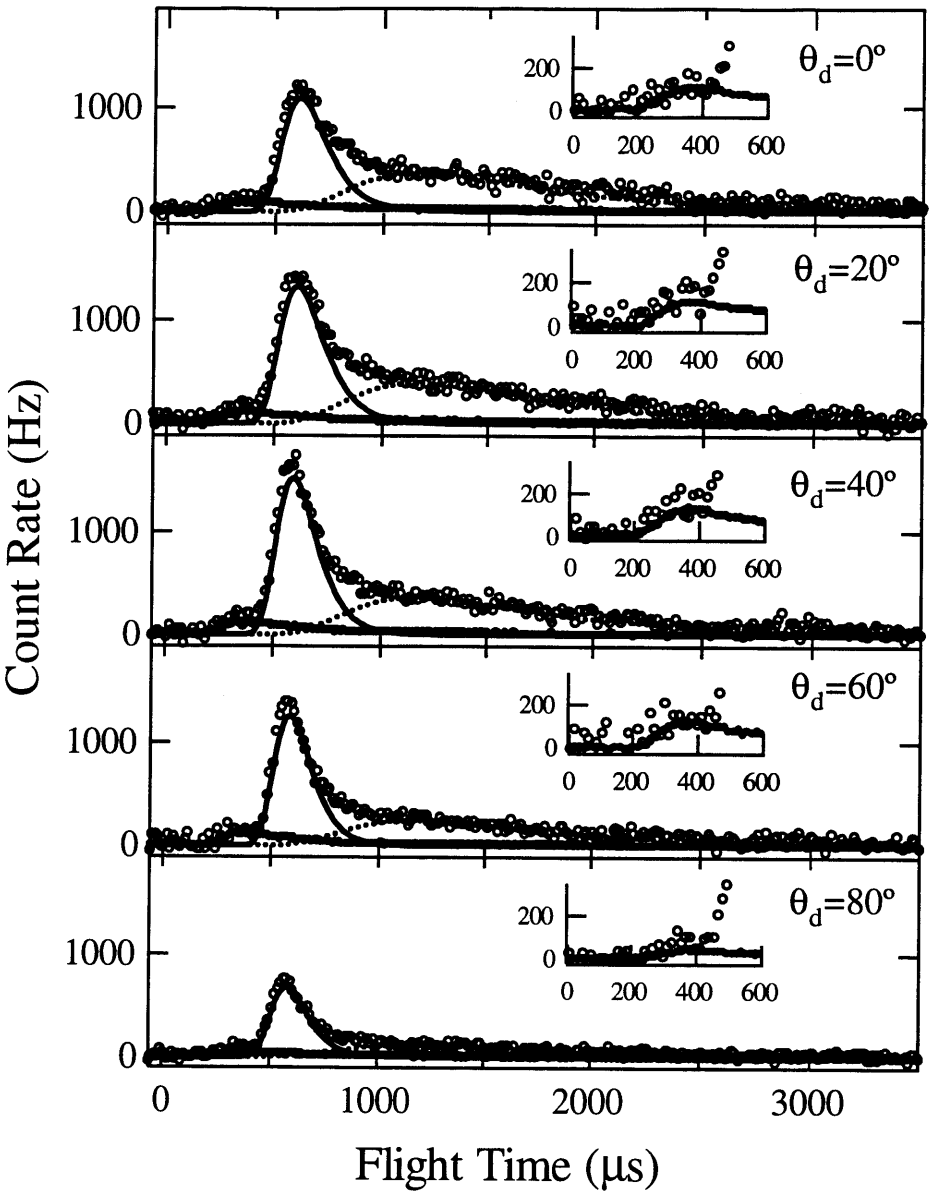

Figure 61 TOF distributions of scattered products at m/e=129 as a function of detector angle over a coverage range of 0-0.4 ML F upon exposure to high energy Xe and XeF_2
TOF spectra at m/e=129 measured at five detector angles θ_d and T_s=250 K upon exposure to high energy XeF_2 (solid circles) and simultaneous exposure to high energy XeF_2 and Xe (hollow circles) at θ_i=35°. The solid and dashed lines show fits to the DI and TD scattering components, respectively, of the TOF distributions of unreactively scattered Xe, which is the difference spectrum of the two TOF spectra in each panel. TOF spectra are averaged over a 10 s high energy XeF_2 exposure corresponding to a fluorine coverage range of 0-0.4 ML F. The insets are enlargements of the fast part of the TOF spectra to show the presence of reactively scattered Xe in the TOF distribution arising from the simultaneous exposure to high energy XeF_2 and Xe.

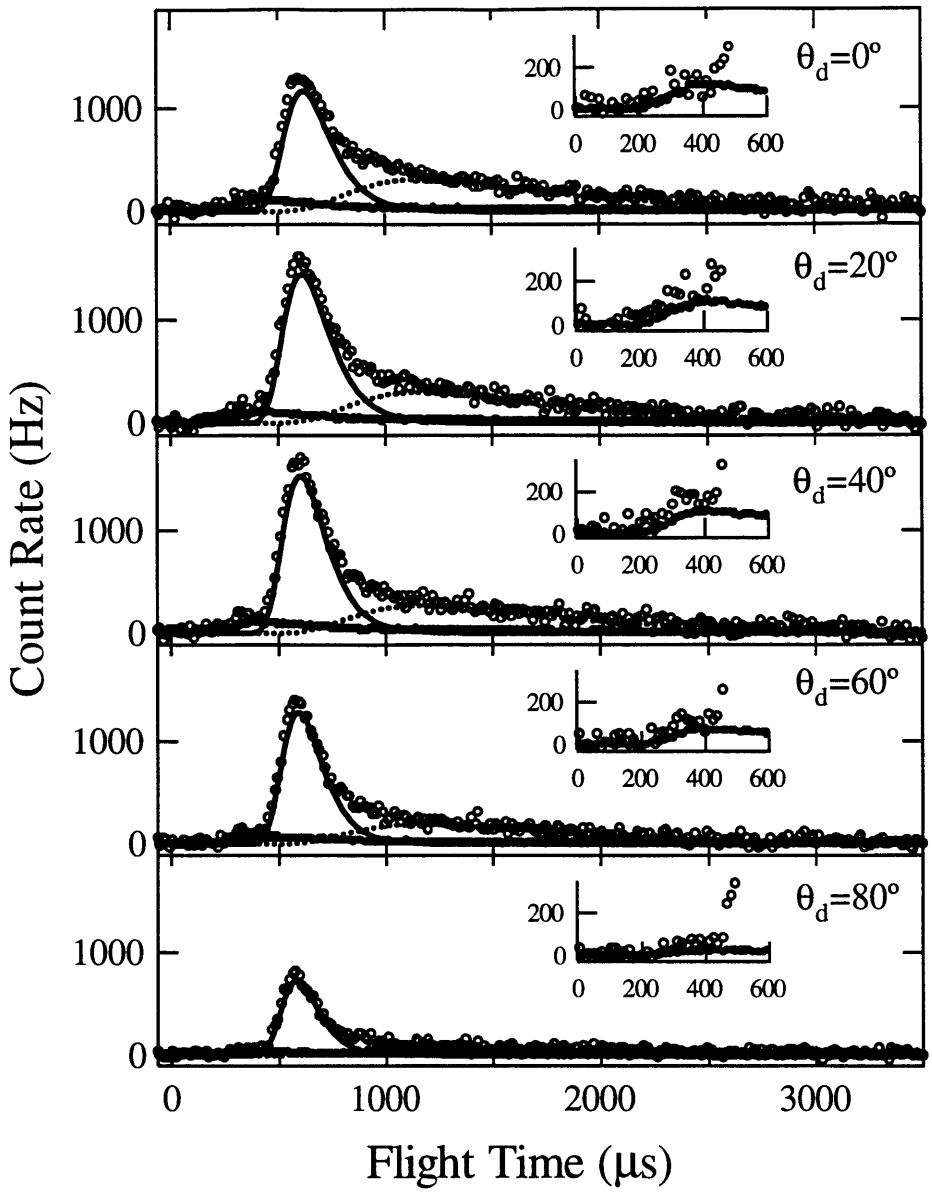

Figure 62 TOF distributions of scattered products at m/e=129 as a function of detector angle over a coverage range of 0.4-0.7 ML F upon exposure to high energy Xe and XeF_2
TOF spectra at m/e=129 measured at five detector angles θ_d and T_s=250 K upon exposure to high energy XeF_2 (solid circles) and simultaneous exposure to high energy XeF_2 and Xe (hollow circles) at θ_i=35°. The solid and dashed lines show fits to the DI and TD scattering components, respectively, of the TOF distributions of unreactively scattered Xe, which is the difference spectrum of the two TOF spectra in each panel. Spectra are averaged over a 10 s high energy XeF_2 exposure corresponding to a fluorine coverage range of 0.4-0.7 ML F. The insets are enlargements of the fast part of the TOF spectra to show the presence of reactively scattered Xe in the TOF distribution arising from the simultaneous exposure to high energy XeF_2 and Xe.

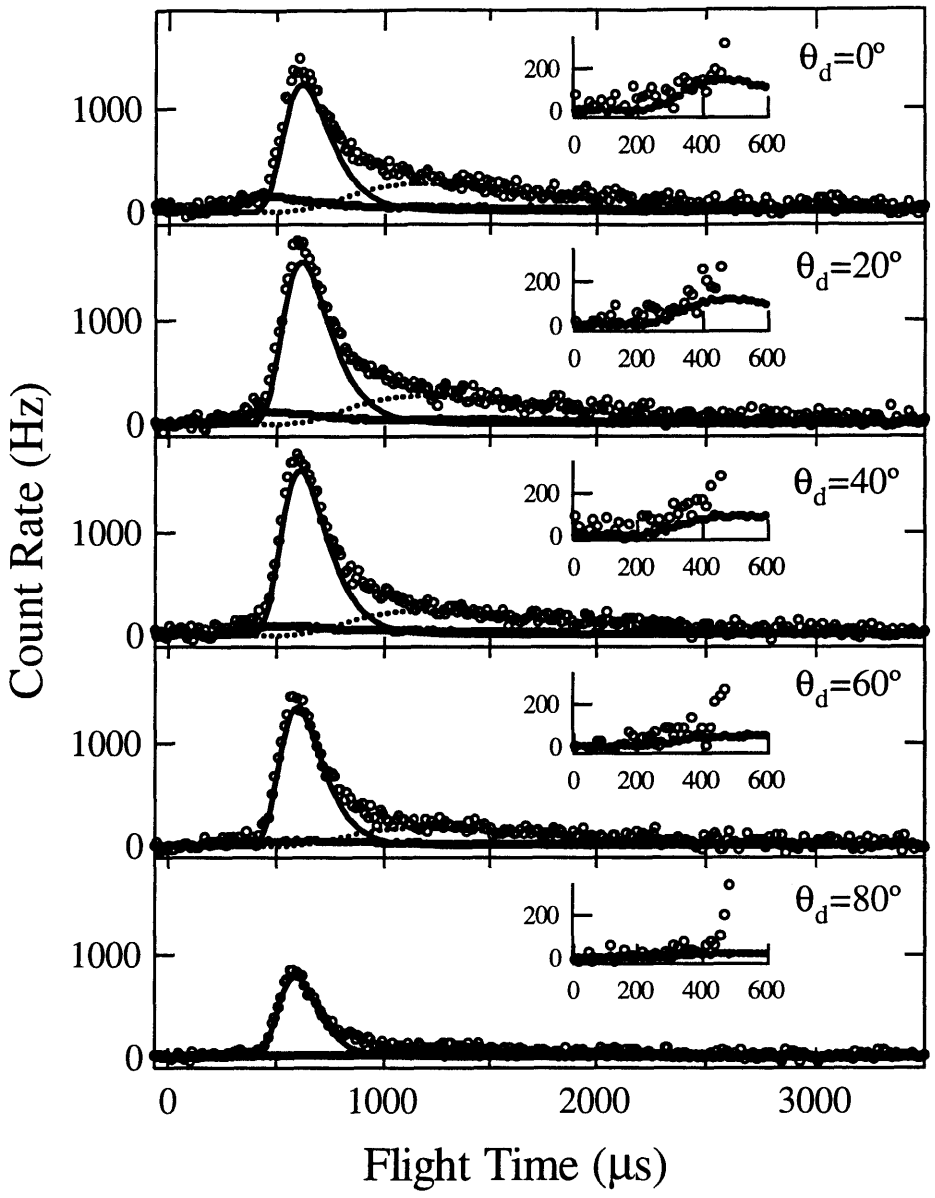

Figure 63 TOF distributions of scattered products at m/e=129 as a function of detector angle over a coverage range of 0.7-0.9 ML F upon exposure to high energy Xe and XeF_2
TOF spectra at m/e=129 measured at five detector angles θ_d and T_s=250 K upon exposure to high energy XeF_2 (solid circles) and simultaneous exposure to high energy XeF_2 and Xe (hollow circles) at θ_i=35°. The solid and dashed lines show fits to the DI and TD scattering components, respectively, of the TOF distributions of unreactively scattered Xe, which is the difference spectrum of the two TOF spectra in each panel. Spectra are averaged over a 10 s high energy XeF_2 exposure corresponding to a fluorine coverage range of 0.7-0.9 ML F. The insets are enlargements of the fast part of the TOF spectra to show the presence of reactively scattered Xe in the TOF distribution arising from the simultaneous exposure to high energy XeF_2 and Xe.

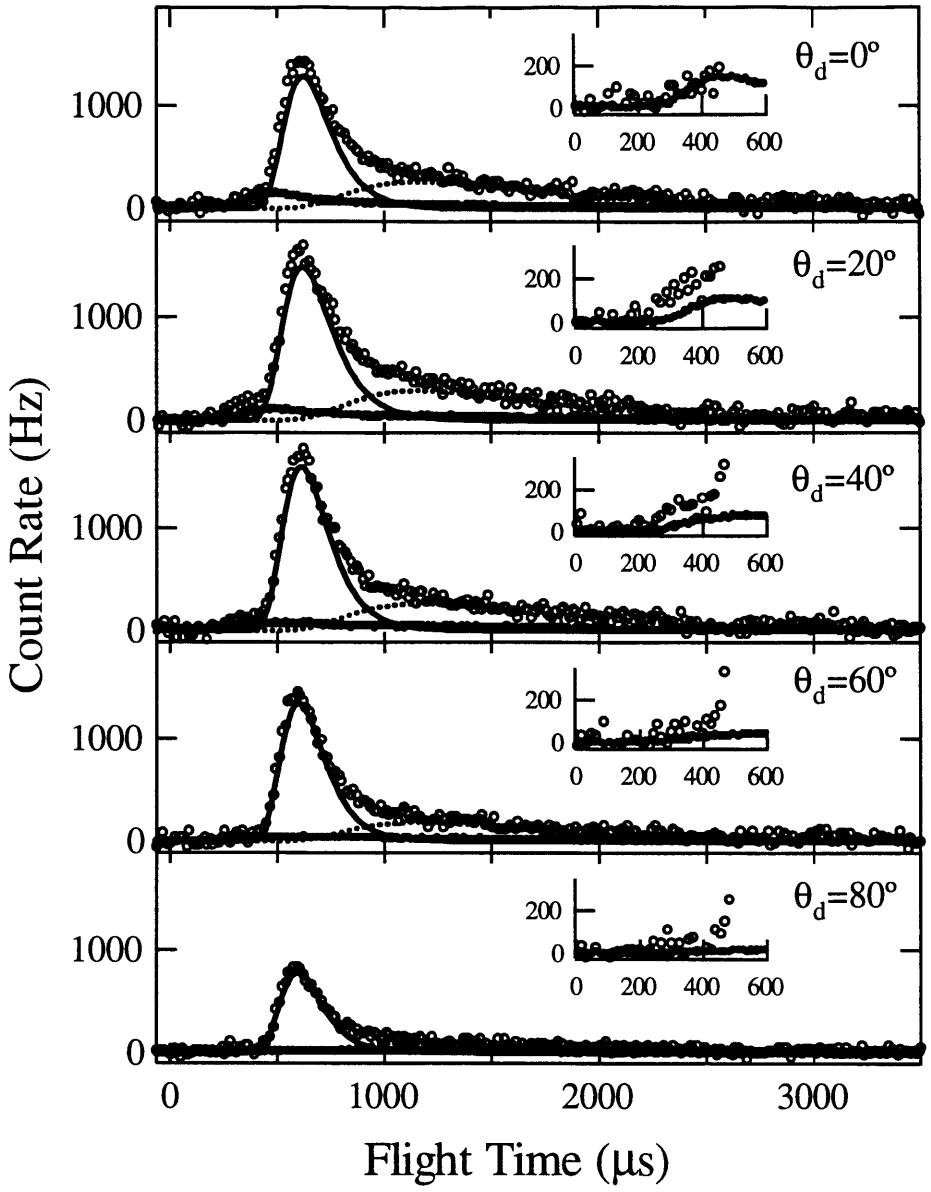

Figure 64 TOF distributions of scattered products at m/e=129 as a function of detector angle over a coverage range of 0.9-1.1 ML F upon exposure to high energy Xe and XeF_2
TOF spectra at m/e=129 measured at five detector angles θ_d and T_s=250 K upon exposure to high energy XeF_2 (solid circles) and simultaneous exposure to high energy XeF_2 and Xe (hollow circles) at θ_i=35°. The solid and dashed lines show fits to the DI and TD scattering components, respectively, of the TOF distributions of unreactively scattered Xe, which is the difference spectrum of the two TOF spectra in each panel. Spectra are averaged over a 10 s high energy XeF_2 exposure corresponding to a fluorine coverage range of 0.9-1.1 ML F. The insets are enlargements of the fast part of the TOF spectra to show the presence of reactively scattered Xe in the TOF distribution arising from the simultaneous exposure to high energy XeF_2 and Xe.

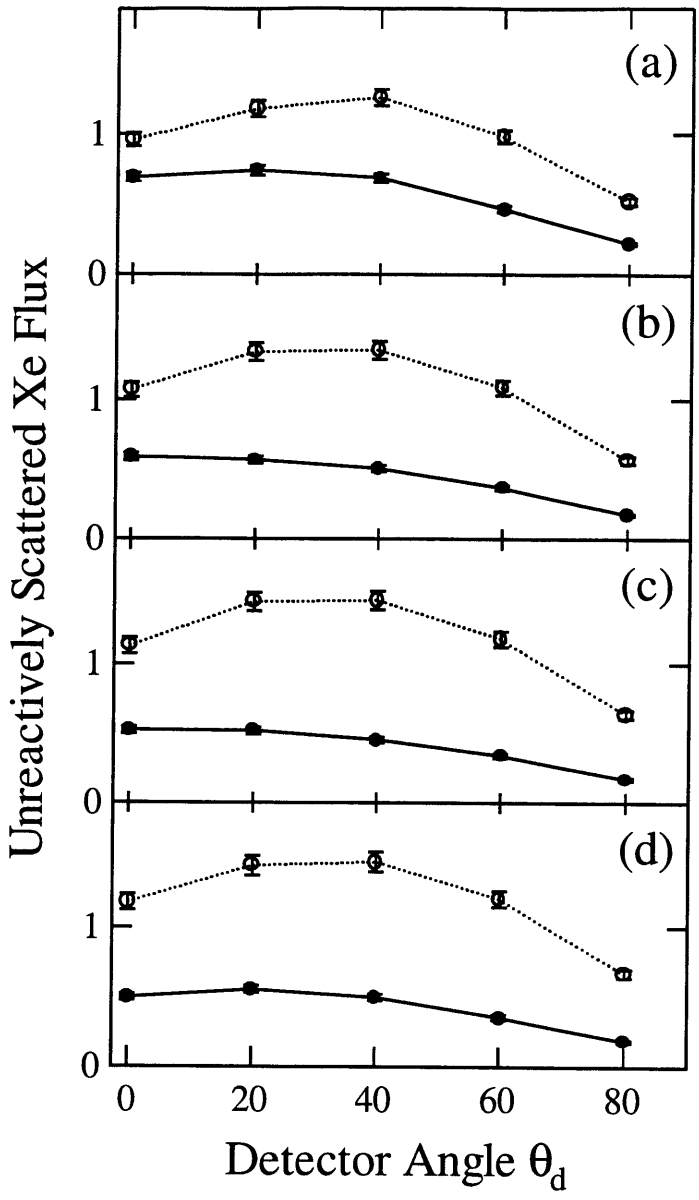

Figure 65 Angular distribution of flux of Xe unreactively scattered from Si(100)
Unreactively scattered flux of Xe determined from velocity-weighted integration of the fits to the TOF distributions shown in Figures 61-64 of unreactively scattered Xe attributable to DI scattering (hollow circles) and TD scattering (solid circles) as a function of detector angle over successive 10 s high energy XeF_2 exposure intervals corresponding to coverage ranges of (a) 0-0.4 ML F, (b) 0.4-0.7 ML F, (c) 0.7-0.9 ML F, and (d) 0.9-1.1 ML F. Error bars represent uncertainty of the integral of the fit to the TOF distribution.

III.C.4.b. Low incident energy XeF_2 (E_i=1.8 kcal/mol)

Figure 66 shows a TOF distribution of the products at m/e=129 that are scattered as a result of the interaction of low energy XeF_2 with Si(100) at 250 K. The TOF distribution is for a scattering geometry in which the XeF_2 beam is along the surface normal, θ_i=0°, and the detector is positioned at θ_d=35°. The TOF distribution is signal averaged over an exposure to low energy XeF_2 that corresponds to a fluorine coverage range of 0-1.1 ML. The TOF distribution at m/e=129 is bimodal with a narrow fast feature and a broad slow feature. Analogous to Figure 54, the fit to the XeF_2 TOF distribution shown in Figure 23 is scaled by the XeF_2 cracking ratio and superimposed onto the TOF distribution at m/e=129 in Figure 66. Comparison of Figure 66 with Figure 54 shows that the TOF distributions at m/e=129 arising from the interaction of low and high energy XeF_2 with Si are remarkably similar. The TOF distribution in Figure 66 is signal averaged over a 24 s exposure to low energy XeF_2. To test the exposure dependence of the scattered signal at m/e=129, TOF distributions have been signal averaged over shorter 6 s exposures to low energy XeF_2. Figure 67 shows the TOF distributions at m/e=129 signal averaged over four successive 6 s exposures to low energy XeF_2. The fast feature in the TOF distributions decreases in intensity as a function of XeF_2 exposure and shifts slightly to longer flight times. Although these observations are analogous to those of the TOF distributions of the scattered products at m/e=129 as a result of the interaction of high energy XeF_2 with Si, a more direct comparison can be made which allows for the isolation of the TOF distribution of the reactively scattered Xe.

The contribution of unreactively scattered Xe, if present, to the fast feature in the TOF distribution at m/e=129 arising from the interaction of low energy XeF_2 is minimal because the

TOF distribution of unreactively scattered Xe is shifted to longer flight times as a result of the lower incident energy. The same is true for the contribution of unreactively scattered XeF_2 to the fast feature of the TOF distribution at m/e=129. In fact, the maximum contribution from XeF_2 to the entire TOF distribution at m/e=129 can be separated by subtracting the signal at m/e=167 multiplied by the maximum XeF_2 cracking ratio. The maximum contribution of unreactively scattered XeF_2 is superimposed on the TOF distribution of the scattered products at m/e=129 in Figures 66-67. With the unreactively scattered products shifted away from the fast feature, there are only three contributions to the fast feature in the TOF distribution of the scattered products at m/e=129: XeF from single atom abstraction, and reactively scattered Xe arising from both two atom adsorption and XeF dissociation.

Assuming that the TOF distribution of the reactively scattered products at m/e=129 is reasonably insensitive to incident XeF_2 energy over the range 1.8-6.3 kcal/mol, a simple self-consistent analysis is used to separate the contribution from XeF arising from single atom abstraction. Although it has been shown that the maximum XeF cracking ratio is 8 in Figures 56-59, it is improbable that this value is realistic since it assumes that under certain conditions all of the fast feature in the TOF distribution of the scattered products at m/e=129 is from XeF arising from single atom abstraction. Instead, an ideal XeF cracking ratio is determined by point-by-point subtraction of the TOF distribution of scattered XeF multiplied by a scaling factor from the TOF distribution of scattered products at m/e=129 from both low and high energy XeF_2 such that the shape of the fast features of the TOF distributions for the two incident energies are similar. Figure 68 is a plot of the TOF distributions of scattered products at m/e=129 that are attributed to reactively scattered Xe as a function of fluorine coverage due to exposure to low

and high XeF_2. The signal attributed to Xe results from the point-by-point subtraction of the contributions of XeF_2 and XeF from the signal at m/e=129. The ideal XeF cracking ratio is 4, which is half of the maximum possible value according to the results presented in Sec. III.C.3.a.ii. Note that no unreactively scattered Xe contribution has been subtracted from the TOF distributions suggesting that the contribution of unreactively scattered Xe to the signal at m/e=129 may not be significant, even in the high energy XeF_2 results. The low energy results are scaled by a factor of two to match the signal intensities.

The TOF distributions of the scattered products at m/e=129 arising from the interaction of low and high energy XeF_2 are remarkably similar. In particular, the fast feature of the TOF distributions are similar suggesting that the reactively scattered products are indeed reasonably insensitive to incident energy in the range 1.8-6.3 kcal/mol. The slow features of the TOF distributions are described well by a velocity distribution arising from the TD scattering of Xe. Although the shapes of the TOF distributions are similar, the relative intensity of the slow feature with respect to the fast feature is greater for the low energy XeF_2 than the high energy XeF_2. This subtle difference is certainly a result of the different scattering kinematics at different incident energies. In particular, the possible presence of free Xe in both the low and high energy XeF_2 would be extremely sensitive to this effect because it is unreactively scattered and cannot gain significant energy from the surface. This incident energy effect is exemplified by the TOF distributions of unreactively scattered XeF_2 that result from the interaction of both low and high energy XeF_2 with Si.

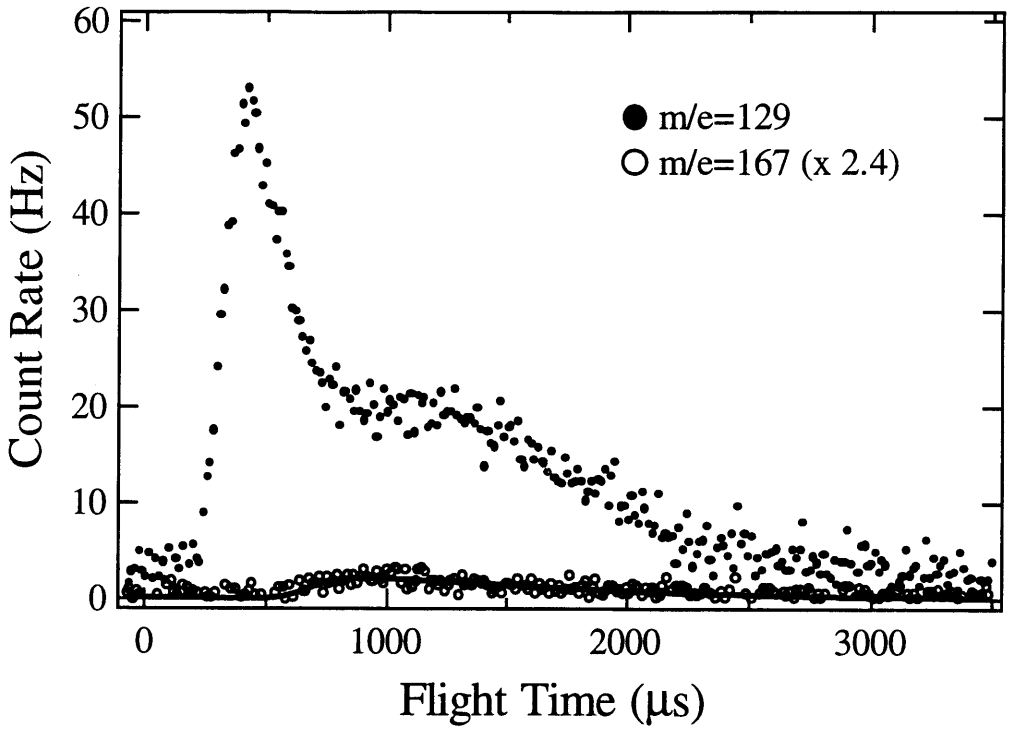

Figure 66 TOF distribution of scattered products at m/e=129 upon exposure to low energy XeF_2

TOF spectrum at m/e=129 measured at θ_d=35° and T_s=250 K upon exposure to low energy XeF_2 at θ_i=0°. Signal at m/e=167, taken from Figure 23, is multiplied by maximum XeF_2 cracking ratio and superimposed to show maximum contribution from unreactively scattered XeF_2. The solid line shows the fit to the TOF distribution at m/e=167 multiplied by the maximum XeF2 cracking ratio.

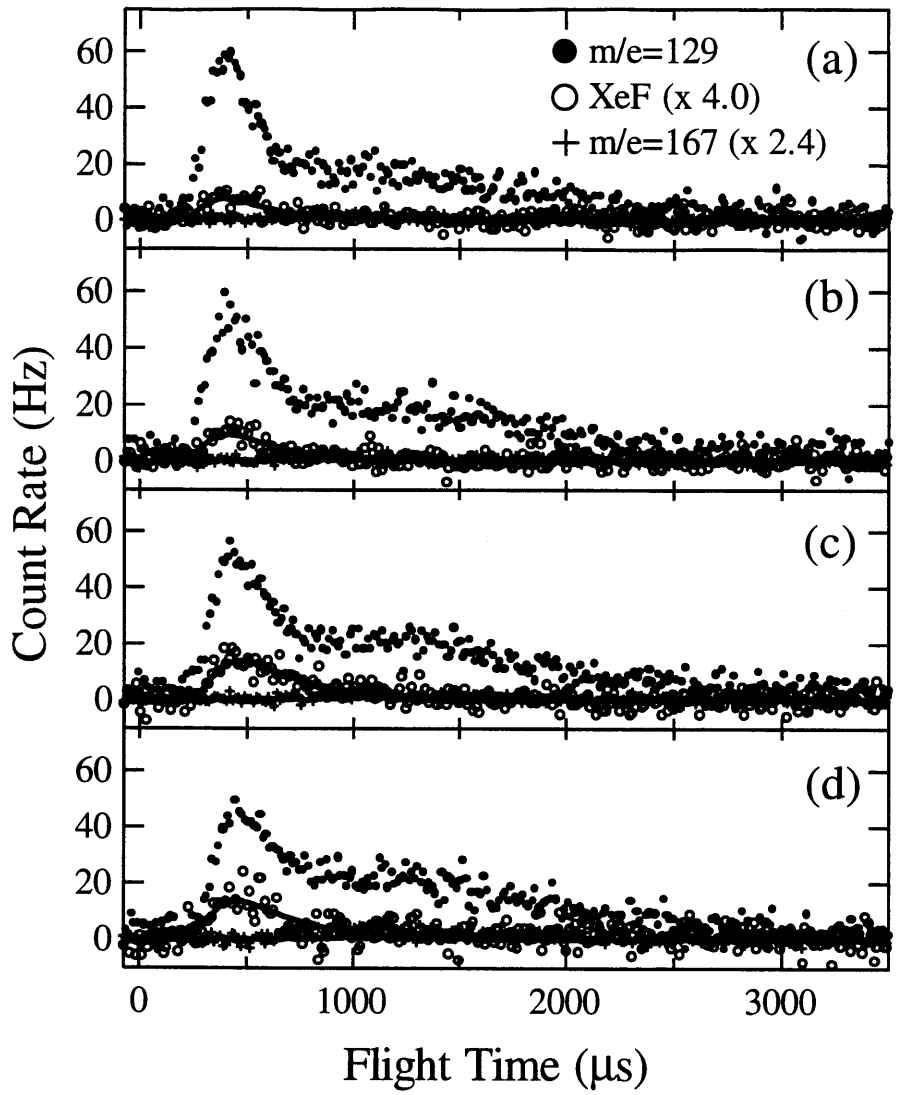

Figure 67 TOF distribution of scattered products at m/e=129 as a function of coverage upon exposure to low energy XeF_2

TOF spectra of scattered Xe measured at θ_d=35° and T_s=250 K upon exposure to low energy XeF_2 at θ_i=0°. The TOF distribution at m/e=167 multiplied by the maximum XeF_2 cracking ratio and the TOF distribution of XeF (hollow circles) multiplied by an optimized scaling factor of 4.0 are superimposed for comparison. Solid lines show fits to the TOF distributions of XeF_2 and XeF. Spectra are averaged over XeF_2 exposures corresponding to coverage ranges of (a) 0-0.4 ML F, (b) 0.4-0.7 ML F, (c) 0.7-0.9 ML F, and (d) 0.9-1.1 ML F.

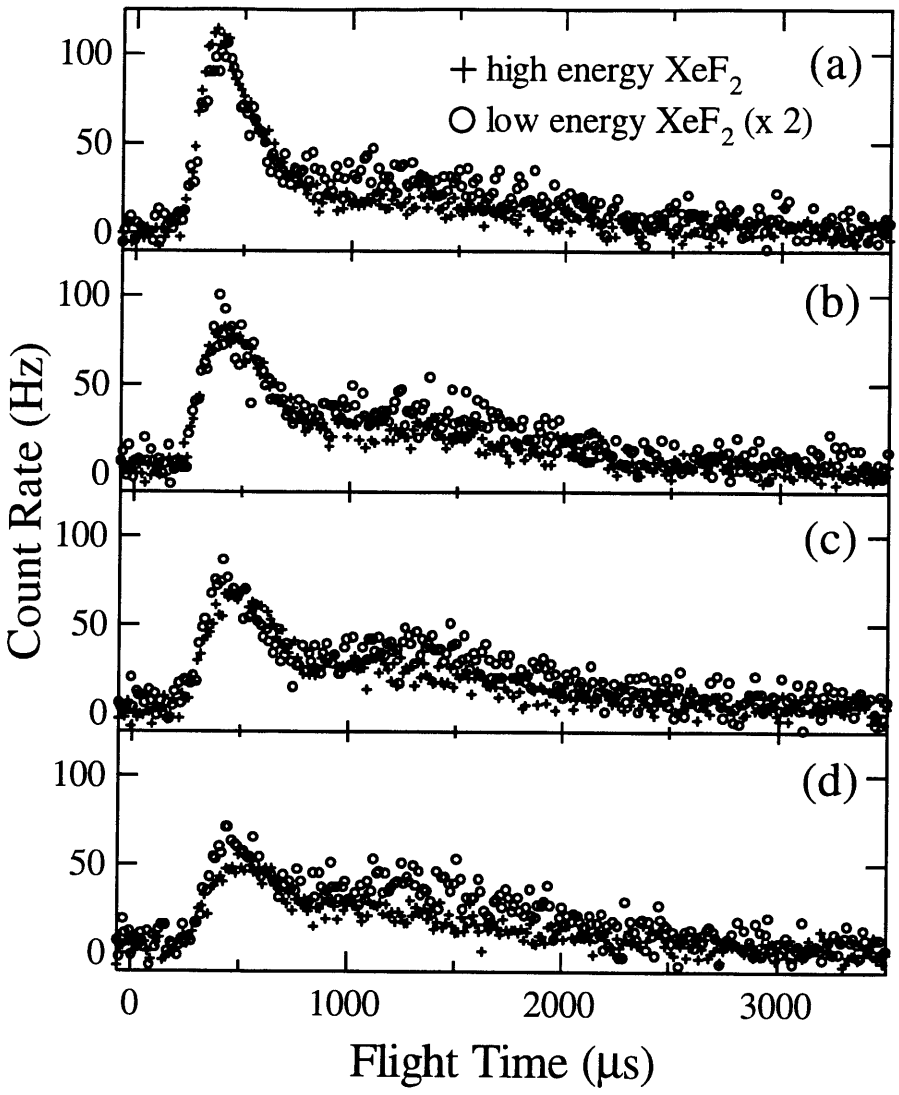

Figure 68 TOF distribution of reactively scattered Xe as a result of the interaction of low and high energy XeF_2 with Si as a function of coverage

TOF spectra of reactively scattered Xe measured at T_s=250 K upon exposure to low energy XeF_2 (solid circles) and high energy XeF_2 (crosses). For the low energy XeF_2, the scattering geometry is θ_i=0° and θ_d=35°; for the high energy XeF_2, the scattering geometry is θ_i=35° and θ_d=40°. The Xe TOF distribution is obtained by point-by-point subtraction of m/e=167 signal multiplied by XeF_2 cracking ratio and the XeF signal multiplied by an optimized scaling factor of 4.0. Spectra are averaged over XeF_2 exposures corresponding to coverage ranges of (a) 0-0.4 ML F, (b) 0.4-0.7 ML F, (c) 0.7-0.9 ML F, and (d) 0.9-1.1 ML F.

III.C.4.c. Angular distribution of reactively scattered Xe

Analogous to the XeF_2 and XeF TOF measurements in Sec. III.C.1 and Sec. III.C.2, TOF distributions at m/e=129 were measured at several detection angles θ_d spanning the entire forward scattering region in the scattering plane and signal averaged over shorter 10 s XeF_2 exposure intervals. Figure 69 shows the TOF distributions of the reactively scattered Xe into five detection angles, θ_d, from the interaction of high energy XeF_2 at θ_i=35°. The XeF_2 contribution was separated by subtracting the TOF distribution at m/e=167 multiplied by the XeF_2 cracking ratio. The XeF contribution was separated by subtracting the TOF distribution of XeF multiplied by the XeF cracking ratio determined in the previous section. The TOF distributions are signal averaged over a coverage range of 0-0.4 ML F. The results shown in Figures 70, 71, and 72 were measured under identical conditions to those in Figure 69 except that the TOF distributions are signal averaged over coverage ranges of 0.4-0.7 ML F, 0.7-0.9 ML F, and 0.9-1.1 ML F, respectively. A bimodal velocity distribution is fit to the TOF distributions. The slow component is attributed to a scattering mechanism analogous to trapping-desorption and is described by a Maxwell-Boltzmann function for Xe at a temperature of 250 K, the surface temperature. The rest of the TOF distribution is attributed to a scattering mechanism that yields fast Xe atoms and is described by a Maxwell-Boltzmann function that is analogous to the unreactive DI scattering of XeF_2 and free Xe. Figure 73 shows plots of the angular distribution of the flux of fast and slow Xe scattered from Si(100) parameterized by fluorine coverage due to XeF_2 exposure. The flux of Xe is defined as the integral of the velocity-weighted TOF distributions of the fast and slow components. The angular distributions of both components are cosinelike. The magnitude of the slow component is insensitive to fluorine coverage, whereas

the magnitude of the fast component decays monotonically with coverage. Figure 74 shows a plot of the average translational energy of the fast component of the reactively scattered Xe as a function of detector angle as well as fluorine coverage. The average translational energy of the fast component of reactively scattered Xe from the interaction of low energy XeF_2 with Si measured at a single detector angle is superimposed for comparison. Not only is the translational energy insensitive to detector angle, but it is also insensitive to incident energy over the range 1.8-6.3 kcal/mol. However, the translational energy of the fast component of the reactively scattered Xe decreases with fluorine coverage. All of these features of the reactively scattered Xe are reminiscent of those of the scattered XeF arising from single atom abstraction.

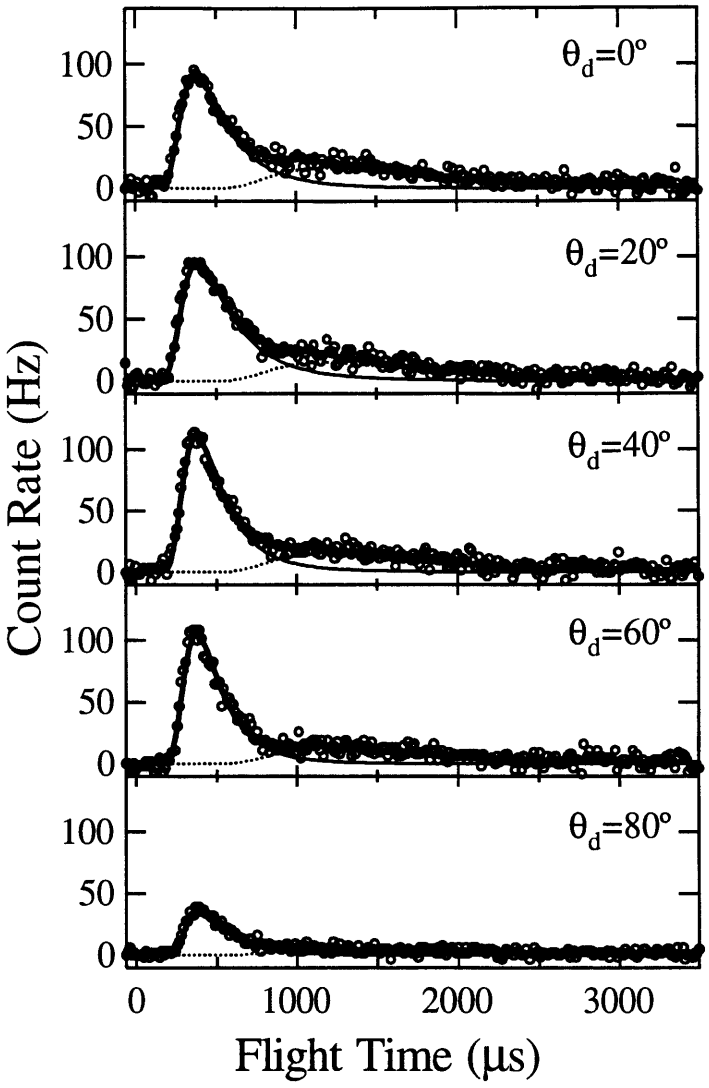

Figure 69 TOF distribution of reactively scattered Xe as a function of detector angle over a coverage range of 0-0.4 ML F

TOF spectra of reactively scattered Xe measured at five detector angles θ_d and T_s=250 K upon exposure to high energy XeF_2 at θ_i=35°. The Xe TOF distribution is obtained by point-by-point subtraction of m/e=167 signal multiplied by the maximum XeF_2 cracking ratio and the XeF signal multiplied by an optimized scaling factor of 4.0. Fit to TOF distribution (thick line) is separated into two components representing DI scattering (thin solid line) and TD scattering (thin dashed line). Spectra are averaged over XeF_2 exposure corresponding to a fluorine coverage range of 0-0.4 ML F.

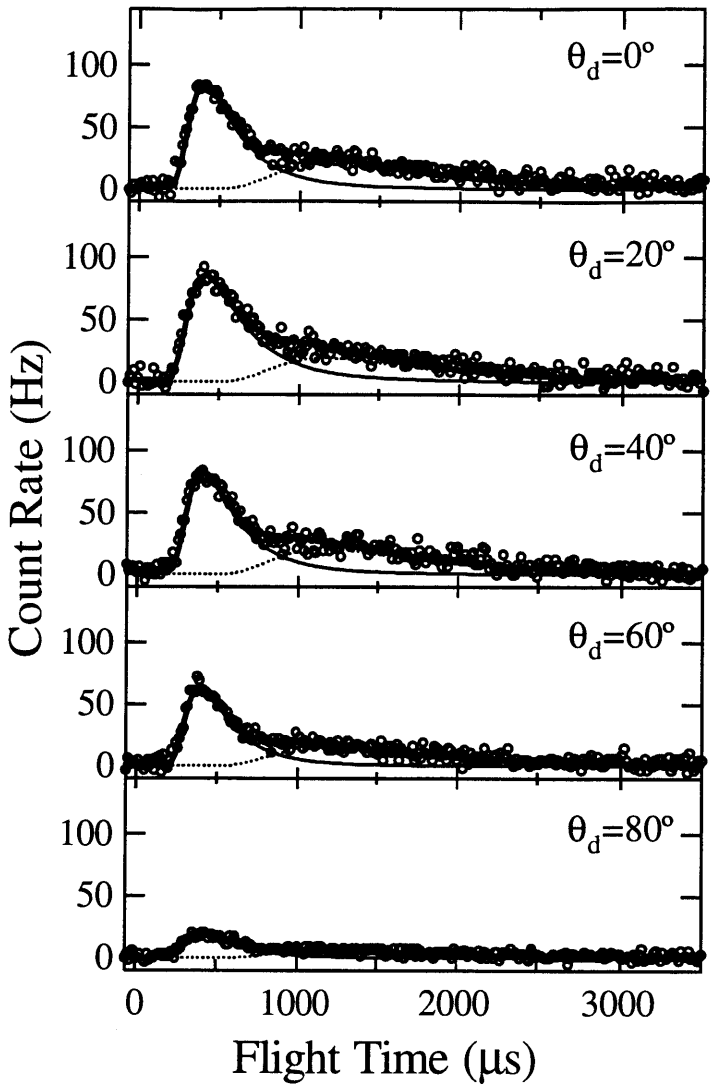

Figure 70 TOF distribution of reactively scattered Xe as a function of detector angle over a coverage range of 0.4-0.7 ML F

TOF spectra of reactively scattered Xe measured at five detector angles θ_d and T_s=250 K upon exposure to high energy XeF_2 at θ_i=35°. The Xe TOF distribution is obtained by point-by-point subtraction of m/e=167 signal multiplied by the maximum XeF_2 cracking ratio and the XeF signal multiplied by an optimized scaling factor of 4.0. Fit to TOF distribution (thick line) is separated into two components representing DI scattering (thin solid line) and TD scattering (thin dashed line). Spectra are averaged over XeF_2 exposure corresponding to a fluorine coverage range of 0.4-0.7 ML F.

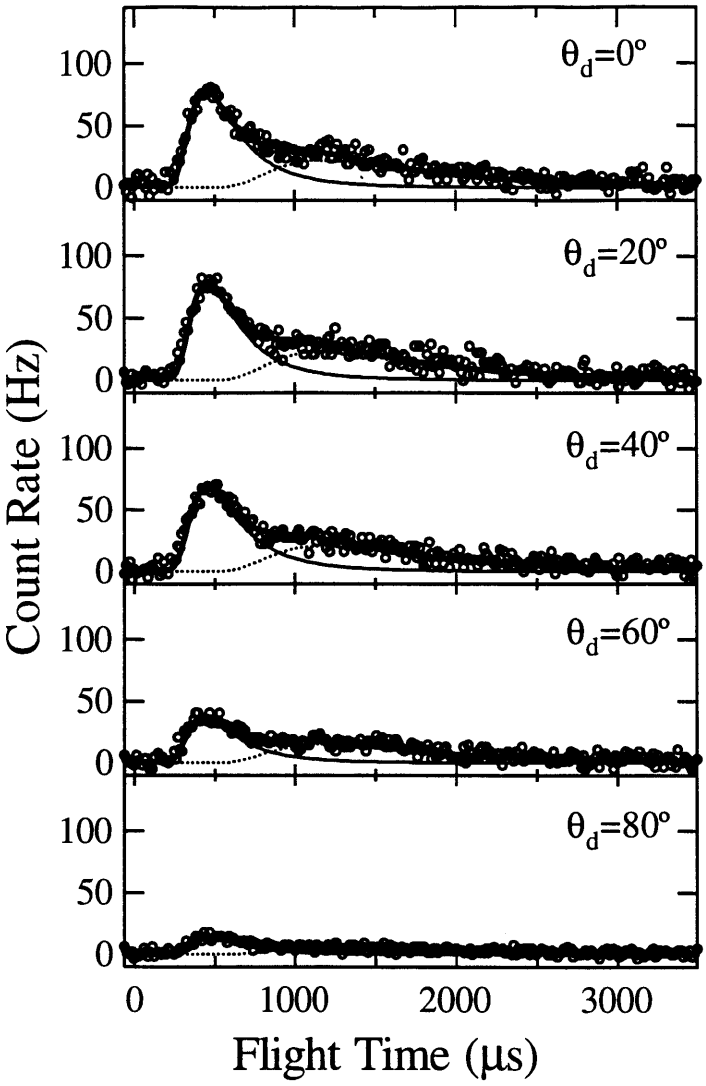

Figure 71 TOF distribution of reactively scattered Xe as a function of detector angle over a coverage range of 0.7-0.9 ML F

TOF spectra of reactively scattered Xe measured at five detector angles θ_d and T_s=250 K upon exposure to high energy XeF_2 at θ_i=35°. The Xe TOF distribution is obtained by point-by-point subtraction of m/e=167 signal multiplied by the maximum XeF_2 cracking ratio and the XeF signal multiplied by an optimized scaling factor of 4.0. Fit to TOF distribution (thick line) is separated into two components representing DI scattering (thin solid line) and TD scattering (thin dashed line). Spectra are averaged over XeF_2 exposure corresponding to a fluorine coverage range of 0.7-0.9 ML F.

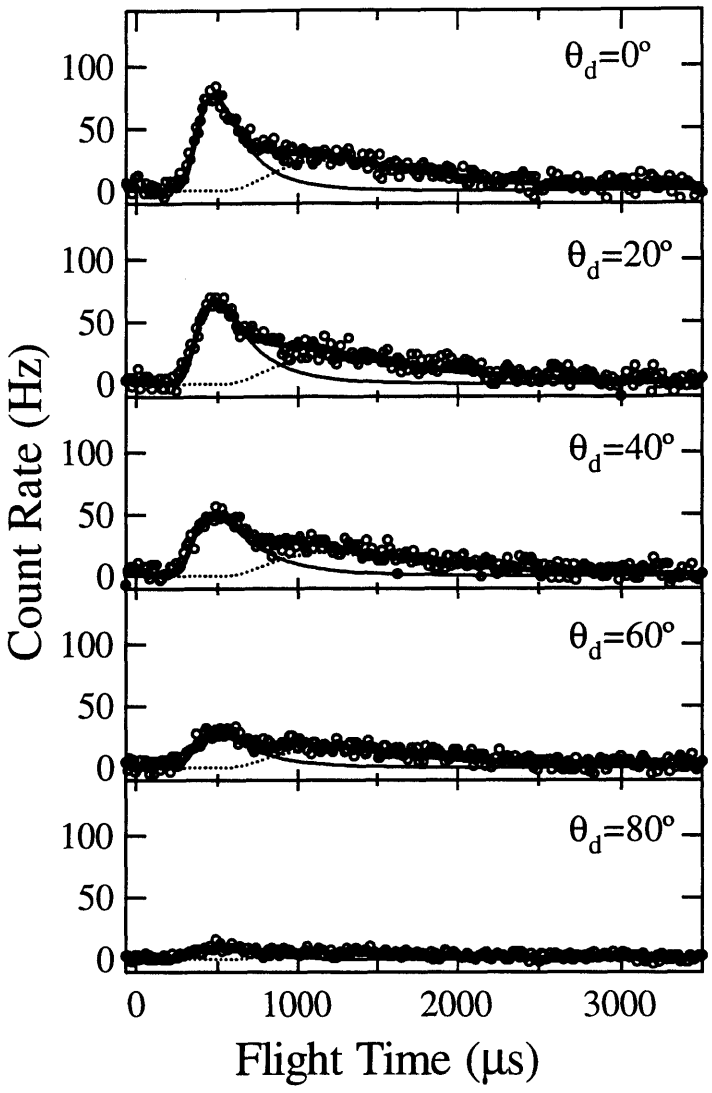

Figure 72 TOF distribution of reactively scattered Xe as a function of detector angle over a coverage range of 0.9-1.1 ML F

TOF spectra of reactively scattered Xe measured at five detector angles θ_d and T_s=250 K upon exposure to high energy XeF_2 at θ_i=35°. The Xe TOF distribution is obtained by point-by-point subtraction of m/e=167 signal multiplied by the maximum XeF_2 cracking ratio and the XeF signal multiplied by an optimized scaling factor of 4.0. Fit to TOF distribution (thick line) is separated into two components representing DI scattering (thin solid line) and TD scattering (thin dashed line). Spectra are averaged over XeF_2 exposure corresponding to a fluorine coverage range of 0.9-1.1 ML F.

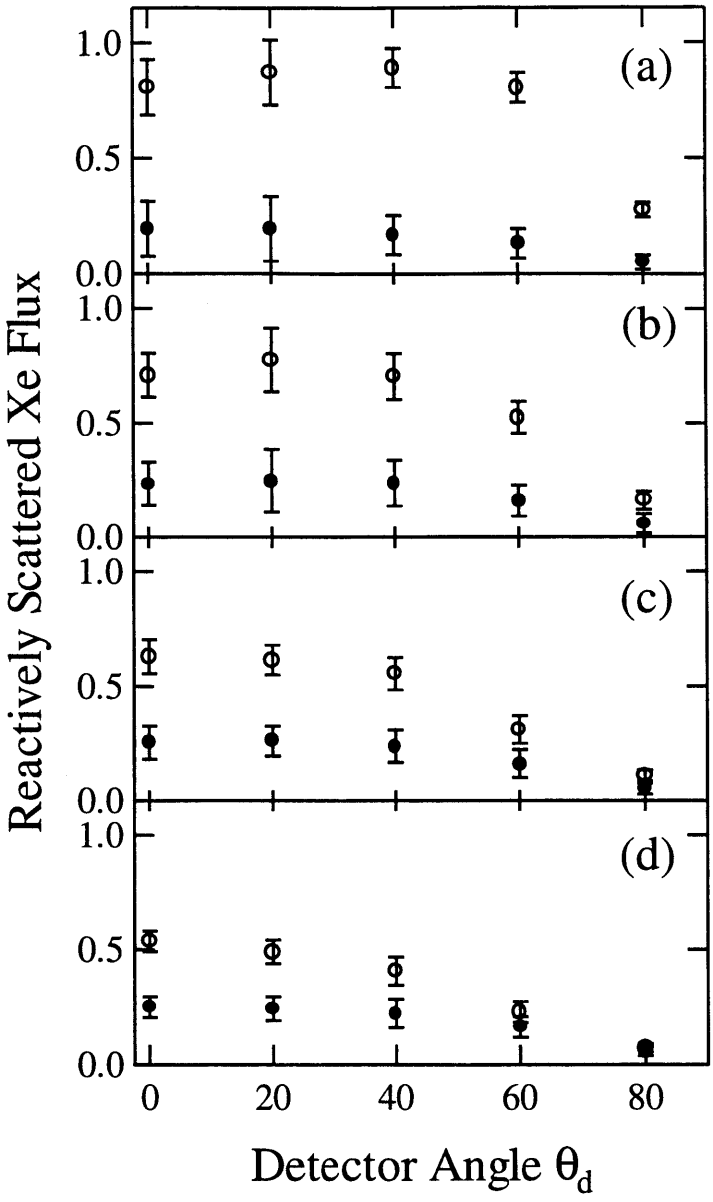

Figure 73 Angular distribution of flux of Xe reactively scattered from Si(100)
Reactively scattered flux of Xe determined from velocity-weighted integration of the fits to the TOF distributions shown in Figures 69-72 attributable to DI scattering (hollow circles) and TD scattering (solid circles) as a function of detector angle over successive 10 s high energy XeF_2 exposure intervals corresponding to coverage ranges of (a) 0-0.4 ML F, (b) 0.4-0.7 ML F, (c) 0.7-0.9 ML F, and (d) 0.9-1.1 ML F. Error bars represent uncertainty of the integral of the fit to the TOF distribution.

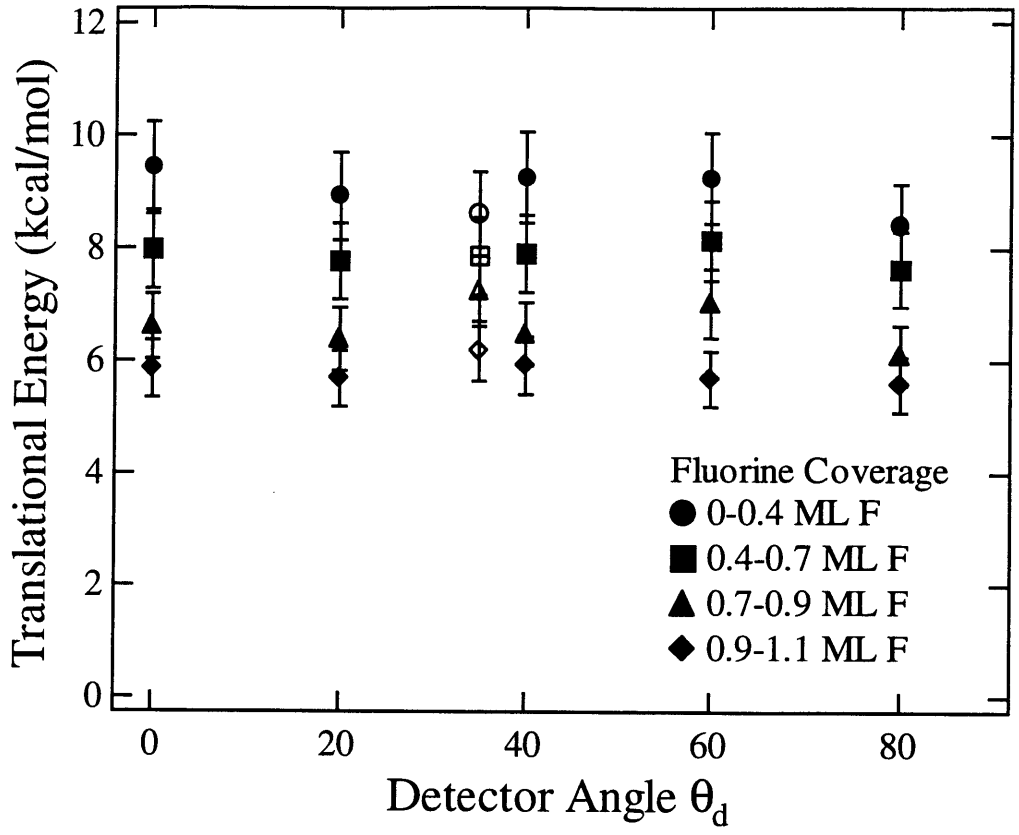

Figure 74 Translational energy of fast Xe reactively scattered from Si(100) as a function of detector angle

Average translational energy of fast Xe reactively scattered as a result of exposure to high energy XeF_2 (solid symbols) and low energy XeF_2 (hollow symbols) as a function of detector angle over four different fluorine coverage ranges. The average translational energy is determined from the velocity-weighted TOF distributions shown in Figures 69-72. Error bars represent the uncertainty of the determination of the average translational energy (Sec. II.D) from the fits to the TOF distributions.

IV. DISCUSSION

A picture of the interaction of XeF_2 with Si(100) is apparent from these experimental results. In general, the interaction of XeF_2 with Si(100) is remarkably similar to the interaction of F_2 with Si(100), especially at fluorine coverages below 1 ML. Three basic scattering channels are present in both XeF_2 and F_2: unreactive scattering and dissociative chemisorption via single atom abstraction and two atom adsorption. In the event of dissociative chemisorption, the adsorption of fluorine occurs at the Si dangling bonds and no Si lattice bonds, not even Si dimer bonds, are broken according to thermal desorption and He diffraction results. However at a coverage around 1 ML F, F_2 ceases to react with the Si surface whereas XeF_2 continues to react, breaking Si dimer bonds and Si lattice bonds, resulting in etching, the removal of Si from the surface.

The focus of this investigation is the initial fluorination of Si up to a coverage of 1 ML F upon exposure to XeF_2 to allow for comparison of these results to those of the interaction of F_2 with Si presented in Chapter 1. There are significant differences between the two fluorine compounds. First, whereas the reaction probability of F_2 displays a strong coverage dependence, the reaction probability of XeF_2 is only weakly dependent on coverage. Unreactive scattering is the subject of Sec IV.A. Second, the velocity of the scattered F atom that results from single atom abstraction in the interaction of F_2 with Si is independent of coverage and the angular distribution of the scattered F atom is isotropic over the entire coverage range 0-1 ML F. This is in stark contrast to the velocity and angular distribution of the scattered XeF which is strongly dependent on the coverage. Single atom abstraction is the subject of Sec. IV.B. Finally, the spectator atom Xe in XeF_2 opens up novel opportunities to probe the dynamics of the gas-surface

interaction via the scattering of the Xe atom. Based on the results, two sources of reactively scattered Xe are believed to exist: Xe that arises from the dissociation of weakly bound XeF to gas phase Xe and F atoms, and Xe that arises from two atom adsorption. The distinct difference between these two processes is that the former is simply a dissociative process without adsorption while the other process is dissociative chemisorption. The dissociation of XeF is the subject of Sec. IV.C and two atom adsorption is the subject of Sec. IV.D. The discussion concludes with a proposal of future experiments to better understand the dynamics of the interaction of XeF_2 with Si as well as speculation as to the nature of the enhanced reactivity of XeF_2 with Si relative to that of F_2.

IV.A. Unreactive scattering

IV.A.1. Kinetics of unreactive scattering

The probability of unreactive scattering is equal to the total flux of scattered XeF_2 relative to the incident XeF_2 flux. In Figure 4(a) the intensity of the signal at m/e=167, which corresponds to unreactively scattered XeF_2, is relatively low and is only weakly dependent on exposure to high energy XeF_2 during the initial fluorination of Si. The reactivity of XeF_2 with Si(100) at 250 K, defined as the disappearance of the reactant XeF_2 and measured as the absence of unreactively scattered XeF_2, is large at coverages below 1 ML F. In the case of high energy XeF_2, a simple comparison of the signal intensity at m/e=167 from XeF_2 scattered from a reactive Si(100) surface to that scattered from an unreactive oxidized O-Si(100) surface yields an approximate reaction probability of 0.9 at coverages below 1 ML and 0.2 in the steady state regime [53]. However, although the exposure dependence of the intensity of the signal at m/e=167 is related to the rate of unreactive scattering, the signal intensity is not necessarily directly proportional to the flux, especially if the velocity and angular distribution of the scattered products change as a function of XeF_2 exposure. A better method for determining the rate of unreactive scattering is to integrate the flux of scattered XeF_2, which is determined by integration of the velocity-weighted TOF distribution, over the hemisphere above the surface to determine the total flux of unreactively scattered XeF_2. Figure 75 shows a plot of the total flux of high energy XeF_2 unreactively scattered from Si(100) as a function of fluorine coverage, which is determined from the exposure dependence of the thermal desorption yield. The integral is approximated as the sum of the flux into each detector angle θ_d, which is multiplied by the Jacobian, $\sin\theta_d$, to account for the larger solid angle area at larger detector angles. Because only

the angular distribution in the forward direction in the scattering plane is known, the angular distribution is assumed to be independent of azimuthal angle. This approximation is valid for the TD component which is scattered isotropically, but it likely exaggerates the contribution from the DI component which is preferentially scattered along the specular angle, which lies in the scattering plane. However, the highly corrugated nature of the covalent surface of Si(100) presents a broad distribution of local surface normals from which the incident particles scatter, which is evident in the extremely broad angular distribution of the DI component with respect to the detector or polar angle, θ_d. Thus, the approximation that the angular distribution is similarly broad with respect to the azimuthal angle is probably reasonably valid. The total flux of unreactively scattered high energy XeF_2 is essentially constant over the coverage range 0-0.6 ML, and then the flux increases dramatically as all of the highly reactive dangling bonds are occupied by fluorine.

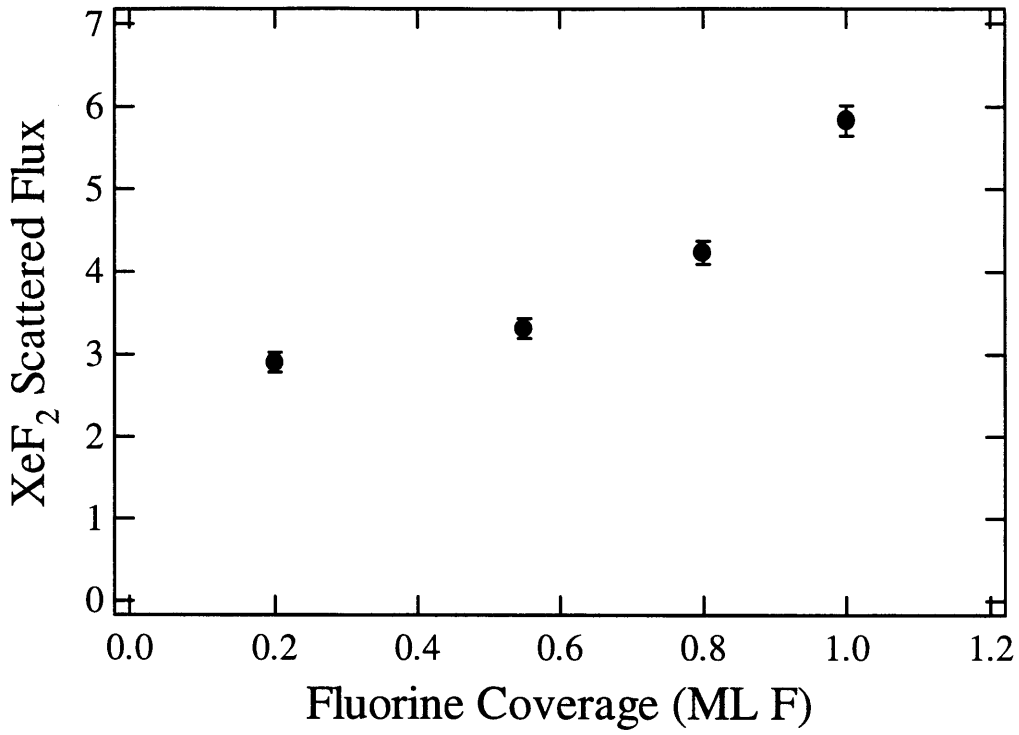

Figure 75 Coverage dependence of total flux of unreactively scattered XeF_2
The total scattered XeF flux as a function of fluorine coverage due to high energy XeF_2 exposure at θ_i=35° and T_s=250 K. The total flux is determined by integrating the angular distribution of the scattered flux shown in Figure 21. The total flux is over the entire hemisphere above the surface so the angular distribution is weighted by the Jacobian, $\sin\theta_d$. The scattered flux is assumed to be independent of azimuthal angle. The error bars represent the propagated uncertainties from the fits to the TOF distributions.

Although the relative fluxes of the low and high energy XeF_2 molecular beams are unknown which precludes a relative comparison of the probability of unreactive scattering for the two incident energies, the similar exposure dependence of the scattered product signal intensities arising from the unreactive scattering of high and low energy XeF_2 (cf. Figure 8(a)) suggests that the reaction probability of low energy XeF_2 is large during the initial fluorination. The similarity of the XeF_2 reactivity over this range of incident energy suggests that the reaction is not activated, i.e., there is no significant energetic barrier to reaction. The absence of an energetic barrier to reaction is not surprising considering that no significant energetic barrier is observed in the fluorination of Si(100) by low energy F_2. In fact, close examination of the exposure dependence of the unreactively scattered product signals in Figure 8(a) reveals that the intensity arising from low energy XeF_2 is distinctly flatter than that from high energy XeF_2 during the initial fluorination. After the initial fluorination, the intensity of the signal at m/e=167 increases dramatically at a similar exposure for both incident energies, as the surface becomes substantially less reactive at a coverage around 1 ML F. This subtle difference in the exposure dependence suggests that low energy XeF_2 may be more reactive than high energy XeF_2. The increase in reactivity with decreasing energy indicates that a longer interaction time between the reactants is a critical element for reaction.

In the interaction of F_2 with Si, the reaction probability is strongly dependent on fluorine coverage, decaying monotonically from almost unity on the clean surface to zero at a coverage of about 1 ML with a dependence that is directly related to the number of unoccupied sites, i.e., $(1-\theta)$. The lack of coverage dependence of the reactivity of XeF_2 with Si over a wide coverage range and the enhanced reactivity of lower energy XeF_2 are suggestive of the presence of an

extrinsic physisorbed precursor mechanism in which the reactant molecule diffuses along the occupied sites on the surface until it encounters an unoccupied site and reacts. The presence of a precursor mechanism is in accord with previous investigations of the surface temperature dependence that showed that the reactivity of XeF_2 with Si, defined as the etch rate of Si, increased with decreasing temperature in the range of 150-400 K [4,6]. The lower surface temperature enhances the reactivity by increasing the residence time of XeF_2 on the surface through the inhibition of the desorption of XeF_2 from its physisorbed state on top of occupied sites. The increase in reactivity with decreased surface temperature provides further support to the conclusions based on the experimental results presented above that there is no significant energetic barrier in the initial reaction of XeF_2 with Si, and that the critical element to the reaction is the probability of the incident XeF_2 interacting with a reactive site on the Si surface.

IV.A.2. Branching between direct-inelastic and trapping desorption scattering

The effect of the residence time of XeF_2 on the Si surface on the reactivity is also apparent in the branching between the two unreactive scattering mechanisms, direct-inelastic (DI) scattering and trapping-desorption (TD) scattering. One of the most important differences between DI and TD scattering is that the residence time of the particle in the vicinity of the surface is extremely short (~ps) for DI scattering and extremely long (>μs) for TD scattering.

A useful parameter is the branching ratio of the flux of unreactively scattered XeF_2 via the DI and TD scattering channels. Figure 76 shows a plot of the branching ratio of XeF_2 as a function of fluorine coverage due to high energy XeF_2 exposure. The branching ratio is calculated by determining the total flux of XeF_2 scattered into the hemisphere above the surface via either DI scattering or TD scattering. The analysis of the flux arising from the two

mechanisms is identical to the calculation of the total flux of unreactively scattered XeF_2 shown in Figure 75 except that the integration is performed for the individual components of the TOF distribution. The branching ratio is the ratio of the total flux of XeF_2 unreactively scattered via DI scattering to that scattered via TD scattering. Although this ratio is not exact because of the anisotropy of the angular distribution of the DI scattered XeF_2, the ratio is a reasonable representation of the branching as long as the shape of the DI angular distribution does not have a strong dependence on fluorine coverage over the range 0-1.1 ML. Based on the observation that the shape of the DI angular distribution in the scattering plane does not change as a function of fluorine coverage (cf. Figure 21), it is reasonable to assume that the angular distribution of the out-of-plane DI scattering does not change as well.

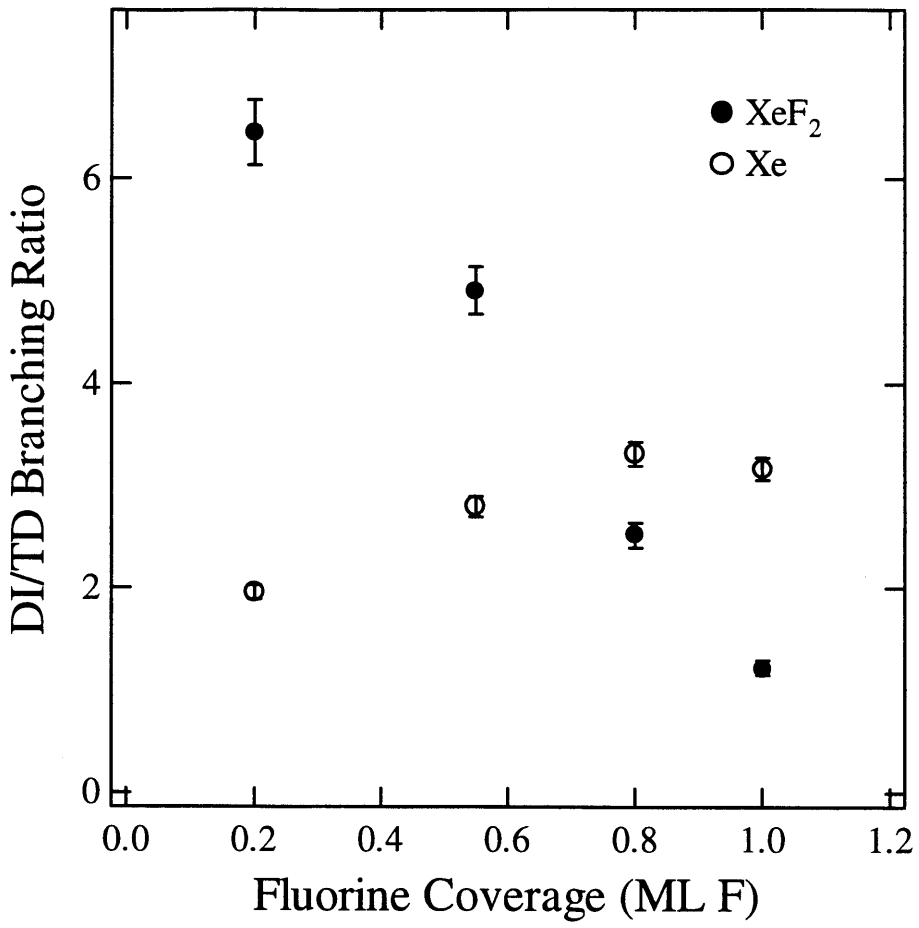

Figure 76 Branching ratio of unreactively scattered Xe and XeF_2 from Si(100)
Branching ratio of the flux of XeF_2 (solid circles) and Xe (hollow circles) unreactively scattered via DI scattering relative to TD scattering as a function of fluorine coverage due to high energy XeF_2 exposure at θ_i=35° and T_s=250 K. The total flux of XeF_2 is determined by integrating the angular distributions of the flux of XeF_2 unreactively scattered via DI scattering and TD scattering shown in Figure 21. The total flux of XeF_2 is determined by integrating the angular distributions of the flux of XeF_2 unreactively scattered via DI scattering and TD scattering shown in Figure 65. The total flux is over the entire hemisphere above the surface so the angular distribution is weighted by the Jacobian, $\sin\theta_d$. The scattered flux is assumed to be independent of azimuthal angle. The error bars represent the propagated uncertainties from the fits to the TOF distributions.

The DI:TD branching ratio of unreactively scattered XeF_2 is quite sensitive to high energy XeF_2 exposure, decreasing by a factor of more than five over a coverage range of 0-1.1 ML F. The profound change in the branching ratio with coverage is the result of a dramatic increase of the flux TD scattering. There are two possible causes for the increase in TD scattering that are based on a change in the interaction potential between XeF_2 and Si surface as the surface is fluorinated. The change could result in purely kinematic effects on the nature of the scattered products. For example, the energy transfer from the particle to the surface is more efficient making trapping more likely. On the other hand, the change could result in purely reactive effects on the nature of the scattered products. For example, the XeF_2 that proceeds along a trajectory leading to trapping on the surface is more likely to react than the XeF_2 that proceeds along a trajectory leading to inelastic scattering. Therefore, over a coverage range of 0-0.6 ML the reaction probability of XeF_2 is high, and the TD component of the unreactively scattered XeF_2 will be depleted relative to the DI component. However, as the coverage increases beyond 0.6 ML, the reaction probability decreases and the flux into TD scattering will increase relative to the flux into DI scattering. To test these two possibilities, the branching ratio of a inert particle can be measured. If the first case is true, then the branching ratio of the inert particle will behave in a similar fashion to that of XeF_2 and decrease with coverage. Otherwise, if the second case is true, then the branching ratio of the inert particle will be unaffected by the increase in fluorine coverage.

In Sec. III.C.4.a.ii, the TOF distributions of unreactively scattered Xe at several detector angles as a function of XeF_2 exposure are presented as a means of identifying the contribution of free Xe in the high energy XeF_2 molecular beam to the signal at m/e=129. Analogous to the

TOF distribution of unreactively scattered XeF_2, the TOF distribution of unreactively scattered Xe is comprised of two components, a narrow fast feature arising from DI scattering and a broad slow feature arising from TD scattering. The branching ratio of the unreactively scattered Xe into the DI scattering channel relative to the TD scattering channel is superimposed on the plot of the unreactively scattered XeF_2 branching ratio in Figure 76. Unlike the branching ratio of unreactively scattered XeF_2, the branching ratio of unreactively scattered Xe is reasonably insensitive to XeF_2 exposure increasing by only 60% over a range of fluorine coverage of 0-1.1 ML F. Interestingly, despite the Si surface becoming further fluorinated and eventually disordered due to etching, suggesting that the surface becomes "softer" and, therefore, better able to act as a sink for the energy of the incident particle, the DI:TD branching ratio of unreactively scattered Xe increases with fluorine coverage. This observation suggests that during the initial fluorination the surface is reasonably well-ordered since an increasingly more disordered, and more hence corrugated, surface would be more likely to trap the incident particles. This suggestion that the surface is well-ordered during the initial interaction of XeF_2 with Si is in agreement with the thermal desorption and He diffraction experiments presented in Sec. III.B that show that the initial fluorination of Si by XeF_2 is similar to that of F_2 which simply passivates the dangling bonds with fluorine and is unable to etch Si.

To a first approximation, the kinematics of unreactive Xe and XeF_2 scattering ought to be similar since the masses of the two particles are similar and are both large with respect to the mass of a Si atom, the collision partner. Therefore, significant differences can be attributed to the reactive nature of the interaction potential between XeF_2 and Si(100). In the case of purely unreactive scattering, the branching ratio between DI scattering and TD scattering is a

macroscopic property that represents the dynamics of the gas particles in the gas-surface interaction potential, albeit after averaging over a wide range of parameters. Therefore, the branching ratio of an inert particle is a macroscopic measure of the probability of an incident particle proceeding through a trajectory that will lead to DI scattering relative to TD scattering. In the case of the unreactive scattering of XeF_2, the observation that the branching ratio is strongly dependent on fluorine coverage and behaves differently from other heavy unreactive particles suggests that the reactive nature of XeF_2 is affecting the branching ratio. In this case, a third scattering channel, reactive scattering, eliminates the XeF_2 molecules that, prior to reaction, would unreactively scatter via either DI or TD scattering mechanisms with a ratio determined entirely from inert scattering dynamics. The significant depletion of the TD component relative to the DI component at low fluorine coverage suggests that the XeF_2 molecules that react with the surface are primarily the molecules that would have accommodated with the surface if reaction had not occurred. This conclusion lends further support to the presence of an extrinsic physisorbed precursor in which the reaction is enhanced by increasing the residence time of the reactant particle on the surface or alternatively, increasing the interaction period of the two reactants.

Nathanson and coworkers similarly attributed the absence of an unreactively scattered TD component to reaction via the accommodated gas particles in the scattering of water [64] and small organic molecules of similar mass and varying basicity [65,66] from a liquid surface of sulfuric acid. The more basic molecules are solvated more readily as evidenced by the overall loss of unreactively scattered flux from the acid surface relative to scattering from an inert Teflon surface. In addition, of the molecules that do scatter unreactively, DI scattering is

increasingly more prevalent than TD scattering with increasing molecule basicity. The molecules all have similar masses so the scattering kinematics in the absence of reaction ought to be similar. Indeed, scattering of n-butanol, a basic organic molecule, from a liquid surface of reactive sulfuric acid and a liquid surface of inert glycerol shows that the unreactive molecules are scattered exclusively via DI scattering from the acid surface whereas from the inert surface, TD scattering is preferred over DI scattering. According to the inert scattering dynamics of n-butanol from the glycerol surface, TD scattering is the dominant scattering mechanism. However, in the presence of a third reaction channel, deprotonation and solvation, the n-butanol that resides in the vicinity of the acid surface longer and has more interactions with the surface is much more likely to react than the n-butanol that only interacts a few times with the surface. Thus, the reactive channel preferentially depletes the TD scattering channel relative to DI scattering channel.

IV.A.3. Summary

Several observations suggest the presence of a physisorbed precursor mechanism in the interaction of XeF_2 with Si(100). First, the probability of unreactive scattering is nearly unity and reasonably insensitive to the incident XeF_2 energy, and, in fact, may increase with increasing energy over the range 1.8-6.3 kcal/mol. This non-Langmuirian behavior which is characteristic of an extrinsic precursor mechanism, also indicates that there is no significant barrier to reaction. The absence of an energy barrier is analogous to the interaction of F_2 with Si(100), but the presence of an extrinsic physisorbed precursor distinguishes the interaction of XeF_2 with Si from that of F_2. Second, the probability of unreactive scattering is constant over a wide fluorine coverage range of 0-0.6 ML. The weak coverage dependence of the probability of unreactive

scattering is indicative of an extrinsic physisorbed precursor mechanism because despite the loss of reactive sites, incident XeF_2 is able to interact with a reactive site with the same likelihood. A reaction probability that is independent of the number of unoccupied sites is only possible if XeF_2 is able to physisorb on top of the occupied sites and diffuse along them until it encounters a reactive site. Finally, the TD component of the unreactively scattered XeF_2 is substantially depleted relative to the TD component of unreactively scattered Xe over the fluorine coverage range of 0-0.6 ML. The particles that scatter via TD scattering are the particles that interact sufficiently with the surface to become physisorbed to the surface.

The presence of an extrinsic physisorbed precursor mechanism in the interaction of XeF_2 with Si(100) is in stark contrast to the interaction of F_2 with Si(100) in which there is no evidence of a physisorbed precursor mechanism. This difference can be understood in terms of the efficacy of trapping XeF_2 and F_2 on the Si surface. XeF_2 is much larger than F_2 and is, therefore, much more polarizable, i.e., the electron cloud is easily distorted by an external force. Physisorption is a van der Waals interaction, a weak interaction caused by the correlation of the electronic motion in the two particles of interest. The strength of the interaction is related to the ability of the electrons on one particle to influence the electrons on another particle and is, therefore, proportional to the polarizabilities of the two particles.

The kinetics of unreactive scattering are different in the interactions of XeF_2 and F_2 with Si(100), implying that the kinetics of the reaction of these two molecules with the surface must also be different. However, despite the difference in the kinetics of the reaction, the dynamics of the reactive interaction of XeF_2 and F_2 with Si(100) are not necessarily different. In the next

three sections, the focus of the discussion shifts from unreactive XeF_2 scattering to the reactive scattering of XeF_2 via single atom abstraction and two atom adsorption.

IV.B. Single atom abstraction

IV.B.1. Identification of F atom abstraction

The first direct experimental observation of the dissociative chemisorption mechanism of atom abstraction was the mass spectrometric detection of scattered F atoms, further characterized by a fast velocity distribution using a TOF technique, in the interaction of low energy F_2 with Si(100). The proposed criterion for atom abstraction is that the energy liberated by the formation of one surface-adsorbate bond is sufficient to cleave the incident molecular bond. There is no thermodynamic driving force for forming two surface-adsorbate bonds as there is in classic dissociative chemisorption. The energetics of the interaction of XeF_2 with Si satisfy this criterion so atom abstraction ought to be present. Indeed, the mass spectrometric detection of scattered XeF is demonstrated in Sec. III.A and Sec. III.C.2 providing direct evidence of atom abstraction in the interaction of XeF_2 with Si(100). Although atom abstraction is present in the interactions of F_2 and XeF_2 with Si, a comparison of the dynamics of this mechanism in these two gas-surface systems reveals a few common traits and several significant differences.

IV.B.2. Kinetics of single atom abstraction

The probability of single atom abstraction is proportional to the flux of scattered XeF. In Figure 4(b) and Figure 8(b) the intensity of the signal at m/e=148 that is attributable to scattered XeF is distinctly nonzero and shows a nonmonotonic dependence on exposure to high energy XeF_2 and low energy XeF_2, respectively. This unusual exposure dependence is reminiscent of the exposure dependence of the probability of single atom abstraction in the interaction of F_2 with Si (cf. Figure 12 in Chapter 1). However, two important differences exist. The first difference is that in the case of exposure to high energy XeF_2 shown in Figure 4(b), the scattered

XeF signal intensity does not decay to zero indicating that single atom abstraction does not cease at coverages greater than 1 ML F as it does in the interaction of F_2 with Si. However, because the mechanisms of single atom abstraction and two atom adsorption are believed to share a common step, this result is not unusual since the reaction of XeF_2 with Si, which must necessarily proceed through single atom abstraction and/or two atom adsorption, does not cease at a coverage of 1 ML F. Although the branching between the two dissociative chemisorption mechanisms may change as a function of coverage, it is unlikely that one mechanism would disappear completely. In the case of exposure to low energy XeF_2 shown in Figure 8(b), the scattered XeF signal intensity appears to decay to zero. However, it should be noted that the incident angle and detector angle are different in Figures 4 and 8. Although no dependence on incident angle has been observed, the highly anisotropic angular distribution of scattered XeF results in a dramatic difference in the exposure dependence of the scattered product signal intensity depending on the detector angle. Indeed, the scattered XeF signal intensity as a function of high energy XeF_2 exposure at the same detector angle also shown in Figure 8 decays to zero as well.

The second difference is that the maximum in the intensity of the scattered XeF signal is at a XeF_2 exposure that corresponds to about 1 ML F. This is unusual because according to the thermal desorption and He diffraction results, the surface is well-ordered up to a coverage of 1 ML so there should be few unoccupied dangling bonds available for reaction when the maximum is attained. These contradictory observations can be reconciled by considering the angular distribution of the scattered XeF flux. The signal intensities shown in Figures 4(a) and 8(c) are proportional to the number density of XeF scattered into the small solid angle in the hemisphere

above the surface that is subtended by the detector. If the shape of the velocity distribution is constant and the angular distribution of the scattered flux is isotropic as a function of exposure, the measurement at any angle yields the exposure dependence of total scattered flux, the relevant quantity for determining the reaction probability. For example, in the interaction of F_2 with Si(100), the signal intensity at any detector angle is directly proportional to the rate of single atom abstraction because the velocity distribution of the scattered F atom is constant and the exposure dependence of the F atom signal is independent of the detector angle. However, in the interaction of high energy XeF_2 with Si(100), the exposure dependence of the scattered XeF signal is strongly dependent on detector angle as well as fluorine coverage (cf. Figure 34). In addition, the velocity of the scattered XeF, which is necessary to transform the mass spectrometer signal to a signal that is proportional to flux, is not constant as a function of XeF_2 exposure (cf. Figure 36). Analogous to the calculation of the total flux of scattered XeF_2 shown in Figure 75, the total flux of scattered XeF can be determined by integration of the flux of scattered XeF, which is determined by integration of the velocity-weighted TOF distribution, over the hemisphere above the surface. As with the scattered XeF_2 flux, this integration assumes that the velocity and angular distribution are independent of the azimuthal angle. This assumption is justified by the observation that the angular distribution displays a maximum along the surface normal, not the specular scattering angle, suggesting that the dynamics of the reactive interaction overwhelm the incident trajectory of XeF_2. The insensitivity of the scattering dynamics of XeF to the incident XeF_2 trajectory is not surprising given the tremendous exothermicity of single atom abstraction (90 kcal/mol) relative to the incident XeF_2 energy (1.8-6 kcal/mol). Figure 77 shows a plot of the total flux of scattered XeF as a function of fluorine

coverage. In stark contrast to the exposure dependence of the XeF signal intensity shown in Figure 4(b) and Figure 8(b), the total flux of scattered XeF, which is directly proportional to the probability of single atom abstraction, is remarkably constant over the entire coverage range 0-1.1 ML. However, the unusual nonmonotonic exposure dependence is still present, with the maximum occurring at a XeF_2 exposure that corresponds to 0.5 ML F, just as it does in the interaction of F_2 with Si(100). Although the scattered XeF flux along the surface normal increases dramatically with coverage, the scattered flux into detector angles away from the surface normal decreases substantially with coverage. The result is a relatively weak coverage dependence for the scattered XeF flux. This analysis demonstrates the importance of considering the velocity and angular distributions of the scattered products when relating mass spectrometer intensities of the scattered products measured along a given detector angle to reaction probabilities.

The weak fluorine coverage dependence of the probability of single atom abstraction is a consequence of the presence of an extrinsic physisorbed precursor mechanism. Since the probability of unreactive scattering is reasonably constant as a function of fluorine coverage over the range of 0-0.6 ML, the probability of reactive scattering via either single atom abstraction or two atom adsorption must be similarly insensitive to fluorine coverage.

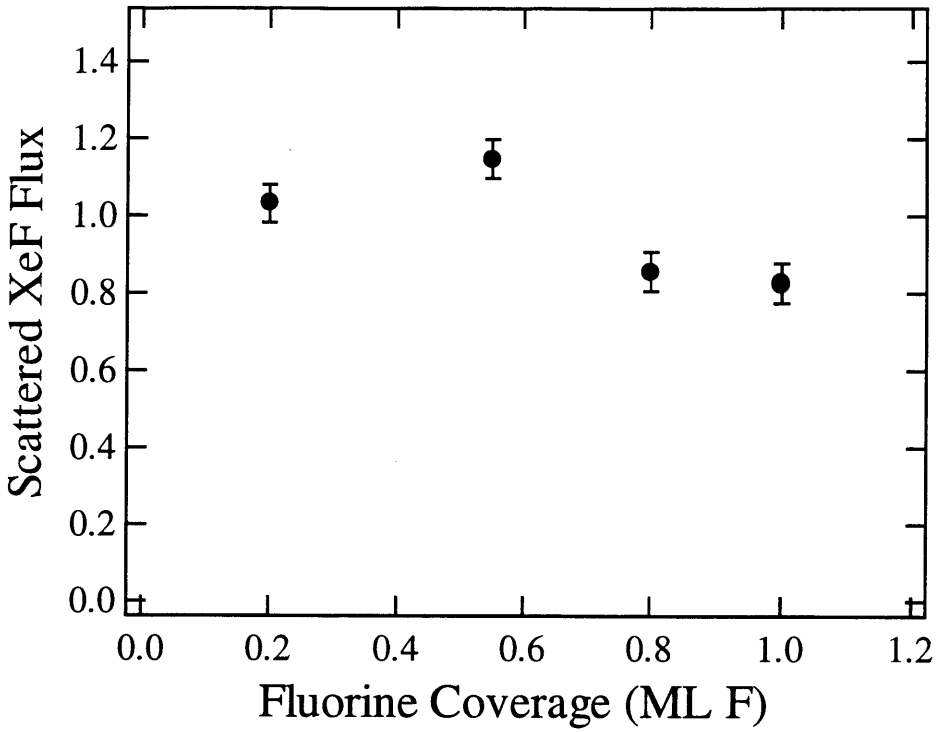

Figure 77 Coverage dependence of total flux of XeF scattered as a result of single atom abstraction

The total scattered XeF flux as a function of fluorine coverage due to high energy XeF_2 exposure at θ_i=35° and T_s=250 K. The total flux is determined by integrating the angular distribution of the scattered flux shown in Figure 34. The total flux is over the entire hemisphere above the surface so the angular distribution is weighted by the Jacobian, $\sin\theta_d$. The scattered flux is assumed to be independent of azimuthal angle. The error bars represent the propagated uncertainties from the fits to the TOF distributions.

IV.B.3. Angular distribution of single atom abstraction product

The anisotropic angular distribution shown in Figure 34 of the F atom abstraction product of XeF_2 is very different from the isotropic angular distribution of the F atom abstraction product resulting from the interaction of F_2 with Si. Although the angular distribution of XeF is broad and cosinelike at the low fluorine coverages, there is a substantial increase in the scattered XeF flux along the surface normal with increasing coverage.

A possible explanation for the coverage dependence of the angular distribution of the scattered XeF invokes steric hindrance and the phenomenon of molecular steering in gas-surface interactions that was considered in Sec. IV.A.5.c of Chapter 1 as well as incorporates the presence of an extrinsic physisorbed precursor. Recall that in molecular steering the incident molecule is oriented by the gas-surface interaction potential in such a way that reaction with the surface is more favorable than it would have been had the reaction occurred with a random orientation of the incident molecule with respect to the surface [67,68,69,70,71]. On the clean surface, a XeF_2 molecule will readily lose a F atom to any unoccupied site in almost any orientation because there is no steric hindrance to access the surface dangling bonds. Therefore, the angular distribution of the scattered XeF is isotropic. On the other hand, on the fluorinated surface, the adsorbed fluorine will sterically hinder the large XeF_2 molecule from freely accessing the few unoccupied dangling bonds. Figure 78 shows a pictorial representation of the interaction of XeF_2 with fluorinated Si(100). The top picture shows a cross section perpendicular to the dimer rows, and the bottom picture shows a cross section parallel to the dimer rows. The XeF_2 molecule is ~5 Å long based on the XeF bond length and the covalent radius of F, which is much larger than the relevant Si lattice spacings of 2.36 Å for the dimer

bond and 3.84 Å between dimers within the dimer row. Regardless of the azimuthal orientation of the incident XeF_2, there is no approach geometry that allows one of the F atoms on XeF_2 to access an unoccupied dangling bond with the molecular axis parallel to the surface because of steric hindrance from the adsorbed fluorine. However, this steric hindrance can be overcome by the combination of the physisorption potential, which keeps the XeF_2 in the vicinity of the surface for sufficiently long periods of time so that the XeF_2 can access a reactive unoccupied site, and the attractive interaction between a F atom and an unoccupied dangling bond, which is strong enough to pull one of the F atom ends of the XeF_2 molecule towards the reactive site, tilting the molecular axis along the surface normal, and leading to ejection of the product XeF away from the surface along the surface normal. Although the same attractive interaction likely exists in the interaction of F_2 with Si, there is also less steric hindrance of the small F_2 molecule which is only 2.54 Å long.

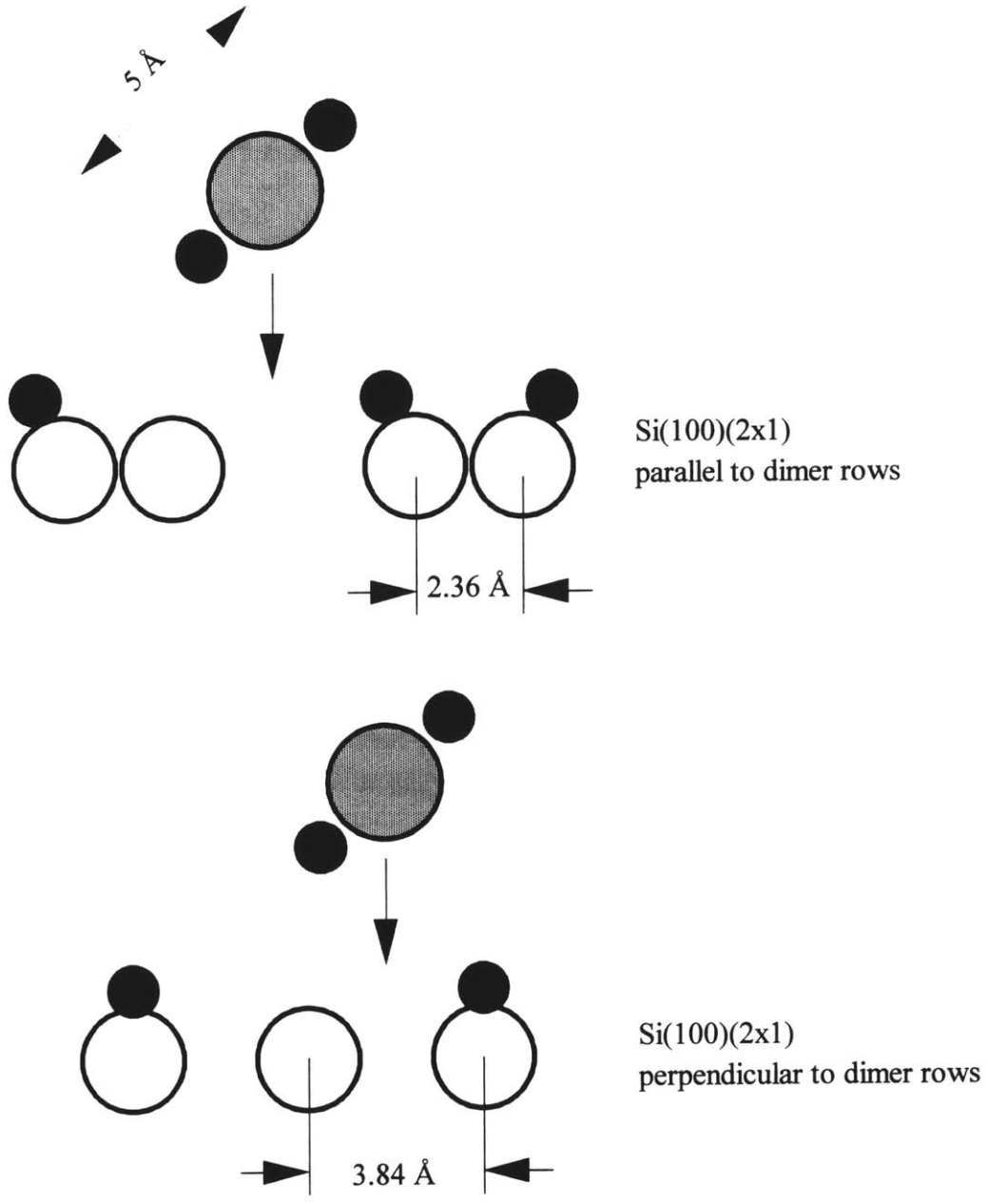

Figure 78 Pictorial representation of steric hindrance of XeF_2 at high coverage

IV.B.4. Energy distribution of single atom abstraction product

In Sec. III.C.2, the dynamics of single atom abstraction were determined by measuring the TOF distribution of the scattered signal at m/e=148 as a function of XeF_2 exposure and subtracting the contribution from unreactively scattered XeF_2 which is determined by multiplying the scattered signal at m/e=167 by the XeF_2 cracking ratio. Analogous to the F atom TOF distribution of the single atom abstraction product of the interaction of F_2 with Si, the XeF TOF distribution is distinctly hyperthermal with an average velocity of 620±27 m/s and an average energy of 7.8±0.7 kcal/mol. For comparison, in the fluorine atom abstraction of F_2 by Si, the scattered F atom is significantly faster (1084 m/s), but its energy is significantly lower (3.7 kcal/mol) because the F atom is much lighter than the XeF molecule. Although the absolute energies are dramatically different, the fraction of the reaction exothermicity that is channeled into the translational energy of the gas phase product is very small (<10%) in both cases. Even though the surface is a bath for energy transfer, the gas phase products in direct gas-surface reactions have been observed to carry away large fractions of the reaction exothermicity [72]. The observation that the gas phase product of atom abstraction gains only a small fraction of the reaction exothermicity yields insight into the gas-surface interaction potential. The low translational energy of the products is consistent with an "early barrier" or "attractive potential" type of potential energy surface first described by Evans and Polanyi for gas phase reactions [73]. In the prototypical three atom reaction $A+B_2 \rightarrow AB+B$, an "attractive potential" surface leads to low translational energy in the products and high vibrational energy in the product AB. In the case of a gas-surface system, like the interaction of F_2 and XeF_2 with Si(100), the vibrational excitation is in the newly formed surface Si-F bond. Indeed, in the interaction of

XeF_2 with Si, emission at about 1400 cm^{-1} has been attributed to the decay of such a vibrationally excited fluorinated Si surface species [28].

The observation that the translational energy of the reactively scattered products, XeF arising from single atom abstraction (cf. Figure 36) as well as Xe arising from two atom adsorption (cf. Figure 74), decreases substantially as a function of fluorine coverage as a result of both high and low energy XeF_2 exposure over the range 0-1.1 ML indicates a change in the dynamics of atom abstraction, despite the absence of a noticeable concomitant change in the kinetics of single atom abstraction. The effect may be a result of the increased efficacy of coupling the exothermicity of atom abstraction into the fluorinated surface relative to the clean surface. However, this coverage dependence is not observed for the translational energy of the reactively scattered F atom arising from the interaction of F_2 with Si. Without additional knowledge of the localized changes in the surface upon reaction as a function of fluorine coverage, it is difficult to speculate as to the nature of the strong coverage dependence of the translational energy of the reactively scattered products of the interaction of XeF_2 with Si.

IV.C. XeF dissociation

IV.C.1. Evidence for XeF dissociation

The presence of a very fast feature in the TOF distribution of the scattered products at m/e=19 can only be attributed to F atoms arising from the dissociation of XeF. The only source of F atoms in the incident molecular beam is XeF_2, which is too strongly bound (63 kcal/mol [51]) to dissociate upon collision at these relatively low collision energies (1.8-6.3 kcal/mol). No F_2 or other fluorides (i.e., NiF_2 from reaction of XeF_2 with the walls of the Ni molecular beam nozzle) are present in the molecular beam within the limit of the detection sensitivity (~10^{-5} ML/s). Although it is impossible to conclusively eliminate the possibility of the presence of F atoms because some XeF_2 fragments to F^+ in the ionization region, even if there are F atoms in the molecular beam, they cannot unreactively scatter from the surface and gain sufficient energy (~5 kcal/mol) to be detected at such short flight times. The only scattered products that contain F atoms are XeF_2, XeF, and SiF_4. It is highly unlikely that F atoms could arise from the desorption from the Si surface or from the dissociation of etch products like SiF_4, given the strength of any Si-F bond is at least 125 kcal/mol [74]. On the other hand, XeF arising from single atom abstraction is weakly bound by only 3 kcal/mol [51]. The XeF molecule is extremely susceptible to dissociation.

Assuming that the probability of XeF dissociation is independent of fluorine coverage, the flux of scattered Xe and F should be similar to the flux of XeF. Figure 79 shows a plot of the total flux of XeF and F as a function of fluorine coverage. The total flux of stable XeF is known from the angular distribution of the XeF TOF distributions (cf. Figure 77). The flux of F is known from the TOF distributions at m/e=19. Analogous to the total flux of scattered XeF

shown in Figure 77, the total flux of scattered F atoms is determined by integration of the flux of F atoms, which is determined by integration of the velocity-weighted TOF distribution, over the hemisphere above the surface. This integration assumes that the velocity and angular distributions are independent of azimuthal angle. This assumption is justified by the observation that the observed angular distribution is cosinelike suggesting an isotropic distribution. Despite the dramatic difference in the angular distributions of XeF and F as a function of fluorine coverage, the coverage dependence of the total flux is remarkably similar. Thus, the scattered F atom flux is consistent with the mechanism of XeF dissociation. Knowledge of the coverage dependence of the total flux of Xe arising from XeF dissociation would provide further evidence for XeF dissociation, but it is unknown because of the coincidence of the velocity distributions of three contributions to the m/e=129 signal: cracking of XeF, Xe from two atom adsorption, and Xe from XeF dissociation.

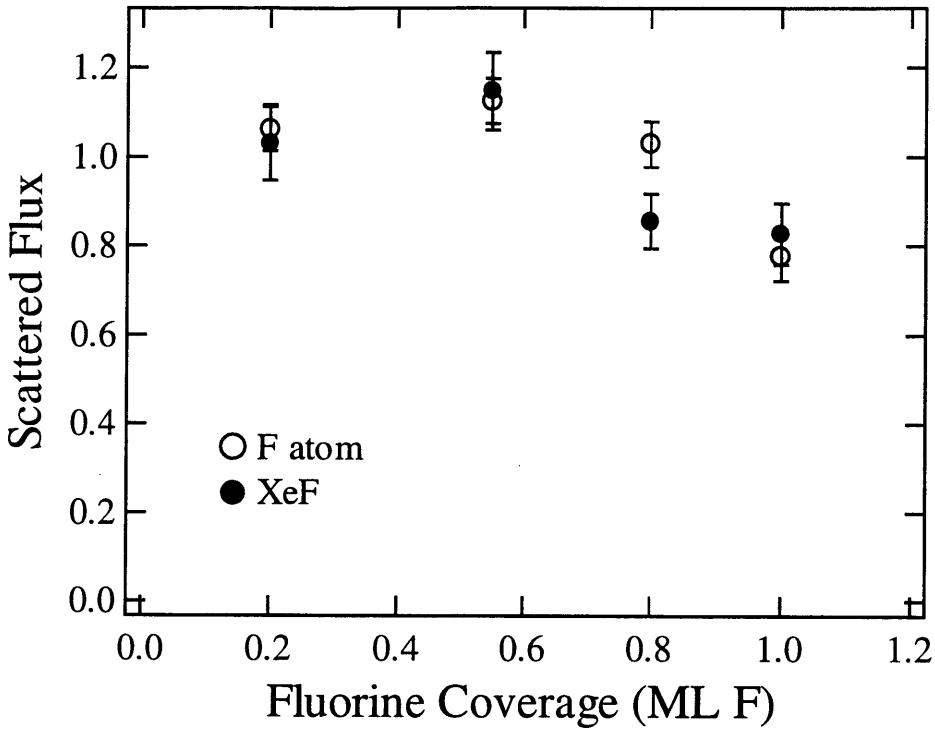

Figure 79 Coverage dependence of total flux of scattered XeF and F
The total scattered XeF and F atom flux as a function of fluorine coverage due to high energy XeF_2 exposure at θ_i=35° and T_s=250 K. The total flux is determined by integrating the angular distribution of the scattered flux shown in Figure 34 and Figure 49. The total flux is over the entire hemisphere above the surface so the angular distribution is weighted by the Jacobian, $\sin\theta_d$. The scattered flux is assumed to be independent of azimuthal angle.

IV.C.2. Mechanisms for XeF dissociation

There are two possible mechanisms for XeF dissociation in the interaction of XeF_2 with Si. The first mechanism is that dissociation occurs if XeF interacts with the surface. The XeF produced in single atom abstraction has sufficient translational energy for it to dissociate upon collision with the Si surface if the transfer of energy from translation to vibration excites the XeF molecule above the dissociation limit. This mechanism is called collision-induced dissociation. Note that if the XeF collides with an empty site and the geometry of the collision is appropriate, then the F atom may adsorb onto the Si surface yielding two atom adsorption. Although two atom adsorption is a likely cause of XeF dissociation because it is an exothermic dissociative chemisorption process, the collision-induced dissociation of XeF into gas phase Xe and F atoms at collision energies of 6-10 kcal/mol is less likely because a substantial fraction of the collision energy must be transferred to the internal energy of the XeF. The second mechanism is that a sufficient fraction of the energy liberated in the extremely exothermic F atom abstraction from XeF_2 is transferred to the internal energy of the XeF such that the excited XeF spontaneously dissociates. This mechanism is called chemically-induced dissociation. There is sufficient exothermicity in the reaction of XeF_2 with silicon to excite XeF into an electronically excited state. Both the repulsive A state (ΔE=16.4 kcal/mol) and bound charge-transfer excimer B and C states (ΔE~85 kcal/mol) are energetically accessible [75]. Dissociation from the dissociative A state would be direct whereas dissociation from the predissociative B and C states would require relaxation (τ=10 ns) to the repulsive A state or the repulsive wall of the ground electronic state. Even if electronic excitation does not occur, it is certainly possible that the XeF is excited into a rovibrational state in the ground electronic state that is above the dissociation threshold. Because

there is only one vibrational mode and two degenerate rotational modes in a diatomic molecule, there are few degrees of freedom to store internal energy prior to dissociation. Thus, regardless of the type of internal energy excitation, chemically-induced dissociation must occur within a short time with respect to the collision and, therefore, must occur near the surface. Chemical-induced dissociation is more likely than collision-induced dissociation because there is so much energy available to dissociate XeF from the initial F atom abstraction than there is in a subsequent collision with the surface. In addition, it is expected from an "attractive potential" that the exothermicity of the reaction will be deposited into internal energy in the products as opposed to translational energy.

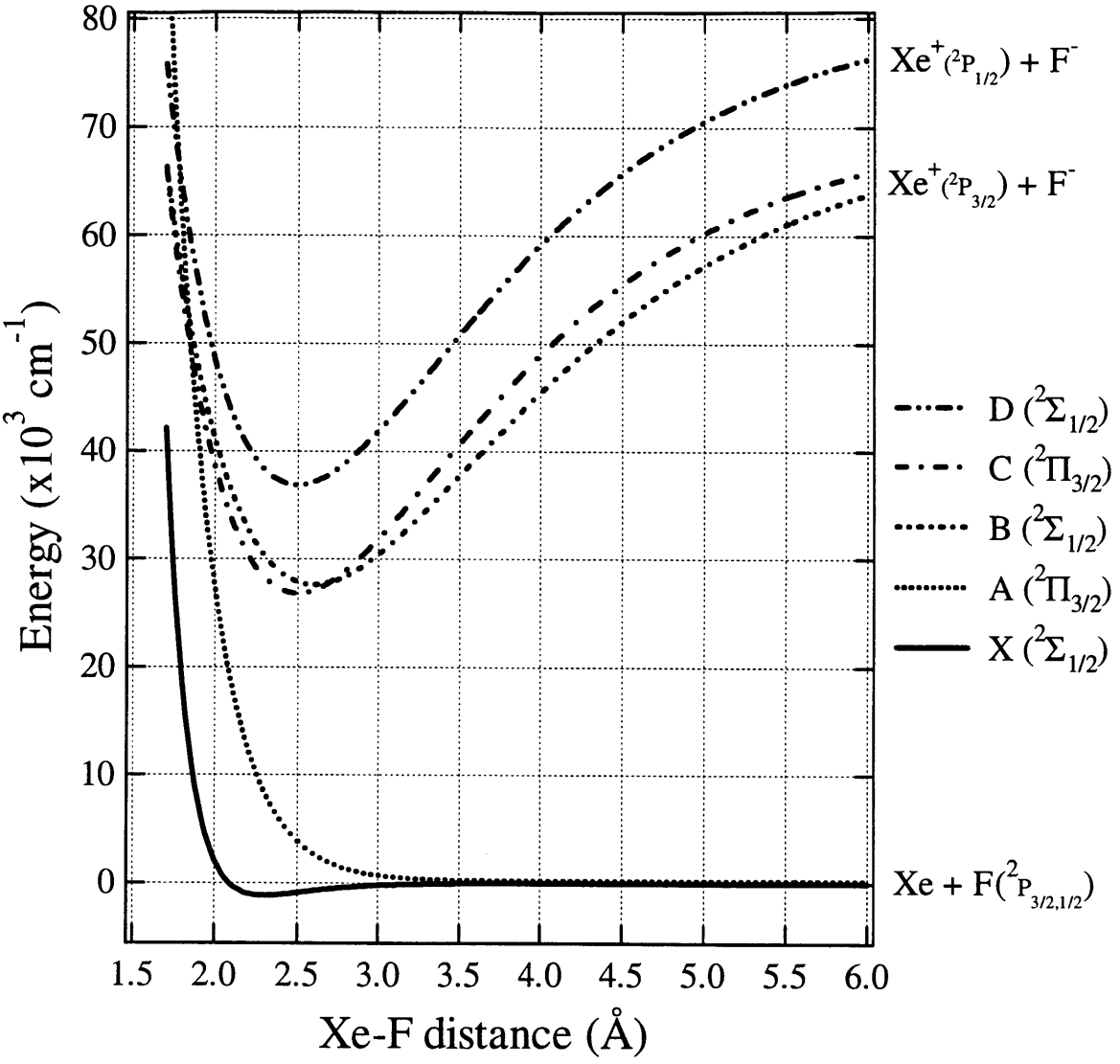

Figure 80 Potential energy diagram of the electronic states of XeF
Morse potentials based on parameters from References 51 and 75.

Chemically-induced dissociation is essentially a gas phase dissociation process, and is, therefore, amenable to a momentum conservation analysis of the velocity and angular distributions of the dissociated atoms. In the laboratory (LAB) reference frame, the conservation of linear momentum in the event of XeF dissociation is given by:

$$m_{XeF}\vec{v}_{XeF}^{LAB} = m_{Xe}\vec{v}_{Xe}^{LAB} + m_F\vec{v}_F^{LAB}. \qquad \text{(IV.1)}$$

In the center of mass (CM) frame:

$$(m_{Xe} + m_F)\vec{v}_{XeF}^{CM} = m_{Xe}\vec{v}_{Xe}^{CM} + m_F\vec{v}_F^{CM}, \qquad \text{(IV.2)}$$

where $\vec{v}_{XeF}^{CM} = 0$ because the center of mass velocity is simply the scattered XeF velocity so:

$$\vec{v}_{Xe}^{CM} = -\left(\frac{m_F}{m_{Xe}}\right)\vec{v}_F^{CM}, \qquad \text{(IV.3)}$$

To confirm that the measured LAB velocity of Xe is consistent with XeF dissociation, consider the simplest scenario in which the XeF molecule is ejected with the molecular axis parallel to the direction of the XeF velocity with the F-end in the forward direction (see pictorial representation of geometry in inset in Figure 81). The average LAB velocities for XeF and F are assumed to be 620 m/s (450 m/s FWHM) and 1550 m/s (1130 m/s FWHM), respectively, based on data shown in Figure 25 and Figure 40, respectively. The CM velocity of the dissociating system is simply the LAB velocity of the XeF. Therefore, the CM velocity of the F atom is 930 m/s in the forward direction, which, by Eq. (IV.3), yields a CM velocity for the Xe atom of 135 m/s in the opposite direction.

The goal of this analysis is to show that the velocity distributions of the scattered F atom and Xe atom are consistent with a gas phase dissociation event corresponding to chemically-induced dissociation. Figure 81 shows a plot of a simulated TOF distribution of the scattered products at m/e=129, calculated by assuming only two contributions: Xe atoms arising from the

dissociation of XeF and Xe^+ arising from cracking of XeF in the ionization region. The TOF distribution of Xe^+ from the cracking of XeF is described by the fit to the TOF distribution of scattered XeF in Figure 25(b) multiplied by the ideal XeF cracking ratio of 4. The simulated TOF distribution of Xe is described by a Maxwell-Boltzmann function F(t) such that the average velocity and width of the distribution match the expected LAB velocity distribution, where the average LAB velocity of Xe is calculated from Eq. (IV.1) as 455 m/s (350 m/s FWHM). The intensity of the feature is simulated such that the flux of Xe arising from XeF dissociation is equal to the flux of XeF cracking to Xe^+. It is important to note that the Xe flux attributable to Xe arising from XeF dissociation is unknown because the relative cross sections for ionization of XeF and Xe are unknown, and because the fraction of XeF that dissociates is also unknown. However, the resulting simulated TOF distribution at m/e=129 is certainly consistent with the experimental results from Figure 54 which are superimposed in Figure 81. However, because of the width of the TOF distributions, the distinction between the contribution due to XeF fragmentation in the ionizer and the contribution due to Xe arising from the dissociation of XeF near the surface prior to ionization is not readily apparent.

To better understand the mechanism for dissociation, the internal energy of the dissociating XeF above the dissociation limit is determined from these velocities using the conservation of energy which in the LAB frame is given by:

$$E_{trans}^{LAB}(XeF) + E_{int}(XeF) = E_{trans}^{LAB}(Xe) + E_{trans}^{LAB}(F) + E_{diss}(XeF), \qquad \text{(IV.4)}$$

which in the CM frame simplifies to:

$$E_{int}(XeF) - E_{diss}(XeF) = E_{trans}^{CM}(Xe) + E_{trans}^{CM}(F). \qquad \text{(IV.5)}$$

Substituting the relationship between the momentum of the F atom and Xe atom from Eq. (IV.2) into Eq. (IV.4) yields:

$$E_{int}(XeF) - E_{diss}(XeF) = E_{trans}^{CM}(F)\left[1 + \frac{m_F}{m_{Xe}}\right]. \qquad \text{(IV.6)}$$

The internal energy of the dissociating XeF above the dissociation limit is 2.0 kcal/mol (1.4 kcal/mol FWHM). Thus, significant energy is channeled into the internal energy of the dissociating XeF.

Although the results of this analysis are consistent with the experimental results, the inability to distinguish the contributions from XeF fragmentation in the ionization region and Xe arising from XeF dissociation prior to ionization precludes the conclusive determination of the mechanism of XeF dissociation. In addition, there are several questionable assumptions with the simple analysis presented above. First, the measurements which are made in the LAB frame cannot rigorously be transformed into the CM frame because the trajectory of the dissociating XeF molecule, or in other words, the position of the center of mass of the dissociating system, is unknown. The assumption could be made that the trajectory of the dissociating XeF is identical to that of the stable XeF. This assumption is questionable since the energy transfer into the two types of XeF must be different to yield such different outcomes. Second, regardless of the validity of this assumption, the orientation of the molecule with respect to its trajectory is unknown. Because dissociation is likely on the order of a vibrational period which is much less than a rotational period, there will be little rotational motion leading to an anisotropic distribution of molecular orientations. There is no basis for assuming any particular distribution of orientations because the distribution is entirely dependent on the orientation effects of the interaction potential during atom abstraction.

In addition to the problems of analyzing the velocity and angular distributions of the scattered products of an uncharacterized gas phase dissociation, the presence of the surface presents further complications. Because there are so few internal degrees of freedom to store energy in the XeF molecule, the dissociation must occur rapidly and therefore, occurs near the surface. The likelihood of a subsequent interaction, i.e., collision, of the Xe atom and the F atom with the surface is extremely high. This interaction will obscure the velocity distribution of the two scattered products of the dissociation, the only measurable observable with the current apparatus.

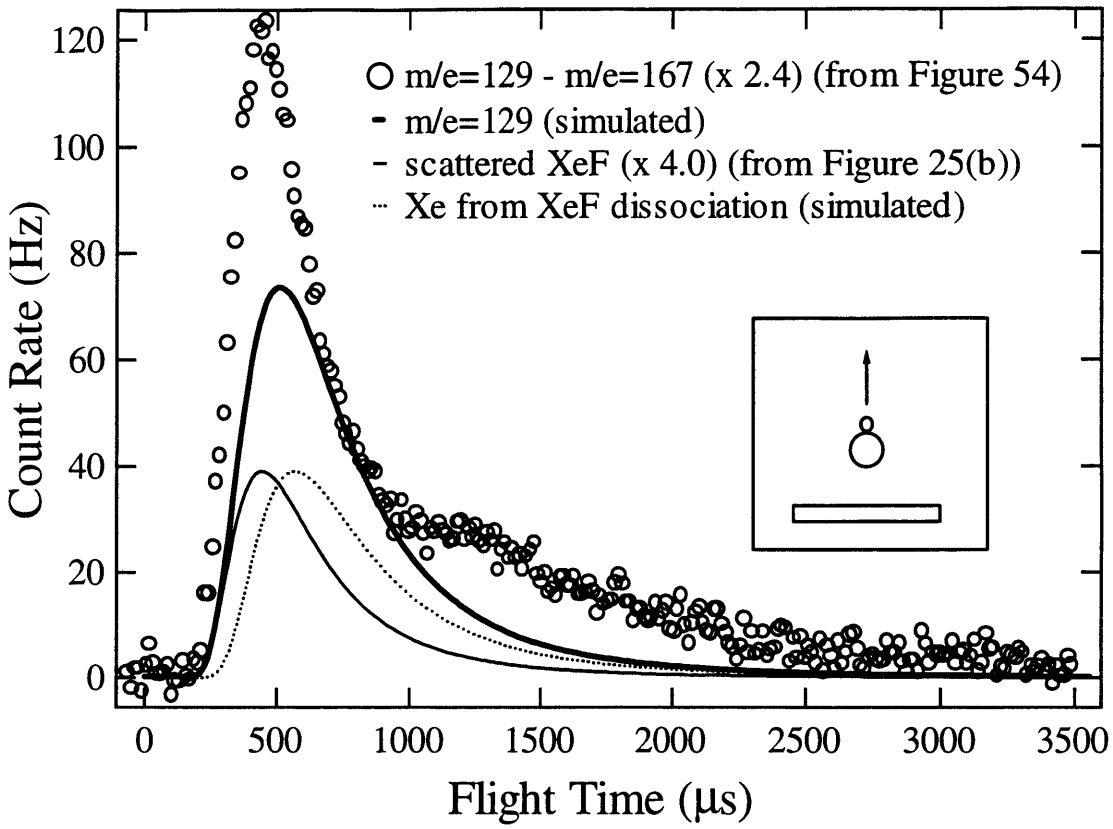

Figure 81 Simulated TOF distribution of scattered products at m/e=129
One component is taken as the fit to the scattered XeF arising from single atom abstraction from Figure 25(b) multiplied by the ideal XeF cracking ratio of 4.0. The other component is the simulation of the scattered Xe arising from the dissociation of XeF assuming the simplified geometry shown in the inset in which the XeF molecular axis is parallel to the XeF velocity with the F-end away from the surface. The total signal at m/e=129 is the sum of these two components. The measured TOF distribution at m/e=129 from Figure 54 is superimposed for comparison. The maximum contribution from unreactively scattered XeF_2 has been subtracted from the signal at m/e=129, however, the contributions from reactively scattered Xe arising from two atom adsorption or unreactively scattered Xe from free Xe in the XeF_2 molecular beam have not been subtracted. The measured TOF distribution is scaled such that the simulated TOF distribution is a physically reasonable component of the measured TOF distribution.

IV.C.3. Dependence of F atom energy distribution on incident XeF_2 energy

The discussion of XeF dissociation has focussed on the results of the interaction of high energy XeF_2 with Si. However, very fast scattered F atoms are present in the interaction of low energy XeF_2 with Si as well. The scattered flux of F atoms shown in Figure 49 displays a similar weak dependence on XeF_2 exposure which is likely a consequence of the weak coverage dependence of the scattered XeF arising from single atom abstraction. Without knowledge of the angular distribution of scattered products, this similarity between low and high energy XeF_2 is merely conjecture.

The most striking difference between the scattered F atoms arising from the interaction of low energy XeF_2 with Si and those arising from high energy XeF_2 is their translational energy. Whereas the translational energy of the scattered XeF is reasonably insensitive to the incident XeF_2 energy (cf. Figure 36), the translational energy of the scattered F atom is noticeably lower (cf. Figure 50) in the interaction of low energy XeF_2 with Si, 5.6±0.5 kcal/mol for low energy XeF_2 versus 6.7±0.1 kcal/mol for high energy XeF_2. These two observations suggest that collisions with the surface may play a role in the XeF dissociation because the kinematics of scattering low and high energy XeF_2 from Si are different.

IV.D. Two atom adsorption

Atom abstraction is a dissociative chemisorption mechanism in which the formation of only a single surface-adsorbate bond liberates sufficient energy to cleave the incident molecular bond. In the interaction of F_2 with Si(100), atom abstraction has been directly observed by detection of the complementary F atom that is scattered into the gas phase. This atom abstraction mechanism is called single atom abstraction because only one F atom is adsorbed onto the surface. In addition to single atom abstraction, it has also been indirectly observed that the complementary F atom may also adsorb to the surface. This atom abstraction mechanism is called two atom adsorption because both F atoms are adsorbed onto the surface. In the interaction of XeF_2, the presence of Xe as a spectator affords the opportunity to directly observe two atom adsorption by detection of the Xe atom that is scattered into the gas phase. In principle the measurement is simple, however, the presence of many other sources of scattered Xe prevent the unambiguous identification of the Xe scattered as a result of two atom adsorption in the interaction of XeF_2 with Si. A self-consistent method described in Sec. III.C.4 revealed a possible TOF distribution of reactively scattered Xe. Although it is not possible to distinguish the Xe that is scattered as a result of XeF dissociation from that which is scattered as a result of two atom adsorption, the results yield some insight into the dynamics of the interaction of XeF_2 with Si. In particular, the results show that after the initial atom abstraction, the XeF that is produced will either escape intact into the gas phase or dissociate near the surface. If the F atom interacts with and adsorbs to the surface, the result is two atom adsorption, but if the F atom escapes into the gas phase, the result is XeF dissociation.

IV.D.1. Kinetics of two atom adsorption

The probability of two atom adsorption is related to the scattered flux of Xe arising from the interaction of XeF_2 with Si. Figure 82(a) shows a plot of the total flux of reactively scattered Xe resulting from the scattering of high energy XeF_2 from Si(100) as a function of fluorine coverage. Analogous to the total flux of the other scattered products shown in Figures 75, 77 and 79, the total flux of reactively scattered Xe atoms is determined by integration of the flux of Xe atoms, which is determined by integration of the velocity-weighted TOF distribution, over the hemisphere above the surface. This integration assumes that the velocity and angular distributions are independent of azimuthal angle. This approximation is justified by the observation that the angular distribution of both the slow and fast components of the reactively scattered Xe flux are broad and cosinelike indicative of an isotropic angular distribution. The flux of Xe decays monotonically with fluorine coverage in agreement with the results of a self-consistent analysis of the exposure dependence of the scattered Xe signal intensity [53]. The flux of scattered Xe can be further separated because the TOF distribution of scattered Xe is bimodal with a fast feature and a slow feature. The total flux into these two distinct scattering channels as a function of fluorine coverage is shown in Figure 82(b) and Figure 82(c). The flux of scattered slow Xe is essentially constant as a function of coverage, while the flux of scattered fast Xe decays monotonically by more than a factor of two over the coverage range 0-1.1 ML F.

The coverage dependence of the total flux of reactively scattered Xe is consistent with that of the other scattered products arising from other scattering channels. Recall that over the coverage range 0-0.6 ML F, the probability of unreactive scattering is reasonably constant, increasing by about 14%. Because the reaction probability is high in this coverage range, the

absolute change of the probability of unreactive scattering is relatively small. Therefore, the total reaction probability, which must complement any change in the probability of unreactive scattering, must be reasonably constant decreasing by much less than 14% over this coverage range. The total flux of scattered XeF arising from single atom abstraction increases by about 11% while the total flux of reactively scattered Xe decreases by 18%. Although the relative flux of scattered XeF to that of reactively scattered Xe is unknown and the contribution of Xe arising from two atom adsorption as opposed to XeF dissociation is unknown, which are necessary for a quantitative calculation of the reaction probabilities, the qualitative trends of the reaction probabilities at low coverage are consistent with each other.

The coverage dependence of the total flux of reactively scattered Xe suggests that although two atom adsorption and XeF dissociation are similar processes in that both lead to the complete dissociation of XeF_2, they are distinct processes. After the initial atom abstraction, a fraction of the XeF dissociates into gas phase Xe and F atoms. Because the coverage dependence of the total flux of scattered F atoms and scattered XeF are similar (cf. Figure 79), the probability of XeF dissociation is independent of coverage. This result is in accordance with the chemical-induced dissociation mechanism which does not involve the participation of the surface after the initial atom abstraction. If there is no two atom adsorption, the coverage dependence of the flux of reactively scattered Xe (cf. Figure 82) should also be similar to that of the scattered XeF, but it is not. Of course, in the event of XeF dissociation the fate of the F atom is not necessarily as a gas phase atom since the extremely reactive F atom will interact with the surface if the dissociating XeF is oriented such that the F-end is directed towards the surface. However, considering the similarity of the coverage dependence of the flux of scattered XeF and

F atoms, either the reaction probability of F atoms is independent of coverage, which is unlikely, or the dissociating XeF is aligned with the F-end directed away from the surface, implying that few F atoms interact with the surface. In addition, if this F atom adsorption mechanism was present, the total flux of F atom would be depleted due to adsorption whereas the total flux of Xe, which cannot adsorb to the surface, would not. On the contrary, it is the flux of reactively scattered Xe that decreases as a function of coverage, because the remaining fraction of scattered XeF does not dissociate after the initial atom abstraction. Although some stable XeF scatters directly into the gas phase, a fraction of the stable XeF interacts with the surface in an analogous fashion to the F atoms arising from single atom abstraction in the interaction of F_2 with Si. If the XeF interacts with an unoccupied site, adsorption may occur. Thus, the probability of two atom adsorption decreases with coverage as the number of unoccupied sites decreases.

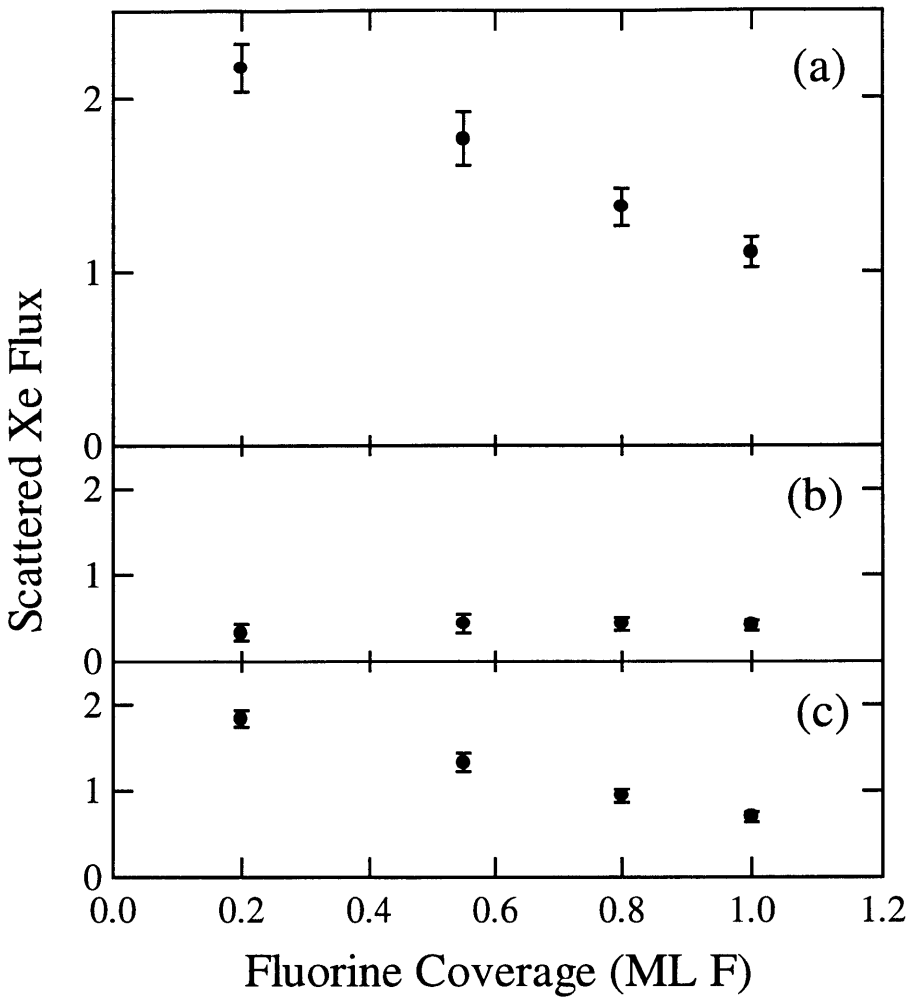

Figure 82 Coverage dependence of total flux of reactively scattered Xe
(a) The total scattered Xe flux as a function of fluorine coverage due to high energy XeF_2 exposure at θ_i=35° and T_s=250 K. The total flux is determined by integrating the angular distribution of the scattered flux shown in Figure 73. The total flux is over the entire hemisphere above the surface so the angular distribution is weighted by the Jacobian, $\sin\theta_d$. The scattered flux is assumed to be independent of azimuthal angle. The total flux is separated into the (b) slow and (c) fast components of the TOF distribution. The error bars represent the propagated uncertainties from the fits to the TOF distributions.

IV.D.2. Energy distribution of two atom adsorption product

The fastest Xe atoms in the velocity distribution of the reactively scattered Xe are similar to the velocities of the fastest XeF molecules despite the exothermicity of two atom adsorption being more than double that of single atom abstraction. The reason for the absence of substantially faster reactively scattered Xe is twofold. First, based on the results of the investigation of the interaction of F_2 with Si presented in Chapter 1, two atom adsorption is not necessarily a concerted process, so the energy liberated in the formation of two surface-adsorbate bonds is deposited into the reaction system in a stepwise process. Thus, the small fraction of the exothermicity gained by XeF in the initial F atom abstraction from XeF_2 can be dissipated through collisions with the surface prior to the final F atom abstraction from XeF. In fact, the translational energy of the scattered XeF is only 6-10 kcal/mol which is similar to the translational energy of the high energy XeF_2 molecular beam. Thus, to a first approximation, the translational energy with which XeF interacts with the surface is similar to the that of the high energy XeF_2 molecular beam. Thus, the scattering dynamics of Xe arising from two atom adsorption ought to be analogous to the scattering dynamics of XeF arising from single atom abstraction. Second, it is likely that only a small fraction of the exothermicity is channeled into the scattered Xe atom during the final F atom abstraction because just like the initial F atom abstraction from XeF_2, there is an attractive interaction between the F atom and the unoccupied dangling bond that results in the exothermicity being channeled into the vibrational energy, as opposed to the translational energy, of the products. In addition, it is difficult for the light F atom to impart significant momentum on the heavy Xe atom.

IV.D.3. Summary

The investigation of the Xe scattered as a result of the interaction of XeF_2 with Si is incomplete. The myriad contributions to the scattered products at m/e=129 make it difficult to separate the contribution from reactively scattered Xe. There are three sets of complications that make this separation especially difficult. First, the cracking ratio of XeF is unknown because there is no experimentally feasible method for producing a pure source of XeF. In addition, the shape of the TOF distribution of scattered XeF is almost identical to the fast feature in the TOF distribution of the scattered products at m/e=129. In the analysis presented here, a maximum XeF cracking ratio of 8 is determined. However, a XeF cracking ratio of 4 yields TOF distributions with similarly shaped fast features for the reactively scattered Xe arising from the interaction of both low and high energy XeF_2 with Si.

Second, the possible presence of free Xe in the XeF_2 molecular beam may lead to *unreactively* scattered Xe which will obscure the signal attributable to reactively scattered Xe. By simultaneously exposing Si to Xe and XeF_2, the TOF distribution of unreactively scattered Xe could be identified. However, the contribution, if any, to the TOF distribution of the scattered products at m/e=129 is unknown. Future experiments in this laboratory will try to further characterize the extent of free Xe in the molecular beam.

Finally, the presence of two reaction mechanisms that produce Xe, two atom adsorption and XeF dissociation, make it difficult to identify and characterize the individual contributions to the reactively scattered Xe flux. It is especially difficult since the two sources of Xe seem to have similar TOF distributions. Although the separation of the two sources of reactively scattered Xe has been unsuccessful so far, the simple observation that there is no Xe that is

remarkably faster than the XeF arising from single atom abstraction, suggests that two atom adsorption is a stepwise process in which the exothermicity is not effectively channeled into the translational energy of the Xe scattered into the gas phase. Future experiments in this laboratory will try to better separate these two sources of reactively scattered Xe which arise from related, but distinct, mechanisms.

V. CONCLUSION

The results suggest the following scheme for the interaction of XeF_2 with Si(100). On impact with the clean surface, the incident XeF_2 can either unreactively scatter or deposit one of its F atoms onto a surface dangling bond. In the unreactive case, the XeF_2 suffers an inelastic collision and is directly scattered back to the gas phase or is trapped and desorbed. In the coverage range 0-0.6 ML F, most of the incident XeF_2 dissociatively chemisorbs via F atom abstraction. The weak coverage dependence of the total flux of unreactively scattered XeF_2 over this wide coverage range is indicative of an extrinsic physisorbed precursor mechanism in which the incident XeF_2 physisorbs on top of an occupied site and diffuses along occupied sites until it encounters an unoccupied site. The presence of a physisorbed precursor in the interaction of XeF_2 with Si is in stark contrast to the interaction of F_2 with Si in which there is no evidence of any physisorbed precursor.

The XeF that is produced from the initial F atom abstraction may scatter directly into the gas phase or interact with the surface. Although scattered XeF is detected, which is indicative of single atom abstraction, the concomitant detection of very fast F atoms suggests that not all of the XeF scattered as a result of single atom abstraction survives, but instead dissociates into gas phase Xe and F atoms. The mechanism for the dissociation of weakly bound XeF cannot be determined from the present results, but it is possible that dissociation is induced by collision with the surface which leads to energy transfer into the weak Xe-F bond. It is also possible that a small fraction of the exothermicity of the initial F atom abstraction is channeled into the internal energy of XeF sufficient to cause dissociation. Although the probability of single atom abstraction, as determined from the total flux of scattered XeF, is only weakly dependent on

coverage, the angular distribution of the scattered XeF flux is strongly dependent on coverage. This observation is consistent with the alignment of the XeF_2 molecule by an attractive interaction between the fluorine and an unoccupied reactive site. The effect is dependent on coverage because alignment is only necessary at higher coverages when the reactive sites are less accessible due to steric hindrance of the large XeF_2 molecule by neighboring adsorbates.

In the interaction of F_2 with Si, the fate of the complementary F atom is not necessarily as a gas phase atom, but it may also adsorb leading to two atom adsorption. In the interaction of XeF_2 with Si, there are two possible mechanisms that lead to the adsorption of both F atoms. First, the F atom produced upon dissociation of XeF may interact with the surface and adsorb. Second, XeF may interact with the surface and dissociatively chemisorb. Although the former mechanism is certainly plausible, and may have significant implications on the reaction because F atoms are extremely reactive with Si, the latter mechanism is likely the dominant mechanism for the adsorption of both F atoms and is, therefore, termed two atom adsorption. There is no evidence to conclusively identify and characterize the scattered Xe produced from these two mechanisms, but the presence of fast F atoms indicates that the first mechanism is plausible and the divergence of the coverage dependence of the reactively scattered Xe flux from that of the scattered XeF and F atom flux suggests that the second mechanism is present as well.

The fluorination of the surface by XeF_2 occurs in a remarkably similar fashion to fluorination by F_2 up to 1 ML. Thermal desorption and He diffraction results show that the reaction of F_2 and XeF_2 with Si(100) occurs almost exclusively at the dangling bonds at coverages below 1 ML. However, at coverages beyond 1 ML, the reaction of F_2 with Si ceases while XeF_2 continues to react, breaking Si dimer bonds and lattice bonds and producing SiF_4, the

product of etching. Why does XeF_2 etch Si whereas F_2 does not? Although the results of this chapter focus on the interaction of XeF_2 with Si at coverages below 1 ML, conditions under which there is no significant etching, the differences in the reactivity of XeF_2 and F_2 yield insight into the possible mechanism of etching. The large mass of XeF_2 (169 amu) relative to F_2 (38 amu) affects the energy transfer of the gas-surface collision since heavy particles are better able to transfer energy to the surface than light particles. The effects of this energy transfer are twofold. First, the efficiency of trapping XeF_2 is greater than F_2. In addition, the large size of XeF_2 relative to F_2, enhances the van der Waals attraction which inhibits desorption thereby increasing the probability of the XeF_2 reacting with an unoccupied site on the surface. Second, the large transfer of energy to the surface concomitant with the availability of reactive F atoms may yield a localized reaction system with sufficient energy to overcome any barriers that may be present at coverages above 1 ML. Not only do these arguments pertain to the incident molecule, but they are also valid for the molecule or atom produced by the initial F atom abstraction. The fast F atoms scattered from single atom abstraction in the interaction of F_2 with Si easily escape into the gas phase whereas the slower XeF produced in the interaction of XeF_2 with Si is more likely to subsequently interact with the surface. In addition, the possibility that the scattered XeF dissociates such that the F atom is directed towards the surface is identical to the interaction of F atoms with Si which is known to etch Si. Thus, the production of extremely reactive atoms and radicals that results from atom abstraction may have a significant effect on the overall reactivity of the system. The advantage of XeF_2 over F_2 is that the heavy mass of the Xe helps to effectively anchor the reactive F atom to the surface.

Future experiments in this laboratory will focus on understanding the importance of energy transfer in the etching of semiconductor surfaces. To understand the importance of multiple collisions and atom abstraction in etching, a molecular beam of van der Waals complexes of Xe and F_2 to form $Xe(F_2)$ will be prepared using standard clustering techniques [76]. The peculiar nature of van der Waals complexes is ideal for testing our hypothesis. The weak interaction between the constituents of the complex confines them together spatially, but maintains their distinct chemical identity; the properties of the F_2 molecule of $Xe(F_2)$ are essentially identical to those of a lone F_2 molecule. In the simplest experiment, the $Xe(F_2)$ will be scattered from the Si surface, and the evolution of etch product will be measured and compared with the results of the F_2 investigation. The $Xe(F_2)$ complexes in the molecular beam that are properly oriented, i.e., F_2-end towards the surface, ought to behave like "heavy" F_2 molecules because of the momentum of the weakly bound Xe driving them repeatedly towards the surface. If it is simply the additional mass of Xe that leads to etching by F_2, then an enhancement in etching relative to F_2 alone ought to be observed. If enhanced etching is observed, subsequent experiments using van der Waals complexes of varying mass (i.e., $Kr(F_2)$, $Ar(F_2)$) would be useful in gaining a detailed understanding of the effects of additional mass to the F_2 molecule.

However, if the subsequent interaction of reactive radicals, i.e., F atoms and XeF, with the surface is important for etching, no enhancement in etching will be observed with the use of small van der Waals complexes. This is because van der Waals complexes are weakly bound by energies on the order of kcal/mol, so a perturbation as weak as a collision will likely lead to dissociation. Thus, it is unlikely that the F atom produced by atom abstraction from $Xe(F_2)$ will

remain trapped on the surface by the heavy Xe atom. Instead of using small complexes, large van der Waals clusters comprised of noble gas and F_2 could be used to trap the F_2 and, more importantly, the F atoms produced from F atom abstraction, to the surface until the necessary reaction occurs. Experimental [77] and theoretical [78] investigations have shown that large noble gas clusters not only impart significant energy to a surface upon collision, but that the particles at the cluster-surface interface reside in the vicinity of the surface for a significant period of time as the rest of the cluster dissipates its energy into the surface as well as through evaporation. Thus, with a large cluster with F_2, the F_2 and F atoms that are trapped at this interface at the surface would have ample time to react leading to etching. The results of the two experiments proposed above will certainly yield further insight into the disparate reactivity of XeF_2 and F_2 with Si.

REFERENCES

1. H.F. Winters and J.W. Coburn, *Appl. Phys. Lett.* **34**, 70 (1979).
2. H.F. Winters and J.W. Coburn, *Surf. Sci. Rep.* **14**, 165 (1992) and references therein.
3. M.J. Vasile, *J. Appl. Phys.* **54**, 6697 (1983).
4. D.E. Ibbotson, D.L. Flamm, J.A. Mucha, and V.M. Donnelly, *Appl. Phys. Lett.* **44**, 1129 (1984).
5. R.B. Alexander, D.M. Heffelfinger, K.R. Padmanabhan, and J.C. Buchholz, *J. Appl. Phys.* **57**, 5268 (1985).
6. M.J.M. Vugts, G.L.J. Verschueren, M.F.A. Eurlings, L.J.F. Hermans, and H.C.W. Beijerinck, *J. Vac. Sci. Tech. A* **14**, 2766 (1996).
7. A. Cassuto and D.A. King, *Surf. Sci.* **102**, 388 (1981).
8. H.F. Winters and F.A. Houle, *J. Appl. Phys.* **54**, 1218 (1983).
9. F.A. Houle, *J. Chem. Phys.* **87**, 1866 (1987).
10. J.A. Dagata, D.W. Squire, C.S. Dulcey, D.S.Y Hsu, and M.C. Lin, *J. Vac. Sci. Tech. B* **5**, 1495 (1987).
11. F.A. Houle, *J. Appl. Phys.* **60**, 3018 (1986).
12. M.J. Mitchell, M. Suto, L.C. Lee, and T.J. Chuang, *J. Vac. Sci. Tech. B* **5**, 1444 (1987). M. Suto, J.C. Han, L.C. Lee, and T.J. Chuang, *J. Chem. Phys.* **90**, 2834 (1989).
13. T.J. Chuang, *J. Appl. Phys.* **51**, 2614 (1980).
14. F.R. McFeely, J.F. Morar, N.D. Shinn, G. Landgren, and F.J. Himpsel, *Phys. Rev. B* **30**, 764 (1984).
15. J.F. Morar, F.R. McFeely, N.D. Shinn, G. Landgren, and F.J. Himpsel, *Appl. Phys. Lett.* **45**, 174 (1984).
16. N.D. Shinn, J.F. Morar, and F.R. McFeely, *J. Vac. Sci. Tech. A* **2**, 1593 (1984).
17. B. Roop, S. Joyce, J.C. Schultz, N.D. Shinn, and J.I. Steinfeld, *Appl. Phys. Lett.* **46**, 1187 (1985).
18. B. Roop, S. Joyce, J.C. Schultz, and J.I. Steinfeld, *Surf. Sci.* **173**, 455 (1986).
19. J.A. Yarmoff and F.R. McFeely, *Phys. Rev. B* **38**, 2057 (1988).
20. C.W. Lo, D.K. Shuh, V. Chakarian, T.D. Durbin, P.R. Varekamp, and J.A. Yarmoff, *Phys. Rev. B* **47**, 15648 (1993).
21. C.W. Lo, D.K. Shuh, and J.A. Yarmoff, *J. Vac. Sci. Tech. A* **11**, 2054 (1993).
22. C.W. Lo, P.R. Varekamp, D.K. Shuh, T.D. Durbin, V. Chakarian, and J.A. Yarmoff, *Surf. Sci.* **292**, 171 (1993).
23. T. Takahagi, A. Ishitani, and S. Wakao, *J. Appl. Phys.* **76**, 3140 (1994).
24. J.A. Yarmoff, A. Taleb-Ibrahimi, F.R. McFeely, and Ph. Avouris, *Phys. Rev. Lett.* **60**, 960 (1988).
25. J.A. Yarmoff and S.A. Joyce, *Phys. Rev. B* **40**, 3143 (1989).
26. V.M. Bermudez, *J. Vac. Sci. Tech. A* **10**, 3478 (1992).
27. S. Haraichi, F. Sasaki, S. Kobayashi, M. Komuro, and T. Tani, *J. Vac. Sci. Tech. A* **13**, 745 (1995).
28. T.J. Chuang, *Phys. Rev. Lett.* **42**, 815 (1979).
29. H.F. Winters and D. Haarer, *Phys. Rev. B* **36**, 6613 (1987).
30. J.W. Coburn and H.F. Winters, *J. Appl. Phys.* **50**, 3189 (1979).
31. Y.Y. Tu, T.J. Chuang, and H.F. Winters, *Phys. Rev. B* **23**, 823 (1981).

32. R.A. Haring, A. Haring, F.W. Saris, and A.E. de Vries, *Appl. Phys. Lett.* **41**, 174 (1982).
33. F.A. Houle, *Appl. Phys. Lett.* **50**, 1838 (1987).
34. M.J.M. Vugts, L.J.F. Hermans, and H.C.W. Beijerinck, *J. Vac. Sci. Tech. A* **14**, 2138 (1996).
35. M.J.M. Vugts, L.J.F. Hermans, and H.C.W. Beijerinck, *J. Vac. Sci. Tech. A* **14**, 2820 (1996).
36. T.J. Chuang, *J. Chem. Phys.* **74**, 1461 (1981).
37. F.A. Houle, *Chem. Phys. Lett.* **95**, 5 (1983).
38. F.A. Houle, *J. Chem. Phys.* **79**, 4237 (1983).
39. F.A. Houle, *J. Chem. Phys.* **80**, 4851 (1984).
40. F.A. Houle, *Phys. Rev. Lett.* **61**, 1871 (1988).
41. F.A. Houle, *Phys. Rev. B* **39**, 10120 (1989).
42. B. Li, U. Streller, H.P. Krause, I. Twesten, and N. Schwentner, *J. Appl. Phys.* **77**, 350 (1995).
43. F.I. Chang, R. Yeh, G. Lin, P.B. Chu, E. Hoffman, E.J.J. Kruglick, and K.S.J. Pister, and M.H. Hecht, *Proc. SPIE* **2641**, 117 (1995).
44. D.J. Gladstone, Ph.D. thesis, Massachusetts Institute of Technology (1989).
45. M. McGonigal, Ph.D. thesis, Massachusetts Institute of Technology (1989).
46. M.T. Schulberg, Ph.D. thesis, Massachusetts Institute of Technology (1990).
47. S.T. Ceyer, D.J. Gladstone, M. McGonigal, and M.T. Schulberg, Physical Methods in Chemistry, ed. B.W. Rossiter and R.C. Baetzwold (Wiley, New York, 1993), 2nd ed., Vol. IXA, p. 383.
48. F. Schreiner, G.N. McDonald, and C.L. Chernick, *J. Phys. Chem.* **72**, 1162 (1968).
49. A. Ishizaka and Y. Shiraki, *J. Electrochem. Soc.* **133**, 666 (1986).
50. K. Kuhnke, K. Kern, R. David, and G. Comsa, *Rev. Sci. Inst.* **65**, 3458 (1994).
51. P.C. Tellinghuisen, J. Tellinghuisen, J.A. Coxon, J.E. Velazco, and D.W. Setser, *J. Chem. Phys.* **68**, 5187 (1978).
52. S.T. Ceyer and coworkers, unpublished.
53. D. Gosalvez-Blanco, Ph.D. thesis, Massachusetts Institute of Technology (1997).
54. J.J. Yang, Ph.D. thesis, Massachusetts Institute of Technology (1993).
55. Y.L. Li, D.P. Pullman, J.J. Yang, A.A. Tsekouras, D.B. Gosalvez, K.B. Laughlin, Z. Zhang, M.T. Schulberg, D.J. Gladstone, M. McGonigal, and S.T. Ceyer, *Phys. Rev. Lett.* **74**, 2603 (1995).
56. M.R. Tate, D. Gosalvez-Blanco, D.P. Pullman, A.A. Tsekouras, Y.L. Li, J.J. Yang, K.B. Laughlin, S.C. Eckman, M.F. Bertino, and S.T. Ceyer, *J. Chem. Phys.*, in press.
57. H.F. Winters and F.A. Houle, *J. Appl. Phys.* **54**, 1218 (1983).
58. M.J. Cardillo and G.E. Becker, *Phys. Rev. B* **21**, 1497 (1980).
59. J.R. Engstrom, M.M. Nelson, and T. Engel, *Surf. Sci.* **215**, 437 (1989).
60. J.E. Hurst, C.A. Becker, J.P. Cowin, K.C. Janda, L. Wharton, and D.J. Auerbach, *Phys. Rev. Lett.* **43**, 1175 (1979); J.E. Hurst, L. Wharton, K.C. Janda, and D.J. Auerbach, *J. Chem. Phys.* **78**, 1559 (1983).
61. M.R. Tate, D. Gosalvez-Blanco, M.F. Bertino, and S.T. Ceyer, unpublished.
62. Commission on Atomic Weights and Isotopic Abundances "Table of Isotopic Compositions of the Elements as Determined by Mass Spectrometry," (1989).
63. H.C. Straub, P. Renault, B.G. Lindsay, K.A. Smith, and R.F. Stebbings, *Phys. Rev. A* **52**, 1115 (1995).
64. S.T. Govoni and G.M. Nathanson, *J. Am. Chem. Soc.* **116**, 779 (1994).

65. J.K. Klassen and G.M. Nathanson, *Science* **273**, 333 (1996).
66. J.K. Klassen, K.M. Fiehrer, and G.M. Nathanson, *J. Phys. Chem. B* **101**, 9098 (1997).
67. M. Beutl, M. Riedler, K.D. Rendulic, *Chem. Phys. Lett.* **247**, 249 (1995).
68. M. Gostein and G.O. Sitz, *J. Chem. Phys.* **106**, 7378 (1997).
69. A. Gross, S. Wilke, and M. Scheffler, *Phys. Rev. Lett.* **75**, 2718 (1995).
70. M. Kay, G.R. Darling, S. Holloway, J.A. White, and D.M. Bird, *Chem. Phys. Lett.* **245**, 311 (1995).
71. G.R. Darling, M. Kay, and S. Holloway, *Surf. Sci.* **400**, 314 (1998).
72. C.T. Rettner and D.J. Auerbach, *Science* **263**, 365 (1994).
73. M.G. Evans and M.C. Polanyi, *Trans. Faraday. Soc.* **35**, 178 (1939).
74. R. Walsh, *Acc. Chem. Res.* **14**, 246 (1981).
75. P.J. Hay and T.H. Dunning, Jr., *J. Chem. Phys.* **69**, 2209 (1978).
76. M. Kappes and S. Leutwyler, in *Atomic and Molecular Beam Methods*, edited by G. Scoles, Vol. 1 (Oxford, New York, 1988), pp. 380-415 and references therein.
77. H. Vach, A. DeMartino, M. Benslimane, M. Châtelet, and F. Pradère, *J. Chem. Phys.* **100**, 8526 (1994).
78. C.L. Cleveland and U. Landman, *Science* **257**, 355 (1992).

Appendix A: Least Squares Fitting Algorithm

The determination of the reaction probabilities in the interaction of F_2 with Si(100) requires the numerical solution of the system of coupled differential equations given by Eq. (III.35) and Eq. (III.37) in Chapter 1. There are four independent variables, cross sections A, B, D and E′, of which two, A and D, are determined from the experimentally determined reaction probabilities in the limit of zero coverage. The remaining two parameters, B and E′, are determined by a least squares fit of the model to the experimental data. The fitting algorithm is based on the standard Levenberg-Marquardt method [1] which is an optimized method for efficiently minimizing the χ^2 function given by Eq. (III.46) in Chapter 1 using the gradient of the χ^2 function with respect to the parameters, B and E′. The standard algorithm, however, is not written to fit a system of differential equations. Therefore, code was written specifically to fit the model to the experimental data. The numerical analysis program MATLAB is used to perform all of the numerical calculations [2]. Common MATLAB functions are used whenever possible.

A. Program *mrqmin*

The central program **mrqmin** provides the framework for the iterative fitting algorithm and calls other programs for a variety of repetitive calculations. The experimental results are called into the program for calculation of the value of the χ^2 function. The experimental results are in a text file **f2krexp.dat** made up of nine columns: exposure (ML F), the average value and uncertainty of P_0, P_1, P_2, and coverage, respectively. The values of the probabilities and the coverage represent the average of six measurements after interpolation to a common exposure interval (0.1 ML F) and range (0-15 ML F). The uncertainty is representative of the uncertainty of one measurement.

```
load f2krexp.dat

ebase=linspace(0.1,15,150)';
p0data(:,1)=f2krexp(:,2);
p0data(:,2)=f2krexp(:,3);
p1data(:,1)=f2krexp(:,4);
p1data(:,2)=f2krexp(:,5);
p2data(:,1)=f2krexp(:,6);
p2data(:,2)=f2krexp(:,7);
covdata(:,1)=f2krexp(:,8);
covdata(:,2)=f2krexp(:,9);
```

The fitting algorithm is initialized by defining the initial guesses for parameters B and E´ in the vector **parameterarray**. The variable **lambda** controls the magnitude of the change in the parameter values during the fitting algorithm. It is set to –1 as a flag to initialize the fitting. The variable **deltachisquare** is the difference between a new minimum value of the χ^2 function and the previous minimum value. The fitting algorithm stops when **deltachisquare** < 0.001 (hence **deltachisquare** is initially set to 1) to avoid unnecessary optimization. The initialization of the fitting algorithm is completed by calculating the value of the χ^2 function as well as the values of the α matrix and β vector, which are necessary for determining the gradient of the χ^2 function, by calling the program **mrqcof**.

```
parameterarray=[1.68     1.03]

parameterarrayinitial=parameterarray;

lambda=-1;
deltachisquare=1;

while deltachisquare > 0.001
      if lambda<=0
            [alpha,beta,p0chisquare,p1chisquare]
                        =mrqcof(p0data,p1data,parameterarray);
            oldchisquare=p0chisquare+p1chisquare;
            lambda=0.001;
      end
```

The new parameter array is determined from the α matrix and β vector, which are related to the gradient of the χ^2 function with respect to the two parameters, B and E´. The α matrix is

modified by multiplying the diagonal elements by (1+λ) and solving the following equation for δB and δE′:

$$\begin{pmatrix} \alpha_{BB}(1+\lambda) & \alpha_{BE} \\ \alpha_{EB} & \alpha_{EE}(1+\lambda) \end{pmatrix} \begin{pmatrix} \delta B \\ \delta E \end{pmatrix} \equiv \begin{pmatrix} \beta_B \\ \beta_E \end{pmatrix}, \tag{A.1}$$

The original guesses for the parameters B and E′ in **parameterarray** are modified by adding δB and δE′, respectively.

```
covar=alpha;
for j=1:length(parameterarray)
      covar(j,j)=alpha(j,j)*(1+lambda);
end
da=beta;

covararg=[covar,da];

covarsol=rref(covararg);
da=covarsol(:,(length(parameterarray)+1));

parameterarrayattempt=parameterarray+da'
```

The value of the χ^2 function is determined for the new guesses for the parameters B and E′ in **parameterarrayattempt**. If the new value of the χ^2 function is less than the previous minimum value, then the value of **lambda** is decreased by a factor of 10 to minimize the extent of the next step in the iteration since the true minimum value is probably nearby. On the other hand, if the new value of χ^2 is greater than the previous minimum value, then the value of **lambda** is increased by a factor of 10, increasing the extent of the next step since the true minimum is probably farther away than the previous best guess. Unless the value of the χ^2 function decreases less than 0.001, another step is calculated to determine a new set of parameters.

```
[alpha,beta,p0chisquare,p1chisquare]
            =mrqcofabc(p0data,p1data,parameterarrayattempt);
chisquare=p0chisquare+p1chisquare

if chisquare<oldchisquare
      lambda=0.1*lambda;
```

```
        deltachisquare=oldchisquare-chisquare
        oldchisquare=chisquare;
        parameterarray=parameterarrayattempt;
else
lambda=10*lambda;
chisquare=oldchisquare;
parameterarrayattempt=parameterarray;
end
```

After the fitting algorithm has determined the best fit values for the two parameters, the uncertainty of the two parameters can be determined from the diagonal elements of the covariance matrix, which is the inverse of the α matrix (alternatively, the **covar** matrix with **lambda**=0).

```
parameterarrayvariance=inv(alpha)
for k=1:length(parameterarray)
      parameterarraysigma(k)=sqrt(parameterarrayvariance(k,k))
end
```

The best fit values for the parameters B and E′ are given by the first and second elements of the vector **parameterarray**, respectively. Similarly, the uncertainties of the best fit values of B and E′ are given by the first and second elements of the vector **parameterarraysigma**, respectively.

B. Subroutine *mrqcof*

The function **mrqcof** determines the contributions of P_0 and P_1 to the χ^2 function as well as the values of the α matrix and the β vector, which are related to the gradient of the χ^2 function.

$$\alpha \equiv \sum_{i=1}^{10}\sum_{j=0}^{1}\frac{1}{\sigma_{P_j}^2(\varepsilon_i)}\begin{pmatrix}\left(\frac{\partial P_j(\varepsilon_i)}{\partial B}\right)^2 & \frac{\partial P_j(\varepsilon_i)}{\partial B}\frac{\partial P_j(\varepsilon_i)}{\partial E'}\\ \frac{\partial P_j(\varepsilon_i)}{\partial E'}\frac{\partial P_j(\varepsilon_i)}{\partial B} & \left(\frac{\partial P_j(\varepsilon_i)}{\partial E'}\right)^2\end{pmatrix}, \tag{B.1}$$

$$\beta \equiv \sum_{i=1}^{10}\sum_{j=0}^{1}\frac{P_j^{exp}(\varepsilon_i)-P_j^{obs}(\varepsilon_i)}{\sigma_{P_j}^2(\varepsilon_i)}\begin{pmatrix}\frac{\partial P_j(\varepsilon_i)}{\partial B}\\ \frac{\partial P_j(\varepsilon_i)}{\partial E'}\end{pmatrix}. \tag{B.2}$$

The α matrix and β vector require knowledge of the derivatives of P_0 and P_1 with respect to the two parameters, B and E´, which are calculated by another program **abcfit**.

```
function [alpha,beta,p0chisquare,p1chisquare]
            = mrqcofabc(data0,data1,parameterarray)

alpha=zeros(length(parameterarray));
beta=zeros(length(parameterarray),1);
p0chisquare=0;
p1chisquare=0;

[model,dp0da,dp1da]=abcfit(parameterarray);
for i=1:10
      dy0=data0(i,1)-model(i,2);
      dy1=data1(i,1)-model(i,3);
      for j=1:length(parameterarray);
            dy0da=dp0da(i,j);
            dy1da=dp1da(i,j);
            weight0=dy1da/(data0(i,2)^2);
            weight1=dy1da/(data1(i,2)^2);
            for k=1:length(parameterarray)
                  dy0da=dp0da(i,k);
                  dy1da=dp1da(i,k);
                  alpha(j,k)=alpha(j,k)+weight0*dy0da+weight1*dy1da;
            end
            beta(j)=beta(j)+weight0*dy0+weight1*dy1;
      end
      p0chisquare=p0chisquare+(dy0/data0(i,2))^2;
      p1chisquare=p1chisquare+(dy1/data1(i,2))^2;
end
```

C. Subroutine *abcfxn*

The function **abcfxn** along with the function **abcode** numerically solve the system of differential equations given values for parameters B and E´ in **parameterarray**.

```
function model = abcfxn(parameterarray)

global A
global B
global D
global E
global If2

A=0.955;
B=parameterarray(1);
%B=A;
D=0.872;
E=parameterarray(2);
```

```
%E=D;
If2=0.17;                %F2 flux (ML F/sec)

theta0=0;
theta0(1)=0;
theta0(2)=0;
theta=0;
theta(1)=0;
theta(2)=0;
```

The system of differential equations is solved numerically using the MATLAB function **ode45**. The system of differential equations is defined by function **abcode** described in the next section. The `[0 120]` refers to the range of the solution and corresponds to the F_2 exposure in seconds, and **theta0** refers to the boundary conditions defined above.

```
[e,theta]=ode45('abcode', [0 120], theta0);
```

The solutions for θ_1 and θ_2 are returned to Eqs. (III.29)-(III.31) in Chapter 1 to determine the reaction probabilities.

```
emptypair=(1-(2*theta(:,1)+theta(:,2)));
coverage=theta(:,1)+theta(:,2);

p2=(A*emptypair + B*theta(:,1)).*(D*emptypair + E*theta(:,1));
p1=(A*emptypair + B*theta(:,1)).*(1-(D*emptypair + E*theta(:,1)));
p0=1-(A*emptypair + B*theta(:,1));
```

Finally, the results of the model are interpolated to match the exposure range (0-15 ML F) and interval (0.1 ML F) for comparison to the experimental results.

```
ebase=linspace(0.1,15,150)';

covbase=interp1(e*If2,coverage,ebase);
p0base=interp1(e*If2,p0,ebase);
p1base=interp1(e*If2,p1,ebase);
p2base=interp1(e*If2,p2,ebase);

model=[ebase,p0base,p1base,p2base,covbase];
```

D. Subroutine *abcode*

The function abcode defines the system of differential equations, θ_1 (**theta1prime**) and θ_2 (**theta2prime**), to be numerically solved by the MATLAB function **ode45**.

```
function thetaprime = abcode(e,theta)

global A
global B
global D
global E
global If2    %F2 flux (ML F/s)

emptypair=(1-(2*theta(1)+theta(2)));

theta1prime=0.5*If2*((A*emptypair.*(1+D*emptypair-E*theta(1)))
                        - B*theta(1).*(1-D*emptypair+E*theta(1)));

theta2prime=If2*(B*theta(1).*(1 + E*theta(1)) + A*emptypair.*(E*theta(1)));

thetaprime=[theta1prime theta2prime]';
```

E. Subroutine *abcfit*

The function **abcfit** numerically calculates the derivative of the two independent functions, P_0 and P_1, with respect to the two parameters B and E´. This differentiation is performed by solving the differential equations for parameter values that are 0.001% above and below the current value and then calculating the slope.

```
function [model, dp0da, dp1da]=abcfit(parameterarray)

model=abcfxn(parameterarray);

for i=1:(length(parameterarray))
      parameterarrayminus=parameterarray;
      parameterarrayminus(i)=parameterarray(i)*(1-1e-5);
      modelminus=abcfxn(parameterarrayminus);
      parameterarrayplus=parameterarray;
      parameterarrayplus(i)=parameterarray(i)*(1+1e-5);
      modelplus=abcfxn(parameterarrayplus);
      dp0da(:,i)=(modelplus(:,2)-modelminus(:,2))/(parameterarray(i)*2e-5);
      dp1da(:,i)=(modelplus(:,3)-modelminus(:,3))/(parameterarray(i)*2e-5);
end
```

REFERENCES

1. W.H. Press, S.A. Teukolsky, W.T. Vetterling and B.P. Flannery, *Numerical Recipes in C: The Art of Scientific Computing*, 2nd ed., (Cambridge University Press, Cambridge, 1992), 681-688.
2. MATLAB Version 5.2 (The Mathworks, Inc., Natick, MA, 1998).

Appendix B: Detector Modification

I. INTRODUCTION

The ionizer cryostat is one of the most important parts of the scattering chamber and serves two essential purposes. First, it holds the electron bombardment ionizer in a precise position to optimally transform the beam of "invisible" neutral particles scattering from the crystal surface into a "visible" beam of ions that are subsequently filtered by the quadrupole according to their mass-to-charge ratio and detected by a channeltron electron multiplier. Second, the ionizer cryostat is cooled to cryogenic temperatures (77 K) with liquid nitrogen (LN_2) which acts as a cryopump to minimize the number of background particles that are ionized and detected as spurious signal. A leak to atmosphere in the ionizer cryostat led to significant efforts to repair, modify, and align this essential part of the experimental apparatus. This Appendix describes in detail the complete renovation of the ionizer cryostat and the detector as a whole.

The original ionizer cryostat has been described in detail elsewhere [1]. Figure 1 is a schematic of the side and top views of the ionizer cryostat. The various components are referred to throughout this Appendix by letters denoted in Figure B.1. The vacuum side of the cryostat consists of a welded stainless steel double-walled reservoir, made of the outer tube B, the inner tube D, the lower tube coupling C and the upper tube coupling E, which is brazed to the hollow copper block P. The ionizer and the collimating apertures are mounted into two bores that are precisely located to ensure that the axis of the ionizer is parallel to the axis of the detector as a whole. The inner tube J extends from the side of the reservoir and acts as an inlet for a LN_2 storage dewar. All of these cryogenically cooled parts are vacuum-insulated and supported by a tubular structure that consists of the cryostat support ring F, the vertical cryostat support tube G,

the cryostat mating flange H, the vertical pumping support tube I and the horizontal LN_2 storage dewar support tube K. The ionizer cryostat is mounted on the scattering chamber via the flat-faced flange H with a locating step and dowel pin to ensure proper alignment of the ionizer axis with respect to the detector axis. A special aluminum knife-edge gasket (Leybold, Model 88626, inner diameter bored to 6.130") seals the two mating flat faces. The 6" conflat flange L welded to the vertical pumping support tube I on the top of the cryostat is the connection to a pneumatic gate valve, a dual-flanged turbomolecular pump and a closed cycle He refrigerator cryopump.

The two bores for mounting the ionizer and collimating apertures, B1 and B2, are precisely located and aligned with respect to three reference planes defined by the flange H that mates the cryostat to the rest of the detector. Three reference planes are denoted by -A-, -B- and -C- and are shown in Figure B.1. Reference plane -A- is the horizontal surface of the mating flange. The vertical position of the ionizer and of the collimating apertures relative to the rest of the detector is defined by reference plane -A-. Reference plane -C- is the diameter of the vertical step that protrudes from the mating flange H. The horizontal position of the cryostat relative to the rest of the scattering chamber is defined by reference plane -C-. Finally, reference plane -B- is the mirror plane defined by the intersection of the diameter -C- with a dowel pin hole on the mating flange H. The perpendicularity of the two bores with respect to the detector axis is defined by reference plane -B-. Plates with precisely machined steps fit into these bores. These plates have the ionizer and collimating apertures precisely located on them.

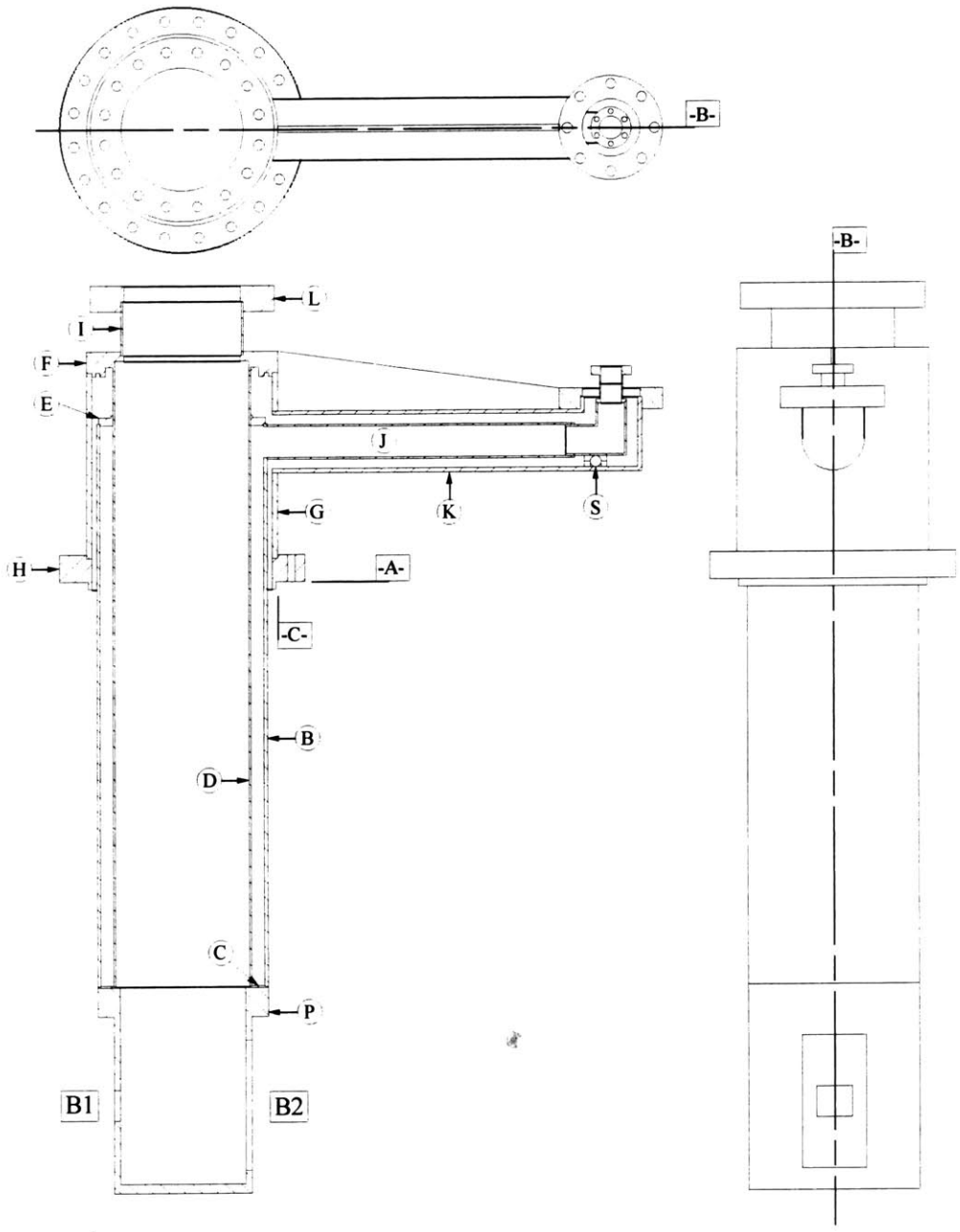

Figure 1 Drawing of ionizer cryostat
All distinct parts are labeled by encircled letters. Three reference planes are labeled as -A-, -B-, and -C-. The bores for the entrance aperture plate and ionizer and exit aperture plate are labeled B1 and B2, respectively.

The leak was located in the vicinity of the junction between the inner tube J and the top of the double-walled reservoir at the junction of the outer and inner vertical tubes, B and D, and the upper tube coupling ring E. The cryostat had to be disassembled to access and repair the leak. The subsequent reassembly required substantial welding which resulted in the misalignment of the precisely located bores on the cryostat. The critical surfaces of the cryostat were machined to align the cryostat to the original design specifications.

II. REPAIR

II.A. Welding

The disassembly of the cryostat started with the removal of the entire structure that provides vacuum and structural integrity. Because of the double-walled construction and the right angles leading to both the double-walled reservoir of the cryostat and the LN_2 storage dewar, the outer and inner tubes, K and J, were removed and discarded. A section of the inner tube J, sufficiently short that the vertical cryostat support tube G could be removed, was left on outer vertical tube D to facilitate the reattachment of a new inner tube J. The main support structure, which consists of the cryostat support ring F, the vertical cryostat support tube G, the cryostat mating flange H, and the vertical pumping support tube I, was removed by cutting tube inner tube D at the junction where it is welded to cryostat support ring F. With the leak fully exposed, new welds were made at the junctions between the upper coupling ring E and the outer and inner tubes D and B. A short horizontal section of the inner tube J was welded to outer tube B. The integrity of the welds of the double walled reservoir were checked with a He leak detector.

The first step of the reconstruction was the attachment of the outer supporting structure, which consists of the tube G and the flange F and the reference flange H, to the main body of the cryostat. The inner vertical tube D was extended to compensate for the material lost in the cutting process by welding a short length of tube and machining it to the appropriate length such that the distance from reference plane -A- to the middle of the bores in the copper block were approximately correct. A step was precisely machined with respect to the reference diameter -C- into the mating surface on the cryostat support ring F to align the outer support structure with the double-walled reservoir. The support structure was welded to the double-walled reservoir. The vacuum integrity of this weld could not be checked, but it is not essential since both sides of the weld are maintained at ultrahigh vacuum.

The second step of the reconstruction was with the attachment of the arm connecting the double-walled reservoir to the LN_2 storage dewar. This involved a sequence of welds to attach the outer and inner tubes, K and J, to the vertical cryostat support tube G and the outer wall of the double-walled reservoir, respectively. The first weld was to reattach the horizontal section of the inner tube J to the outer vertical tube D. Instead of using a single tube, two sections of tube of 1 1/8" OD and 1" OD were welded together to create a step at the end of the tube near the elbow. These welds was He leak checked via tube J. The second weld was to reattach the horizontal section of the outer tube K to the outer vertical cryostat support tube G. This weld was He leak checked via tube K. The third weld was to reattach the short vertical section of the inner tube J which has a knife-edge miniconflat flange. The final weld was the attach the short vertical outer tube K which has a 3 3/8" knife-edge conflat flange.

Prior to the final weld, a modification was made to the original design of the cryostat. A support was inserted between the horizontal sections of tubes J and K to constrain the motion of the inner tube J. The vacuum integrity at the end of the arm to the LN_2 storage dewar is maintained by a double-walled knife-edge seal adapter. The inner tube is attached to a welded bellows such that the inner knife-edge seal can be attached before attaching the outer knife-edge seal. The compression of the bellows imparts a significant downward force on the horizontal section of tube J producing a substantial torque on the weld of inner tube J to the outer vertical tube B, the location of the leak. This strain was alleviated by placing a support between inner tube J and outer tube K directly below the bellows. The step in inner tube J prevents the support from moving away from the elbow towards the main body of the cryostat. The support consists of a half cylinder of stainless steel with holes that fit two 3/8" diameter glass spheres. The support arises entirely from the glass spheres; the stainless steel half cylinder merely constrains the motion of the glass spheres. Glass was chosen because of its extremely low thermal conductivity at cryogenic temperatures.

II.B. Machining

The substantial disassembly and welding necessary to repair the leak in the ionizer cryostat resulted in its misalignment. Specifically, the bores in the copper block were no longer precisely located with respect to the three reference planes. In addition, the surface of mating flange H that defined reference plane -A- was no longer flat.

The only reference surface that was unaffected by the disassembly and welding was the reference diameter -C-. The ionizer cryostat was mounted on a lathe and indicated on reference

diameter -C-. A minimal cut was taken along reference plane -A- to attain flatness while maintaining perpendicularity with respect to reference diameter -C-.

With the recovery of reference plane -A-, the final machining of the apertures proceeded on a mill. Minimal cuts were taken from the two faces of the copper block P that contain the bores to make the two faces parallel to each other as well as attain perpendicularity with respect to reference plane -A-. Next, the bores were expanded to attain perpendicularity of the vertical sides with respect to reference plane -A- and squareness of the apertures themselves. In addition, the vertical sides were cut such that the horizontal centers of the two bores were aligned with respect to each other, and the horizontal sides were cut such that the vertical centers of the two apertures were precisely 16.976" from reference plane -A-. The final dimensions of the front bore were 1.015" high by 1.175" wide and the final dimensions of the rear bore were 4.331" high by 2.085" wide.

Finally, reference plane -B- was recovered by reboring the dowel pin hole to attain perpendicularity with respect to reference plane -A- and to center and attain perpendicularity between the bores in the copper block P and the detector axis. A sleeve with a quarter inch dowel pin hole was press fit into the new bore. This was done to maintain the original dowel pin size since the mating dowel pin hole in the mating flange on the detector could not be machined.

III. MODIFICATION

Because the two bores on the copper block were rebored to larger dimensions, new plates for the ionizer and the collimating apertures that are mounted into these bores had to be constructed. In addition, the design of the original ionizer flange was plagued by two problems that made its maintenance an intimidating task. First, the original ionizer mounting plate could

not be removed without removing the ionizer cryostat itself because it was too large to fit through the bore where the housing for the quadrupole is attached to the detector chamber. Second, the electrical feedthroughs on the original ionizer mounting plate were fragile and extremely difficult to repair if broken since they were brazed onto the plate.

Figure 2 is a drawing of the new ionizer plate. The new ionizer plate is similar to the original ionizer plate except that its size is significantly smaller and the electrical feedthroughs are more robust and, most importantly, replaceable. The size of the ionizer mounting plate was decreased by eliminating all but four of the mounting holes. A step on the plate is precisely fit into the larger bore of the copper block so only a few bolts are necessary to secure the plate to the block. A 0.1" wide shoulder along the perimeter of the locating step insures flat positioning and sufficient vacuum integrity between the two ultrahigh vacuum regions of the detector.

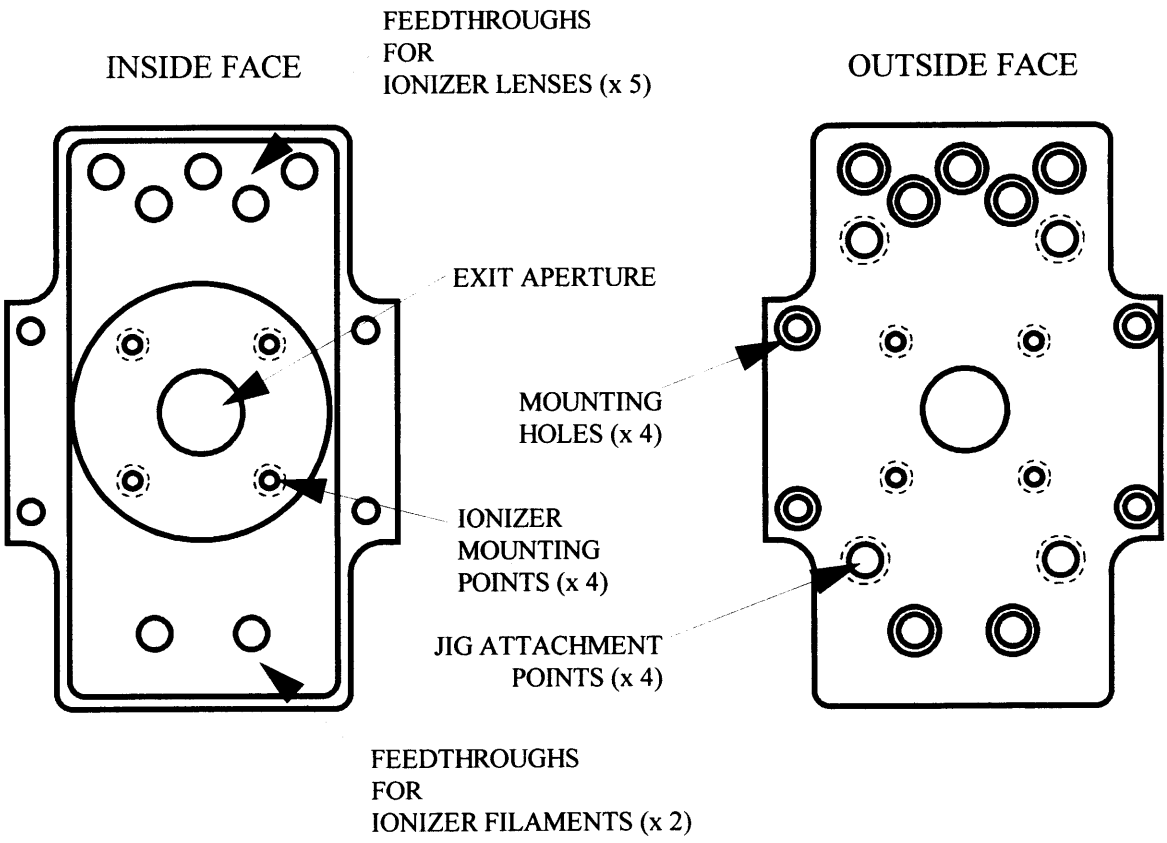

Figure 2 Drawing of ionizer plate

Figure 3 is a cross sectional drawing of the electrical feedthroughs for the ionizer filaments and lenses. The electrical feedthroughs are constructed of Macor and OFHC copper. A 0.30" long rod of 5/16" OD Macor with a 0.15" long section that is only 0.25" OD acts as the electrical insulation and structural support for the copper rod as well as insures that sufficient vacuum integrity is maintained between the two stages of differential pumping in the detector. This piece fits into one of the seven 0.25" holes in the ionizer plate that have been counterbored 3/16" deep to a diameter of 0.316". The Macor rod is tapped for a 2-56 screw thread. A 3" long, 3/32" OD copper rod with a 1" 2-56 threaded section screws into the Macor rod; the opposite ends of the copper rod are etched with nitric acid to a diameter of 0.050" which is equivalent to 16 AWG and is capable of handling several amperes of current. Although this high current capacity is only necessary for the filament feedthroughs, an identical design for all of the feedthroughs was utilized for the sake of simplicity. Finally, a Macor washer with a 0.10" ID and a stainless steel 2-56 nut completely restricts the motion of the feedthrough. Because the feedthroughs are replaceable, there are only seven electrical feedthroughs on the ionizer mounting plate, the minimum number necessary to fully operate the ionizer.

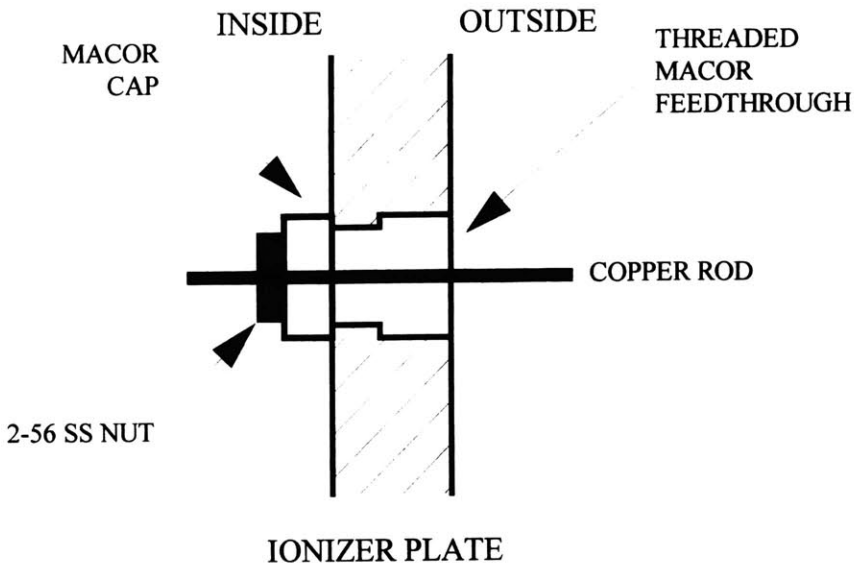

Figure 3 Cross sectional drawing of electrical feedthroughs for ionizer filaments and lenses

IV. ALIGNMENT

IV.A. Ionizer Cryostat Measurements

The precise alignment of the entrance and exit apertures from ionization region as well as the ionizer itself with respect to the detector axis, which is defined by the line of centers through the two collimating slits that are located in front of the ionizer and the quadrupole rods that are located directly behind the ionizer exit aperture, is essential for the optimal operation of the detector. Because the intensity of the scattered signals is low because of the limited solid angle imaged by the detector as well as the general lack of efficiency (10^{-5}) of electron bombardment ionization, the precise positioning of the ionizer with respect to the rest of the detector is critical for making the measurements described in this thesis.

The precise measurement of the critical dimensions of the ionizer cryostat is complex because of its large size and unusual shape. All of the measurements were performed with a digital height gage (0.0001" resolution). Two different setups were required to make the necessary measurements.

In the first setup the ionizer cryostat was in a vertical position resting on the bottom of the copper block. Although the base of the copper block is not a reference surface, shims were used to make reference surface -A- parallel to the measuring surface within 0.0005". The first critical measurement was the vertical distance from reference surface -A- to the vertical centers of the front and back bores in the copper block. This distance defines the vertical position of the apertures. The distance from the mating flange on the detector chamber to the detector axis is 16.822". The aluminum sealing gasket adds 0.045" to this distance and the contraction of the whole ionizer cryostat due to LN_2 cooling adds about 0.050" for a total approximate distance of

16.917" from the mating flange to the detector axis. The critical height from the mating flange to the detector axis was determined by measuring the offset of alignment apertures that were positioned approximately on the plates with respect to the detector axis when the cryostat was cold. The second critical measurements were the vertical heights of the two bores; these dimensions define the vertical heights of the locating steps for the two plates. The final approximate measurements were the vertical distances from the top edges of the bores to the centers of the tapped mounting holes; these dimensions locate the mounting holes for the plates. Note that the mounting hole patterns were no longer perfectly square with respect to the bores; the loose tolerance of the mounting holes of the plates made these deviations insignificant. Finally, the perpendicularity of the faces with the bores with respect to reference surface -A- was checked with a test indicator to be within 0.001".

In the second setup the ionizer cryostat was in a horizontal position resting on a pair of V-blocks with the cryostat arm approximately parallel to the measuring surface. Shims were used to make the reference surface -A- perpendicular to the measuring surface within 0.0005" and to make the reference plane -B- as defined by the reference diameter –C- and the dowel pin on flange H parallel to the measuring surface within 0.0005". The first measurement was the horizontal width of the two bores; these dimensions define the horizontal widths of the locating steps for the two plates. The second measurement was the horizontal distance from the left edge of the bores to the centers of the tapped mounting holes; these dimensions locate the mounting holes for the plates. Finally, the perpendicularity of the faces with the bores with respect to reference plane -B- was checked with a test indicator to be within 0.001".

Table 1 Critical measurements of position and size of bores for the entrance aperture and for the ionizer and exit aperture plate

Dimension	Front bore	Back bore
Vertical distance to -A- from vertical center	16.973"	16.973"
Vertical height of bore	1.015"	4.331"
Horizontal width of bore	1.175"	2.085"
Horizontal distance to -B- from horizontal center	+0.0035"	-0.0015"

IV.B. Alignment Procedure

The plates for the collimating slits and the ionizer were made in a two step process to optimize the alignment with the rest of the detector. In the initial step, the plates were made with the precisely machined locating step, but instead of the final apertures, 1/32" diameter holes were precisely positioned where the final apertures ought to be located according to the measurements of the ionizer cryostat alone. The entrance aperture plate was installed on the cryostat which was mounted on the scattering chamber. Since the position of alignment hole changes due to contraction upon cooling the cryostat with LN_2, the cryostat was cooled prior to alignment. This measurement must be performed in vacuum to avoid water condensation. Instead of the quadrupole, a plexiglass window with an o-ring seal was mounted on the quadrupole flange. The detector was pumped down with the turbomolecular pumps and the cryostat was cooled with liquid nitrogen. The position of the alignment hole was measured relative to the incident beam using the alignment procedure described below. The final aperture was machined according to the measurements of the cold cryostat give in Sec. IV.B.3. This procedure was then repeated for the ionizer plate.

IV.B.1. Detector axis

The alignment was performed with a theodolite [2] mounted on a tripod with two orthogonal degrees of translational freedom, vertical and horizontal, which are both orthogonal to the detector axis which is defined by the axis of the incident beam. The position of the incident beam is defined by the axis through the center of the skimmer and of the entrance aperture of the primary molecular beam into the main chamber. A set of orthogonal scribe marks on a precisely located flange on the main chamber wall opposite the molecular beam sources locates the incident beam in a third position. The skimmer and two collimating apertures as well as the scribe marks were confirmed to be aligned. Subsequent measurements utilized the molecular beam entrance aperture and the scribe marks to align the theodolite.

The theodolite is positioned on the side of the main chamber opposite the molecular beam sources aiming towards the primary molecular beam. Note that this differs from the original alignment in which the theodolite was positioned where the molecular beam sources are now located [1]. The horizontal translation stage is positioned such that the motion is perpendicular to the detector axis. The initial setup of the theodolite requires leveling the tripod and subsequently leveling the theodolite itself. After the system is leveled, the theodolite is aligned with the incident beam axis. The iterative procedure involves alternately correcting the far location with the horizontal and vertical angular adjustment and the near location with the horizontal and vertical linear translation adjustment.

IV.B.2. Detector angle

The theodolite is aligned with the incident beam axis. Therefore, to align the apertures with respect to the detector axis, the detector is rotated such that the detector axis, which is

defined by the centers of the two collimating slits before the ionizer cryostat and the quadrupole flange after the ionizer cryostat, is aligned with the incident beam axis. In principle, the detector ought to be rotated to an angle of 270°0', but in reality, the detector must be rotated to an angle of 270°15'. The reasons for the offset are unclear.

IV.B.3. Ionizer cryostat

The vertical and horizontal deviations of the alignment holes with respect to the incident beam were measured separately using a dial indicator (0.001" resolution) mounted to the base of the tripod. The deviations shown in Table 2 are from the point of view of the theodolite looking at the primary molecular beam source; positive values are up and to the right. The final machining of the apertures of the entrance aperture plate and ionizer plate were made based on these measurements.

Table 2 Deviations of entrance aperture and of ionizer and exit aperture from detector axis

Dimension	Entrance aperture	Ionizer and exit aperture
Horizontal	+0.015"	+0.019"
Vertical	+0.017"	+0.004"

V. FURTHER MODIFICATIONS

V.A. Ionizer cryostat temperature control

The ability to heat and cool the ionizer cryostat efficiently is a necessity for optimal operation of the detector. Heating to ~425 K is necessary to bake out water and hydrocarbon contamination thoroughly after venting, and cooling to ~80 K is essential to pump cryogenically

the remaining background gas particles. The original design did not allow for efficient heating because of the intentional thermal isolation of the ionizer cryostat from the rest of the chamber. In addition, the absence of a temperature measurement device, i.e., a thermocouple junction, on the ionizer cryostat made it impossible to know whether the ionizer cryostat was sufficiently hot or cold.

V.A.1. Ionizer cryostat heater element

The ionizer cryostat is heated with a tungsten filament that is clamped between two 1/8" thick copper plates that are clamped together via four bolts and attached via another four bolts to the bottom of the copper block of the cryostat. The filament was made from approximately 2' of 0.040" diameter tungsten wire insulated with alumina ceramic rod. A combination of copper braid and 16 AWG copper wire were used to connect the tungsten filament to an electrical feedthrough that was mounted on the adapter flange between the pneumatic gate valve and turbomolecular pump of the second differential stage of the detector. A chromel-alumel thermocouple was clamped between the upper heater plate and the bottom of the cryostat and connected to the same electrical feedthrough.

The tungsten filament requires about 12 A of current to dissipate about 50 W of power and effectively heat the copper cryostat. The heater is able to warm the cryostat from 80 K to room temperature in about 12 hours after removing the LN_2 from the cryostat, which is significantly less than the 36 hours necessary without active heating. The power supply limits the power delivered to the heater. During baking, the heater is able to maintain the cryostat at a temperature of 420 K while the rest of the chamber is less than 420 K. The independent heating

of the cryostat allows for it to be baked while the rest of the chamber is cooling, ensuring that minimal contamination remains in the cryostat itself.

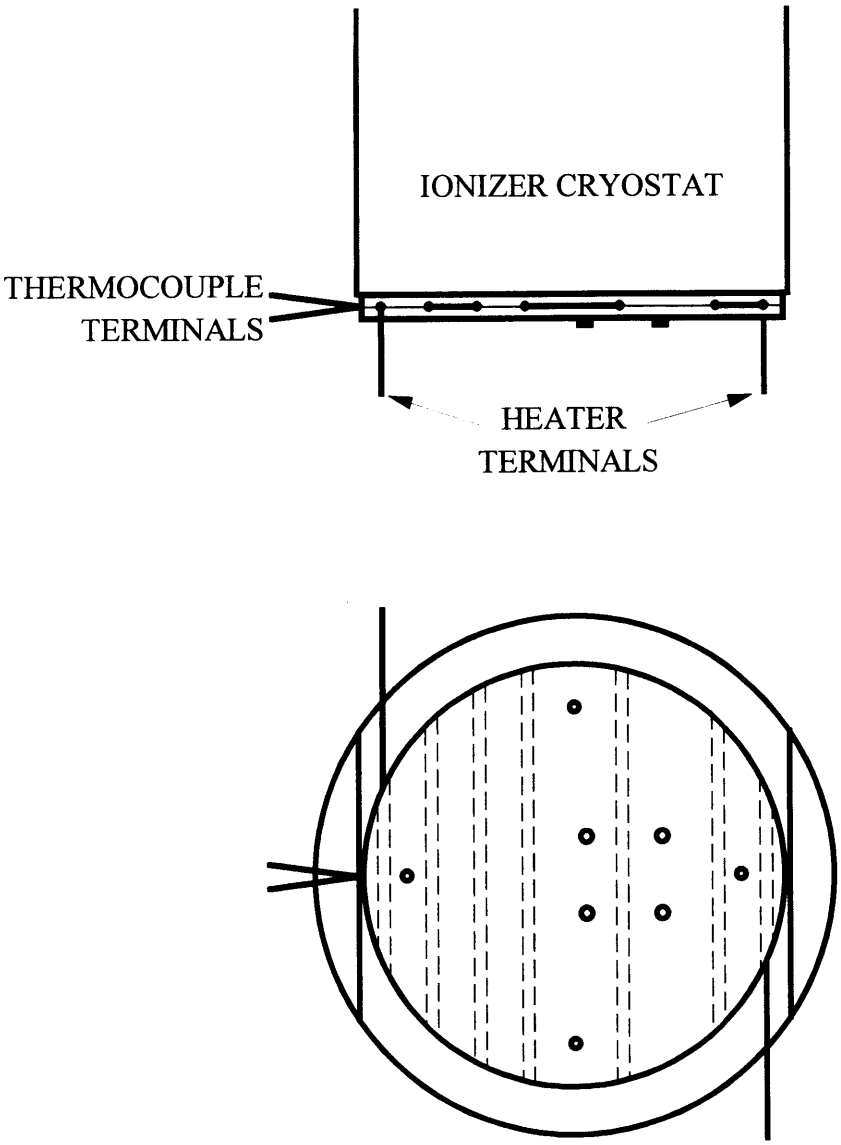

Figure 4 Drawing of ionizer cryostat heating element and temperature measurement device

V.A.2. Ionizer cryostat liquid nitrogen cooling

The cooling of the ionizer cryostat is simple in principle. Liquid nitrogen is stored in a 20 L LN_2 storage dewar (Precision Cryogenics) attached to the arm of the ionizer cryostat. The LN_2 is gravity fed into the cryostat where it is in thermal contact with the copper block that houses the ionizer. In practice, however, without proper exhausting of the gaseous nitrogen that boils off during the initial cooling process, the narrow path that the liquid nitrogen travels is blocked by high pressure gas. This slows the cooling process dramatically such that proper cooling is not achieved even after one day of maintaining a constant supply of LN_2.

The key to efficient cooling of the ionizer cryostat is to pump out the exhaust with the house vacuum. The overpressure valve of the storage dewar is insufficient to properly exhaust the system. It is important to note that this exhaust is not from the inlet into the storage dewar, but the base of the cryostat. Ideally, an exhaust line would remove the gas at the base of the cryostat, but this is impossible with the present design. Instead, an exhaust line was installed at the outlet of the storage dewar. The exhaust line is pumped on with the house vacuum line while the storage dewar is being filled with LN_2 to ensure that no gas is trapped in the cryostat during the filling process. With this setup, the ionizer cryostat can be cooled from room temperature to ~80 K in about one hour. A valve isolates the system when equilibrium is attained. After approximately 10 hours the cryostat begins to warm, despite the storage dewar still containing plenty of LN_2. This occurs because there is a buildup of pressure in the cryostat. To cool the cryostat, the exhaust line is pumped on for approximately 30 minutes until the temperature returns to ~80 K. The storage dewar is typically filled twice daily to ensure that there is always

LN_2 in the system to prevent the formation of ice in the cryostat from the condensation of ambient water vapor.

V.B. Further reduction of detector background with a cryopump

To further reduce the background signal, a closed cycle He refrigerator (Displex, UHV-202) cryopump was installed to better pump the ionization region of the detector. The turbomolecular pump on the third differential pumping stage, which consists of the ionizer and ionizer cryostat, is a custom design with two 6" knife-edge conflat flanges on the high vacuum side of the pump. One flange is attached to a pneumatic gate valve which is attached to flange L on the cryostat. The cryopump head was attached via a 10"-6" reduction flange to the other flange.

The cryopump power is interlocked to the turbomolecular pumping system to ensure that the cryopump does not operate in the event of a shutdown and venting of the turbomolecular pumps. The power supply for the three primary turbomolecular pumps as well as the ionizer controller also supplies 120 Vac power to a relay that allows the cryopump to be powered by 220 Vac. A timer is incorporated into the power switching so that the cryopump can be started automatically in the early morning each day. Complete cooling of the cryopump to ~20 K requires about two hours. The cryopump is shutdown daily to remove the trapped gas and avoid unnecessary damage in the event of a failure of the turbomolecular pumping system.

Figure 5(a) shows a mass spectrum of the background signal in the detector with the cryostat cold and the cryopump warm. In addition to the common background signals at m/e=12-18 (C, CH_x, N, O, and H_2O), m/e=28 (CO, N_2), and m/e=44 (CO_2), there is also detectable signal at m/e>50 which corresponds to turbomolecular pump oil. Figure 5(b) shows a

plot of a mass spectrum of the background signal in the detector with the cryostat and cryopump cold. Not only is the signal at m/e>50 reduced to near zero, but the levels of the common background signals are also reduced substantially, especially m/e=18 (H_2O) and m/e=28 (CO, N_2).

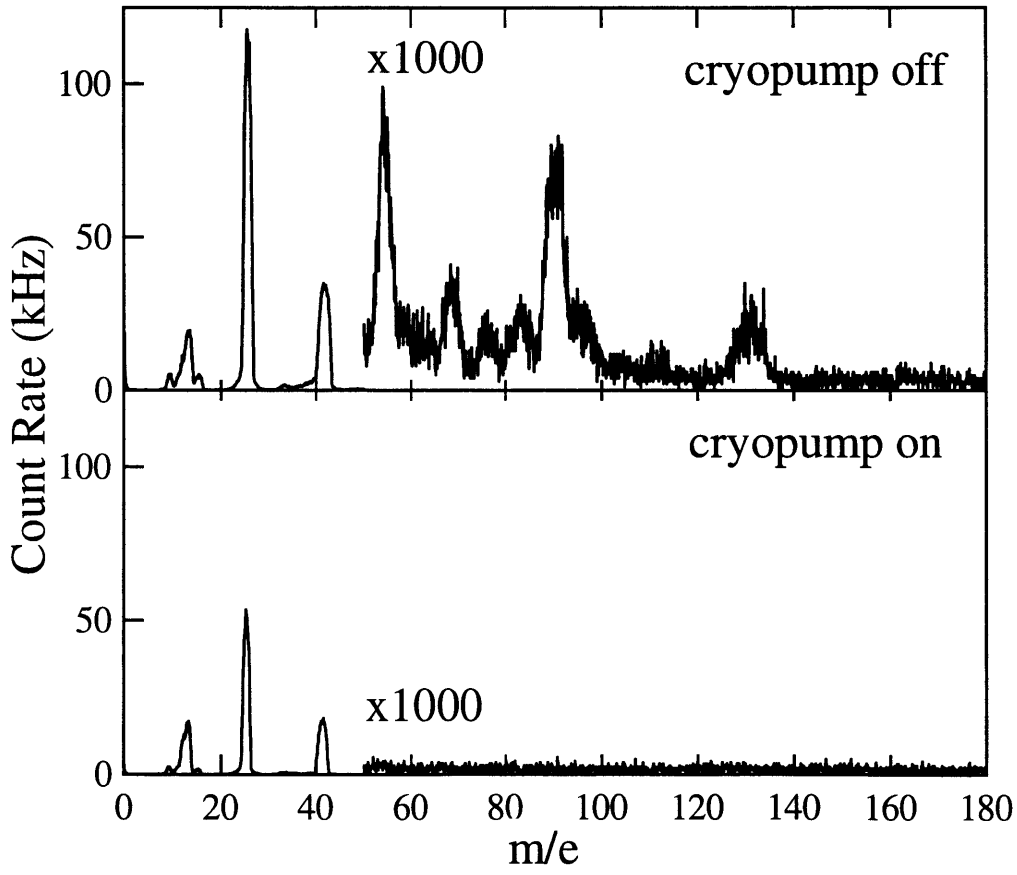

Figure 5 Mass spectra of detector background with and without cryopump

V.C. Modification of quadrupole mass filter to detect higher mass-to-charge ratios

The need to be able to detect large mass-to-charge ratios to check for the presence or absence of van der Waals clusters of XeF_2 in the incident molecular beam, necessitated the modification of the quadrupole mass filter to detect high mass-to-charge ratios. The original system was able to reach m/e=200.

The quadrupole mass filter is essentially a resonant LC circuit. The maximum mass-to-charge ratio is determined by the ability to deliver RF power to the quadrupole which is determined by the relationship $m_{max} \propto \nu^2 V$ where n is the resonant RF frequency and V is the maximum voltage that can be supplied by the power supply. The resonant frequency of operation is inversely proportional to the square root of the capacitance of the quadrupole system which includes the quadrupole rods as well as the leads from the rods to the high-Q head. Therefore, the maximum mass-to-charge ratio can be increased by adding capacitance to the quadrupole system [3]. This is accomplished by adding a high power 90 pF capacitor (HEC HT50 and HEC HT40 in parallel) in parallel to the each of the two terminals of the system. One end of each capacitor is connected to each terminal near the high-Q head and the other end is grounded via a grounding braid that is common to the entire apparatus. The quadrupole is tuned to the new resonant frequency resulting in a dramatic increase in the maximum mass. With the additional capacitance, the maximum mass-to-charge ratio is m/e=400.

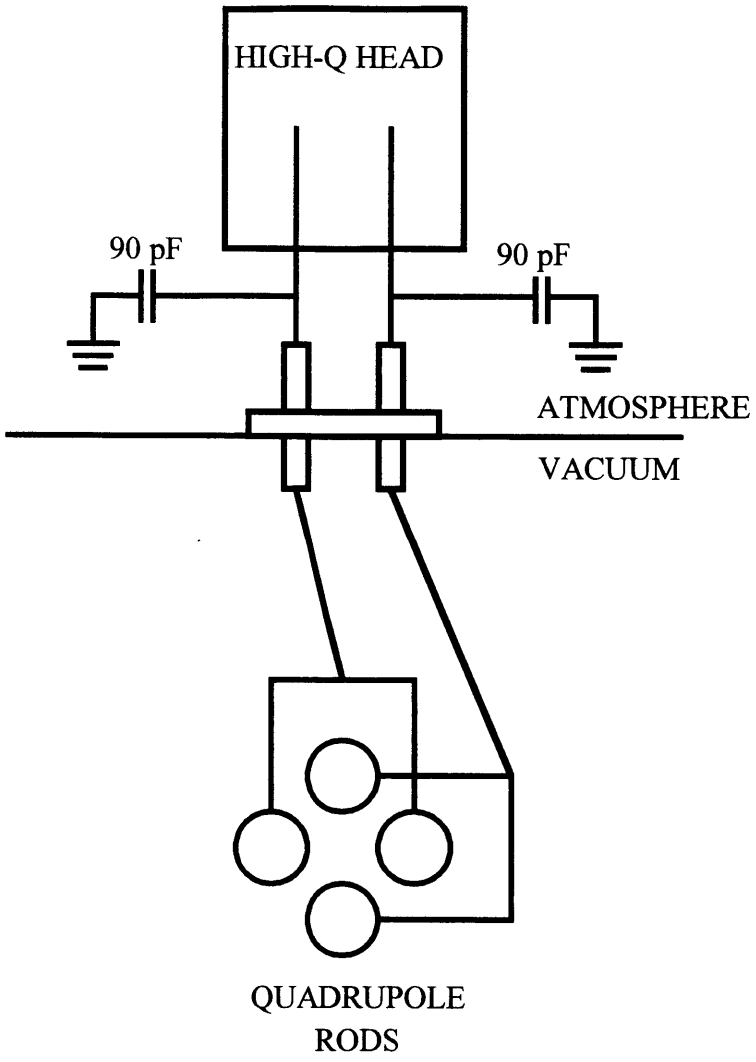

Figure 6 Circuit diagram for increasing maximum mass-to-charge ratio of quadrupole mass filter

Figure 7 demonstrates the successful operation of the modified quadrupole mass filter. The top panel shows a mass spectrum of a molecular beam of Ar clusters formed by using a high stagnation pressure and a cold molecular beam nozzle. Ar clusters up to Ar_{10}^+ are visible showing that the mass calibration is correct and that the transmission function at large mass-to-charge ratios is not extraordinarily low. The bottom panel shows a mass spectrum of the quasi-effusive molecular beam of XeF_2. The source of the small signal around m/e=320 coincides with $(XeF_2...XeF)^+$, but the absence of signal corresponding to both $(XeF_2...Xe)^+$ and $(XeF_2...XeF_2)^+$ suggests that this is not the case.

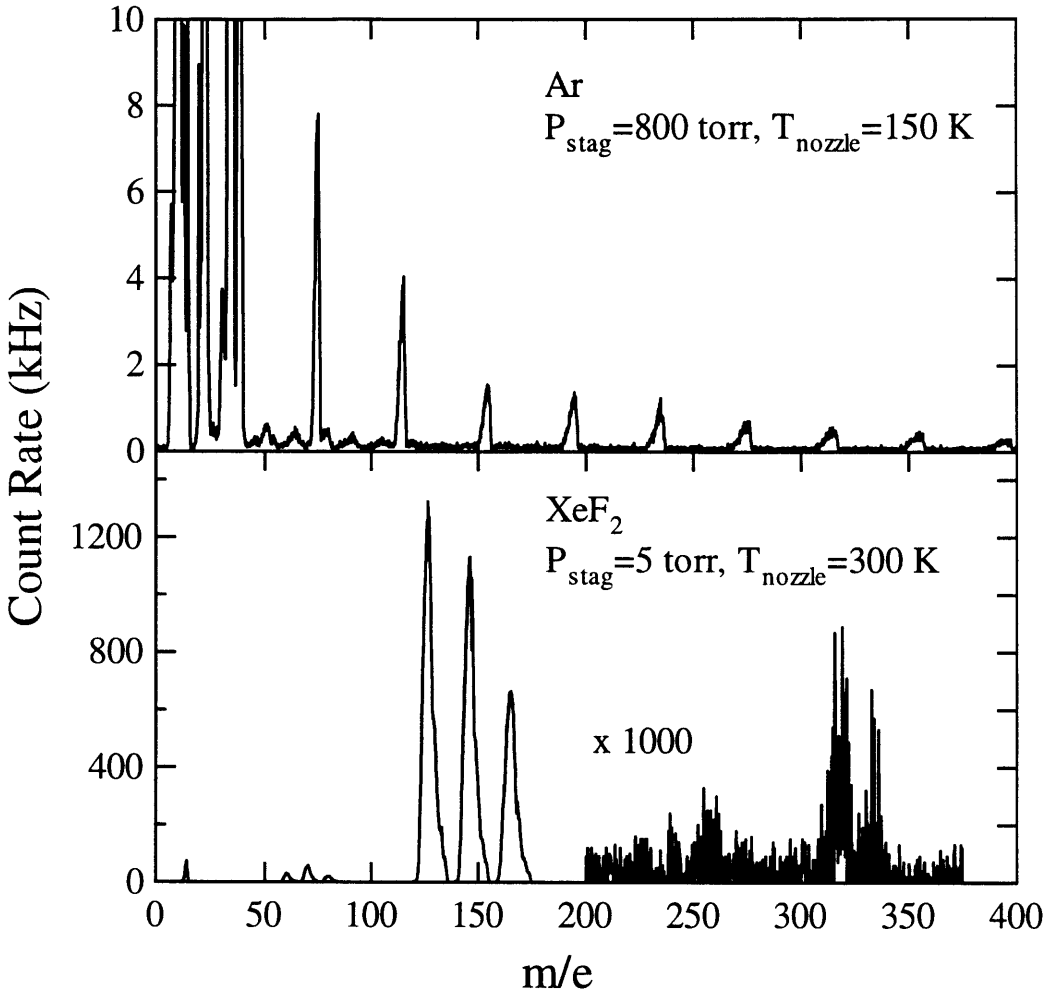

Figure 7 Mass spectrum of Ar van der Waals clusters and XeF_2

REFERENCES

1. M. McGonigal, Massachusetts Institute of Technology, Ph.D. thesis, 1989.
2. The theodolite, tripod, and translation stage were generously loaned to us by Bates Linear Accelerator.
3. Manual for Quadrupole Power Supply 011-1, Extranuclear Laboratories, p 48.

Appendix C: Turbomolecular Pump Interlock

I. INTRODUCTION

The triply-differentially pumped rotatable quadrupole mass spectrometer of the scattering chamber is pumped by three 330 L/s turbomolecular pumps (Pfeiffer, TPU330) that together backed by a single 65 L/s turbomolecular drag pump (Pfeiffer, TMH065) and a two stage rotary mechanical pump (Pfeiffer Duo 1.5A) in series. Because of the large investment of both time and money in maintaining the scattering chamber, it is essential that the detrimental effect of any failure be minimized. Careful interlocking of elements susceptible to failure is essential. In the case of the turbomolecular pumping system, if any of the pumps fail, the pumping system must be isolated from the main chamber and properly shut down to avoid unnecessary contamination and damage. In addition, if there is a power failure, the pumping system must be isolated. If the power is not recovered within a short period of time the system must be properly shut down. In the case of a brief power loss, the system ought to resume full operation.

The original interlock system [1] was designed to monitor two of the 330 L/s turbomolecular pumps [2]. Neither the backing turbomolecular pump nor the backing mechanical pump were monitored. There were several drawbacks to this interlock system. First, the system did not monitor all of the pumps. Failure of one of these unmonitored pumps would go unnoticed until its failure directly affected one of the interlocked pumps. By that time, serious damage or contamination may have already occurred. Secondly, the power supply was unable to properly vent the turbomolecular pumps. Serious contamination may occur when a turbomolecular pump is stopped without venting because as the low vacuum side equilibrates with the high vacuum side of the pump, oil also migrates or creeps into the high vacuum area. Proper venting via the vent port occurs at the high vacuum side, so that the rush of air flows from

the high to low vacuum side of the pump. Finally, there was no memory of where the failure was initiated so there was a risk of further damage or contamination when troubleshooting after a failure.

The new interlock system incorporates all of the pumps and is able to properly shut them down when there is a failure. It is also designed to remember the initial fault. The interlock system monitors six conditions that must be satisfied for full operation of the pumping system: the satisfactory operating conditions of the four turbomolecular pumps and the pressure both in the foreline of the three large turbomolecular pumps and in the foreline of the small turbomolecular pump. A seventh input, the ac line power to the entire turbomolecular pumping system, is indirectly monitored via these six inputs which are also powered by the ac line. The interlock is powered by a dual +5V/+24V DC power supply. Two 12 V lead-acid batteries are connected in parallel with the power supply in the case of a power failure. Because the batteries are constantly charged by the ac power line and the current load is minimal (~1 A normal operation, ~3 A maximum during venting), the lifetime of the batteries is expected to be many years. However, the water level in the battery cells should be checked annually.

II. ELECTRONIC LOGIC

II.A. Monitoring status of turbomolecular pumping system

The status of each of the turbomolecular pumps is monitored by its controller and relayed to the main interlock. Figure 1 is a schematic diagram of the input signals from the turbomolecular pumping system. In the original two 330 L/s turbomolecular pump controllers (Pfeiffer, TCP300, labeled TMP2 and TMP3 in Figure 1), an internal relay K2 is closed when two conditions, rotor speed and temperature, are satisfactory. The circuit is accessed at points

X4:b2 and X4:b4 on each controller and is designed such that 110 Vac is present across these points when the pump is operating properly. In the interlock system, the coil of a 125 Vac relay is connected across points X4:b2 and X4:b4. When the relay is activated, a +5 Vdc signal is connected to the logical input, and when it is deactivated (as shown in Figure 1) because of a fault, the logical input is grounded. The third 330 L/s turbomolecular pump controller (Pfeiffer, TCP121/TCS303, labeled TMP1 in Figure 1) also closes an internal relay K2 when rotor speed and temperature are satisfactory. The circuit is accessed at points X9:b4 and X9:b5 on the TCS303 part of the controller. The point X9:b4 is grounded and the point X9:b5 is utilized as a logical input. The logic is opposite that of the other two turbomolecular pump controllers. When the relay is activated the logical input is grounded, and when it is deactivated (as shown in Figure 1) because of a fault, the logical input is open which is equivalent to a logical high. This logical input is subsequently inverted with a 7404 hex TTL inverter. The 65 L/s turbomolecular drag pump controller (Pfeiffer, TCP015/TCP035, labeled backing TMP in Figure 1) closes an internal relay K1 when the rotor speed and temperature are satisfactory. The circuit is accessed at points X5:d26 and X5:d30. A 110 Vac signal is sent to point X5:d26 and point X5:d30 is sent through the coil of a 125 Vac relay. When the relay is activated, a +5 Vdc signal is connected to the logical input, and when it is deactivated (as shown in Figure 1) because of a fault, the logical input is grounded.

The pressure is measured with a thermocouple gauge. There is one thermocouple gauge on the common foreline of the three primary turbomolecular pumps and one thermocouple gauge on the foreline of the backing turbomolecular pump. When the pressure exceeds an adjustable setpoint, an internal double pole single throw switch in each thermocouple controller changes

state. The "normally open" input is connected to +5 Vdc while the "normally closed" input is grounded. The common output of the relay is delivered to the interlock system; a logical high results when the pressure is satisfactory. All of these inputs may be bypassed via switches on the front panel of the interlock. These six input signals are directed into a digital circuit that determines the appropriate actions to take.

The interlock system is divided into two logical pathways corresponding to the two regions of the pumping system, the primary system of three large turbomolecular pumps and the backing system consisting of the small turbomolecular pump and mechanical pump. The interlock of the primary system monitors four conditions: the status of each of the three turbomolecular pumps and the pressure of the common foreline. The four signals are sent to one half of a 7440 dual 4-input NAND gate. The interlock on the backing system monitors three conditions: the status of the small turbomolecular pump and its foreline pressure as well as the status of the primary pumping system. These three signals are sent to the other half of the NAND gate. In both cases, the output of the NAND is normally low, but in the case of any failure the output goes high. At the same time, the four input signals of the primary system and the first two input signals of the backing system are sent to a pair of 7475 4-bit bistable latches whose outputs (two per input) are sent to an array of green and red LEDs on the front of the interlock. These LEDs display the status of each input independent of any bypassing. The outputs of the latches are updated constantly as long as the enable is high. The enable input comes from the inverted output of the NAND gate. In the event of a failure, this signal goes low and the latches are no longer updated. Because of noise caused by the switching of relays, the NAND output is buffered by updating the latches one time per second, not continuously, via a

7474 positive-edge triggered D-type flip-flop that is triggered with a 1 Hz 555 clock. Thus, the status of the system, as indicated by the LED array, is recorded at the time of the fault. This record of the initial fault is an invaluable resource when troubleshooting a failure of the system.

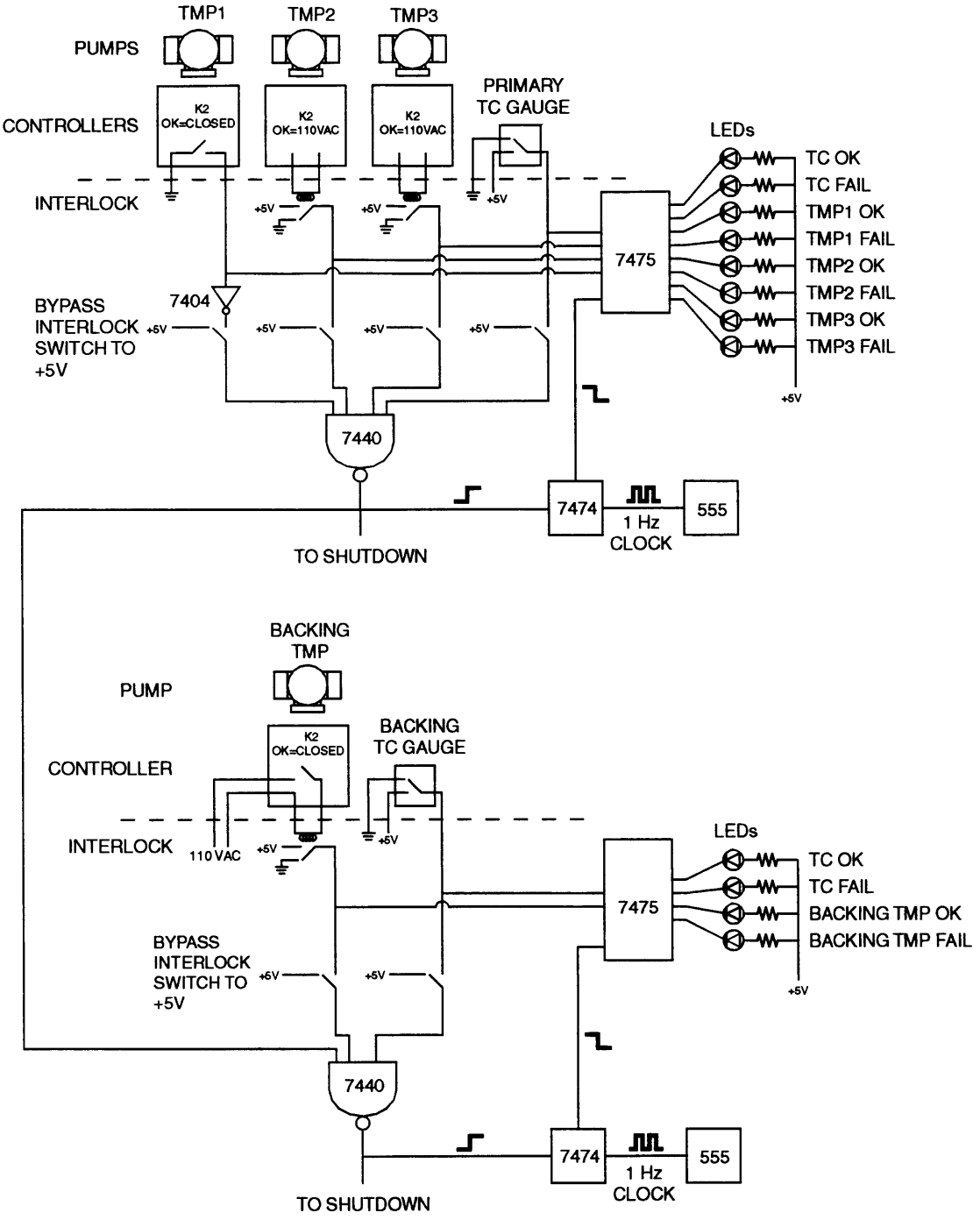

Figure 1 Schematic diagram of input signals from turbomolecular pump system

II.B. Isolation and shutdown of turbomolecular pumps

Figure 2 is a schematic diagram of the shutdown logic of one of the systems, the primary or backing system. The logic is identical, but separate, for the two systems. During a failure, the logical high output of the NAND gate is inverted with a 7404 inverter and sent directly to the base of a 2N2102 transistor. The collector is connected to +24Vdc via a 24Vdc relay, and the emitter is grounded. During normal operation, the input at the base of the transistor is a logical high so the transistor conducts and the relay is activated. The relay closes a circuit that delivers power to the gate valve solenoid valve. In the event of a failure, the base of the transistor changes to a logical low and the transistor no longer conducts and the relay is deactivated. In the primary interlock, power is lost to the primary gate valve solenoid valve, thereby closing the gate valves at the inlets of the three turbomolecular pumps and isolating the primary pumping system from the main chamber. In the backing interlock, power is lost to the backing valve solenoid valve, thereby closing the gate valve at the inlet to the backing turbomolecular pump and the butterfly valve at the foreline of the backing turbomolecular pump, isolating the backing system from the primary pumping system and the main chamber as well as from the backing mechanical pump. In addition, a failure in the primary system triggers a fault in the backing system causing these valves to close. Any detection of a fault leads to the immediate isolation of the turbomolecular pumping systems from the main chamber to avoid any unnecessary contamination.

After the turbomolecular pumping systems are isolated from the main chamber, the systems are shutdown and vented. While the isolation of the turbomolecular pumping systems is a reversible procedure, the shutdown and venting of the systems is irreversible in the sense that

part of the ultrahigh vacuum system will be exposed to atmosphere. Therefore, the shutdown and venting procedure does not begin immediately upon detection of a fault since it may be a false alarm. However, the closing of the various valves to isolate the turbomolecular pumping systems is immediate regardless of the validity of the fault. For example, momentary power losses in the laboratory are not uncommon and although not detrimental to the pumping system, they would trigger a fault in the interlock system that would lead to an unnecessary total shutdown. To avoid this undesirable situation, a "grace period" of about 10 seconds has been incorporated into the interlock. If the system recovers during the grace period, no signals are sent to trigger the shutting down and venting of the turbomolecular pump system and the system is opened up to the main chamber. This is accomplished using a 74221 monostable multivibrator as a ten second timer and a 7474 positive edge-triggered D-type flip-flop as a trigger for the shutdown and venting of the system. The inverted output of the multivibrator is sent to the clock input of the flip-flop. After the grace period, the inverted output of the monostable goes high which triggers the output of the flip-flop to also go high. This leads to the total shutdown and venting of the pumping system. In the case of a recovery during the grace period, the shutdown is avoided by taking the original NAND output and sending it to the clear of the flip-flop. The clear is held low forcing the output to remain low even when the flip-flop is triggered by the multivibrator at the end of the grace period. There is no memory of brief failures. A subsequent fault will initiate the same response as the first fault.

However, if the fault is not corrected before the grace period expires, the turbomolecular pumps are shutdown. The primary turbomolecular pumps and the backing turbomolecular pump are shutdown separately, but the logic is similar for the two systems. The falling inverted output

of the flip-flop triggers the clear of another flip-flop forcing its output to go low. This output is sent to the base of a 2N2102 transistor. Analogous to the control of the gate valves, the state of the base of the transistor determines the state of a relay. In the primary system, the power for the turbomolecular pumps as well as the ionizer controller of the quadrupole mass spectrometer is delivered through the relay. In the event of a failure, the power is directly disconnected shutting down the turbomolecular pumps and the ionizer controller. The ionizer controller is shutdown to avoid burning out the filament in the event of a loss of vacuum in the detector. In the backing system, the relay is connected across points X5:z2 and X5:z6 on the TCP015 controller. In the event of a failure, points X5:z2 and X5:z6 are bridged by the deactivated relay and the controller shuts down the turbomolecular pump. The backing mechanical pump is not shutdown.

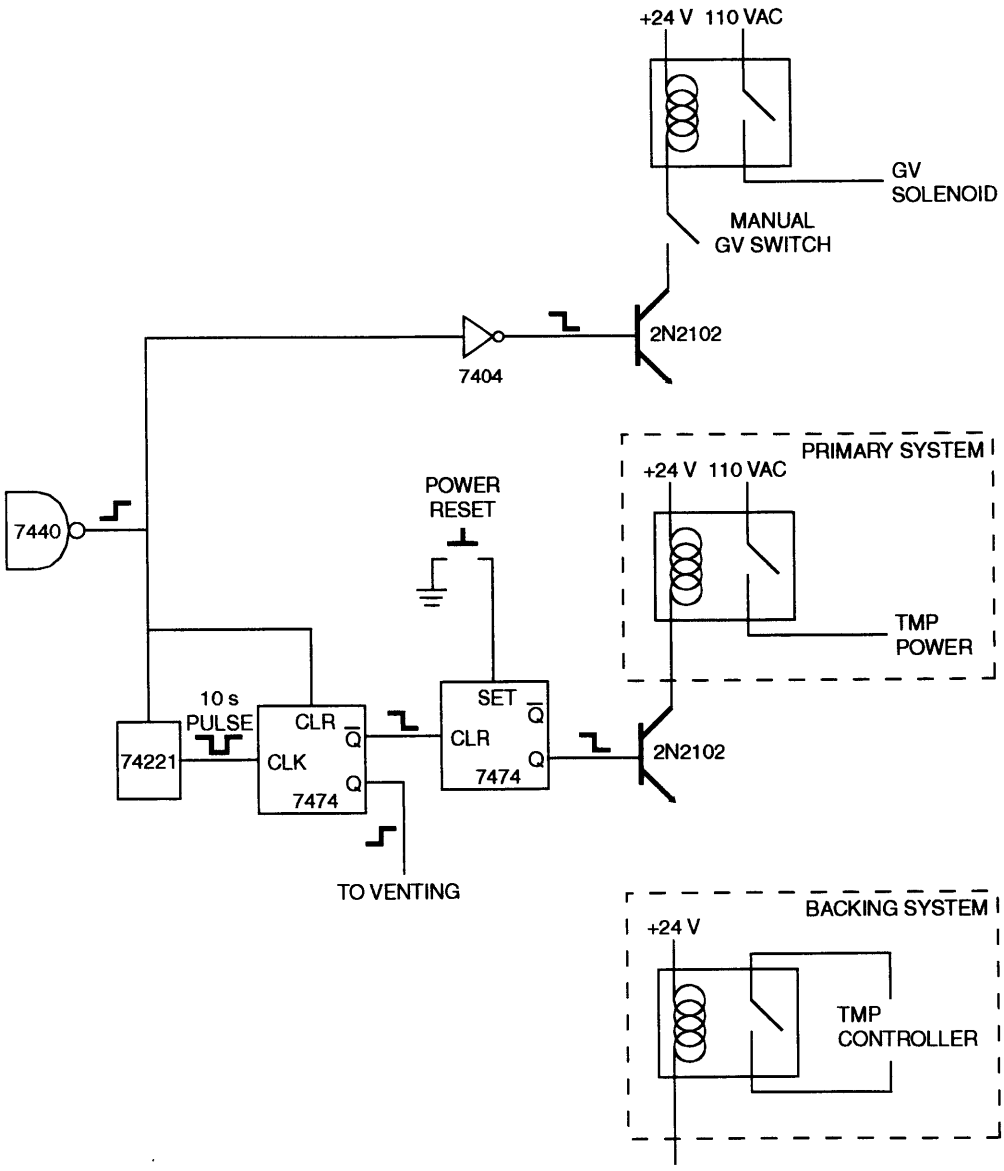

Figure 2 Schematic diagram of logic for isolation and shutdown from turbomolecular pump system

II.C. Venting of turbomolecular pumps

Serious contamination may occur when a turbomolecular pump is stopped without venting because the gas flow from the low vacuum side to the high vacuum side of the pump drives oil into the high vacuum area. Venting at the high vacuum side of the pump via the vent port is ideal for preventing this contamination. Venting occurs through a vent valve (Pfeiffer, TVF012), a bistable valve that changes states via 24Vdc pulses of opposite polarities.

Figure 3 is a schematic diagram of the venting logic for the two systems. At the same time that the falling inverted output of the flip-flop triggers the shutdown of the turbomolecular pump(s), the rising output of the flip-flop triggers the two step venting sequence. The first step is a time delay after the shutdown of the turbomolecular pumping system to ensure that the gate valves are closed and to allow the turbomolecular pumps to spin down to a fraction of their full speed to avoid unnecessary wear on the bearings during the rapid rotor deceleration incurred in venting. In the primary system, this delay is accomplished using a series of 74190 BCD counters that are triggered by an astable 555 timer set at a frequency of 1 Hz. The output of the flip-flop is sent into the load input of the three counters. In the case of a failure, the input goes high and the load is disabled. The output of the flip-flop is also sent to the set input of another 7474 flip-flop, terminating the counting after it is complete. The three counters allow for a user-adjustable delay between 1-991 seconds at 10 second increments. The delay is adjusted with two sets of four binary switches; the set of four binary switches are ordered from most significant bit (MSB) to least significant bit (LSB) and define a decimal number in the range 0-9. A delay of five minutes is currently in use. The low pulse of the final counter both disables the counting system via a flip-flop and sends a high signal to vent. In the backing system, there is only a fixed two

second delay from a 74221 monostable multivibrator before sending a high signal to vent. According to the manufacturer's specifications, there is no need to delay the venting of the backing turbomolecular pump after it is shutdown.

After the delay in both the primary and backing systems, the rising output of the delay circuit triggers a 74221 monostable multivibrator delivering a half second positive pulse to the base of a 2N2102 transistor. Again, the collector is connected to +24Vdc via a 24Vdc relay, and the emitter is grounded. The pulse activates the relay, connecting the vent valve to +24V and 0 such that the valve opens, venting the turbomolecular pump. In the primary system, only one vent valve is used to vent the three turbomolecular pumps simultaneously via their vent ports.

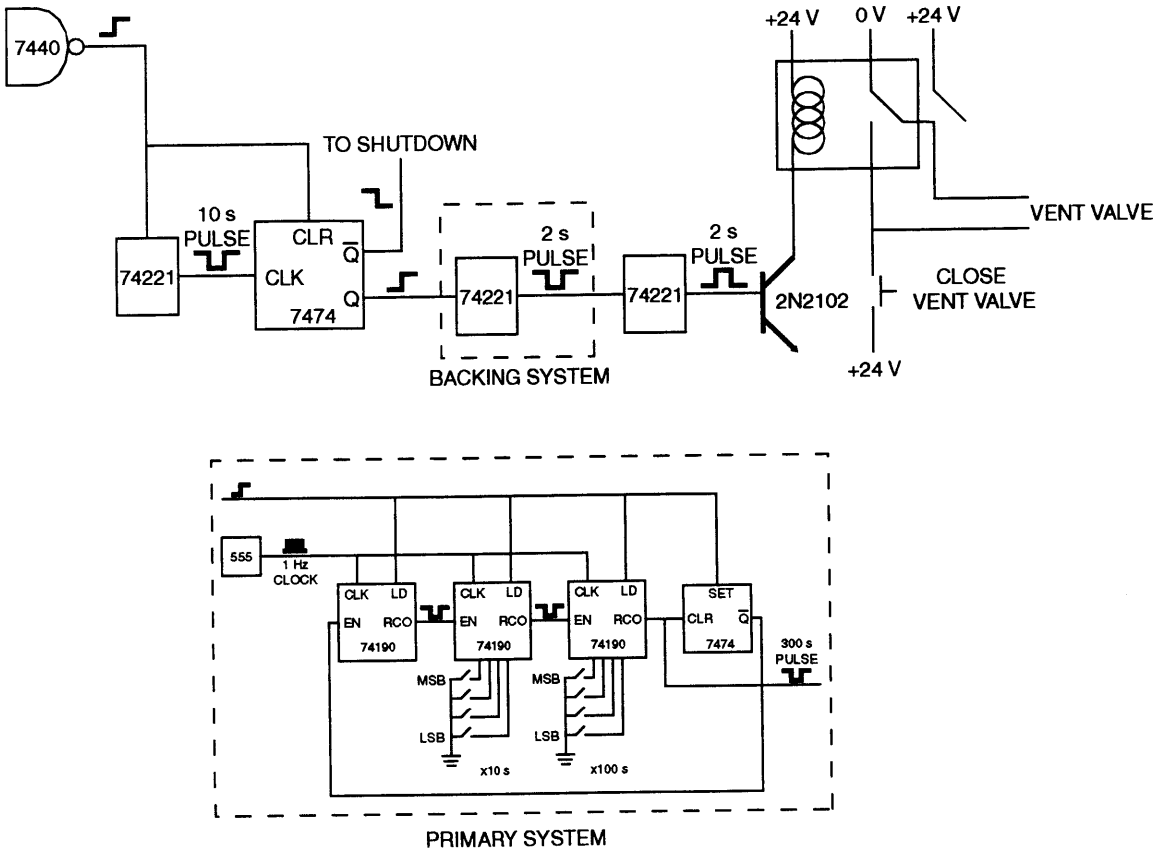

Figure 3 Schematic diagram of electronic logic for venting turbomolecular pumps

III. OPERATION

III.A. Resetting the system after a failure

After a failure, the system must be reset before normal operation can resume. The primary gate valves ought to be actively closed via a switch on the front panel of the interlock system. Otherwise the gate valves will open when the system is reset and the pressure monitors are bypassed, venting the main chamber. Of course, the cause of the fault must be fixed. When the system is ready for operation, the interlock can be reset in the following manner. First, the interlock must be temporarily bypassed via the individual switches for each monitored input. This is necessary because the initial state of the turbomolecular pumping system is not satisfactory upon startup. The interlock is bypassed to prevent the detection of a failure and the shutdown of the system. Second, the vent valves must be closed; this is done by pushing the two "close vent valve" buttons on the front panel of the interlock system. Third, the foreline valve needs to be open so that the three primary turbomolecular pumps can be exhausted. Finally, the power to the turbomolecular pumps must be reset; this is done by pushing the two reset buttons on the front panel of the interlock system. When the pumping system reaches a satisfactory state, the interlock should no longer be bypassed.

III.B. Intentionally venting the system

There are times when the turbomolecular pumps are actively shutdown. This is accomplished via the interlock system by holding down the appropriate vent button for more than 10 seconds. This creates an artificial fault in the system which leads to the proper shutdown and venting. The 10 second activation conveniently utilizes the logic of the grace period and prevents accidental venting from reckless switch flipping and button pushing.

REFERENCES

1. D.J. Gladstone, Massachusetts Institute of Technology, Ph.D. thesis, 1989.
2. The first pumping stage was originally pumped by an ion pump; recently a third TPU330 turbomolecular pump replaced this ion pump.

Appendix D: Translation of Molecular Beam Nozzle

The scattering chamber was originally designed with two molecular beam sources. The chambers for two sources were constructed, but only the primary molecular beam source was completed. The secondary molecular beam source is distinctly different from the other molecular beam sources in this laboratory in that the position of the molecular beam nozzle is adjustable in all three translational degrees of freedom from outside of the vacuum chamber. Control of the nozzle position allows for optimization of the supersonic molecular beam expansion. Of course, the direction of the molecular beam is defined by the positions of the skimmer and the two defining apertures. Only the position of the nozzle relative to the skimmer is adjustable; this position is critical in determining the supersonic and effusive flux into the chamber.

Figure 1 shows a drawing of the side view of the molecular beam nozzle and nozzle mount. The mount is attached via an aluminum bracket to the front wall that separates the source chamber from the first differential stage. The aluminum bracket is attached to a standard translation stage (Daedal, Model 3952) that controls the vertical motion of the nozzle. The only modification to the translation stage was to remove the knurled knob from the micrometer to expose a short length of 1/4" diameter steel rod. A custom built stainless steel barrel connector couples the micrometer on the translation stage to a 1/4" flexible shaft (S.S. White, Model 185S34A). The flexible shaft is coupled to a o-ring-sealed rotary feedthrough (Lesker, Model FMH-25A) via another stainless steel barrel connector which allows for the translation stage to be adjusted from outside of the vacuum chamber.

A second aluminum bracket is attached to the opposite face of the vertical translation stage. This bracket supports the remaining two translational degrees of freedom and the bracket

that supports the nozzle. The horizontal translation and longitudinal translation, the motion along the molecular beam axis, are performed by two translation stages that are identical to the vertical translation stage and are stacked such that the translational motion of the two stages is orthogonal to each other. Again the translation stages are modified so that they can be adjusted from outside of the vacuum chamber.

Finally, a third aluminum bracket is attached to the opposite face of the stack of translation stages. The nozzle threads into this bracket. The nozzle and mount are precisely machined such that the nozzle axis, which is defined as the normal to the face of the nozzle, is parallel to the molecular beam axis, which is defined by the skimmer and collimating slits. The nozzle design is simpler than that of the previous nozzles in this laboratory because of the lack of the capability to control the nozzle temperature. For the experiments described in this thesis, nozzle temperature control is not necessary so it has been eliminated in favor of reducing the weight of the nozzle and mount to limit the strain on the translation stages and avoid misalignment of the nozzle axis with respect to the molecular beam axis. The nozzle is constructed of stainless steel because of its superior chemical resistance to fluorine compounds. The nozzle is a single-walled tube with a cap welded to the end. An orifice of 0.002" diameter is created by electrodisharge machining (EDM). A VCR fitting is welded to the end of the tube and is attached to a section of coiled 1/16" stainless steel tubing that leads to the gas handling manifold. The section coil is necessary to allow for relative translational motion of the nozzle with respect to the stationary vacuum chamber.

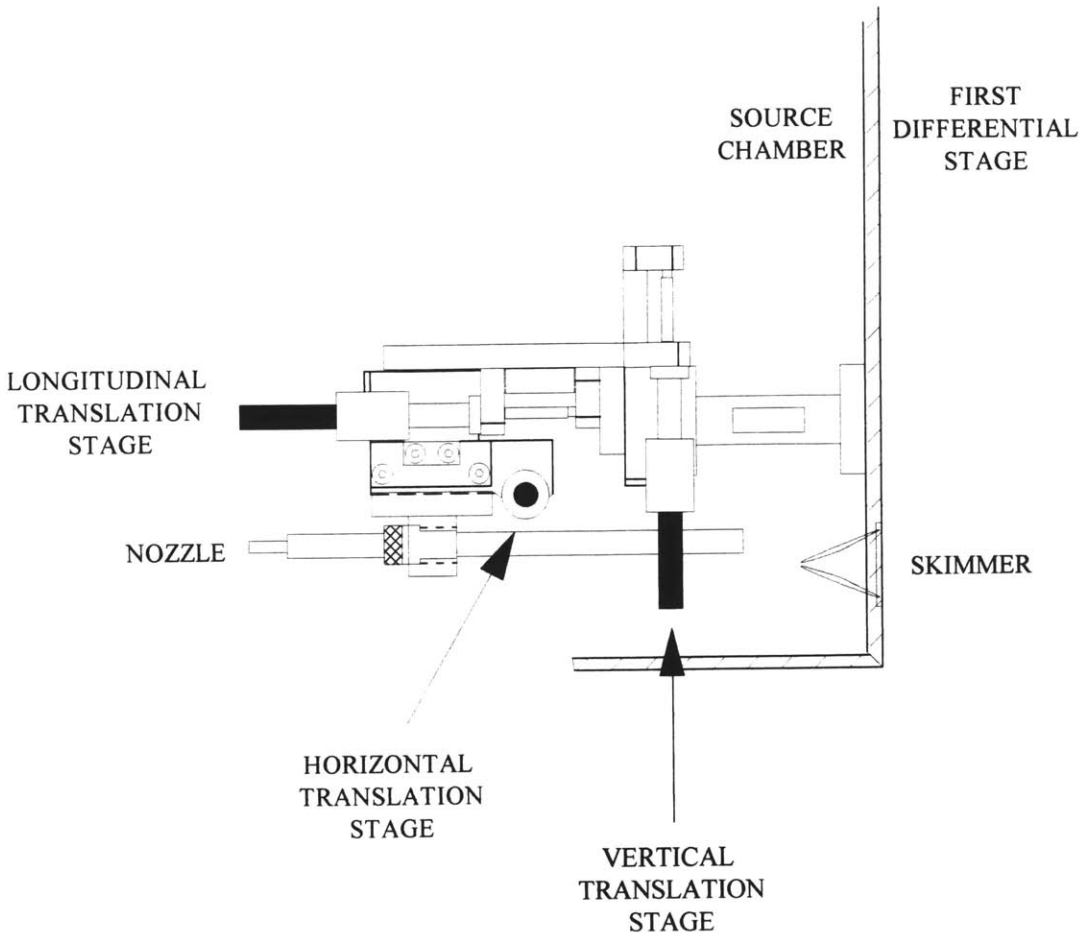

Figure 1 Side view of molecular beam nozzle and mount

Appendix E: Data Sources

CHAPTER 1

Figure 1

θ_i=0°, θ_d=0°, T_s=250 K, 1% F_2/Kr, 1.9 ML F exposure.

m/e=19. 20 sets. TF1303-6.692, TF1401-4.692, TF1503-6,9-12,15-18.692.

m/e=38. 11 sets. TF1301-2.692, TF1405-6.692, TF1501-2,7-8,13-14,19.692.

Figure 2

θ_i=0°, θ_d=35°, T_s=250 K, 1% F_2/Kr, 1.9 ML F exposure. See Figure 1.

θ_i=0°, θ_d=65°, T_s=250 K, 1% F_2/Kr, 1.9 ML F exposure.

m/e=19. 29 sets. TF1718-19,21-30.692, TF1801-4,7-19.692.

m/e=38. 11 sets. TF1714,16-17.692, TF1805-6.692.

θ_i=0°, θ_d=35°, T_s=250 K, 1% F_2/Kr, 0.68 ML F exposure.

m/e=19. 42 sets. TF2002-6,9-10.o92, TF2101-4,6-8,10-13,15.o92, TF2201-4,6-8,11-14.o92, TF2301-2,4,6-9.o92, TF2401,3-6.o92.

m/e=38. 14 sets. TF2001,7-8.o92, TF2105,9,14.o92, TF2205,9,15.o92, TF2305.o92, TF2402,7-9.o92.

θ_i=35°, θ_d=0°, T_s=250 K, 1% F_2/Kr, 0.68 ML F exposure.

m/e=19. 11 sets. TF0702-5,7-10,12-14.d92.

m/e=38. 3 sets. TF0701,6,11.d92.

θ_i=35°, θ_d=20°, T_s=250 K, 1% F_2/Kr, 0.68 ML F exposure.

m/e=19. 12 sets. TF0801-4,6-9,11-13.d92, TF0902.d92.

m/e=38. 2 sets. TF0805,10.d92.

θ_i=35°, θ_d=40°, T_s=250 K, 1% F_2/Kr, 0.68 ML F exposure.

m/e=19. 12 sets. TF0904-6,9,11-14,16.d92, TF1001-3.d92.

m/e=38. 3 sets. TF0903,10,15.d92.

θ_i=35°, θ_d=65°, T_s=250 K, 1% F_2/Kr, 0.68 ML F exposure.

m/e=19. 17 sets. TF1005-8,10-14.d92, TF1102-5,7-10.d92.

m/e=38. 5 sets. TF1004,8,15.d92, TF1101,6.d92.

Figure 3

θ_i=0°, θ_d=35°, T_s=250 K, 1% F_2/Kr, 1.9 ML F exposure. See Figure 1.

θ_i=0°, θ_d=35°, T_s=1000 K, 3.8% F_2/Kr.

m/e=19. TF1045.590.

m/e=38. TF1046.590.

m/e=47. TF1047.590.

Figure 4

θ_i=0°, θ_d=35°, T_s=250 K, 1% F_2/Kr. 25 sets. ST1301-25.197.

Figure 5

θ_i=0°, θ_d=35°, T_s=250 K, 1% F_2/Kr. 15 sets. ST1607-16,27-31.892.

θ_i=0°, θ_d=65°, T_s=250 K, 1% F_2/Kr. 15 sets. ST1617-26,32-36.892.

Figure 6

θ_i=35°, θ_d=0°, T_s=250 K, 1% F_2/Kr.

m/e=19. 15 sets. ST0402-6,8-9,11-14,16-19.d92.

m/e=38. 4 sets. ST0401,10,15,20.d92.

θ_i=35°, θ_d=20°, T_s=250 K, 1% F_2/Kr.

m/e=19. 16 sets. ST0421-24,26-29,31-34,36-39.d92.

m/e=38. 4 sets. ST0425,30,35,40.d92.

θ_i=35°, θ_d=40°, T_s=250 K, 1% F_2/Kr.
m/e=19. 16 sets. ST0502-5,7-10,12-15,17-20.d92.
m/e=38. 3 sets. ST0506,11,16.d92.
θ_i=35°, θ_d=65°, T_s=250 K, 1% F_2/Kr.
m/e=19. 16 sets. ST0521,23-25,27-30,32-35,37-40.d92.
m/e=38. 4 sets. ST0522,26,31,36.d92.

Figure 7

θ_i=0°, θ_d=35°, (10) azimuth, T_s=250 K, 1% F_2/Kr. See Figure 5.
θ_i=0°, θ_d=35°, (11) azimuth, T_s=250 K, 1% F_2/Kr.
m/e=19. 21 sets. ST1004-5,8-9,14-16,19-20,23-24,29-30,33-34,37-38,41-42,45-46.393.
m/e=38. 21 sets. ST1001,3,6-7,10-11,13,17,21,25-28,31-32,35-36,39-40,43-44.393.

Figure 8

θ_i=0°, T_s=250 K, 1% F_2/Kr. ST0803-10.695, ST0901-12.695.
θ_i=35°, T_s=250 K, 1% F_2/Kr. ST2101-9,11-12,14-20.695.

Figure 9

θ_i=59°, θ_d=0°, T_s=250 K, 1% F_2/Ar. TD1153.592.

Figure 10

θ_i=59°, θ_d=0°, T_s=250 K, 1% F_2/Ar. TD0502-27.692.

Figure 11

Clean Si(100). HE0101.492
F-Si(100). θ_i=60°, T_s=250 K, 1% F_2/Ar. HE0224.492.

Figure 12

θ_i=0°, θ_d=35°, Ts=250 K, 1% F_2/Kr.
ST1301-25.197, ST1701-15.197, ST2001-10.197, ST2201,8,10,14,17.197, ST1801-15.297, ST1901-10.297.

Figure 13, 15-16

See Figure 12.

CHAPTER 2

Figure 1

High energy XeF_2. 0.25% XeF_2/Ar. m/e=167. TF0301.697.
Low energy XeF_2. XeF_2. m/e=167. TF1903.399.

Figure 2

Xe. MS2607.399.
XeF_2. MS1610.399.

Figure 3-5

θ_i=35°, θ_d=0°, T_s=250 K, 0.25% XeF_2/Ar. ST0701-2.695.

Figure 6

θ_i=35°, θ_d=0°, T_s=250 K, 0.25% XeF_2/Ar. m/e=19. ST0403-5.895.

Figure 7

θ_i=0°, θ_d=35°, T_s=250 K, XeF_2.
m/e=85. ST2001-4.299, ST2503-4.299 ST2601-4.299, ST0101-4.399, ST0201-6.399,ST0301-2.399, ST0401-6.399, ST0503-8.399, ST0801-8.399, ST0901-2.399.

Figures 8-9

θ_i=0°, θ_d=35°, T_s=250 K, XeF_2.

m/e=148,167. ST2001-4.299, ST2503-4.299 ST2601-4.299, ST0101-4.399, ST0201-6.399,ST0301-2.399, ST0401-6.399, ST0503-8.399, ST0801-8.399, ST0901-2.399.

θ_i=0°, θ_d=35°, T_s=250 K, 0.25% XeF_2/Ar.

m/e=148,167. ST2301-2.695.

Figure 10

θ_i=0°, θ_d=35°, T_s=250 K, XeF_2. m/e=19. ST0511-17.599.

Figure 11

F_2. θ_i=20°, θ_d=0°. T_s=250 K, 1% F_2/Ar. ST0903.896.

XeF_2. θ_i=20°, θ_d=0°. T_s=250 K, 0.25% XeF_2/Ar. ST0901.896.

XeF_2 and F_2. θ_i=20°, θ_d=0°. T_s=250 K, 0.25% XeF_2/Ar and 1% F_2/Ar. ST0902.896.

Figure 12

θ_i=35°, θ_d=0°. T_s=250 K, 0.25% XeF_2/Ar. TD0106-21.797, TD0201-0212.797.

Figure 13

Clean. HE2301.896.

F-Si(100). θ_i=20°, T_s=250 K, 1% F_2/Kr. HE2302.896.

F-Si(100). θ_i=20°, T_s=250 K, 0.25% XeF_2/Ar. HE1508.896.

Figure 14

θ_i=35°, θ_d=55°. T_s=250 K, 1% F_2/Kr, 50%He/Ar. ST0901.697.

θ_i=35°, θ_d=55°. T_s=250 K, 0.25% XeF_2/Ar, 50%He/Ar. ST2001.198.

Figure 15

θ_i=35°, θ_d=0°. T_s=250 K, 0.25% XeF_2/Ar. m/e=167. 48 sets of four TOF spectra taken 10/8/97-1/9/98.

Figure 16

See Figure 12.

Figure 17-20

θ_i=35°, T_s=250 K, 0.25% XeF_2/Ar

m/e=167.

θ_d=0°. 48 sets of four TOF spectra taken 10/8/97-1/9/98.
θ_d=10°. 47 sets of four TOF spectra taken 10/8/97-1/9/98.
θ_d=20°. 47 sets of four TOF spectra taken 10/8/97-1/9/98.
θ_d=30°. 48 sets of four TOF spectra taken 10/8/97-1/9/98.
θ_d=40°. 47 sets of four TOF spectra taken 10/8/97-1/9/98.
θ_d=50°. 49 sets of four TOF spectra taken 10/8/97-1/9/98.
θ_d=60°. 50 sets of four TOF spectra taken 10/8/97-1/9/98.
θ_d=70°. 49 sets of four TOF spectra taken 10/8/97-1/9/98.
θ_d=80°. 51 sets of four TOF spectra taken 10/8/97-1/9/98.

Figures 21-22

See Figures 17-20.

Figures 23-24

θ_i=0°, θ_d=35°. T_s=250 K, XeF_2. m/e=167. 75 sets of 20 TOF spectra taken 3/8-9/99.

Figure 25

θ_i=35°, θ_d=0°. T_s=250 K, 0.25% XeF_2/Ar.

m/e=167. See Figure 16.

m/e=148. 35 sets of four TOF spectra taken 10/8/97-1/9/98.

Figure 26-33

θ_i=35°, T_s=250 K, 0.25% XeF_2/Ar.

m/e=167. See Figures 17-20.

m/e=148.

θ_d=0°. See Figure 25.

θ_d=10°. 35 sets of four TOF spectra taken 10/8/97-1/9/98.

θ_d=20°. 38 sets of four TOF spectra taken 10/8/97-1/9/98.

θ_d=30°. 41 sets of four TOF spectra taken 10/8/97-1/9/98.

θ_d=40°. 37 sets of four TOF spectra taken 10/8/97-1/9/98.

θ_d=50°. 41 sets of four TOF spectra taken 10/8/97-1/9/98.

θ_d=60°. 43 sets of four TOF spectra taken 10/8/97-1/9/98.

θ_d=70°. 44 sets of four TOF spectra taken 10/8/97-1/9/98.

θ_d=80°. 40 sets of four TOF spectra taken 10/8/97-1/9/98.

Figure 34-36

See Figures 26-33.

Figures 37-39

θ_i=0°, θ_d=35°. T_s=250 K, XeF_2. m/e=148. 107 sets of 20 TOF spectra taken 3/1-5/99.

Figure 40

θ_i=35°, θ_d=0°. T_s=250 K, 0.25% XeF_2/Ar.

m/e=167. See Figure 16.

m/e=148. See Figure 25.

m/e=40. TF1509.198.

m/e=19. 60 sets of four TOF spectra taken 10/8/97-1/9/98.

Figure 41-48

θ_i=35°, T_s=250 K, 0.25% XeF_2/Ar.

m/e=167. See Figures 17-20.

m/e=148. See Figures 26-33.

m/e=40. TF1501-9.198.

m/e=19.

θ_d=0°. See Figure 25.

θ_d=10°. 35 sets of four TOF spectra taken 10/8/97-1/9/98.

θ_d=20°. 38 sets of four TOF spectra taken 10/8/97-1/9/98.

θ_d=30°. 41 sets of four TOF spectra taken 10/8/97-1/9/98.

θ_d=40°. 37 sets of four TOF spectra taken 10/8/97-1/9/98.

θ_d=50°. 41 sets of four TOF spectra taken 10/8/97-1/9/98.

θ_d=60°. 43 sets of four TOF spectra taken 10/8/97-1/9/98.

θ_d=70°. 44 sets of four TOF spectra taken 10/8/97-1/9/98.

θ_d=80°. 40 sets of four TOF spectra taken 10/8/97-1/9/98.

Figures 49-50

See Figures 41-48.

Figure 51-53

θ_i=0°, θ_d=35°. T_s=250 K, XeF_2. m/e=19. 60 sets of 20 TOF spectra taken 3/10-11/99.

Figures 54-55

θ_i=35°, θ_d=0°. T_s=250 K, 0.25% XeF_2/Ar.

m/e=167. See Figure 16.

m/e=129. 33 sets of four TOF spectra taken 10/8/97-1/9/98.

Figure 56-59

θ_i=35°, T_s=250 K, 0.25% XeF_2/Ar.

m/e=167. See Figures 17-20.

m/e=148. See Figure 26-33.

m/e=129.

θ_d=0°. See Figure 25.

θ_d=10°. 32 sets of four TOF spectra taken 10/8/97-1/9/98.

θ_d=20°. 30 sets of four TOF spectra taken 10/8/97-1/9/98.

θ_d=30°. 31 sets of four TOF spectra taken 10/8/97-1/9/98.

θ_d=40°. 30 sets of four TOF spectra taken 10/8/97-1/9/98.

θ_d=50°. 33 sets of four TOF spectra taken 10/8/97-1/9/98.

θ_d=60°. 32 sets of four TOF spectra taken 10/8/97-1/9/98.

θ_d=70°. 29 sets of four TOF spectra taken 10/8/97-1/9/98.

θ_d=80°. 32 sets of four TOF spectra taken 10/8/97-1/9/98.

Figures 60-64

θ_i=35°, T_s=250 K, 0.25% XeF_2/Ar.

See Figures 54-55.

θ_i=35°, T_s=250 K, 0.25% XeF_2/1% Xe/Ar.

Figure 65

See Figures 60-64.

Figures 66-67

θ_i=0°, θ_d=35°. T_s=250 K, XeF_2. m/e=129. 57 sets of 20 TOF spectra taken 2/20/99-3/10/99.

Figure 68

Low energy XeF_2. See Figures 66-67.

High energy XeF_2. See Figures 56-59.

Figure 69-72

See Figures 56-59.

Figures 73-74

See Figures 69-72.

Figures 75-76

XeF_2. See Figure 21.

Xe. See Figures 65

Figure 77

See Figure 34.

Figure 79

XeF. See Figure 34.

F. See Figure 49.

Figure 82

See Figure 73.

APPENDIX B
Figure 5
With cryopump. MS2601.399.
Without cryopump. MS3001.399.
Figure 7
Ar clusters. MS2805.898.
XeF_2. MS1314.599.